

ADSORPTION OF PURE AND MULTI-COMPONENT
GASES OF IMPORTANCE TO
ENHANCED COALBED METHANE RECOVERY:
MEASUREMENTS AND SIMPLIFIED LOCAL
DENSITY MODELING

By

JAMES EDWARD FITZGERALD

Bachelor of Science

Oklahoma State University

Stillwater, Oklahoma

May 1999

Submitted to the Faculty of the
Graduate College of the
Oklahoma State University
in partial fulfillment of
the requirements for
the Degree of
DOCTOR OF PHILOSOPHY
July 2005

ADSORPTION OF PURE AND MULTI-COMPONENT
GASES OF IMPORTANCE TO
ENHANCED COALBED METHANE RECOVERY:
MEASUREMENTS AND SIMPLIFIED LOCAL
DENSITY MODELING

Dissertation Approved:

KHALED A. M. GASEM

Thesis Advisor

ROBERT L. ROBINSON, Jr.

LIONEL M. RAFF

ARLAND H. JOHANNES

A. GORDON EMSLIE

Dean of the Graduate College

ACKNOWLEDGMENTS

I would like to express my gratitude to my adviser, Professor Khaled A. M. Gasem, for giving me the opportunity to work on this project. My sincere appreciation goes to Dr. Gasem for his intelligent guidance, invaluable assistance and endless support throughout my graduate studies at Oklahoma State University.

My gratitude is also extended to Dr. Robert L. Robinson, Jr., for his expertise, valuable advice and encouragement during my Ph. D. program.

I would also like to thank my graduate advisory committee members, Dr. A.J. Johannes and Dr. Lionel Raff, for their valuable input and guidance during the course of this study.

To many people who have provided me friendship and support during my graduate studies, I say thank you very much, especially, to my colleagues Dr. Zhejun Pan, Dr. Mahmood Sudibandriyo, and Arunkumar Arumugam, who have been great partners in all phases of our collective project dealing with high-pressure adsorption modeling. Their friendship and insight was most critical to the successful completion of this study.

Acknowledgment is due to the United States Department of Energy for the financial support of the research upon which this report is based.

Finally, I would like to extend my sincere thanks to my family for their patience, understanding, and support during the long course of my graduate program.

PREFACE

The Simplified Local Density (SLD) theory was investigated to facilitate precise representations and accurate predictions for high-pressure, supercritical adsorption isotherms encountered in coalbed methane (CBM) recovery and CO₂ sequestration. Specifically, the ability of the SLD model to describe pure and mixed-gas adsorption was assessed using a modified Peng-Robinson (PR) equation of state (EOS). High-pressure adsorption measurements acquired in this study and data from the literature were used in this evaluation. In addition, a new pure-fluid EOS was developed to accommodate the future needs of high-pressure adsorption modeling.

Precise gas adsorption measurements were completed using a constant-pressure, volumetric technique at temperatures between 318 and 328 K (113-131°F) and pressures to 13.8 MPa (2000 psia). These measurements included the pure-gas adsorption of methane, nitrogen, ethane, and CO₂ on eight coals and one activated carbon (wet Fruitland, wet Lower Basin Fruitland coal, wet / dry Illinois #6, wet Tiffany, dry Beulah Zap, dry Wyodak, dry Upper Freeport, dry Pocahontas, and dry Calgon Filtrasorb 400). Mixed-gas measurements for methane, nitrogen and CO₂ were conducted on the activated carbon and wet Tiffany coal.

Analysis of the SLD-PR model indicated that the limiting high-pressure adsorption behavior is governed by the high-density limit of the EOS, which is determined by the EOS covolume. Consequently, modification of the EOS covolume

allowed for precise representation of pure-gas high-pressure adsorption and the reliable prediction of binary and ternary gas mixture adsorption. Specifically, the model can (a) represent adsorption on activated carbon and coals within their expected experimental uncertainties, and (b) provide generalized binary and ternary predictions, within two to three times the experimental uncertainties, based on regressed parameters from pure-gas adsorption data.

A new pure-fluid EOS capable of accurate representation of high-density behavior was developed. This EOS, which covers a wide range of phase conditions, utilizes an accurate hard-sphere repulsive term. Evaluation results for 19 fluids, including coalbed gases (CO₂, methane, and nitrogen) and water, indicated that the new EOS can represent precisely the volumetric behavior and the saturated vapor-liquid equilibrium properties of these pure fluids with average errors of 1%.

TABLE OF CONTENTS

| Chapter | Page |
|---|------|
| 1. INTRODUCTION | 1 |
| Coalbed Methane Production | 1 |
| Sequestration of Carbon Dioxide | 2 |
| Simulation of Coalbed Methane Processes | 4 |
| Adsorption Models | 6 |
| Objectives | 9 |
| Organization | 10 |
| 2. FUNDAMENTALS OF ADSORPTION: BASIC CONCEPTS | 12 |
| Pure Gas Storage | 23 |
| Mixture Adsorption at High Pressures | 26 |
| Mixed-Gas Storage | 33 |
| Gas Adsorption on Wet Adsorbents | 33 |
| 3. EXPERIMENTAL METHOD AND ANALYSIS | 36 |
| Pure-Gas Adsorption Measurements | 39 |
| Mixed-Gas Adsorption Measurements | 44 |
| Calibrations | 45 |
| OSU Database Employed in this Study | 46 |
| 4. SIMPLIFIED LOCAL DENSITY MODEL FOR PURE-GAS ADSORPTION | 52 |
| Testing the Efficacy of the SLD Adsorption Model | 57 |
| Case Study 1: Pure-Gas Adsorption on Wet Coals | 60 |
| Case Study 2: Literature Pure-Gas Adsorption | 78 |
| 5. SIMPLIFIED LOCAL DENSITY MODEL FOR MIXED-GAS ADSORPTION | 106 |
| Testing the SLD Adsorption Model for Mixtures | 110 |
| Case Study 3: Mixture Adsorption on Calgon F-400 Activated Carbon | 111 |
| Case Study 4: Mixture Adsorption on Wet Tiffany Coal | 131 |
| Case Study 5: Mixture Adsorption on Wet Fruitland Coal | 139 |
| Case Study 6: Mixture Adsorption on Wet Illinois #6 Coal | 148 |
| Comparison of SLD-PR Model to the Ono-Kondo Model | 156 |

| Chapter | Page |
|--|------|
| 6. FLUID HARD-SPHERE EQUATION OF STATE | 160 |
| Introduction | 160 |
| Equations of State and SLD Theory for Adsorption | 161 |
| Development of Equation of State for Fluids | 163 |
| Hard-Sphere Compressibility | 167 |
| Attractive Terms | 170 |
| Methods | 172 |
| Quality of Generalized Predictions | 176 |
| Critical Behavior | 185 |
| Second Virial Coefficient | 185 |
| Conclusions | 193 |
| 7. CONCLUSIONS AND RECOMMENDATIONS | 195 |
| Conclusions | 195 |
| Recommendations | 197 |
| REFERENCES | 199 |
| APPENDIX A: LOCAL $a(z)$ FOR FLUID IN A SLIT | 209 |
| APPENDIX B: DERIVATIONS AND SUPPLEMENTARY INFORMATION FOR THE HARD-SPHERE EOS | 210 |
| APPENDIX C: FUGACITY DERIVATIONS FOR THE HARD-SPHERE EOS | 222 |

LIST OF TABLES

| Table | Page |
|--|------|
| 3-1. Parameters for Gas-Water Solubility at 115°F | 42 |
| 3-2. Parameters for CO ₂ -Water Solubility Relationship | 43 |
| 3-3. OSU Adsorption Database | 49 |
| 3-4. Compositional Analysis of Solid Matrices Used in This Study | 50 |
| 3-5. Compositional Analysis of Coals Used in the DOE-NETL Round Robin Study | 51 |
| 3-6. Analysis of BPL Activated Carbon Used in This Study | 51 |
| 4-1. Physical Fluid Parameters | 56 |
| 4-2. Modified SLD Model Results on Activated Carbon at 45°C (113°F) | 71 |
| 4-3. Summary Results for the Modified SLD-PR Adsorption Model | 74 |
| 4-4. Data Used for Pure Gas Adsorption Model Evaluations | 79 |
| 4-5. Results of SLD-PR Model for Pure Gas Adsorption on Activated Carbons, Zeolites and Coals | 85 |
| 4-6. The Effect of Parameter 'k' on the SLD-PR Model Representation | 97 |
| 5-1. Comparison of SLD-PR Model Regression Results for Three Scenarios for the Pure and Binary Mixture Adsorption on Calgon F-400 Activated Carbon | 119 |
| 5-2. Regressed Parameters for SLD-PR Model on Calgon F-400 Activated Carbon | 120 |
| 5-3. Compositional Analyses of Tiffany Coal Samples | 131 |

| Table | Page |
|---|------|
| 5-4. Vitrinite Reflectance Analysis | 133 |
| 5-5. Regressed Parameters for SLD-PR Model on Tiffany Coal at 130°F | 135 |
| 5-6. Summary Results for the SLD-PR Model of Gas-Mixture Adsorption on Wet Tiffany Coal at 130°F | 136 |
| 5-7. Comparison of Regression Results for Two Scenarios for the Pure and Binary Mixture Adsorption on Fruitland Coal at 115°F | 143 |
| 5-8. Regressed Parameters for SLD-PR Model on Fruitland Coal at 115°F | 144 |
| 5-9. Comparison of Regression Results for Two Scenarios for the Pure and Binary Mixture Adsorption on Illinois #6 at 115°F | 151 |
| 5-10. Regressed Parameters for SLD-PR Model on Illinois #6 Coal at 115°F | 152 |
| 5-11. Comparison of the SLD-PR and Ono-Kondo Model Predictions of Mixed-Gas Adsorption on Activated Carbon | 158 |
| 6-1. Most Accurate HS EOS for Different Density Regimes and Comparison to the Yelash EOS | 169 |
| 6-2. NIST Fluids Obtained Used in the HS EOS | 173 |
| 6-3. Absolute Percent Differences in Density and Saturated Pressure between the HS EOS and the NIST EOS for CO ₂ | 179 |
| 6-4. Absolute Percent Differences in Density and Saturated Pressure between the HS EOS and the NIST EOS for Methane | 180 |
| 6-5. Absolute Percent Differences in Density and Saturated Pressure between the HS EOS and the NIST EOS for Nitrogen | 180 |
| 6-6. Absolute Percent Differences in Density and Saturated Pressure between the HS EOS and the NIST EOS for Various Fluids | 181 |
| A-1. Equations for the Local Attractive Parameter $a(z)$ | 209 |
| B-1. NIST Critical Property Values for Fluids Used in the HS EOS | 219 |
| B-2. Regressed Parameter Values for Fluids Used in the HS EOS | 220 |
| B-3. Additional Regressed Parameter Values for Polar Fluids Used in the HS EOS | 221 |

LIST OF FIGURES

| Figure | Page |
|--|------|
| 2-1. The Volume Elements of an Adsorbing System | 15 |
| 2-2. Idealized Depiction of Adsorption at High Pressures | 19 |
| 2-3. Predicted Nitrogen Excess Adsorption at 113°F on Activated Carbon as Function of Pressure | 20 |
| 2-4. Predicted Nitrogen Excess Adsorption at 113°F on Activated Carbon as Function of Gas Density | 20 |
| 2-5. Predicted CO ₂ Excess Adsorption at Various Temperatures | 22 |
| 2-6. Comparison of CO ₂ Excess Adsorption, Absolute Adsorption, and Gas Capacity at 113°F on Activated Carbon | 26 |
| 3-1. Schematic Diagram of the Experimental Apparatus | 37 |
| 3-2. Procedure for Void Volume Determination | 38 |
| 3-3. Procedure for Gas Injection | 40 |
| 4-1. Conceptual Slit Geometry | 53 |
| 4-2. Details of Slit Geometry for SLD Model | 55 |
| 4-3. Excess Adsorption of CO ₂ , Methane, Nitrogen, and Ethane on Filtrasorb 400 Activated Carbon at 45°C (113°F) with Modified SLD Model | 61 |
| 4-4. Comparison of CO ₂ Adsorption Data on Filtrasorb 400 Activated Carbon at 45°C (113°F) | 62 |
| 4-5. Methane Adsorption on Wet Coals at 46.1°C (115°F) with Modified SLD Model | 63 |

| Figure | Page |
|---|------|
| 4-6. Nitrogen Adsorption on Wet Coals at 46.1°C (115°F) with Modified SLD Model | 64 |
| 4-7. CO ₂ Adsorption on Wet Coals at 46.1°C (115°F) with Modified SLD Model | 64 |
| 4-8. Comparison of Pure CO ₂ Density and the CO ₂ Density with Water | 65 |
| 4-9. Improvement of the SLD Model Predictions by PR Covolume Modification | 68 |
| 4-10. Determination of Adsorbed-Phase Density on Activated Carbon at 45°C | 69 |
| 4-11. Effect of PR Covolume on Local Density: CO ₂ at 45°C | 72 |
| 4-12. Effect of PR Covolume on Normalized Local Density: CO ₂ at 45°C | 72 |
| 4-13. Absolute Adsorption Calculated by SLD Model for Activated Carbon at 45°C | 75 |
| 4-14. Absolute Adsorption Calculated by SLD Model for Fruitland Coal at 46.1°C | 76 |
| 4-15. Absolute Adsorption Calculated by SLD Model for Lower Basin Fruitland Coal at 46.1°C | 76 |
| 4-16. Absolute Adsorption Calculated by SLD Model for Illinois #6 Coal at 46.1°C | 77 |
| 4-17. Cumulative Distribution Function of Pressure For Pure-Gas Adsorption on Activated Carbons and Zeolites (2140 data points) | 82 |
| 4-18. Cumulative Distribution Function of Percentage Errors of Adsorption for Activated Carbons and Zeolites | 93 |
| 4-19. Cumulative Distribution Function of Weighted Percentage Errors of Adsorption for Coals | 94 |
| 4-20. Scatter Plot of Percentage Errors of Adsorption for Activated Carbons and Zeolites | 94 |
| 4-21. Methane Adsorption on Carbon Black at Various Temperatures with SLD Model Predictions | 95 |

| Figure | Page |
|--|------|
| 4-22. Methane Adsorption on Charcoal at Various Temperatures with SLD Model Predictions | 96 |
| 4-23. Propane Adsorption on Charcoal at Various Temperatures with SLD Model Predictions | 98 |
| 4-24. Methane Adsorption on Activated Carbon from Coconut Shell with KOH Activation at Various Temperatures with SLD Model Predictions | 98 |
| 4-25. CO ₂ Adsorption on H-Modernite at Various Temperatures with SLD Model Predictions | 101 |
| 4-26. Adsorption on Norit R1 Extra Activated Carbon at 298 K with SLD Model Predictions | 102 |
| 4-27. Adsorption of CO ₂ on Various Dry Coals at 328 K with SLD Model Predictions | 102 |
| 4-28. Adsorption of Methane on Various Wet Coals with SLD Model Predictions | 103 |
| 4-29. Adsorption of Nitrogen on Various Wet Coals with SLD Model Predictions | 103 |
| 4-30. Adsorption of CO ₂ on Various Wet Coals with SLD Model Predictions | 104 |
| 5-1. SLD Model Error Distribution of Binary and Pure-Gas Adsorption on Calgon F-400 Activated Carbon | 116 |
| 5-2. SLD Model of Methane Adsorption in Methane/Nitrogen Mixtures on Calgon F-400 Activated Carbon | 122 |
| 5-3. SLD Model of Nitrogen Adsorption in Methane/Nitrogen Mixtures on Calgon F-400 Activated Carbon | 123 |
| 5-4. SLD Model of Methane Adsorption in Methane/CO ₂ Mixtures on Calgon F-400 Activated Carbon | 123 |
| 5-5. SLD Model of CO ₂ Adsorption in Methane/CO ₂ Mixtures on Calgon F-400 Activated Carbon | 124 |
| 5-6. SLD Model of Nitrogen Adsorption in Nitrogen/CO ₂ Mixtures on Calgon F-400 Activated Carbon | 124 |

| Figure | Page |
|--|------|
| 5-7. SLD Model of CO ₂ Adsorption in Nitrogen/CO ₂ Mixtures on Calgon F-400 Activated Carbon | 125 |
| 5-8. SLD Model Prediction of Gas Phase Compositions for Methane/Nitrogen Feed Mixtures on Calgon F-400 Activated Carbon | 125 |
| 5-9. SLD Model Prediction of Local Densities and Adsorbed Phase Compositions for a 20/80 Methane/Nitrogen Gas Mixture on Calgon F-400 Activated Carbon | 126 |
| 5-10. SLD Model of Ternary Adsorption of 10/40/50 Methane/Nitrogen/CO ₂ Mixture on Calgon F-400 Activated Carbon | 127 |
| 5-11. SLD Model of Methane/Nitrogen Excess Volumes at 25 psia and 2000 psia at C _{ij} Values of 0.0, -0.5 and 0.5 | 129 |
| 5-12. SLD Model of Methane/CO ₂ Excess Volumes at 25 psia and 2000 psia at C _{ij} Values of 0.0, -0.5 and 0.5 | 129 |
| 5-13. SLD Model of Nitrogen/CO ₂ Excess Volumes at 25 psia and 2000 psia at C _{ij} Values of 0.0, -0.5 and 0.5 | 130 |
| 5-14. Tiffany Well #1 Coal Particle Size Distribution | 132 |
| 5-15. SLD Model of Pure-Gas Adsorption on Wet Tiffany Coal at 130°F | 136 |
| 5-16. SLD Model of Methane/Nitrogen 50/50 Feed Gas Adsorption on Wet Tiffany Coal at 130°F | 137 |
| 5-17. SLD Model of Methane/CO ₂ 41/59 Feed Gas Adsorption on Wet Tiffany Coal at 130°F | 137 |
| 5-18. SLD Model of Nitrogen/CO ₂ 20/80 Feed Gas Adsorption on Wet Tiffany Coal at 130°F | 138 |
| 5-19. SLD Model of Methane/Nitrogen/CO ₂ 10/40/50 Feed Gas Adsorption on Wet Tiffany Coal at 130°F | 138 |
| 5-20. SLD Model of Methane Adsorption in Methane/Nitrogen Mixtures on Wet Fruitland Coal at 115°F | 144 |
| 5-21. SLD Model of Nitrogen Adsorption in Methane/Nitrogen Mixtures on Wet Fruitland Coal at 115°F | 145 |

| Figure | Page |
|---|------|
| 5-22. SLD Model of Methane Adsorption in Methane/CO ₂ Mixtures on Wet Fruitland Coal at 115°F | 145 |
| 5-23. SLD Model of CO ₂ Adsorption in Methane/CO ₂ Mixtures on Wet Fruitland Coal at 115°F | 146 |
| 5-24. SLD Model of Nitrogen Adsorption in Nitrogen/CO ₂ Mixtures on Wet Fruitland Coal at 115°F | 146 |
| 5-25. SLD Model of CO ₂ Adsorption in Nitrogen/CO ₂ Mixtures on Wet Fruitland Coal at 115°F | 147 |
| 5-26. SLD Model of Methane Adsorption in Methane/Nitrogen Mixtures on Wet Illinois #6 Coal at 115°F | 152 |
| 5-27. SLD Model of Nitrogen Adsorption in Methane/Nitrogen Mixtures on Wet Illinois #6 Coal at 115°F | 153 |
| 5-28. SLD Model of Methane Adsorption in Methane/CO ₂ Mixtures on Wet Illinois #6 Coal at 115°F | 153 |
| 5-29. SLD Model of CO ₂ Adsorption in Methane/CO ₂ Mixtures on Wet Illinois #6 Coal at 115°F | 154 |
| 5-30. SLD Model of CO ₂ Adsorption in Nitrogen/CO ₂ Mixtures on Wet Illinois #6 Coal at 115°F | 154 |
| 5-31. SLD Model of Nitrogen Adsorption in Nitrogen/CO ₂ Mixtures on Wet Illinois #6 Coal at 115°F | 155 |
| 6-1. Comparison of Various Hard-Sphere Equations of State | 163 |
| 6-2. Comparison of Critical Isotherms in Reduced Coordinates | 167 |
| 6-3. Hard-Sphere Compressibility Data at Very High Compressibilities and Comparison with the Yelash EOS | 169 |
| 6-4. Ratios of the Critical Volume to the Hard-Sphere Volume for the Hard-Sphere EOS and the Peng-Robinson EOS for Several Fluids | 175 |
| 6-5. Overall PVT Representation for CO ₂ Using NIST EOS as Reference | 177 |
| 6-6. Deviation Plot for CO ₂ Density Using NIST EOS as Reference | 178 |

| Figure | Page |
|---|------|
| 6-7. Overall PVT Representation for Methane Using NIST EOS as Reference | 178 |
| 6-8. Representation of Saturated and Compressed Liquid Densities for Water Using NIST EOS as Reference | 179 |
| 6-9. CO ₂ Critical Isotherm Close to the Critical Point | 186 |
| 6-10. Correlation of Hard Sphere Volumes Regressed from the HS EOS and versus Tabulated Values from Reid et al., 1987 | 189 |
| 6-11. Correlation of Hard Sphere Volumes Regressed from the HS EOS versus Tabulated Values from McFall et al., 2004 | 189 |
| 6-12. Comparison of the Second Virial Coefficient from the HS EOS and the Lennard-Jones Potential for Methane | 191 |
| 6-13. Comparison of the Second Virial Coefficient from the HS EOS and the Lennard-Jones Potential for CO ₂ | 192 |
| 6-14. Comparison of the Predicted Boyle Temperatures from Several Gases | 192 |
| 6-15. Comparison of the Second Virial Coefficient from the HS EOS and from the 1974 Tsonopoulos Correlation for non-Polar Gases | 193 |

NOMENCLATURE

| | |
|------------------|--|
| A | surface area |
| a | Peng-Robinson attractive parameter |
| a_{ads} | local Peng-Robinson attractive parameter for adsorbed phase |
| AAD | average absolute deviation |
| %AAD | average absolute percent error |
| B_2 - B_4 | hard-sphere model constants |
| b | Peng-Robinson covolume |
| b_{ads} | modified Peng-Robinson covolume for adsorbed phase |
| C | constant for excess volume model |
| C | constant in model for HS EOS, $C=9$ |
| C_{ij} | binary interaction parameter for species i and j |
| C_1 - C_7 | parameters in temperature functions for HS EOS |
| d | parameter in excess volume model |
| f | fugacity |
| F | Fahrenheit |
| i | dummy index |
| k_B | Boltzmann constant |
| k | empirical parameter for temperature function of ϵ_{fs} |
| GC | gas capacity on a mass basis |
| GCV | gas capacity on a volume basis |
| K | Kelvin |
| L | slit width; defined as the normal distance between the carbon planes |
| N | number of points in regression or number of gas species |
| N_A | Avogadro's number |
| NPTS | number of data points |
| n | amount in moles |

| | |
|------------------------|--|
| n^{Ex} | the excess adsorption |
| P | pressure |
| psia | pounds per square inch absolute |
| R | universal gas constant; Rankine |
| RMSE | root mean square error |
| T | temperature |
| V_{ads} | adsorbed-phase volume |
| $V_{\text{container}}$ | volume of the system container |
| V_{void} | void volume |
| v | specific volume of fluid |
| WAAD | weighted average absolute deviation |
| WRMS | weighted root mean square deviation |
| x | reduced density (reduced to critical density) |
| x_i | composition of species i in the adsorbed phase |
| y_i | composition of species i in the gas phase |
| y | parameter in polar HS EOS |
| Z | compressibility factor |
| z_i | composition of species i in the feed gas |
| z | normal position between carbon planes |
| z' | dummy position variable: $z'=z+\sigma_{\text{ff}}/2$ |

Subscripts and Superscripts

| | |
|-----|-------------------------|
| abs | absolute |
| ads | adsorbed-phase property |
| att | attractive |
| b | bulk property |
| c | critical condition |
| ex | excess |
| ff | fluid-fluid interaction |
| fs | fluid-solid interaction |

| | |
|-------|------------------------------|
| gas | gas phase |
| Gibbs | Gibbsian adsorption quantity |
| hs | hard-sphere |
| He | Helium |
| inj | injected |
| rep | repulsive |
| sol | soluble |
| ss | solid-solid interaction |
| tot | total |
| unads | unadsorbed |

Greek

| | |
|-----------------|--|
| α | temperature dependent function for Peng-Robinson EOS |
| ϵ_{fs} | fluid-solid interaction parameter |
| ξ | hard-sphere packing fraction, excess mole fraction |
| Δ_i | $y_i - \xi_i$ |
| Δ | difference of state 2 from 1; e.g., $\Delta V = V_2 - V_1$ |
| Λ_b | modification parameter to Peng-Robinson covolume |
| λ | parameter in adsorption model |
| μ | chemical potential |
| π | 3.14159... |
| ρ | density |
| ρ_{atoms} | carbon lattice density |
| σ | particle diameter |
| σ_{exp} | expected experimental uncertainty |
| θ | packing fraction |
| Ψ | fluid-solid potential function |

CHAPTER 1

INTRODUCTION

COALBED METHANE PRODUCTION

Deep coalbeds retain large quantities of gases such as methane, nitrogen, and carbon dioxide (CO₂) through the phenomenon of adsorption. In the U.S. alone, estimates predict that coalbeds hold about 135 trillion cubic feet of recoverable gas. This is approximately 14% of U.S. natural gas reserves (Clayton, 1998). The implementation of coalbed methane recovery technology accounted for 6% of the U.S. natural gas production in 1997 (Stevens, 1998), and accounted for 8% in 2003 (EIA, 2005).

In coalbed reservoirs, methane resides inside the microporous coal structure typically at higher densities than the free gas phase due to physical adsorption; in adsorption, when a gas (adsorbate) interacts with the surface of the adsorbent, the solid-gas interactions increase the apparent fluid density near the solid-gas interface to that comparable of a liquid. The adsorbate density is dependent on temperature, pressure, and its molar composition, which comprises other gas species than methane. A typical reservoir will have roughly 90% methane, 8% CO₂, and 2% nitrogen, with traces of other hydrocarbons (Mavor et al., 1999).

Although primary coalbed methane (CBM) recovery operations have been the main mechanism for CBM gas production, recently, efforts have been directed to the development of enhanced CBM recovery (ECBMR) processes using CO₂ and nitrogen

injections. Through the ECBMR process, nitrogen injection was used at coalbed methane well sites to help displace CBM gas (Stevens et al., 1998) and increase the amount of methane production. By combining CO₂ with nitrogen, ECBMR can displace more methane from the coalbed than with nitrogen alone (Arri and Yee, 1992). Injection of nitrogen results in rapid breakthrough in the recovered natural gas, which consequently raises separation costs after recovery (Stevenson and Pinczewski, 1993). CO₂, however, can replace the adsorbed methane on the coal surface and, thus, has a delayed breakthrough in the recovered gas. Although the injection of CO₂ has more technical benefits than that of nitrogen, CO₂ is currently more costly to inject than nitrogen. Studies of economic feasibility and subsequent optimization hinge on coalbed equilibrium models that predict both the quality (purity) and quantity of natural gas recovered.

SEQUESTRATION OF CARBON DIOXIDE

Many scientists, engineers, and government officials have focused on methods to reduce anthropogenic CO₂ emissions. These emissions are responsible for the rising atmospheric CO₂ concentrations and may contribute partially to the rise of global surface temperatures. The Kyoto Protocol has enumerated many potential environmental concerns whose risk of occurrence is correlated with global surface temperatures. This international treaty, ratified recently in 2005 among certain countries (excluding the U.S., Australia, and third-world nations), would require participating industrialized nations to reduce greenhouse gas emissions to 1990 levels before 2012 in an attempt to hedge against the possible risks of climate change. Thus, anticipating more stringent emission

rules in the future, power industries are searching for novel methods that [1] reduce atmospheric CO₂ emissions, [2] utilize known, reliable resources, [3] and are cost effective. ECBMR is a new technology with the potential to meet such goals.

Specifically, injection of CO₂ into reservoirs may help mitigate the adverse effects of potential climate change. Beyond primary and CO₂/nitrogen enhanced coalbed methane production, coalbeds are also potentially attractive sites for sequestering. As a result, sequestration is receiving widespread international attention. Currently, coalbed sequestration of CO₂ could serve as (a) a complement to CO₂ injection into abandoned oil and gas reservoirs, and (b) a viable alternative to other proposed techniques, such as CO₂ injection into deep, confined aquifers, and the deep ocean (Gunter et al., 1999; Winter and Bergman, 1993; U.S. Dept. of Energy, 1993).

The sequestration of CO₂ in unminable coalbed seams is considered more economic (less costly) than other options, largely due to knowledge and experience gained from enhanced oil recovery processes (Holloway, 2005). However, since 1996, only 100,000 tons of CO₂ have been sequestered in the San Juan Basin, which is the coalbed methane reservoir test case for enhanced coalbed methane production. This amount is insignificant in comparison to the estimated 22 Gt CO₂/year from fossil-fuel burning emissions (Holloway, 2005); nevertheless, for compliance under CO₂ emission regulations, sequestration in coalbeds may present the least-cost option for some industries and provide from 11 - 40 Gt of “capacity” (Yamasaki, 2003).

SIMULATION OF COALBED METHANE (CBM) PROCESSES

Experiments and modeling of the adsorption processes applicable to coalbed reservoirs can help determine the best drilling locations for coalbed methane reserves.

Because ECBMR success depends on many unknown factors before a well can be established, accurate reserve estimates are required to secure new investors. Reservoir simulators were developed to predict coalbed methane production and its economic risk factors. To analyze a CBM reservoir, these simulators require several physical parameters, such as adsorbed gas content, drainage area, characteristic sorption time, relative permeability, porosity, etc. (Zuber, 1999). Among these, the adsorbed gas content and permeability are the key factors considered for a prospective reservoir. Therefore, a framework that can predict gas adsorption based on coal physical attributes would be useful in CBM simulators.

For pure components, approximate qualitative relationships are known between the structure of coal and its adsorptive capacity (Michelson and Khavari-Khorasani, 1999). For example, Michelson and others discovered a general increase of saturation sorption levels with vitrinite reflectance; the adsorptive capacity of methane has a generally increasing relationship with the total carbon content. Coals of higher rank and maturity tend to also have higher adsorption capacities. In general, brighter coals (that are vitrinite rich) have larger adsorption capacities than that of duller coals (Crosdale et al., 1998). Generalized relationships between adsorption capacity and coal properties, however, can have errors as high as 100%. For example, the relationship between the methane capacity at 5 MPa and the fixed carbon content of the coal is highly scattered for Bowen Basin Coals (Killingley et al., 1995). Better research methodologies that emphasize both experimental reproducibility and better adsorption models that are rooted in sound theory may decrease this scatter. In addition, scientific dissemination of better

experimental techniques and data reduction may reduce some of the inter-lab reproducibility scatter, as shown in a recent study (Goodman et al., 2004).

For mixture adsorption at any given pressure, many measurements on carbon adsorbents have shown that CO₂ adsorbs more than methane, and methane adsorbs more than nitrogen. What is less known is how to systematically account for the relative amounts of components adsorbed from a gas mixture, especially for high-pressure adsorption. For example, many gas-mixture adsorption experiments have been performed that relied on theoretical estimates (not validated by other scientific processes) of quantities such as the “adsorbed-phase density” to establish the inferred amount adsorbed (Hall, 1993). Thus, data-reduction procedures for mixture adsorption experiments are often dependent on non-measured or assumed quantities. Sometimes the assumptions used in data reduction are contrary to assumptions involved in the *modeling* of the adsorption. For example, an ideal-mixing assumption may be used to calculate the adsorption from experiment, yet the theory applied to modeling the data involves non-ideal mixing.

Recent coalbed methane simulators (Manik, 1999) have the capacity to describe multi-component gas adsorption and even include water as a separate immiscible, non-adsorbed phase. Models that are popular for pure components include the Langmuir (Langmuir, 1918) and Toth isotherms. To predict the mixture adsorption from pure components, most simulators use Ideal Adsorbed Solution (IAS) theory of Myers and Prausnitz (1965). As such, the CBM industry would benefit from accurate, theory-based models, which avoid the computational intensity of statistical mechanics and the oversimplifications of rudimentary models. Also, beyond the requirement of theory,

certain criteria are desired of an adsorption model to be used in CBM operations. A state-of-the-art model should be capable of:

1. Correlating pure component and mixed-gas adsorption data to within the experimental uncertainties on average for pressures to 1800 psia,
2. Predicting the individual-component adsorption data of mixtures within twice the average experimental uncertainty for pressures to 1800 psia,
3. Predicting temperature dependence for pure component adsorption within the experimental uncertainty, and
4. Employing physically meaningful parameters that can be correlated with commonly-known coal properties such as chemical composition, helium density, and vitrinite reflectance.

ADSORPTION MODELS

Adsorption modeling of methane, nitrogen, CO₂, and ethane on porous media such as coal is essential in modeling ECBMR and CO₂ sequestration processes. Thermodynamic EOS models for adsorption provide crucial information that aid in the process design for sequestering waste CO₂ and recovering natural gas from unminable coalbeds. They provide explicit relations among the equilibrium properties (such as the molar composition of the gas phase, the amount adsorbed of each component, etc.). Models, however, require validation, and for the purpose of economic evaluations that ultimately rely on these models, a systematic experimental program is needed to evaluate the efficacy of adsorption models and to recommend improvements.

Physical adsorption is assumed to be the most dominant phenomenon for the uptake of gas by coals. White et al. (2005) has reviewed various adsorption models used

for gas adsorption on coals. The Langmuir (Langmuir, 1918), Brunauer-Emmett-Teller (BET) (Brunauer et al., 1938), Dubinin-Astakhov (D-A) (Dubinin, 1966), Ono-Kondo (Ono and Kondo, 1960), and two-dimensional (2D) models (see e.g., deGance, 1992, and Zhou et al., 1994) have had varying success in their abilities to correlate the pure-gas adsorption and to predict mixed-gas adsorption. For coals, modeling studies of adsorption are generally limited to low pressures.

Ideal Adsorbed Solution (IAS) theory (Myers and Prausnitz, 1965) is often used in conjunction with pure-gas adsorption models for prediction of mixed gas adsorption. For mixed-gas adsorption using IAS theory and the Langmuir model, predictions of gas composition versus adsorbed gas composition is always symmetric about the composition axis (Zhou et al. 1994). Further, the choice of the pure gas isotherm model has a great effect on the predictive capability of mixture adsorption using IAS theory or non-IAS theory (Zhou et al. 1994). Clark and Bustin have concluded that predictions of mixed-gas adsorption “are strongly dependent upon choice of the pure gas isotherm” (White et al., 2005).

Various methods of developing a non-ideal solution theory through a 2-dimensional EOS have been implemented (deGance, 1992; Zhou et al., 1994; Pan, 2003). Recent studies at OSU have concluded that non-IAS theories are capable of correlating mixed-gas adsorption on activated carbon between 1-2 times the average expected experimental uncertainties of the component amounts (see, e.g., Sudibandriyo et al., 2003; Pan, 2003; Fitzgerald et al., 2005).

For modeling studies on coal, assumptions used in data reduction procedures significantly affect, as will be discussed in Chapter 2, the absolute adsorption calculated,

especially at higher pressures and for CO₂ or ethane. For example, some of the past modeling inadequacies are in part due to uncertain values of the adsorbed-phase density used to calculate the absolute adsorption (Fitzgerald et al., 2005). Thus, caution is appropriate when evaluating high-pressure adsorption measurements in the literature.

Several experimental techniques exist (Keller et al., 1998), and, for each technique, random errors in the measurements can lead to *inferred* adsorption values with high uncertainty if the experiment is not carefully designed. The size and type of errors are determined by experimental setup constraints. While no experimental technique is inclusive of all measurement types (e.g., low-pressure/high-pressure, low-sorbing / high-sorbing fluids), systemic analysis of the experimental errors can be used to gauge the anticipated accuracy of measurements in literature data.

A summary of current research groups (including the OSU Thermodynamics Research Group) investigating supercritical adsorption and their predominantly-used theoretical approaches have been summarized (Do and Do, 2003). Theoretical approaches include the Ono-Kondo model (Ono and Kondo, 1960), 2D EOS models, the Simplified Local Density (SLD) model (Rangarajan et al., 1995), and computer simulations. Our group at OSU initially began work with 2D EOS and Langmuir-type models to model adsorption on coals and other adsorbents (Zhou et al., 1994; Hall et al., 1994). Although our efforts have continued with 2-D EOS modeling (Sudibandriyo et al., 2003; Fitzgerald et al., 2005), more recently our efforts have included the Ono-Kondo (Sudibandriyo, 2003) and SLD theories (Fitzgerald et al., 2003; Gasem et al., 2003).

OBJECTIVES

The main focus for this dissertation is the development of adsorption models based on the SLD theory capable of describing gas adsorption on heterogeneous matrices at elevated pressures, as encountered in CBM operations. The SLD (1) provides a consistent theory which accounts for adsorbate-adsorbate (fluid-fluid) and adsorbate-adsorbent (fluid-solid) molecular interactions, and (2) delineates the adsorbent structural properties based on assumed physical geometries of the adsorbent. Furthermore, the SLD framework allows various fluid EOSs to be used for the prediction of the adsorbate molecular interactions. Among these are the van der Waals EOS (Rangarajan and Lira, 1995) and the Elliot-Suresh-Donohue EOS (Soule et al., 2001). *However, examination of the modeling capabilities of the original SLD model for CBM systems revealed its inadequacy in describing the adsorption behavior of CO₂ and ethane at high pressures.*

The premise of this study is that the SLD framework can be further developed to meet the modeling demands of coalbed methane processes. Specifically, the SLD model coupled with a sufficiently accurate equation of state that exhibits the hard-sphere density limits at high pressures will:

1. Describe high-pressure adsorption because the model physics accounts for adsorption far from the adsorption surface
2. Describe mixture adsorption because the model physics are based on equations of state that account for non-ideality of the adsorbed phase
3. Delineate the adsorbent structural properties from the fluid properties based on assumed physical geometries of the adsorbent

In summary, the *hypothesis* is that the SLD framework, coupled with a sufficiently accurate equation of state, can model accurately the high-pressure mixture adsorption of deep coalbed gases on coal by using the physical-chemical characteristics of the coal and gases.

The main *objectives* of the present work are:

1. Obtain reliable, experimental adsorption data for light hydrocarbon gases, nitrogen, and CO₂ on various coals and activated carbons for temperatures near 115°F and pressures to 2000 psia.
2. Within the SLD framework, modify the Peng-Robinson equation of state so that it (a) correlates the experimental adsorption data to within one standard deviation for pure components, binary mixtures and ternary mixtures, and (b) predicts accurately binary adsorption from pure component information to within two standard deviations.
3. Develop a new pure-fluid EOS capable of accurately describing volumetric fluid behavior at high densities.

ORGANIZATION

Chapter 2 provides an overview of the theory behind the adsorption experiment and the definitions and assumptions required to describe adequately the adsorption phenomenon at high pressures for gas mixtures. Chapter 3 outlines the experimental method and the working equations for calculating the amount adsorbed from observed laboratory measurements. It also provides a database of the measurements where the author had significant involvement. Chapter 4 reviews the SLD framework for pure-gas adsorption. The Peng-Robinson EOS is used within the SLD framework to calculate the

pure-gas adsorption for measurements documented in the literature and those performed at OSU. The correlative results are discussed and new methods are recommended to improve the correlative fit of the model. Chapter 5 outlines the extension of the SLD framework to gas mixtures. The correlative and predictive capabilities of the SLD model for binary and ternary gas mixtures are explored in several case studies. Chapter 6 describes the development a pure-gas EOS that incorporates a hard-sphere repulsion term and reproduces molecular simulation data reasonably well. The ability of the EOS to predict volumetric and saturation properties for several fluids is discussed. Chapter 7 presents conclusions and recommendations from this work.

CHAPTER 2

FUNDAMENTALS OF ADSORPTION: BASIC CONCEPTS

The adsorption of gases on adsorbents such as coals and activated carbons changes the fluid density of the adsorbing gases near the surface of the adsorbent. This density change is why coalbed methane reservoirs hold more gas than would be expected for a traditional gas reservoir at the same pressure. Measurement of the amount of gas adsorbed on a coal or activated carbon at different temperatures and pressures is not a trivial experiment.

The measured adsorption is an inferred quantity from basic measurements such as pressure, temperature, and volume. Adsorption data are reported in a variety of ways due to the varying interests of theorists and practitioners in the field of adsorption. For example, a coalbed methane well operator wants to know the volume of gas that can be extracted from a ton of coal. Often, such practitioners use absolute adsorption to estimate the amount of gas in a reservoir; albeit, they rely on experimental excess adsorption measurements to determine absolute adsorption. A theorist considers the amount of gas adsorbed per unit of adsorbent surface area. An engineer designing compact gas storage containers optimizes the amount of gas adsorbed per unit volume. An engineer separating gas mixtures through adsorption processes wants to know the relative amounts of each component gas adsorbed, as well as concentration differences between the adsorbed-gas phase and the unadsorbed gas.

From the perspective of satisfying as many practitioners as possible, the adsorption experimentalist must present empirical results in compact form by formulation of adsorption theories while adhering to well-known physical principles (such as energy and mass conservation). The experimental approach taken for high-pressure adsorption is to seek the best definition for an inferred adsorption quantity with the smallest possible number of caveats in its inference. For adsorbing gases of high density (i.e., at high pressures), the “excess adsorption” is the experimentally determined quantity most often measured in the laboratory.

For pure-component gases, excess adsorption is defined as the amount of a gas occupying a phase volume near the surface of a solid, in excess of that which would occur without the presence of the surface. The adsorbed gas molecules reside in one or more layers on the surface at a higher density than the gas phase. The volume of space encompassing these layers is called the adsorbed-phase volume, V_{ads} . From a molecular perspective, V_{ads} is the space where fluid-solid interactions exist (which can be represented quantitatively by a potential function). The adsorbed-phase density, $\bar{\rho}_{\text{ads}}$, is averaged over the adsorbed-phase volume. The actual amount adsorbed is the amount of gas residing in the adsorbed-phase volume, often referred to as the absolute adsorption, $n_{\text{ads}}^{\text{abs}}$. Neither the adsorbed-phase volume, the adsorbed-phase density, nor the absolute adsorption is experimentally attainable in a straightforward manner. This is true for most experimental techniques, including adsorption measurements based on gravimetric or volumetric accounting principles. Both methods have been reviewed in detail elsewhere (Keller et al., 1998). For completeness and a new perspective, the principles of the volumetric method (used in the present study) are discussed here.

For an adsorption experiment using volumetric methods, a known mass of adsorbent is placed in a container. A known amount of gas, n_{inj} , is injected (from another container), into the container with the adsorbent. Under the presumption that an experimental method exists that can measure the amount of gas that does not adsorb, i.e. the *unadsorbed gas*, n_{unads} , the difference between the amount injected into the container and the amount of unadsorbed gas is called the absolute adsorption, n^{abs} , usually reported on the basis of a unit mass of adsorbent.

$$n^{abs} = n_{inj} - n_{unads} \quad (2-1)$$

This method has an important assumption: the amount of unadsorbed gas cannot be determined unambiguously at all experimental conditions and, thus, calculating the absolute adsorption by Equation (2-1) is not always feasible. The amount of unadsorbed gas cannot be determined because the volume of unadsorbed gas is not constant with pressure or temperature. The sum of the adsorbed gas and unadsorbed gas volumes, however, can be presumed constant. This volume is the “void volume” and is equal to the container volume minus the adsorbent volume. Because a non-adsorbing gas such as helium determines this volume, it often is referred to as the “helium” void volume, which is the container volume excluding the volume of adsorbent that is impenetrable to helium. Figure 2-1 depicts the various volume elements inside a container.

$$V_{Void}^{He} = V_{Container} - V_{Adsorbent}^{He} = V_{ads} + V_{unads} \quad (2-2)$$

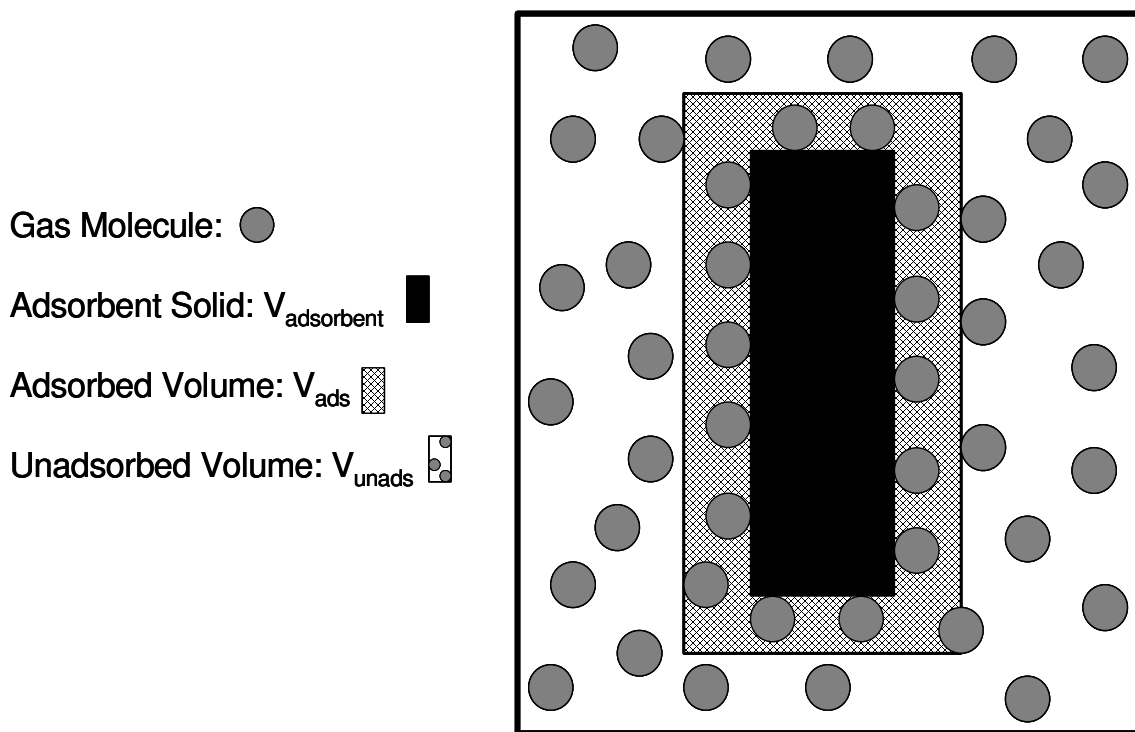


Figure 2-1. The Volume Elements of an Adsorbing System

In determining the helium void volume, the assumption that helium does not adsorb has been explored elsewhere in detail, and Gumma and Talu (2003) proposed a method whereby helium adsorption data are used to estimate a correction for the helium void volume. As they noted, such efforts may not be entirely necessary, and no universal method has been agreed upon to “fix” this problem. All that is required is a thermodynamic reference state, a procedure that has been formalized recently (Myers, 2002). If a “helium adsorption” correction is used, its size depends on other experimental system constraints and experimental design features. In other words, an adsorption experiment can be designed that renders the “helium adsorption” correction as trivial in comparison to other experimental errors.

Another assumption is that the adsorbent volume impenetrable to helium is also impenetrable to all other gases. In other words, an adsorbent would not unfold or unravel

in the presence of a gas (such as CO₂) and thereby have more volume available to that gas (a change in the void volume). For this experimental work, these assumptions appear to be valid based on the invariance of helium void volume measurements before and after the gas adsorption on dry coals. Even in the presence of a reversibly swelling coal (a coal that swells upon adsorption and contracts upon desorption), it is possible that the void volume does not change but the adsorbed-phase volume changes during the adsorption/desorption process. Others have dealt with the possible case where the void volume changes upon adsorption due to swelling (Ozdemir et al., 2003).

At conditions favoring relatively low adsorption amounts (i.e., at low pressures), the volume of the adsorbed phase is negligible when compared to the volume of the unadsorbed phase. Thus, at low pressures, the helium void volume may be assumed equal to the unadsorbed volume:

$$V_{\text{Void}}^{\text{He}} = V_{\text{unads}} \quad (\text{at low pressures}) \quad (2-3)$$

Using the assumption of a zero-volume adsorbed phase allows for the calculation of the amount unadsorbed. The absolute amount adsorbed then can be calculated using Equation (2-1) by recognizing the amount unadsorbed is the product of the gas density and the helium void volume:

$$n^{\text{abs}} = n_{\text{inj}} - \rho_{\text{gas}} V_{\text{Void}}^{\text{He}} \quad (\text{at low pressures}) \quad (2-4)$$

In the use of Equation (2-4), the assumption of a zero-volume adsorbed phase affects the accuracy of the inferred absolute amount adsorbed. As pressure increases, the adsorbed-phase volume will grow in size, and the helium void volume will be larger than

the unadsorbed phase volume. Thus, at higher pressures, Equation (2-4) will under-predict the absolute amount adsorbed. In general, the absolute amount adsorbed cannot be determined experimentally with confidence at high-pressure conditions. Instead, a quantity is defined that is valid at both high-pressure and low-pressure conditions - the “excess” adsorption:

$$n^{\text{Ex}} \equiv n_{\text{inj}} - \rho_{\text{gas}} V_{\text{Void}}^{\text{He}} \quad (\text{all pressures}) \quad (2-5)$$

As noted earlier, the excess adsorption becomes identical to the absolute adsorption in the limit of zero adsorption.

Equation (2-5) is written from the perspective of the experimentalist, i.e., in terms of measured quantities. As mentioned previously, the only assumptions present in Equation (2-5) is the validity of the method used to determine the helium void volume, and whether this volume is applicable to gases other than helium. Another convenient way of writing Equation (2-5) is to define the second term as the *Gibbsian* unadsorbed amount, which is the amount of unadsorbed gas that would occupy the helium void volume:

$$n_{\text{unads}}^{\text{Gibbs}} \equiv \rho_{\text{gas}} V_{\text{Void}}^{\text{He}} \quad (2-6)$$

The term *Gibbsian* is used here to distinguish the actual amount of gas unadsorbed, n_{unads} , from the amount unadsorbed assuming a zero-volume adsorbed phase.

$$n_{\text{unads}}^{\text{Gibbs}} = n_{\text{unads}} + \rho_{\text{gas}} V_{\text{ads}} = \rho_{\text{gas}} (V_{\text{unads}} + V_{\text{ads}}) \quad (2-7)$$

This terminology allows for a more concise definition for the excess adsorption:

$$n^{Ex} = n_{inj} - n_{unads}^{Gibbs} \quad (2-8)$$

Some physical insight can be gained on the nature of the excess adsorption when Equation (2-8) is written in terms of averaged phase densities and phase volumes:

$$n^{Ex} = (V_{ads} \bar{\rho}_{ads} + V_{unads} \rho_{gas}) - \rho_{gas} (V_{ads} + V_{unads}) \quad (2-9)$$

Upon simplification:

$$n^{Ex} = V_{ads} (\bar{\rho}_{ads} - \rho_{gas}) \quad (2-10)$$

An idealized depiction of the adsorption phenomenon in the context of the adsorbed-phase volume and the average adsorbed density is shown in Figure 2-2. As mentioned previously, the adsorbed-phase volume is where fluid-solid interactions are present nearby the solid surface.

For conditions where the gas density is the same as the average adsorbed density, the excess adsorption is zero. At very high gas densities, the excess adsorption can become negative and this can be interpreted physically to indicate that the adsorbed phase is nearly incompressible due to fluid-solid interactions, whereas the gas density, lacking the fluid-solid interactions, is more compressible, and thus can surpass the average adsorbed phase density.

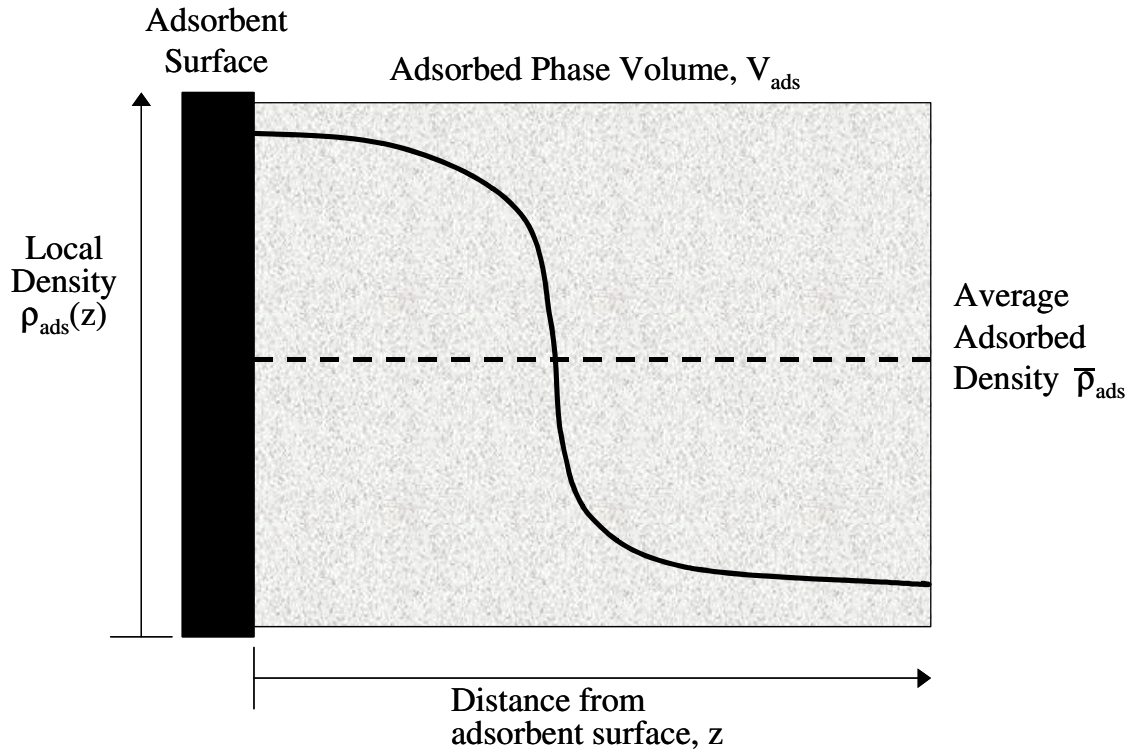


Figure 2-2. Idealized Depiction of Adsorption at High Pressures

At temperatures above the critical temperature of a gas, i.e., supercritical temperatures, an adsorption isotherm will not have any sharp discontinuities due to gas condensation. An example of supercritical adsorption over a wide pressure range is shown in Figure 2-3, which depicts the model-predicted nitrogen excess adsorption at 113°F on an activated carbon. The Simplified Local Density model, which is discussed extensively in Chapters 4 and 6, is used for these predictions. Figure 2-4 depicts this adsorption as a function of gas density. (Note both SI and English engineering units are used in this study to accommodate the needs of engineering practice and modeling efforts.)

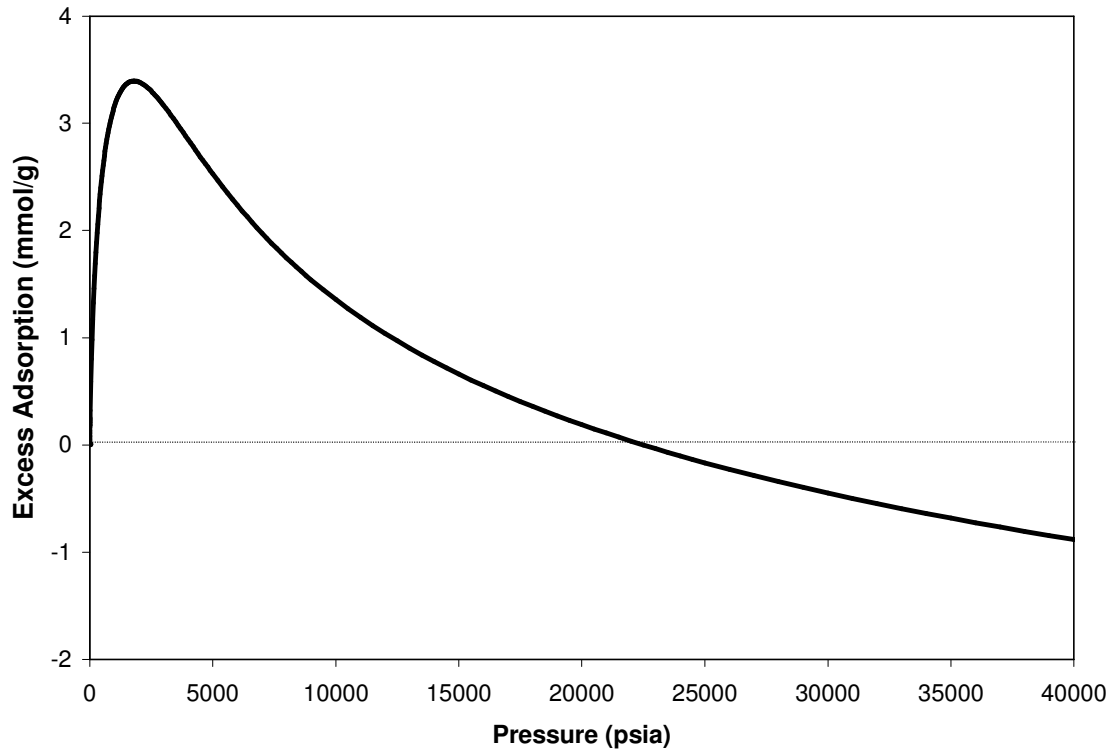


Figure 2-3: Predicted Nitrogen Excess Adsorption at 113 °F on Activated Carbon as Function of Pressure

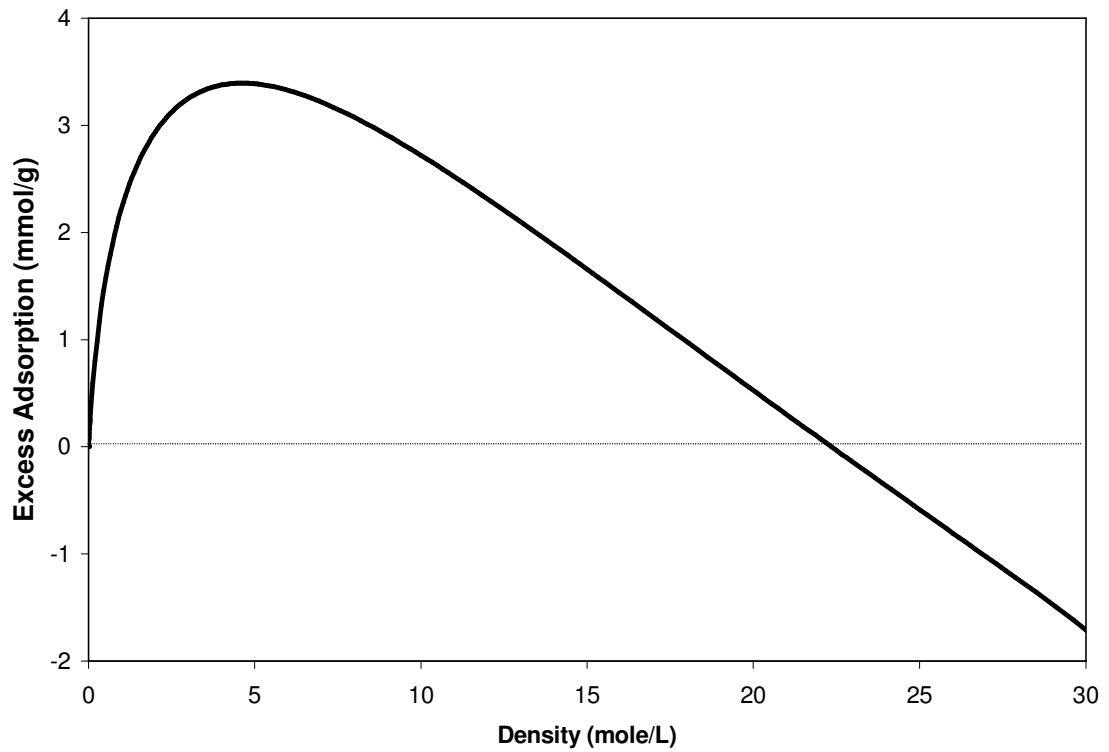


Figure 2-4: Predicted Nitrogen Excess Adsorption at 113°F on Activated Carbon as Function of Gas Density

At subcritical temperatures, an adsorption isotherm discontinuity may arise when the gas reaches its saturation pressure. The density of the bulk phase (the unadsorbed phase) in Equation (2-10) can be estimated in terms of a liquid, a generic fluid, or a gas. Adsorption of liquids can be analyzed theoretically using Equation (2-10); however, experimental methods for liquids via Equation (2-8) would be highly uncertain. (Experimental uncertainty of the fluid amount injected and unadsorbed increase with the amount of fluid material injected, i.e., the density of the fluid). For this work, most adsorption is *gas* adsorption, the nomenclature used. An example of excess adsorption at various temperatures is depicted in Figure 2-5. The isotherms depict the model-predicted CO₂ excess adsorption on activated carbon at subcritical and supercritical temperatures and the critical temperature.

The excess adsorption, an inferred adsorption quantity, can be related to other quantities that are more applicable to engineering tasks, such as the gas capacity and the absolute adsorption. To relate the excess adsorption to quantities such as absolute adsorption, however, sometimes requires additional assumptions on the physical nature of the adsorption. For example, the absolute adsorption can be calculated from the excess adsorption if the adsorbed-phase volume is known:

$$n^{\text{abs}} = n^{\text{Ex}} + \rho_{\text{gas}} V_{\text{ads}} \quad (2-11)$$

Alternatively, Equation (2-10) can be rearranged to express the excess adsorption in terms of adsorbed-phase density. First, the adsorbed-phase volume is expressed in terms of the absolute adsorption and the adsorbed-phase density:

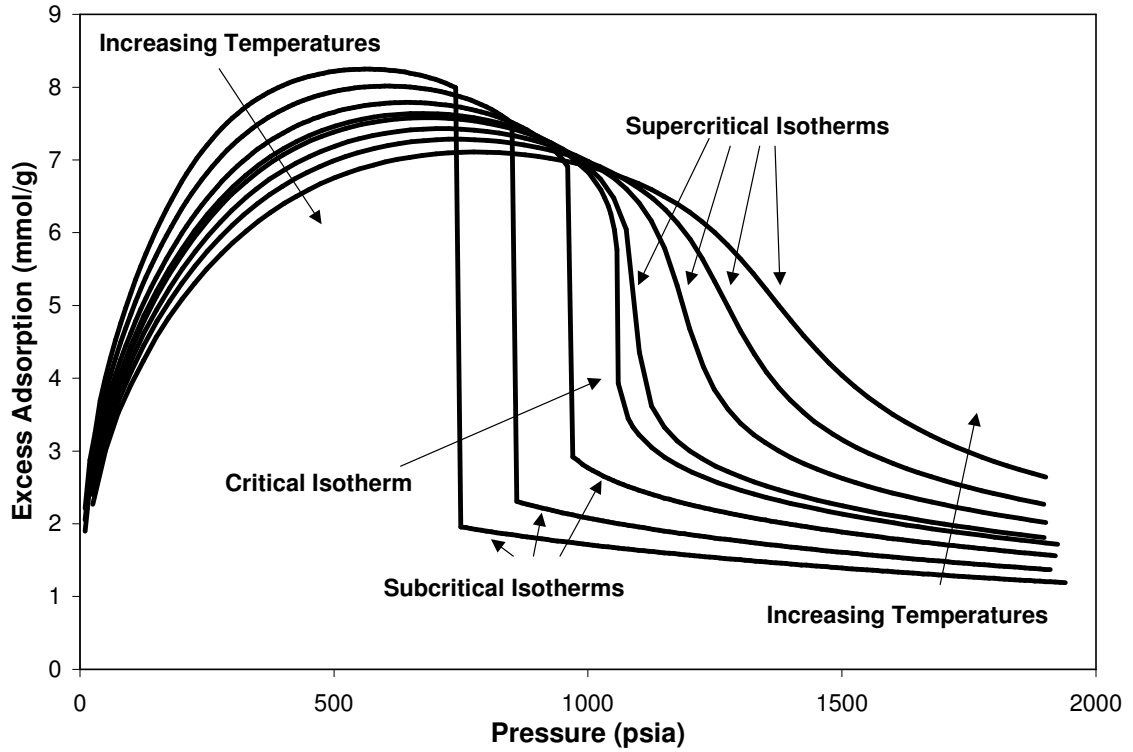


Figure 2-5: Predicted CO₂ Excess Adsorption at Various Temperatures

$$n^{\text{Ex}} = \frac{n^{\text{abs}}}{\bar{\rho}_{\text{ads}}} (\bar{\rho}_{\text{ads}} - \rho_{\text{gas}}) \quad (2-12)$$

Next, Equation (2-9) is rearranged for explicit solution of the absolute adsorption:

$$n^{\text{abs}} = n^{\text{Ex}} \frac{\bar{\rho}_{\text{ads}}}{(\bar{\rho}_{\text{ads}} - \rho_{\text{gas}})} \quad (2-13)$$

As shown in Equation (2-13), the adsorbed phase density is needed to calculate the absolute adsorption. Experimental studies in the literature have used this formula to express the results in terms of absolute adsorption. The adsorbed-phase density is usually assumed to be constant at all pressures. Arri and Yee (1992) and the research group at Oklahoma State University have assumed that the adsorbed-phase density is

approximately equal to the liquid density at the normal boiling point. In the case of CO₂, which sublimates at atmospheric pressure, its solid density is used instead.

Equation (2-13) suffers a deficiency at very high pressures. As mentioned previously, the excess adsorption is zero when the adsorbed-phase density and the gas density are the same. Provided that the adsorbed-phase density is determined by noting the gas density at zero excess adsorption, the absolute adsorption given by Equation (2-13) is indeterminate. If an estimate for the adsorbed phase density is too low, then the absolute adsorption will diverge to infinity at this gas density. If the estimate is too high, the absolute adsorption is under predicted and may even have a maximum and a minimum. In this regard, Equation (2-11) is preferable to Equation (2-13) to estimate the absolute adsorption from the excess adsorption, especially at higher pressures.

For calculating the absolute adsorption, the assumption of a constant adsorbed-phase volume with Equation (2-11) has fewer disadvantages than the assumption of a constant adsorbed phase density with Equation (2-13). If the estimate for the adsorbed phase volume is too low or too high, uncharacteristic effects of the absolute adsorption may be predicted such as a maximum or a minimum; nevertheless, Equation (2-11) will not diverge to infinity for finite values of the excess adsorption, unlike Equation (2-13). Various methods of estimating the adsorbed-phase volume are presented in Chapter 4.

PURE-GAS STORAGE

For coalbed methane simulators and for estimating gas storage by adsorption, the gas capacity is a more useful concept than that of the absolute adsorption. The gas capacity specifies how much gas is stored in a container of given volume occupied by an

adsorbent of given mass and volume for various pressure and temperature conditions. The gas capacity can be shown to be a function of the excess adsorption, the adsorbent helium density, and adsorbent apparent density. The helium density is defined as the reciprocal of the adsorbent specific volume, which is the volume of helium displaced by a unit mass of adsorbent:

$$\rho_{\text{adsorbent}}^{\text{He}} = \frac{\text{mass of adsorbent}}{\text{adsorbent volume}} \quad (2-14)$$

The apparent density is the ratio of the adsorbent mass to the container volume. If the container volume that the adsorbent occupies is compressed or expanded, then the apparent density will change accordingly:

$$\rho_{\text{adsorbent}}^{\text{apparent}} = \frac{\text{mass of adsorbent}}{\text{container volume}} \quad (2-15)$$

The ratio of the apparent density and the helium density is the packing fraction:

$$\theta_{\text{pack}} = \frac{\rho_{\text{adsorbent}}^{\text{apparent}}}{\rho_{\text{adsorbent}}^{\text{He}}} = \frac{\text{adsorbent volume}}{\text{total volume}} \quad (2-16)$$

The packing fraction and the free-space fraction sum to unity:

$$\theta_{\text{free}} + \theta_{\text{pack}} = 1 \quad (2-17)$$

The free-space fraction is related to the helium void volume:

$$\theta_{\text{free}} = \frac{V_{\text{Void}}^{\text{He}}}{\text{total volume}} \quad (2-18)$$

Using this concept of a packing fraction, the gas capacity is:

$$n^{GC} = n^{Ex} + \frac{\rho_{gas}}{\rho_{Helium}} \left(\frac{1}{\theta_{pack}} - 1 \right) = n^{Ex} + \frac{\rho_{gas}}{\rho_{Helium}} \frac{\theta_{free}}{\theta_{pack}} \quad (2-19)$$

The gas capacity derived in Equation (2-19) is the amount of gas per unit adsorbent mass.

The gas capacity can also be written on a per unit volume basis:

$$n^{GCV} = n^{Ex} \rho_{Helium} \theta_{pack} + \rho_{gas} \theta_{free} \quad (2-20)$$

In Equations (2-19) and (2-20), for a specified gas, the excess adsorption and the helium density are sole properties of the adsorbent, whereas the packing fraction depends on the arbitrary constraints of the analyzed system, namely the mass of adsorbent in the system volume. Past experimental attempts in measuring the adsorption of various adsorbents have not always separated arbitrary system constraints (such as packing fractions) to inferred adsorption quantities specific to the adsorbent (such as excess adsorption). Without stating these system constraints, the experimental results are not reproducible on an inter-laboratory basis. For example, by degassing a retrieved coal sample (where the sample volume is known) from the reservoir pressure to a lower pressure, the difference in gas capacities (on a per unit volume basis) can be measured between the two pressures. The difference in excess adsorptions between the two pressures is ambiguous unless the amount of coal and the helium density of the coal are also known.

Figure 2-6 depicts the behavior of the excess adsorption, absolute adsorption and the gas capacity for carbon dioxide at 113°F on activated carbon. For this case, the

absolute adsorption is about 10% greater than the excess adsorption at 600 psia. At this pressure, the percentage of gas in the container that is adsorbed (the percentage of absolute adsorption to the gas capacity) is roughly 80%. At 1300 psia, the percentage is 50%. At increasingly higher pressures, the container will hold more gas; however, this is due mainly to the compressibility of the gas phase and not gas adsorption.

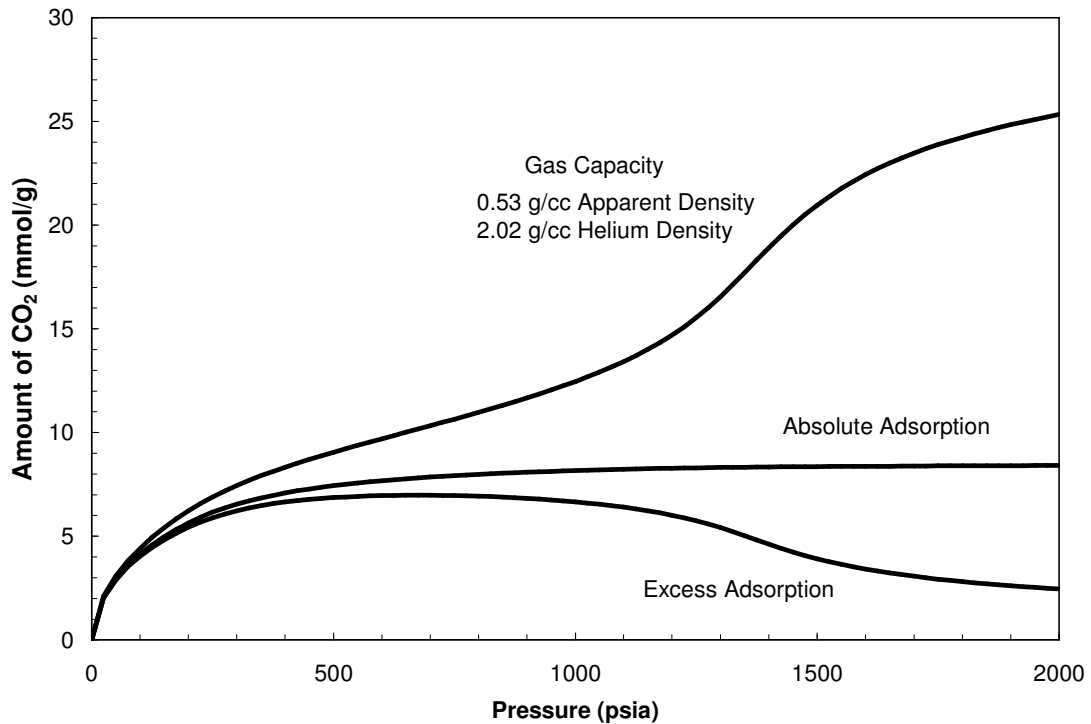


Figure 2-6: Comparison of CO₂ Excess Adsorption, Absolute Adsorption, and Gas Capacity at 113°F on Activated Carbon

MIXTURE ADSORPTION AT HIGH PRESSURES

Data on the adsorption of gas mixtures are necessary to validate theories for mixture adsorption. Few experimental studies have been performed, and of those performed, most are at pressures low enough that differences between the excess and the absolute adsorption are expected to be negligible. Similar to experimental techniques for

pure component adsorption, no technique exists to infer the absolute adsorption of gas mixtures without assumptions on the physical nature of the adsorption. However, applying basic mass and volume conservation principles allows for definitions of the excess adsorption gas mixture components that are extendable from pure-component definitions.

Consider, at equilibrium, a system volume containing an adsorbent and a gas mixture. The volume balance described by Equation (2-2) applies for gas mixtures: a gas mixture occupies volume space either in the adsorbed or unadsorbed phase volumes. Each gas component has a molar composition for these phase volumes and an overall molar gas composition for the system volume, or feed composition. Like the case for pure component adsorption, the adsorbed-phase density or adsorbed-phase volume for the gas mixture adsorption is not experimentally accessible in general. For mixtures, the molar composition of the adsorbed phase, x_i^{abs} , is also inaccessible in general.

Consider a molar amount of the gas mixture, n^{tot} , having feed compositions, z_i , being injected into the system volume with the adsorbent. After equilibrium is reached, the mole fractions of the unadsorbed gas mixture, y_i , are measured. A mass balance can be stated for each component i :

$$z_i n^{total} = V_{ads} \bar{\rho}_{ads} x_i^{Abs} + V_{unads} \rho_{gas} y_i \quad (2-21)$$

In Equation (2-21), the unadsorbed-phase volume or the adsorbed-phase volume is inaccessible in general. However, at pressures low enough where the adsorbed-phase volume can be considered negligible, the unadsorbed-phase volume is equal to the helium

void volume. The absolute adsorption for each component is expressed using either the adsorbed-phase volume or the unadsorbed-phase volume:

$$n_i^{\text{Abs}} = V_{\text{ads}} \bar{\rho}_{\text{ads}} x_i^{\text{Abs}} = z_i n^{\text{total}} - V_{\text{unads}} \rho_{\text{gas}} y_i \quad (2-22)$$

Analogous to the case for pure adsorption, the excess adsorption for mixtures is defined by replacing the experimentally inaccessible unadsorbed-phase volume with the helium void volume:

$$n_i^{\text{Ex}} = z_i n^{\text{total}} - V_{\text{Void}}^{\text{He}} \rho_{\text{gas}} y_i \quad (2-23)$$

Equation (2-23) defines the excess adsorption for a component in a gas mixture from the perspective of the experimentalist using the volumetric technique. The gravimetric technique can also be used to infer the excess adsorption. More physical insight can be gained if Equation (2-23) is rearranged with the use of Equation (2-2):

$$n_i^{\text{Ex}} = V_{\text{ads}} (\bar{\rho}_{\text{ads}} x_i^{\text{Abs}} - \rho_{\text{gas}} y_i) \quad (2-24)$$

At low gas densities, the excess adsorption is the same as the absolute adsorption, and Equation (2-24) becomes Equation (2-10) in the case for a pure component. Because the mole fraction of the adsorbed phase is experimentally inaccessible, a convenient quantity can be defined, the component “excess mole fraction, ξ_i^{Ex} ” of the adsorbed phase:

$$\xi_i^{\text{Ex}} \equiv \frac{n_i^{\text{Ex}}}{n_{\text{tot}}^{\text{Ex}}} \quad (2-25)$$

The excess mole fraction does not have a physical meaning. Its value may range from negative infinity to positive infinity or is undefined if the total excess adsorption is zero. However, by using this definition for the excess adsorption, a relationship between the absolute and excess mole fraction of the adsorbed phase can be expressed, upon rearrangement of Equation (2-24):

$$x_i^{\text{Abs}} = \xi_i^{\text{Ex}} \left(1 - \frac{\rho_{\text{gas}}}{\bar{\rho}_{\text{ads}}} \right) + y_i \left(\frac{\rho_{\text{gas}}}{\bar{\rho}_{\text{ads}}} \right) \quad (2-26)$$

For low gas densities, the excess mole fraction and the absolute mole fraction are identical. To find the absolute mole fraction at higher gas densities requires information on the mixture adsorbed-phase density.

$$\frac{1}{\bar{\rho}_{\text{ads}}} = \sum_{i=1}^n \frac{x_i^{\text{Abs}}}{\bar{\rho}_{\text{ads},i}} + v^{\text{Ex}} \quad (2-27)$$

The usual assumption is to assume ideal mixing of the pure components, where v^{Ex} is set equal to zero.

The absolute mole fraction for each component in a binary mixture can be calculated explicitly in terms of pure component adsorbed-phase densities and excess mole fractions:

$$x_1^{\text{Abs}} = \frac{\xi_1^{\text{Ex}} \bar{\rho}_{\text{ads},2} + \rho_{\text{gas}} (y_1 - \xi_1^{\text{Ex}}) (1 + \bar{\rho}_{\text{ads},2} v^{\text{Ex}})}{\bar{\rho}_{\text{ads},2} + \rho_{\text{gas}} (y_1 - \xi_1^{\text{Ex}}) (1 - \bar{\rho}_{\text{ads},2} / \bar{\rho}_{\text{ads},1})} \quad (2-28a)$$

$$x_2^{\text{Abs}} = \frac{\xi_2^{\text{Ex}} \bar{\rho}_{\text{ads},1} + \rho_{\text{gas}} (y_2 - \xi_2^{\text{Ex}}) (1 + \bar{\rho}_{\text{ads},1} v^{\text{Ex}})}{\bar{\rho}_{\text{ads},1} + \rho_{\text{gas}} (y_2 - \xi_2^{\text{Ex}}) (1 - \bar{\rho}_{\text{ads},1} / \bar{\rho}_{\text{ads},2})} \quad (2-28b)$$

These equations can convert the experimentally obtained excess adsorption to the absolute adsorption, subject to accuracy of the constant, pure-component, adsorbed-phase densities, and a model for v^{Ex} . The method is extendable to a multi-component mixture:

$$x_i^{\text{Abs}} = \xi_i^{\text{Ex}} + \frac{\Delta_i \rho_{\text{gas}} \left(v^{\text{Ex}} + \sum_{j=1}^N \frac{\xi_j^{\text{Ex}}}{\bar{\rho}_{\text{ads},j}} \right)}{1 - \rho_{\text{gas}} \sum_{j=1}^N \frac{\Delta_j}{\bar{\rho}_{\text{ads},j}}}, \quad \text{where } \Delta_i \equiv y_i - \xi_i^{\text{Ex}} \quad (2-29)$$

An equation similar to Equation (2-29) has been derived (DeGance 1992), although the excess volume term was omitted. In general, the excess volume appearing in Equations (2-28) or (2-29) cannot be determined by reconciliation with experimental data because the absolute quantities, such as the absolute mole fraction, are experimentally inaccessible. If such values, however, are determined by means other than experiment, such as an arbitrary adsorption model, then the excess volume can be calculated on assumption of the model accuracy.

For pedagogical purposes, an explicit, one-parameter model of the excess volume can be formulated for a binary mixture:

$$v^{\text{E}} = \text{RTC} x_1^{\text{Abs}} x_2^{\text{Abs}} \quad (2-30)$$

In general, the parameter “C” can be a function of temperature and pressure, and is zero for ideal mixing. By assuming the model form of Equation (2-30), the excess volume is always symmetric about the equimolar concentration (which may or may not be the actual case). The explicit solution of the absolute mole fraction with this model is obtained by means of solving a quadratic equation:

$$x_1^{\text{Abs}} = 1/2 - d_1 + \sqrt{d_1^2 + 2d_1(x_1^{\text{Abs}})^{\text{ideal}} - d_1 + 1/4} \quad \text{if } C < 0 \quad (2-31a)$$

$$x_1^{\text{Abs}} = 1/2 - d_1 - \sqrt{d_1^2 + 2d_1(x_1^{\text{Abs}})^{\text{ideal}} - d_1 + 1/4} \quad \text{if } C > 0 \quad (2-31b)$$

$$\text{where } d_1 = \frac{1 + \rho_{\text{gas}} \Delta_1 \left(\frac{1}{\bar{\rho}_{\text{ads},2}} - \frac{1}{\bar{\rho}_{\text{ads},1}} \right)}{2\rho_{\text{gas}} \Delta_1 \text{RTC}} \quad (2-31c)$$

The absolute mole fraction obtained from ideal mixing (as indicated by the superscripted “ideal”) appears in the above equations, and is obtained using Equation (2-28) or (2-29) with the excess volume set to zero. More complex models for the excess volume than that depicted in Equation (2-30) are certainly possible, although the absolute mole fractions would be found probably by numerical solution. Once the absolute mole fractions are obtained, the adsorbed-phase density is obtained from Equation (2-27).

This adsorbed-phase density is inserted into Equation (2-13) to find the total absolute adsorption. Then, the component absolute adsorptions are found using the absolute mole fractions.

This method of calculating the absolute adsorption has eliminated mathematically the adsorbed-phase volume and has reduced knowledge requirements to pure component adsorbed-phase densities, experimental adsorption data, and an excess volume model. This method, however, does not mandate that the adsorbed-phase density for the pure components be constant with pressure or temperature.

Another method of calculating the absolute adsorption for mixtures from the experimentally obtained excess adsorption is to estimate a value for the adsorbed-phase volume (which may or may not be assumed constant with pressure, temperature, and gas

species). This assumption allows for simple calculation of the absolute adsorption from the excess adsorption:

$$n_i^{\text{Abs}} = n_i^{\text{Ex}} + V_{\text{ads}} \rho_{\text{gas}} Y_i \quad (2-32)$$

A value for the adsorbed-phase volume can be estimated by using a model that fits the experimental excess adsorption data (e.g., the SLD model by Fitzgerald et al., 2003, or the Ono-Kondo model by Sudibandriyo et al., 2003) and incorporates the concept of an adsorbed-phase volume. This method of calculating the absolute adsorption from the experimentally obtained excess adsorption has eliminated mathematically the adsorbed-phase density and reduced knowledge requirements to experimental data and a model estimate for the adsorbed-phase volume. Knowledge of the adsorbed-phase densities (from a model) is required to determine deviations from ideal mixing.

In summary, for these two methods, the calculation of absolute adsorption from excess adsorption can be accomplished either by assuming some value for the adsorbed-phase densities or the adsorbed-phase volume. Adsorption models that predict the excess adsorption and represent well the experimental data can estimate these values. Non-ideal mixing of the adsorbed phase can be inferred and concisely represented by the use of excess volume models.

Determining the extent of non-ideal mixing for adsorption at high pressure differs from other problems in vapor-liquid and liquid-liquid equilibria (VLE and LLE). For VLE or LLE problems, phase densities are directly measured from experiment and then the excess volume is determined. For mixture adsorption at higher pressures, any

determination of whether the adsorbed phase has non-ideal mixing *cannot be made directly from experiment* but made in the context of a model that predicts non-measurable adsorbed-phase densities.

MIXED-GAS STORAGE

The gas storage concept is easily extendable to mixtures. The gas capacity for the amount of each gas component stored in a container volume per unit adsorbent mass in that volume is:

$$n_i^{GC} = n_i^{Ex} + y_i \frac{\rho_{gas}}{\rho_{adsorbent}^{He}} \left(\frac{1}{\theta_{pack}} - 1 \right) = n_i^{Ex} + y_i \frac{\rho_{gas}}{\rho_{adsorbent}^{He}} \frac{\theta_{free}}{\theta_{pack}} \quad (2-33)$$

The gas capacity can also be written on a per unit volume basis:

$$\rho_i^{GC} = n_i^{Ex} \rho_{adsorbent}^{He} \theta_{pack} + y_i \rho_{gas} \theta_{free} \quad (2-34)$$

GAS ADSORPTION ON WET ADSORBENTS

When performing experiments on wet adsorbents for temperatures greater than those at which hydrate formation occur (as is the case for this work), water is present as a component in one of three phases: the adsorbed fluid, the water-rich phase, and the gas phase. The presence of water in a volumetric adsorption experiment entails special attention because the amount of water in the system container does not change with pressure, unlike the amount of gas.

For helium void volume determination (and the subsequent gas isotherms), the coal under investigation is not under water, but only saturated with water; i.e., no water-

rich phase is assumed to exist. The amount of water in a system container $V^{\text{Container}}$ is thus completely adsorbed and has a volume of $V_{\text{ads}}^{\text{Water}}$. The helium gas is assumed to be impermeable to the adsorbed water. This is justified by repeated experiments on wet coals demonstrating that helium void volume determinations do not vary with pressure.

The void volume determination of a wet adsorbent takes into account the volume of the adsorbed water:

$$V_{\text{Void}}^{\text{He}} = V_{\text{Container}} - V_{\text{adsorbent}} - V_{\text{ads}}^{\text{Water}} \quad \text{Wet adsorbent} \quad (2-35)$$

For dry adsorbents, a key assumption made earlier in this chapter was that void volume for helium is identical for other gases, i.e.:

$$V_{\text{Void}}^{\text{He}} = V_{\text{Void}}^{\text{CO}_2} = V_{\text{Void}}^{\text{CH}_4} \quad \text{Dry Adsorbent} \quad (2-36)$$

This assumption does not hold true for wet adsorbents because helium may be assumed impermeable to the adsorbed water; however, for gases such as CO_2 , the water is permeable. For determination of the CO_2 void volume, a volume correction is made for the solubility of the CO_2 in the water-rich adsorbed phase, $n_{\text{CO}_2}^{\text{Sol,Ads}}/\rho_{\text{gas}}$:

$$V_{\text{Void}}^{\text{CO}_2} = V_{\text{Container}} - V_{\text{adsorbent}} - V_{\text{ads}}^{\text{Water}} + \frac{n_{\text{CO}_2}^{\text{Sol,Ads}}}{\rho_{\text{gas}}} \quad \text{Wet adsorbent} \quad (2-37)$$

Moreover, the difference between the CO_2 and the helium void volume is just the correction $n_{\text{CO}_2}^{\text{Sol,Ads}}/\rho_{\text{gas}}$:

$$V_{\text{Void}}^{\text{CO}_2} - V_{\text{Void}}^{\text{He}} = \frac{n_{\text{CO}_2}^{\text{Sol,Ads}}}{\rho_{\text{gas}}} \quad \text{Wet adsorbent} \quad (2-38)$$

For CO₂ adsorption on a wet adsorbent, the experimental excess adsorption is defined by Equation (2-5), but with use of the CO₂ void volume rather than a helium void volume (as they are not always interchangeable).

$$\begin{aligned}
 n_{\text{CO}_2}^{\text{Ex}} &\equiv n_{\text{inj}} - V_{\text{Void}}^{\text{CO}_2} \rho_{\text{gas}} = n_{\text{inj}} - \left(V_{\text{Void}}^{\text{He}} + \frac{n_{\text{CO}_2}^{\text{Sol,Ads}}}{\rho_{\text{gas}}} \right) \rho_{\text{gas}} \\
 & \qquad \qquad \qquad \text{Wet adsorbent} \qquad \qquad (2-39) \\
 &= n_{\text{inj}} - V_{\text{Void}}^{\text{He}} \rho_{\text{gas}} - n_{\text{CO}_2}^{\text{Sol,Ads}}
 \end{aligned}$$

The excess adsorption for a wet adsorbent is lowered by the amount of gas soluble in the adsorbed water. This quantity, however, cannot be determined by any elementary experimental methods. The first estimate is to assume that CO₂ (and other gases) is soluble in the adsorbed phase as much as it is in liquid water:

$$n_{\text{CO}_2}^{\text{Sol,Ads}} = n_{\text{CO}_2}^{\text{Sol,Water}} \qquad \qquad \text{Assumption for Wet Adsorbents} \qquad \qquad (2-40)$$

In this work, the above assumption was invoked in our data reduction procedures for wet adsorption studies.

CHAPTER 3: EXPERIMENTAL METHOD AND ANALYSIS

The experimental method used in the OSU adsorption laboratory is based on a mass balance principle, which employs precise measurements of pressures, volumes and temperatures. The scientific fundamentals for such an approach are discussed in Chapter 2; a description of the apparatus and the experimental procedure follows. These methods have been discussed elsewhere (Hall, 1993; Sudibandriyo, 2003; Pan, 2003), and by the present author (Sudibandriyo et al., 2003), and some aspects of the following discussion are similar to those previous works.

The experimental apparatus is shown schematically in Figure 3-1. The pump and cell sections of the apparatus are maintained in a constant temperature air bath at a pre-determined temperature representative of field conditions of the coal bed, ranging from 90°F to 135°F (305.4K to 330.4K), depending on the location and coal bed depth. The equilibrium cell has a volume of 110 cm³ and is filled with the adsorbent to be studied. The cell section has tubing and various fittings that make the cell section about 40 cm³ larger than the volume of the equilibrium cell.

The cell is placed under vacuum prior to gas injection. The void volume, V_{void} , in the equilibrium cell is then determined by injecting known quantities of helium from a calibrated injection pump (Ruska Pump). Since helium is not adsorbed significantly, the void volume can be determined from measured values of temperature, pressure and

amount of helium injected into the cell. Several injections made into the cell at different pressures show consistency in the calculated void volume. Generally, the void volume calculated from sequential injections varies less than 0.3 cm^3 from the average value (of approximately 100 cm^3). The helium void volume includes all the volume of the cell section exclusive of the adsorbent volume that is impenetrable to helium gas.

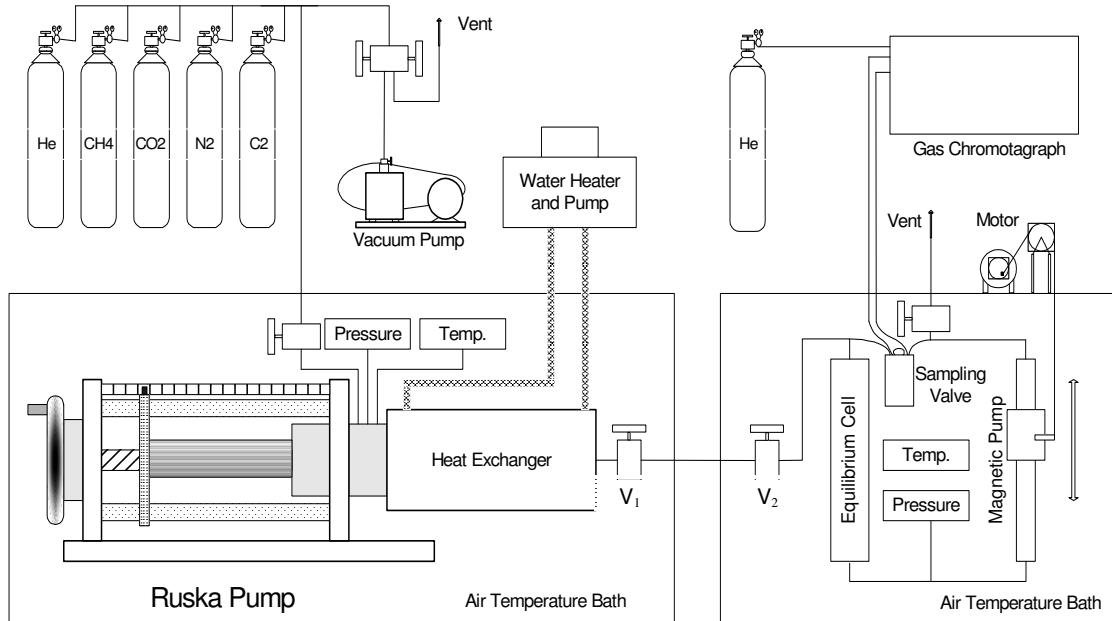


Figure 3-1. Schematic Diagram of the Experimental Apparatus

The steps taken to measure the void volume are outlined in Figure 3-2. The pressures depicted are specific to either the pump or cell section. The initial pump pressure is higher than the initial cell pressure. There are two intermediary valves (V_1 and V_2) between the pump and cell section. The intermediary valve in the pump section (V_1) is always open (except for pressure testing), and the valve in the cell section (V_2) is opened to release gas from the pump into the cell section. In Step 1, the gas is injected from the pump section to the cell section by opening the intermediary valve (V_2). In Step 2, the valve is closed after the appropriate amount of gas is injected. In Step 3, the pump pressure is returned to its original value by decreasing the pump volume. Although the

initial and final temperature may be different for both the cell and the pump, in practice they are kept at the same temperature. If the cell section contains a wet adsorbent, a correction is made for the solubility of helium in the water (Pray et al., 1952), although in practice, this correction is negligible (less than 0.2 cm³).

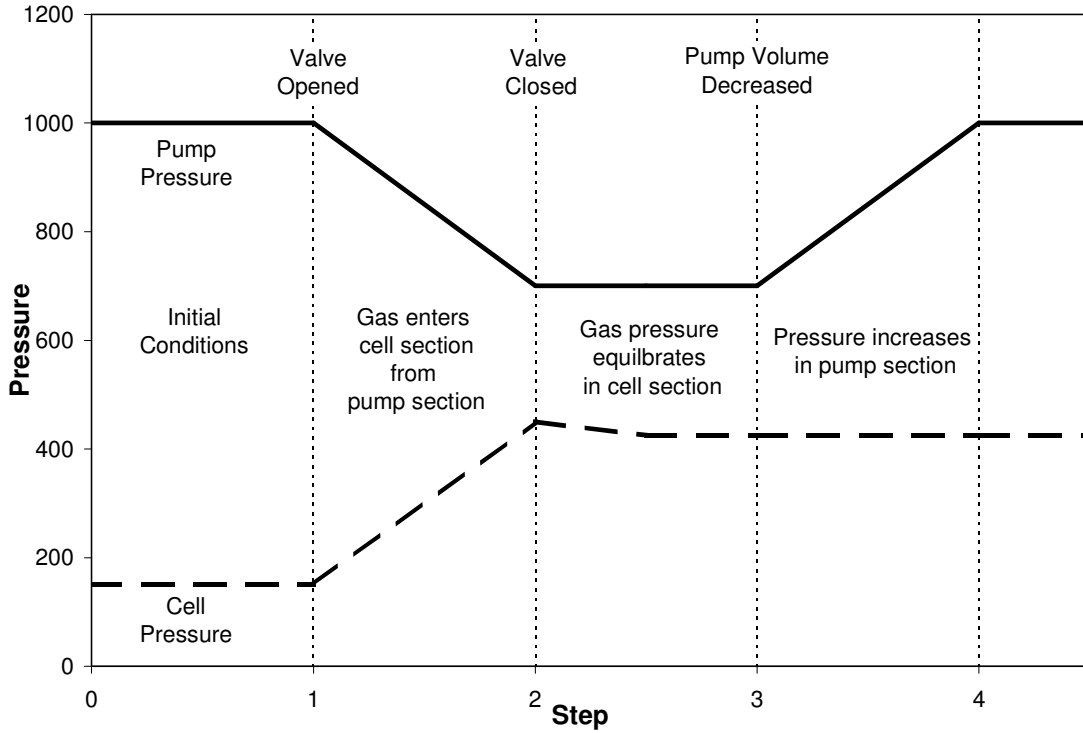


Figure 3-2. Procedure for Void Volume Determination

The governing equation is:

$$V_{\text{void}} = \frac{\left(\frac{P\Delta V}{ZT} \right)_{\text{pump}} - n_{\text{sol}}^{\text{He}}}{\left(\frac{P_2}{Z_2 T} - \frac{P_1}{Z_1 T} \right)_{\text{cell}}} \quad (3-1)$$

For void volume determination, the compressibility of helium is given by:

$$Z_{\text{He}} = 1 + \frac{(1.471 \cdot 10^{-3} - 4.779 \cdot 10^{-6} T + 4.92 \cdot 10^{-9} T^2)}{P}, \quad (3-2)$$

where T is in Kelvin and P is in atmospheres. This expression is based on experimental data from the National Bureau of Standards Technical Note 631 for helium (McCarty, 1972) and has been referenced elsewhere (Hall, 1993).

PURE-GAS ADSORPTION MEASUREMENTS

The excess adsorption can be calculated directly from experimental quantities. For pure-gas adsorption measurements, a known quantity of gas, n_{inj} , (e.g., methane) is injected from the pump section into the cell section. Some of the injected gas, n_{inj} , will be adsorbed. Although the amount of unadsorbed gas cannot be always inferred, the gas amount occupying the void volume, n_{unads}^{Gibbs} , can be inferred, and it is used to calculate the excess adsorption. The amount of gas soluble in water is deducted for systems containing water so that gas-water solubility is not inferred to be adsorption. A molar balance is used to calculate the excess amount adsorbed as

$$n^{Ex} = n_{inj} - n_{unads}^{Gibbs} - n_{sol} \quad (3-3)$$

The amount injected can be determined from pressure, temperature and volume measurements of the pump section:

$$n_{inj} = \left(\frac{P\Delta V}{ZRT} \right)_{pump} \quad (3-4)$$

The steps taken for a gas injection are shown in Figure 3-3. The initial pump pressure may be higher or lower than the cell pressure. In practice, the initial pump pressure is set to about 1000 psia because this is half of the top pressure for the isotherm,

2000 psia. (Because of their compressibilities, carbon dioxide and ethane may require lower pressures than 1000 psia to minimize the expected error in the amount injected). If the initial pump pressure is *higher* than the cell pressure, then the intermediary valve is opened between the pump and cell section, as shown in Figure 3-3. The valve is closed when the appropriate amount of gas has entered the cell section (isotherm equilibrium pressure increments are usually about 200 psia). If the initial pump pressure is *lower* than the cell pressure, then the pump volume is *decreased* so that the pump pressure is high enough to allow the injection (to prevent the backflow of cell-section gas into the pump section).

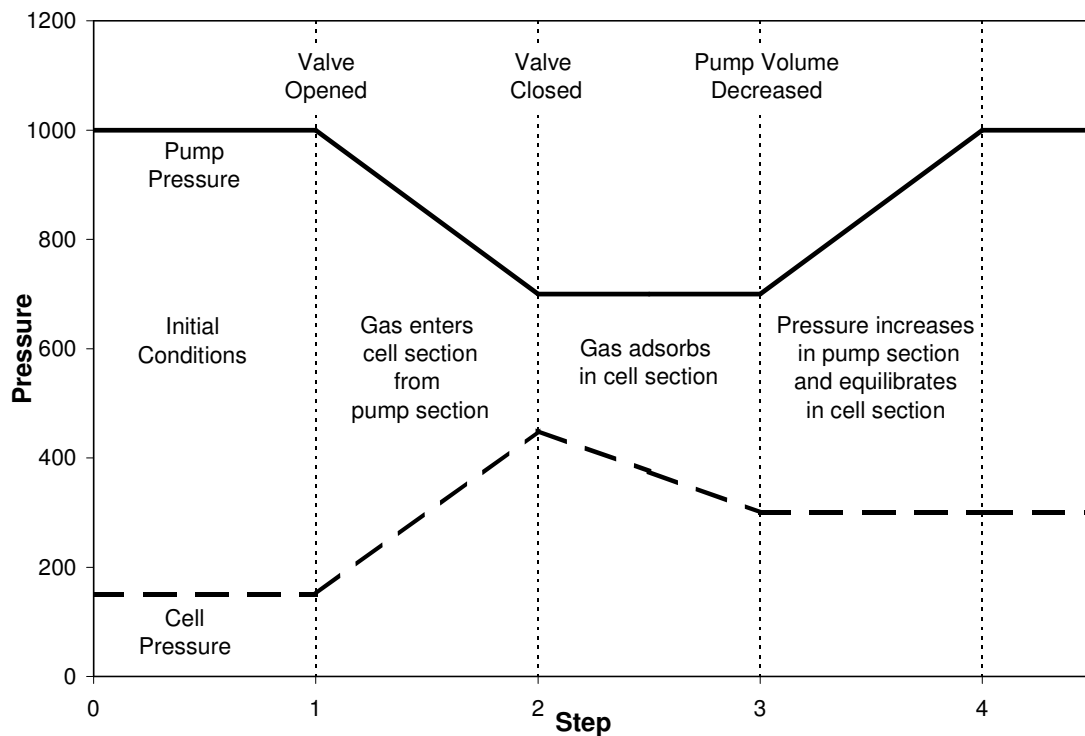


Figure 3-3. Procedure for Gas Injection

During and after the injection step, the pressure and temperature of the cell section will fluctuate (due to adsorption and Joule-Thomson effects). The intermediary valve between the cell and pump section has been placed so that one can open and close

the valve without disturbing the temperature-controlled climate (the valve stem goes through a hole drilled in the oven wall). This reduces the time necessary for adsorption equilibration and void volume determination.

In the last step, the pump section is returned to the original pressure by changing the pump volume. The pressure in the cell section will drop until it reaches its equilibrium pressure. The whole procedure can be repeated at sequentially higher pressures until the whole isotherm is done.

In cases with CO₂ or ethane and at high pressures in the cell section, not enough gas may be present in the pump section to make the pump pressure higher than the cell section pressure. The pump section will have to be “reloaded” with the gas from the gas cylinder when this happens. Although “reloading” may be avoided by starting the initial pump pressure at a higher than normal value (1300 psia instead of 1000 psia, for instance), this may add significant uncertainty in determining the amount of gas injected because the gas density will be closer to states where dp_{gas}/dT and dp_{gas}/dP are larger in magnitude.

The unadsorbed amount of gas is inferred at the final equilibrium pressure:

$$n_{\text{unads}}^{\text{Gibbs}} = \left(\frac{P}{ZRT} \right)_{\text{cell}} V_{\text{Void}}^{\text{He}}, \quad (3-5)$$

where the void volume is assumed to remain constant for all pressures. As indicated by Equations (3-4) and (3-5), gas-phase compressibility factors (Z) are required for methane, nitrogen, and CO₂ to properly analyze the experimental data. The compressibility factors for pure methane, nitrogen, CO₂, and ethane were calculated from highly accurate

equations of state (Angus et al., 1978 and 1979; Span and Wagner, 1996; Friend et al., 1991).

To calculate the amount of gas soluble in water as a function of pressure, an empirical equation obtained from the Amoco Corporation was used for temperatures at 113°F or 115°F.

$$x_{\text{gas}} = \frac{P}{a + bP + cP^2} \quad (3-6)$$

Parameter values for these equations are listed for each gas in Table 3-1. Accounting for the solubility of CO₂ in water can lead to a 50% correction in the excess adsorption, the highest correction encountered in the entire study.

Table 3-1. Parameters for Gas-Water Solubility at 115°F

| Constant | Units of Constant | Methane | Nitrogen | CO ₂ |
|----------|-------------------|-----------|-----------|-----------------|
| a | psia | 769000 | 1480000 | 39840 |
| b | | 150.4 | 127.3 | 9.452 |
| c | 1/psia | -0.005369 | -0.000635 | 0.00833 |

In comparison to nitrogen and methane, the amount of soluble gas in water is significant for CO₂ at temperatures near 115°F. For other temperatures, literature data (Dhima et al., 1999; Weibe and Gaddy, 1940) were used to construct an empirical relationship for CO₂-water solubility at temperatures from 104°F to 167°F. In the 0-2200 psia range, the empirical function represents their data with an average absolute deviation of 1.5%. For higher pressures, different formulations are required. The mole fraction of CO₂ present in water at temperature T (in K) and pressure P (in psia) is given as

$$x_{\text{CO}_2} = \frac{P}{a + (b_1 + b_0 T)P + (c_1 + c_0 T)P^2} \quad (3-7)$$

Parameter values for this correlation are listed in Table 3-2.

Table 3-2. Parameters for CO₂-Water Solubility Relationship

| Constant | Value | Units of Constant |
|----------------|--------------|-------------------|
| a | 39480 | psia |
| b ₁ | -332.637 | |
| b ₀ | 1.06683 | 1/K |
| c ₁ | 0.132207 | 1/psia |
| c ₀ | -0.000386758 | 1/(psia K) |

The amount of water that is soluble in the supercritical gas phase of CO₂ or ethane may be significant enough to alter predictions of the gas-phase density from that of a truly pure gas. As mentioned elsewhere by the author (Fitzgerald et al., 2003), neglecting the water that is soluble in the gas phase may be the partial cause for some anomalous isotherm behavior for CO₂ adsorption on wet coals.

The solubility of water in the CO₂ gas phase is shown below in Figure 3-4 from experimental values (King and Coan, 1971; Weibe and Gaddy, 1940). At 122°F and 167°F, the mole fraction of water in CO₂ is highest at low pressures. As the pressure increases, the water solubility in CO₂ reaches a minimum and then rises again.

No established method exists for calculating the CO₂ density saturated with water. To date, this effect has not been included for measurements conducted at OSU; however, the variability attributed to this effect is estimated as roughly comparable to the uncertainty of the CO₂ density.

MIXED-GAS ADSORPTION MEASUREMENTS

For mixed-gas adsorption measurements, a volumetrically prepared gas mixture of known composition is injected, so the total amount of each component in the cell is known. A magnetic pump (See Figure 3-1) is used to slowly circulate the fluid mixture to ensure that equilibrium is reached.

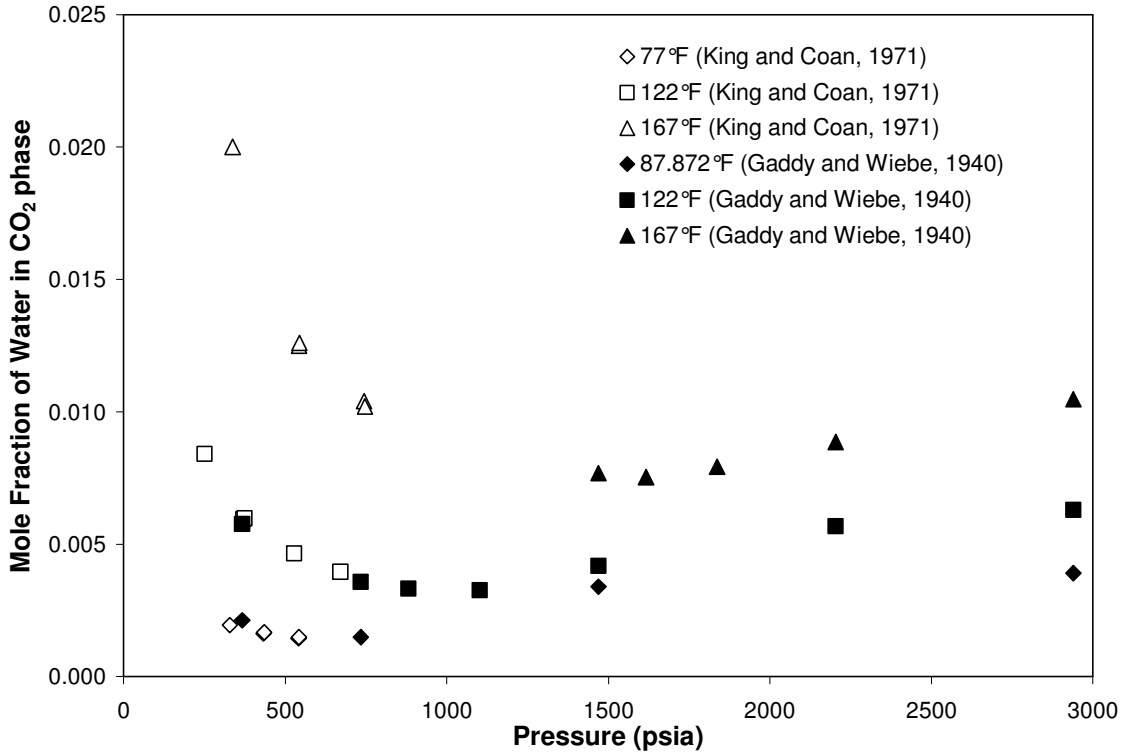


Figure 3-4. Solubility of Water in CO₂ Phase

The composition of the gas mixture remaining in the void volume at equilibrium is determined by gas chromatographic (GC) analysis. A pneumatically-controlled sampling valve, contained in the air bath at the cell section temperature, sends a 20 μ L sample to the GC for analysis. A molar balance is used to calculate the excess amount adsorbed for each component in the gas:

$$n_i^{\text{Ex}} = z_i n_{\text{inj}} - y_i n_{\text{unads}}^{\text{Gibbs}} - n_{\text{sol},i} \quad (3-8)$$

The injection procedure of a gas for a mixture is the same as that for a pure gas as depicted earlier in Figure 3-3. For gas mixtures, however, the equilibrium time may be as long as three days for the first injection (at low pressures) and one day for subsequent ones (high pressures). The solubility of a gas in a mixture in water is estimated by replacing the pressure P with the corresponding partial pressure of the gas, P_{y_i} .

To calculate the excess adsorption for a gas in a mixture requires a gas mixture Z factor. A careful evaluation of the current literature led us to conclude that an adequate predictive capability for the mixture Z factors does not exist. Therefore, we elected to develop such a capability using the Benedict-Webb-Rubin (BWR) equation of state (Pan, 2003). Specifically, we used available pure-fluid and binary mixture data to refit the BWR equation and improve its accuracy significantly; in general, the new BWR EOS parameters yield deviations in the Z factor within 0.5% (Pan, 2003). This allowed us to address our compressibility factor needs for binary adsorption mixtures.

CALIBRATIONS

As deemed necessary, calibration tests were performed during the course of the experiments. Usually, the calibrations were performed before the adsorption experiment for a new coal or carbon adsorbent. The thermocouples and RTDs were calibrated against a Minco platinum reference RTD. Super TJE pressure transducers (range: 0 – 13.8 MPa) were calibrated using helium as the working fluid against a Ruska deadweight tester with a calibration traceable to the National Institute of Science and Technology. Detailed information on calibration procedure is available elsewhere (Hall, 1993).

The GC was calibrated against known mixtures at the nominal concentrations. The GC used for composition analysis is a Varian Chrompack CP-3800 with the helium carrier gas maintained at a 15-mL/min flow rate. A 10-ft HayeSep D packed column was used for methane/CO₂ and nitrogen/CO₂ systems, and a molecular sieve 13X column was used for the methane/nitrogen system for a better separation; column temperature was set at 80°C. A thermal conductivity detector was used for all of the binary systems studied; the bath temperature was set to 100°C. The response factor is defined as $(A_2 / A_1) \cdot (y_1 / y_2)$, where A is the GC response percentage area. The response factor was found to be slightly dependent upon pressure; as such, the GC was calibrated for each nominal composition at pressure intervals of 1.4 MPa (200 psia). Calibration results showed the average deviations of the gas mole fraction determined by the calibration fit were less than 0.001 with the maximum deviation of 0.003. Specific details are documented elsewhere (Sudibandriyo, 2003).

The accuracy in each of the experimentally measured quantities after calibrations are estimated as follows: temperatures, 0.06 K; pressures, 6.9 kPa; injected gas volumes, 0.02 cm³; gas mixture compositions, 0.001 mole fraction.

An error analysis indicates that the uncertainties for the pure adsorption measurements are within 5% for fluid densities less than 10 mole/L. The uncertainties for binary mixture adsorption vary for different compositions and different mixtures. Uncertainties for all the binary gas *total* adsorption measurements are within 5%. The percent uncertainty of component gas adsorption, however, can become high for lower compositions of the less adsorbed gases, i.e., nitrogen in the nitrogen/CO₂ system.

OSU DATABASE EMPLOYED IN THIS STUDY

The experimental measurements completed at Oklahoma State University include pure-gas (methane, nitrogen, ethane, and carbon dioxide) adsorption measurements on nine solid matrices: wet Fruitland coal (OSU#1 and OSU#2), wet Lower Basin Fruitland coal (OSU#3), wet / dry Illinois-6 coal, wet Tiffany coal, dry Beulah Zap coal, dry Wyodak coal, dry Upper Freeport coal, dry Pocahontas coal, and dry activated carbon. The experimental measurements were also conducted for adsorption from the three binary mixtures formed by methane, nitrogen and CO₂ at a series of compositions on four different matrices: Fruitland coal, Illinois #6 coal, Tiffany coal, and activated carbon. Measurements for a single methane/nitrogen/CO₂ ternary mixture were conducted on wet, mixed Tiffany coal and on dry activated carbon. Table 3-3 presents the systems and conditions of the OSU database. Tables 3-4 to 3-6 present the compositional analyses for the various solid matrices considered in the OSU database.

All the adsorption measurements are published elsewhere in a formal report (Gasem et al., 2003). Adsorption measurements for dry activated carbon (Sudibandriyo et al., 2003) and for wet Tiffany coal (Fitzgerald et al., 2005) are also published independently.

Some of the dry-basis compositions presented in Table 3-4 and 3-5 do not add to 100%. For the Tiffany coals in specific, this is because of poor replication of the carbon analysis. The coal appeared oily when ground for analysis and this may be, in part, the reason why poor replication was obtained. The carbon analysis was repeated three times and the values were averaged. Measurements other than carbon were replicated and their values are shown. The oxygen analysis was obtained by the direct method. For coals

listed in Table 3-5, the likely reason the compositions do not add to 100% is that carbonates in the ash content contributed both to the analyses of the carbon and the ash content.

The activated carbon studied was Filtrasorb 400, 12x40 mesh, from Calgon Carbon company. The activated carbon was dried under vacuum at 230°F for two days before being used in the adsorption measurements. The nitrogen BET surface area at 77 K has been reported elsewhere to be 850 m²/g (Humayun and Tomasko, 2000). The surface area value provided by the company, however, is 998 m²/g.

Four different coals were prepared for gas adsorption on wet coals measurements. The Fruitland coal is from the San Juan Basin; it is a medium volatile bituminous coal. This recently prepared sample (OSU #2) is slightly different in composition from the one used in previous measurements (OSU #1). The Lower Basin (LB) Fruitland coal is from the same coal-bed seam as Fruitland coal, but it was taken from a different location. This coal has higher ash content than the Fruitland coal. The Illinois #6 coal is a high volatile bituminous coal. Other coal samples are from BP Amoco Tiffany Injection Wells #1 and #10. The coal samples were ground to 200 μm size of particles and moistened to a water content of 4-15%, which was above the equilibrium moisture content of the coal in all cases. Equilibrium moisture was determined gravimetrically by exposing dry coal to 303.1 K air at 96-99% saturation.

In addition, five coal samples prepared by Argonne National Laboratory were used to study CO₂ adsorption on dry coals. The coals were dried under vacuum in the equilibrium cell at 80°C for 36 hours before being used in the adsorption measurements.

Table 3-3. OSU Adsorption Database

| System No. | Adsorbent | Adsorbate | Temp. (K) | Pressure Range (MPa) |
|-------------------|-------------------------|--|------------------|-----------------------------|
| 1 | Dry AC – F 400 | N ₂ | 318 & 328 | 0.7 – 13.7 |
| 2 | Dry AC – F 400 | CH ₄ | 318 & 328 | 0.7 – 13.7 |
| 3 | Dry AC – F 400 | CO ₂ | 318 & 328 | 0.7 – 13.7 |
| 4 | Dry AC – F 400 | C ₂ H ₆ | 318 | 0.7 – 13.7 |
| 5 | Dry AC – F 400 | N ₂ + CH ₄ | 318 | 0.7 – 12.4 |
| 6 | Dry AC – F 400 | CH ₄ + CO ₂ | 318 | 0.7 – 12.4 |
| 7 | Dry AC – F 400 | N ₂ + CO ₂ | 318 | 0.7 – 12.4 |
| 8 | Dry AC – F 400 | N ₂ + CH ₄ + CO ₂ | 318 | 0.7 – 12.4 |
| 9 | Wet Fruitland Coal | N ₂ | 319 | 0.7 – 12.4 |
| 10 | Wet Fruitland Coal | CH ₄ | 319 | 0.7 – 12.4 |
| 11 | Wet Fruitland Coal | CO ₂ | 319 | 0.7 – 12.4 |
| 12 | Wet Fruitland Coal | N ₂ + CH ₄ | 319 | 0.7 – 12.4 |
| 13 | Wet Fruitland Coal | CH ₄ + CO ₂ | 319 | 0.7 – 12.4 |
| 14 | Wet Fruitland Coal | N ₂ + CO ₂ | 319 | 0.7 – 12.4 |
| 15 | Wet Illinois #6 Coal | N ₂ | 319 | 0.7 – 12.4 |
| 16 | Wet Illinois #6 Coal | CH ₄ | 319 | 0.7 – 12.4 |
| 17 | Wet Illinois #6 Coal | CO ₂ | 319 | 0.7 – 12.4 |
| 18 | Wet Illinois #6 Coal | N ₂ + CH ₄ | 319 | 0.7 – 12.4 |
| 19 | Wet Illinois #6 Coal | CH ₄ + CO ₂ | 319 | 0.7 – 12.4 |
| 20 | Wet Illinois #6 Coal | N ₂ + CO ₂ | 319 | 0.7 – 12.4 |
| 21 | Wet Tiffany Coal | N ₂ | 328 | 0.7 – 13.7 |
| 22 | Wet Tiffany Coal | CH ₄ | 328 | 0.7 – 13.7 |
| 23 | Wet Tiffany Coal | CO ₂ | 328 | 0.7 – 13.7 |
| 24 | Wet Tiffany Coal | N ₂ + CH ₄ | 328 | 0.7 – 13.7 |
| 25 | Wet Tiffany Coal | CH ₄ + CO ₂ | 328 | 0.7 – 13.7 |
| 26 | Wet Tiffany Coal | N ₂ + CO ₂ | 328 | 0.7 – 13.7 |
| 27 | Wet Tiffany Coal | N ₂ + CH ₄ + CO ₂ | 328 | 0.7 – 13.7 |
| 28 | Wet LB Fruitland Coal | N ₂ | 319 | 0.7 – 12.4 |
| 29 | Wet LB Fruitland Coal | CH ₄ | 319 | 0.7 – 12.4 |
| 30 | Wet LB Fruitland Coal | CO ₂ | 319 | 0.7 – 12.4 |
| 31 | Dry Illinois #6 Coal | CO ₂ | 328 | 0.7 – 13.7 |
| 32 | Dry Beulah Zap Coal | CO ₂ | 328 | 0.7 – 13.7 |
| 33 | Dry Wyodak Coal | CO ₂ | 328 | 0.7 – 13.7 |
| 34 | Dry Upper Freeport Coal | CO ₂ | 328 | 0.7 – 13.7 |
| 35 | Dry Pocahontas Coal | CO ₂ | 328 | 0.7 – 13.7 |

Table 3-4. Compositional Analysis of Solid Matrices Used in This Study

| Analysis* | Activated Carbon | Fruitland Amoco | Fruitland OSU #1 | Fruitland OSU #2 | Illinois-6 | Lower Basin Fruitland OSU #3a | Lower Basin Fruitland OSU #3b | Tiffany Well #1 | Tiffany Well #10 |
|------------------|-------------------------|------------------------|-------------------------|-------------------------|-------------------|--------------------------------------|--------------------------------------|------------------------|-------------------------|
| <i>Ultimate</i> | | | | | | | | | |
| Carbon % | 88.65 | 68.56 | 68.63 | 66.58 | 71.47 | 38.92 | 40.20 | 47.78 | 56.75 |
| Hydrogen % | 0.74 | 5.74 | 4.27 | 4.23 | 5.13 | 3.08 | 3.10 | 2.62 | 2.77 |
| Oxygen % | 3.01 | 7.19 | 0.89 | 5.08 | 9.85 | 3.75 | 2.87 | 6.19 | 5.16 |
| Nitrogen % | 0.40 | 1.40 | 1.57 | 1.47 | 1.46 | 0.87 | 0.89 | 0.92 | 1.02 |
| Sulfur % | 0.73 | 0.65 | 4.19 | 0.72 | 1.27 | 1.73 | 2.14 | 0.57 | 0.52 |
| Ash % | 6.46 | 16.45 | 20.45 | 21.92 | 10.81 | 51.66 | 50.81 | 49.71 | 47.74 |
| <i>Proximate</i> | | | | | | | | | |
| Vol. Matter % | 3.68 | 19.12 | 20.2 | 20.33 | 30.61 | 20.01 | 14.00 | 15.48 | 15.35 |
| Fixed Carbon % | 89.86 | 64.42 | 59.35 | 57.75 | 55.90 | 28.33 | 35.19 | 34.82 | 36.91 |

* Huffman Laboratories, Inc., Golden, Colorado.

Table 3-5. Compositional Analysis of Coals Used in the DOE-NETL Round Robin Study

| Analysis* | Beulah Zap | Wyodak | Illinois #6 | Upper Freeport | Pocahontas |
|------------------|-------------------|---------------|--------------------|-----------------------|-------------------|
| <i>Ultimate</i> | | | | | |
| Carbon % | 72.9 | 75.0 | 77.7 | 85.5 | 91.1 |
| Hydrogen % | 4.83 | 5.35 | 5.00 | 4.70 | 4.44 |
| Oxygen % | 20.3 | 18.0 | 13.5 | 7.5 | 2.5 |
| Nitrogen | 1.15 | 1.12 | 1.37 | 1.55 | 1.33 |
| Sulfur % | 0.70 | 0.47 | 2.38 | 0.74 | 0.50 |
| Ash % | 9.7 | 8.8 | 15.5 | 13.2 | 4.8 |
| <i>Proximate</i> | | | | | |
| Moisture % | 32.2 | 28.1 | 8.0 | 1.1 | 0.7 |
| Vol. Matter % | 30.5 | 32.2 | 36.9 | 27.1 | 18.5 |
| Fixed Carbon % | 30.7 | 33.0 | 40.9 | 58.7 | 76.1 |
| Ash % | 6.6 | 6.3 | 14.3 | 13.0 | 4.7 |

* Analyses were provided by the Argonne National Laboratory

Table 3-6. Analysis of BPL Activated Carbon Used in This Study

| Analysis | Units | Value | Lower Limit | Upper Limit |
|--------------------------|--------------|--------------|--------------------|--------------------|
| Abrasion Number | | 87 | 75 | - |
| Apparent Density | g/cc | 0.53 | 0.44 | - |
| Ash | % | 7 | - | 9 |
| Effective Size | mm | 0.64 | 0.55 | 0.75 |
| Iodine Number | mg/g | 1046 | 1000 | - |
| US Sieve Series on 12 | % | 1 | - | 5 |
| US Sieve Series -40 Mesh | % | 1 | - | 4 |
| Fixed Carbon | | 1.7 | - | 1.9 |

CHAPTER 4

SIMPLIFIED LOCAL DENSITY MODEL FOR PURE-GAS ADSORPTION

Rangarajan and Lira (1995) originally developed the physical premises and assumptions of SLD theory. Namely, that (1) the chemical potential at any point near the adsorbent surface is equal to the bulk phase chemical potential, and (2) the chemical potential at any point above the surface is sum of the fluid-fluid and fluid-solid interactions. Accordingly, the equilibrium chemical potential is calculated by contributions from these fluid-fluid and fluid-solid interactions.

The pore geometry most widely used in a local density model for carbon adsorbents is a slit, where the distance between the planes is a distance of L (See Figure 4-1). For a slit of length L the chemical potential is written as:

$$\mu(z) = \mu_{ff}(z) + \mu_{fs1}(z) + \mu_{fs2}(L-z) = \mu_{bulk} \quad (4-1)$$

where the subscript “bulk” refers to the bulk fluid, “ff” refers to fluid-fluid interactions, and “fs” refers to the fluid-solid interactions. As illustrated in Figure 4-1, the position within a slit is z , where z is orthogonal to the plane of the solid phase, defined as a flat surface formed by the peripheral carbon (coal) atoms. A molecule within a slit has fluid-solid interactions with both slit surfaces. The distance between surfaces is the slit length ‘ L ’.

An equation of state, such as the van der Waals or Peng–Robinson, can be used to provide the fluid-fluid potential information. Typically, an integrated potential function, such as the 10-4 Lennard-Jones model is used to describe the fluid-solid interactions.

The SLD model is a “simplification” of the local density theory. According to Henderson (1992), the local density profile is calculated by minimizing the total energy functional which is dependent on all point densities and their spatial derivatives.

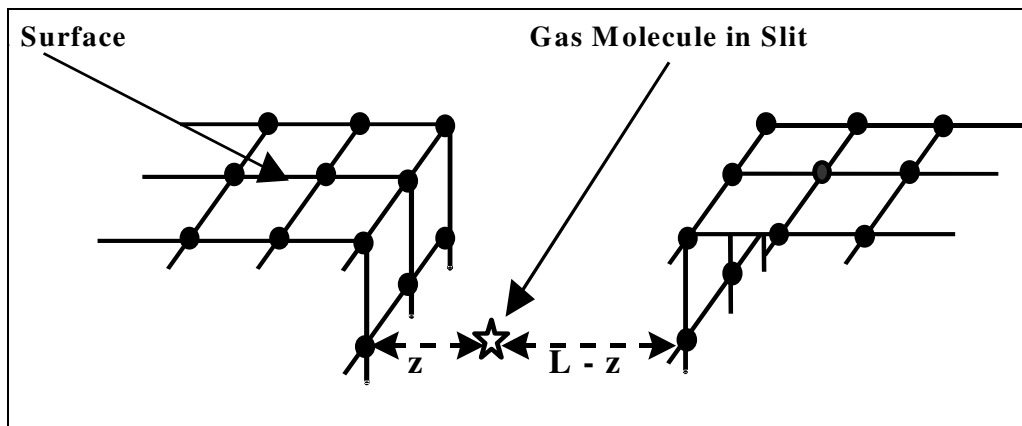


Figure 4-1. Conceptual Slit Geometry

The “simplification” of the SLD model assumes a mean field chemical potential; i.e., no local fluctuations. Further, the chemical potential of the fluid for each point in space is estimated from mean field theory, which is corrected for the proximity of the fluid molecule to the molecular wall of the adsorbent. The SLD model is formulated in terms of the excess adsorption (n^{Ex}), defined as the excess number of moles per unit mass of adsorbent, or:

$$n^{\text{Ex}} = A/2 \int_{\text{Left Side of Slit}}^{\text{Right Side of Slit}} (\rho(z) - \rho_{\text{bulk}}) dz \quad (4-2)$$

For the slit geometry considered here on the left side of the slit, $\sigma_{ff}/2$ is the location of the center of an adsorbed molecule touching the left plane surface. On the right side of the slit, $L-\sigma_{ff}/2$ is the location of an adsorbed molecule touching the right plane surface. For distances less than $1/2 \sigma_{ff}$ away from a surface wall, the local density is assumed to be zero. The left and right sides of the slit each comprise half of the total surface area. As will be discussed later in this chapter, at high pressures the density of the fluid at the wall surface, ρ_{wall} , is close to the reciprocal co-volume of the Peng-Robinson EOS, b . Typical values for the slit length L , obtained from regression of experimental data, are 2-5 times the value of σ_{ff} . These concepts are depicted in Figure 4-2.

Lee's partially integrated 10-4 Lennard-Jones potential (Lee, 1998) is used to describe the fluid-solid interactions. It is represented by $\mu(z)$ and defined on a molecular basis as:

$$\mu_{fs}(z) = N_A \cdot \Psi(z) \quad (4-3)$$

$$\Psi(z) = 4\pi\rho_{atoms} \epsilon_{fs} \sigma_{fs}^2 \left(\frac{\sigma_{fs}^{10}}{5(z')^{10}} - \frac{1}{2} \sum_{i=1}^4 \frac{\sigma_{fs}^4}{(z'+(i-1) \cdot \sigma_{ss})^4} \right) \quad (4-4)$$

where ϵ_{fs} is the fluid-solid interaction energy parameter, and $\rho_{atoms} = 0.382 \text{ atoms}/\text{\AA}^2$. The molecular diameter of the adsorbate and the carbon interplanar distances are σ_{ff} and σ_{ss} , respectively. The carbon interplanar distance is taken to be that of graphite, 0.335 nm (Subramanian et al., 1995). Values for σ_{ff} were obtained elsewhere (Reid et al., 1987). For convenience, the fluid-solid diameter σ_{fs} and the dummy coordinate z' are defined as:

$$\sigma_{fs} = \frac{\sigma_{ff} + \sigma_{ss}}{2} \quad (4-5)$$

$$z' = z + \sigma_{ss}/2 \quad (4-6)$$

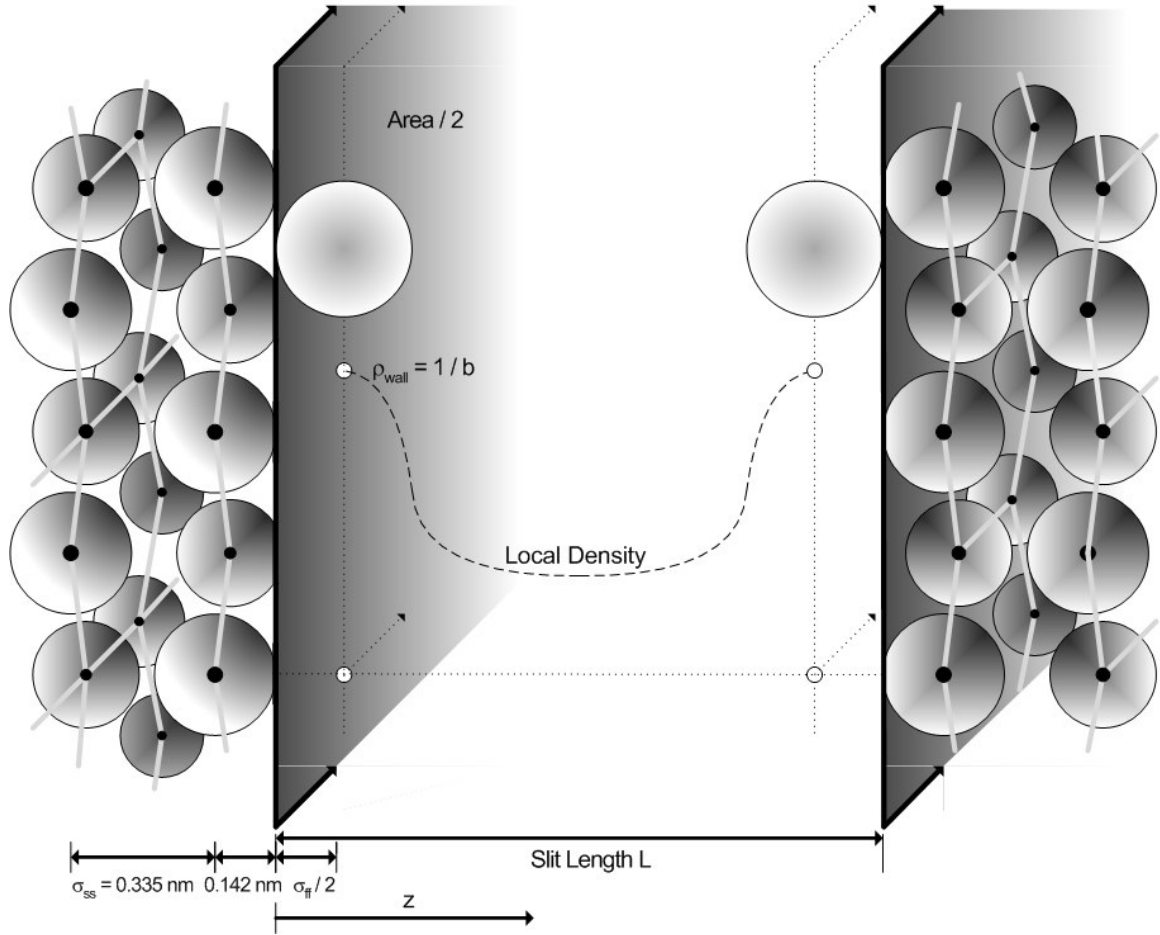


Figure 4-2. Details of Slit Geometry for SLD Model

The local density is determined by relating the fluid-fluid chemical potential to the fugacity f in the PR EOS, as:

$$\ln\left(\frac{f_{ff}[a(z), \rho(z)]}{f}\right) = -\left(\frac{\Psi(z) + \Psi(L-z)}{kT}\right) \quad (4-7)$$

The PR EOS determines the bulk density, the bulk fugacity and fluid fugacities.

The PR EOS may be written as follows:

$$\frac{P}{\rho RT} = \frac{1}{(1-\rho b)} - \frac{a(T)\rho}{RT \left[1 + (1-\sqrt{2})\rho b \right] \left[1 + (1+\sqrt{2})\rho b \right]} \quad (4-8)$$

where

$$a(T) = 0.45724 \alpha(T) R^2 T_c^2 / P_c \quad (4-9)$$

$$b = 0.077796 R T_c / P_c \quad (4-10)$$

For $\alpha(T)$, the Mathias-Copeman expression is used with regressed parameters

(Hernández-Garduza et al., 2002) appearing in Table 4-1:

$$\alpha(T) = 1 + C_1 \left(1 - \sqrt{T/T_c} \right) + C_2 \left(1 - \sqrt{T/T_c} \right)^2 + C_3 \left(1 - \sqrt{T/T_c} \right)^3 \quad (4-11)$$

Table 4-1. Physical Fluid Parameters

| | T_c (K) | P_c (MPa) | σ_{ff} (nm) | C_1 | C_2 | C_3 |
|-----------------|-----------|-------------|--------------------|---------|----------|---------|
| Nitrogen | 126.19 | 3.396 | 0.3798 | 0.43694 | -0.07912 | 0.32185 |
| Methane | 190.56 | 4.599 | 0.3758 | 0.41108 | -0.14020 | 0.27998 |
| CO ₂ | 304.13 | 7.377 | 0.3941 | 0.71369 | -0.44764 | 2.43752 |
| Ethane | 305.30 | 4.872 | 0.4443 | 0.52005 | 0.00430 | 0.10292 |

The bulk fugacity and the fluid fugacity for the PR EOS are:

$$\ln \frac{f}{P} = \frac{b\rho}{1-b\rho} - \frac{a(T)\rho}{RT(1+2b\rho-b^2\rho^2)} - \ln \left[\frac{P}{RT\rho} - \frac{Pb}{RT} \right] - \frac{a(T)}{2\sqrt{2}bRT} \ln \left[\frac{1+(1+\sqrt{2})\rho b}{1+(1-\sqrt{2})\rho b} \right] \quad (4-12)$$

$$\ln \frac{f_{ff}(z)}{P} = \frac{b\rho(z)}{1 - b\rho(z)} - \frac{a_{ads}(z)\rho(z)}{RT(1 + 2b\rho(z) - b^2\rho^2(z))} - \ln \left[\frac{P}{RT\rho(z)} - \frac{Pb}{RT} \right] - \frac{a_{ads}(z)}{2\sqrt{2}bRT} \ln \left[\frac{1 + (1 + \sqrt{2})\rho(z)b}{1 + (1 - \sqrt{2})\rho(z)b} \right] \quad (4-13)$$

The parameter ‘a’ in the Peng-Robinson EOS is a function of position within the slit when calculating the local-phase density. The formulation of Chen et al. (1997) was used for the equations describing ‘a’ as a function of position. This formulation is given in Appendix A for completeness. The pressure terms appearing in Equations (4-12) and (4-13) are the actual hydrostatic pressures of the gas phase.

Once the local-density profile is determined across the slit, the excess adsorption can be obtained by integrating Equation (4-2) numerically. For this work, half of the slit was subdivided into 50 intervals and Equation (4-7) was solved for each interval. The amount adsorbed was calculated by numerical integration using Simpson’s rule.

TESTING THE EFFICACY OF THE SLD ADSORPTION MODEL

The efficacy of the SLD adsorption model was judged by how well the model correlated the sorption data of interest and its predictive capability. Specifically, the model should correlate within the experimental uncertainties:

1. The sorption of pure fluids, multi-component mixtures, and individual components in a mixture on the adsorbents of interest
2. The sorption behavior over the ranges of temperature and pressure of interest.

For this chapter, only pure-gas adsorption is modeled with the SLD theory, and the primary interest is the acceptable model correlation of the adsorption data. If the

model is successful in correlating adsorption data within the desired level of uncertainty, then the model can be developed for its corresponding predictive ability, which is addressed in detail in Chapters 5. Some useful capabilities of adsorption models relevant to ECBM include prediction of:

1. High-pressure sorption from low-pressure sorption data
2. Sorption at one temperature from data at another temperature
3. Sorption behavior of one gas from data on another gas
4. The sorption behavior of multi-component gases from their corresponding pure sorption behaviors.

Although the above capabilities do not provide *a priori* predictions, they would, when fully realized, minimize the amount of data required for ECBM operations involving designated coal seams. In this chapter, the *correlative* ability of the SLD model is tested for the first three capabilities.

For both correlative and predictive capabilities, the adsorption model requires physical or phenomenological parameters. Typically, these parameters characterize either the adsorbing fluid or the adsorbent. For example, the surface area is a characteristic parameter of the adsorbent, and the gas density is a characteristic of the fluid. Models that demarcate these parameters as fluid-dependent or adsorbent-dependent generally are better suited for model parameter generalization. Moreover, existing knowledge on fluid-fluid interactions from volumetric (PVT) and vapor-liquid equilibrium (VLE) experiments and modeling can be used, thus utilizing the adsorption data solely to account for fluid-solid interactions. The characterization of coal and other adsorbents is done frequently by regressing model parameters, such as surface area, from

experimental data. More elaborate models can characterize adsorbents through statistical distributions of surface energy and pore structure (see, e.g., Duong, 1998). Sometimes, the regressed adsorbent parameters are fluid dependent; e.g., the surface area or pore distribution of the adsorbent regressed from data on CO₂ is different than that regressed from nitrogen. Ideally, the same adsorbent parameters would apply to each gas component, and from that, adsorption could be predicted for a variety of fluids. Realistically, each gas isotherm provides information about the adsorbent properties not obtained from other gas isotherms.

In testing the SLD model efficacy, two general case studies were considered when regressing model parameters. The two case studies vary in the way the SLD model is implemented and how the adsorption model parameters are regressed. In the first case study, which has been published elsewhere (Fitzgerald et al., 2003), the surface area that is regressed may vary for each gas for adsorption on the same adsorbent, upon reasoning that the surface area available may be different for different gases. The slit length, however, was constrained to be the same for each gas, upon reasoning that the characterization of the coals by adsorption is more practicable with the minimum number of necessary model parameters.

The first case study tested adsorption data measured at Oklahoma State University. For the second case study, the surface area is constrained to be the same for each gas on the same adsorbent, and tests included adsorption data from the open literature in addition to our measurements.

Evaluating mathematical models to describe adsorption behavior on coals is complicated by (a) the difficulty in characterizing the coal matrix adequately, and (b)

assessing the effect of water on the adsorption behavior. As a result, a dry activated carbon, which represents a moisture-free, well defined carbon matrix, was chosen for Case Study 1.

CASE STUDY 1: PURE-GAS ADSORPTION ON WET COALS

Gas adsorption measurements have been conducted at Oklahoma State University on a number of coal samples (Hall et al., 1994; Liang, 1999; Sudibandriyo, 2003; Pan, 2003) and on activated carbon (Sudibandriyo, 2003; Pan, 2003). Adsorption isotherms for pure methane, ethane, nitrogen, and CO₂ on dry activated carbon, and similar measurements of methane, nitrogen, and CO₂ on wet Illinois #6, Fruitland, and Lower-Basin (LB) Fruitland coals were measured at pressures to 12.4 MPa (1800 psia). All activated carbon measurements were at 318.15 K (113.0°F), and all coal measurements were at 319.3K (115.0°F). All experimental data for dry and wet coals are presented on a dry basis (e.g., mmol adsorbed/g dry adsorbent).

Pure gases were obtained from commercial vendors with reported purities of 99.95% or higher. Ultimate and proximate analyses of the adsorbents conducted by Huffman Laboratories are presented in Table 3-4.

The quality of the SLD model representation (with modifications to be discussed later in this section) of the OSU experimental data appear in Figure 4-3, where the error bars signify one standard deviation uncertainty in the measurements. Normal distributions in error are assumed for the primary measurements of pressure, temperature, volume, and weight. To estimate the error in the excess adsorption, error was propagated

from these primary measurements, including effects of the temperature and pressure sensitivity of the bulk-phase compressibility factor (Sudibandriyo, 2003).

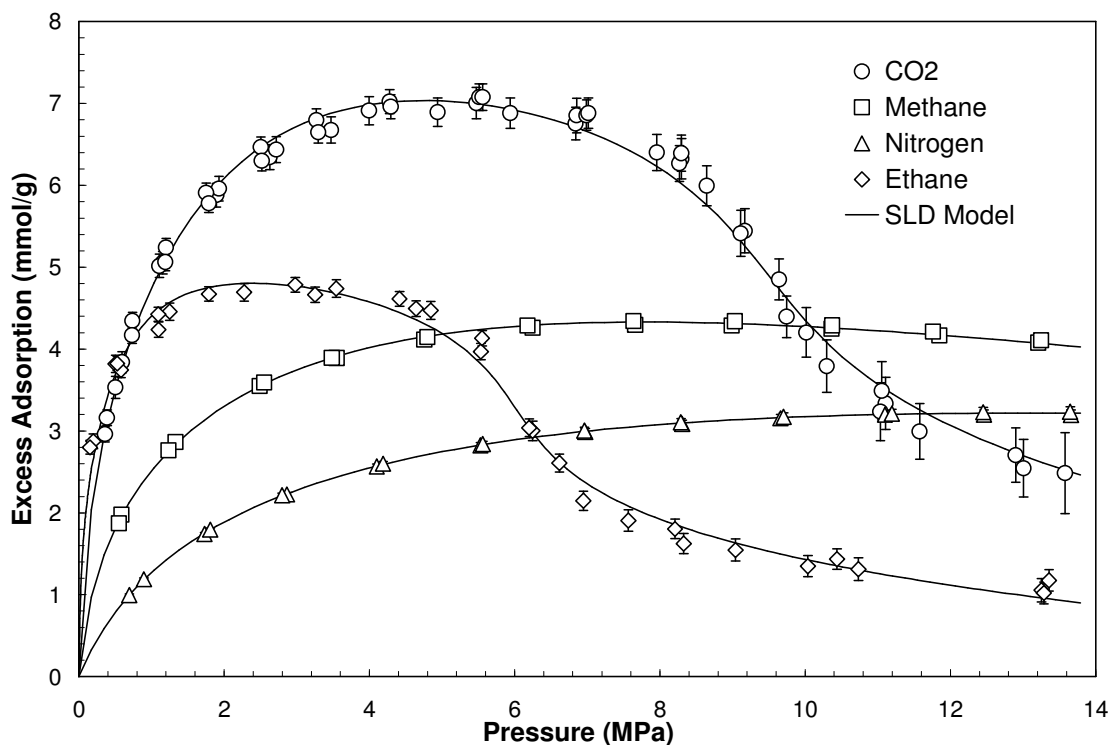


Figure 4-3. Excess Adsorption of CO₂, Methane, Nitrogen, and Ethane on Filtrasorb 400 Activated Carbon at 45°C (113°F) with Modified SLD Model

Figure 4-3 presents excess adsorption data for all four gases on dry activated carbon (Filtrasorb 400, 12x40 mesh, Calgon Carbon). CO₂ and ethane each display a maximum. Methane and nitrogen show less pronounced maxima at higher pressures.

The OSU measurements are compared with the data set Humayun and Tomasko for CO₂ in Figure 4-4. Agreement is within the combined experimental uncertainties. Humayun measured CO₂ adsorption using a gravimetric technique; this method required no helium void volume measurement, in contrast to the volumetric method we used. Their adsorption data were measured continuously at small pressure increments, and therefore, the presentation of their data in Figure 4-4 shows some roughness in the adsorption isotherms. The excellent agreement between the gravimetric and the

volumetric methods implies that the void volume does not change appreciably during the adsorption process for the activated carbon, as well as demonstrating the accuracy of both data sets.

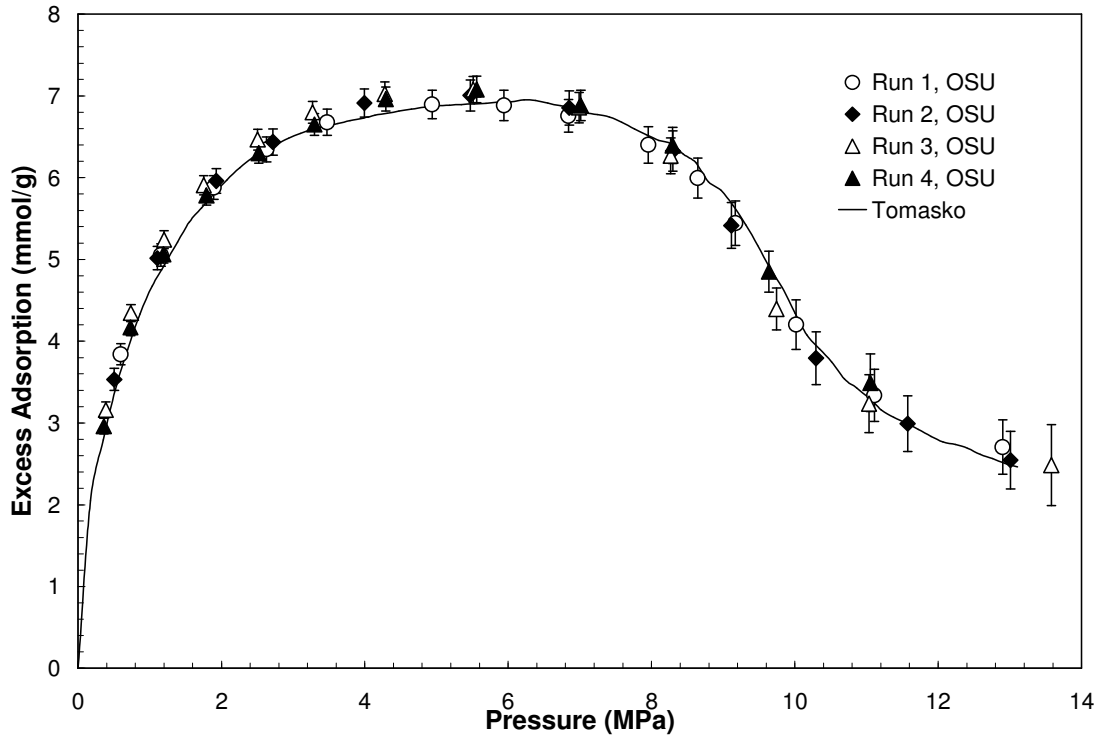


Figure 4-4. Comparison of CO₂ Adsorption Data on Filtrasorb 400 Activated Carbon at 45°C (113°F)

Amoco Corporation (Puri and Yee, 1990; Arri and Yee, 1992) and OSU (Hall et al., 1994; Liang, 1999) have performed several adsorption measurements on Fruitland coal. These measurements span several years, so the coal samples may be slightly different due to variation in handling, oxidation, drying, and rewetting. For modeling purposes in this paper, only the recent measurements on Fruitland coal were used where the ultimate and proximate analyses are available for the samples used. The adsorption isotherms for this coal are shown in Figures 4-5 through 4-7. For CO₂ measurements at pressures above 9 MPa, the reproducibility is visibly lower and an anomalous bump is seen near 9-10 MPa. This bump is also noticeable in the Illinois #6 and Lower Basin

Fruitland coals as well. This experimental artifact is probably due to CO₂'s leaching of water from the coal. The water miscible in the bulk CO₂ fluid will cause the fluid density to change appreciably. Impurities such as water can have an effect on the density of supercritical fluids near the critical temperature (Magee et al., 1994; Chang et al., 1984).

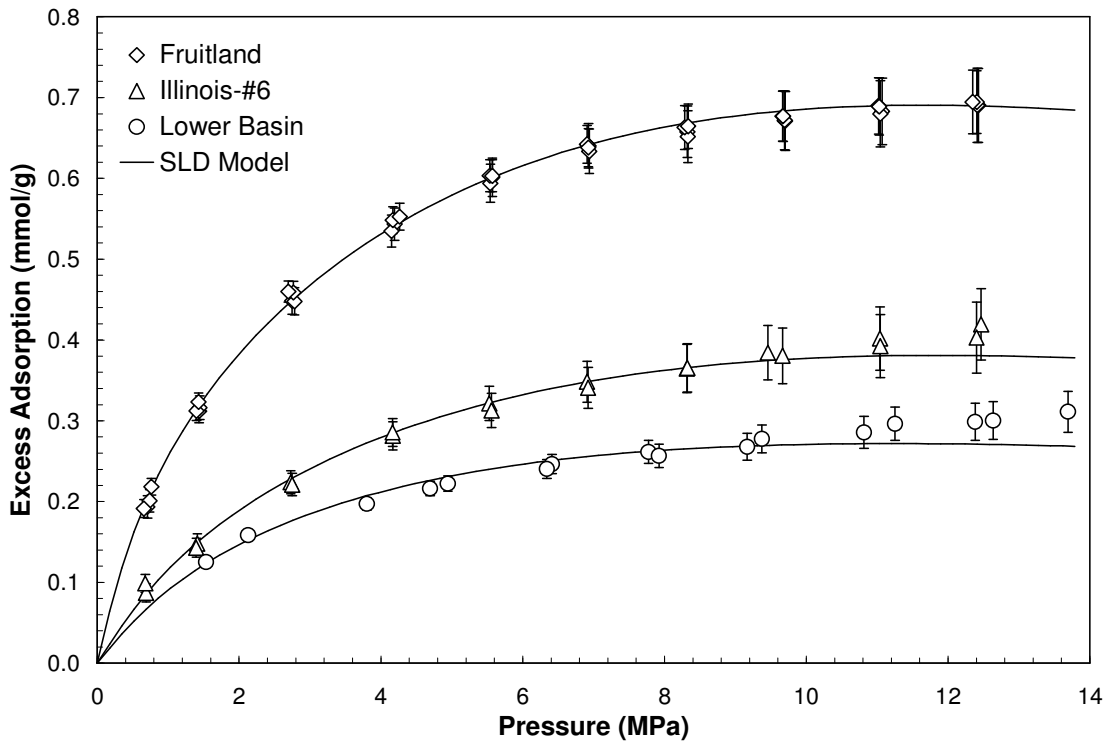


Figure 4-5. Methane Adsorption on Wet Coals at 46.1°C (115°F) with Modified SLD Model

Based on measurements from Yaginuma et al. (2000) and Zhang et al. (2002), the percentage increase of the density of wet CO₂ from dry CO₂ ($100\% \left(\frac{\rho_{\text{CO}_2}^{\text{Wet}} - \rho_{\text{CO}_2}^{\text{Pure}}}{(\rho_{\text{CO}_2}^{\text{Wet}} + \rho_{\text{CO}_2}^{\text{Pure}})/2} \right)$) was calculated using the reference equation of state for the pure CO₂ density (Span and Wagner, 1996). As shown in Figure 4-8, the density of pure CO₂ is greatly affected by water at pressures where the bump occurs in CO₂ isotherms. Besides causing a systematic effect (of anomalous bump near 9.8 MPa), this effect appears to increase the experimental scatter, especially for the Fruitland coal.

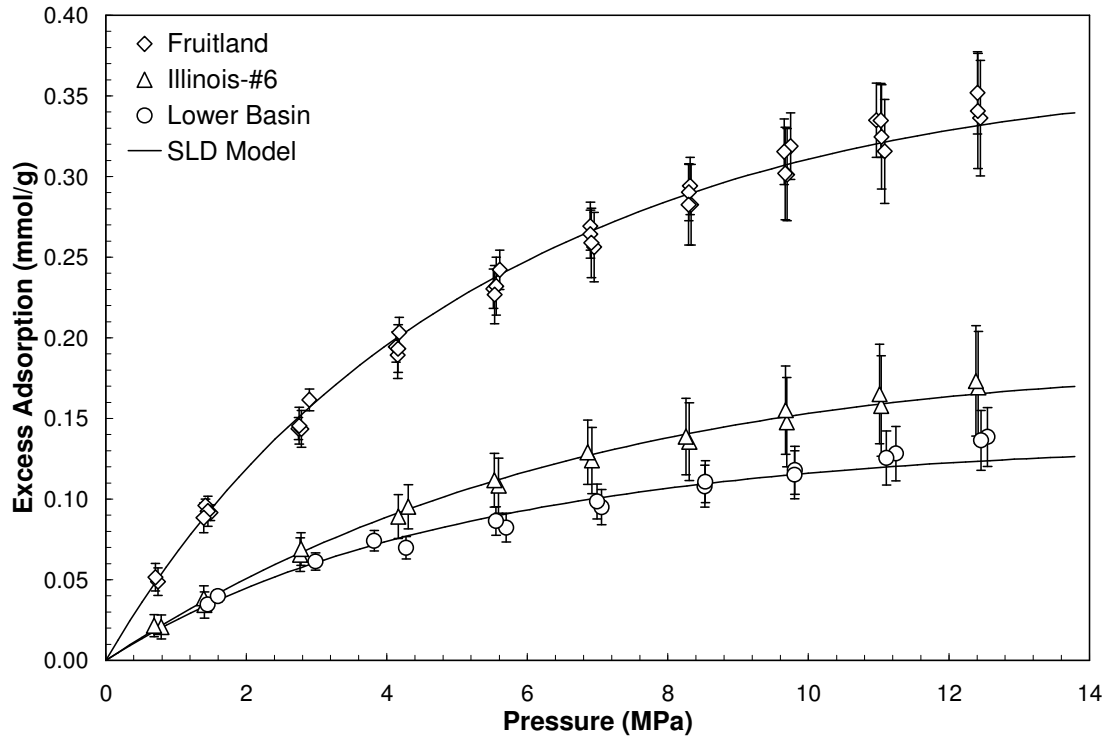


Figure 4-6. Nitrogen Adsorption on Wet Coals at 46.1°C (115°F) with Modified SLD Model

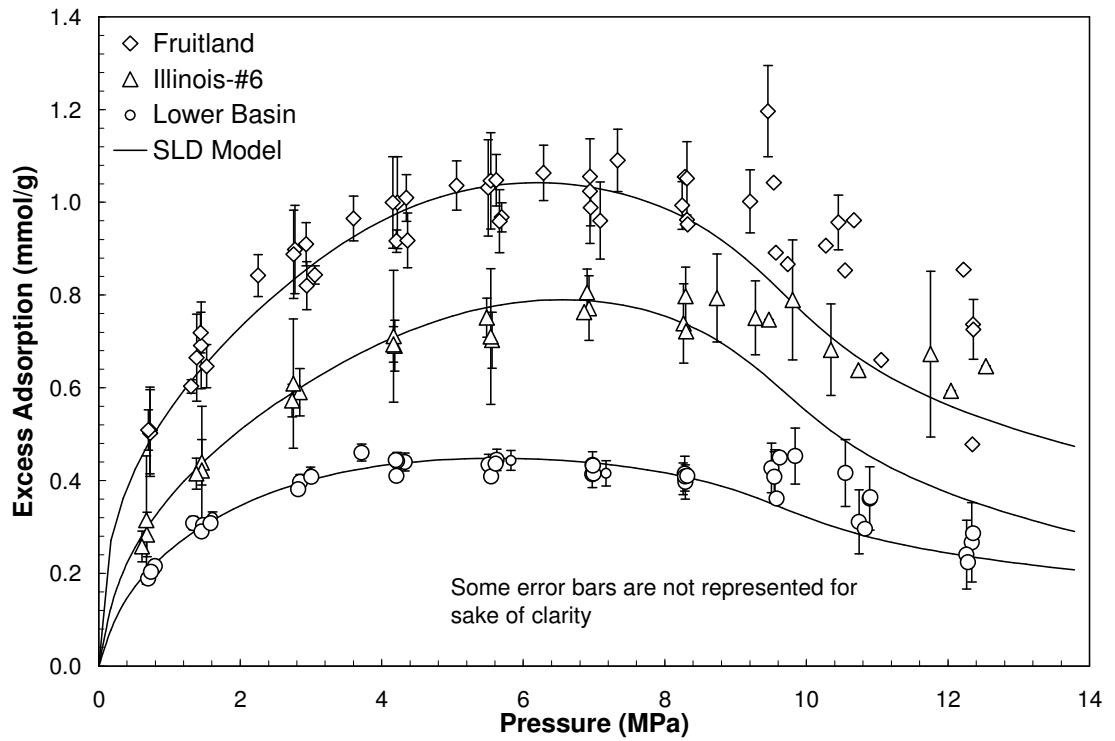


Figure 4-7. CO₂ Adsorption on Wet Coals at 46.1°C (115°F) with Modified SLD Model

The adsorption measurements on wet Illinois #6 are presented in Figures 4-5 through 4-7. These measurements indicate that both methane and nitrogen adsorption on wet Illinois #6 are about half that adsorbed on wet Fruitland coal at the same conditions. Replicate runs were conducted for each gas to confirm the precision of our measurements and to investigate the effect of variations in moisture content and coal sample preparation on the adsorption behavior.

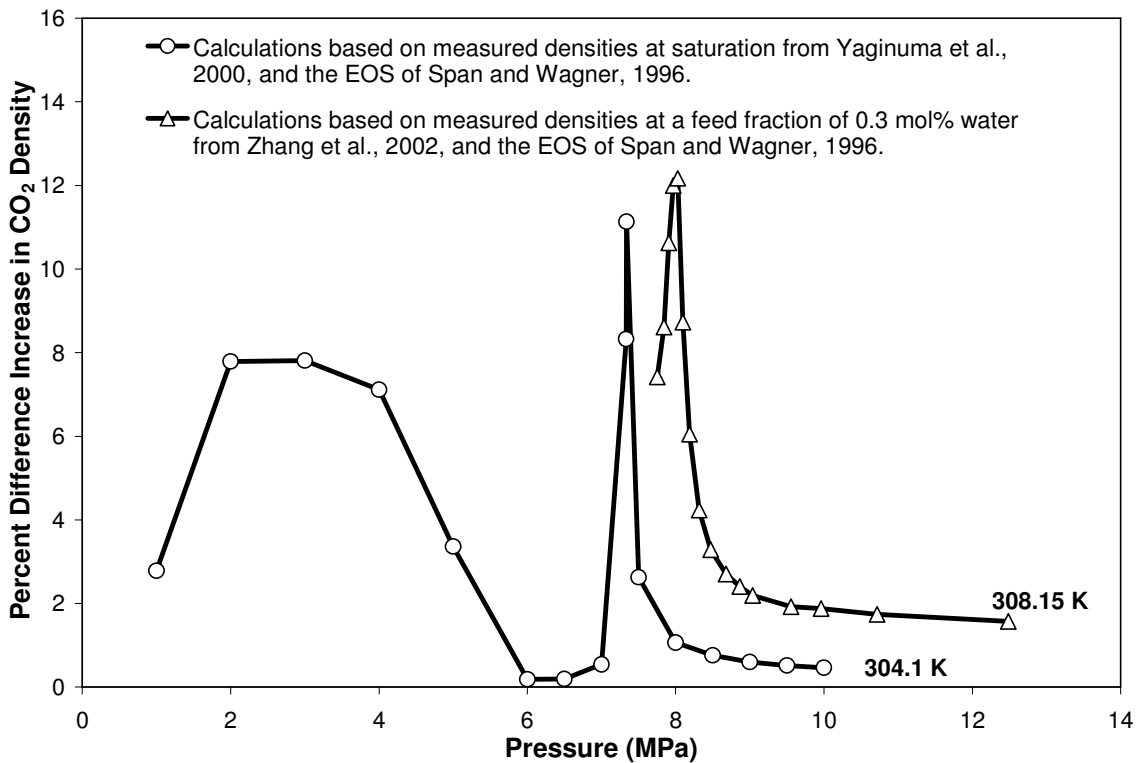


Figure 4-8. Comparison of Pure CO₂ Density and the CO₂ Density with Water

The Illinois #6 data were acquired using two coal samples of different moisture content. Both measurement sets indicate that water content values above the equilibrium water content do not significantly affect the adsorption behavior. These findings support similar conclusions reached in a previous study (Joubert et al., 1973).

Adsorption isotherms for pure methane, nitrogen, and CO₂ on wet Lower-Basin (LB) Fruitland coal are also presented in Figures 4-5 through 4-7. For CO₂, two replicate isotherms show an anomalous “bump” near 9MPa. The increased uncertainty of the CO₂ bulk density at these pressure-temperature conditions amplifies the expected uncertainty in the amount adsorbed. In addition, water in the CO₂ bulk fluid may explain this anomalous behavior, as mentioned previously.

Data Reduction

To correlate data with the SLD model, we used the objective function WRMS, which minimizes the sum of the squared weighted deviations in the predicted excess adsorption:

$$WRMS = \sqrt{\frac{\sum_i^{NPTS} \left(\frac{n_{exp} - n_{calc}}{\sigma_{exp}} \right)_i^2}{NPTS}} \quad (4-14)$$

Here, NPTS is the number of data points, n_{calc} is the calculated excess adsorption, and n_{exp} is the experimental excess adsorption, and σ_{exp} is the expected experimental uncertainty. Detailed procedures for data reduction are given elsewhere (Gasem et al., 1993). The weighted average-absolute deviation (WAAD) is also used to quantify our model evaluations:

$$WAAD = \frac{1}{NPTS} \sum_{i=1}^{NPTS} abs \left(\frac{n_{calc} - n_{exp}}{\sigma_{exp}} \right) \quad (4-15)$$

The average absolute percent error (%AAD) is also given for reference. This is defined by:

$$\%AAD = \frac{1}{NPTS} \sum_{i=1}^{NPTS} abs \left(\frac{n_{calc} - n_{exp}}{n_{exp}} \right) \cdot 100 \quad (4-16)$$

Modeling Results and Discussion

To model the adsorption of methane, ethane, nitrogen, and CO₂ on activated carbon and coals, the SLD theory first implemented by Chen et al. (1997) was used. The model contains three regressed parameters: the surface area A, the slit width L, and the fluid-solid interaction energy parameter ϵ_{fs} . These parameters are used in Equations (4-2) and (4-4). As shown in Figure 4-9, the original SLD model yields poor representation for CO₂ and ethane on activated carbon; the modified version of the SLD model is discussed later in this chapter. The original model cannot correlate the experimental data over the entire pressure range; thus, the results shown in Figure 4-9 are based on regressions at pressures below the excess adsorption maximum. At higher pressures, the observed deviations for both systems are well outside the expected experimental uncertainties. Chen et al. (1997) experienced similar difficulties in modeling CO₂ adsorption on another activated carbon.

Examination of the results from the original SLD model revealed that the calculated adsorbed-phase densities from the EOS in the SLD model are too high for CO₂ and ethane, based on the following reasoning. If the assumption is made that, at sufficiently high pressures, no further adsorption occurs ($V_{ads} \bar{\rho}_{ads}$ becomes constant), then a plot of n^{Ex} versus ρ_{bulk} should become linear with a slope of $-V_{ads}$ (Humayun and

Tomasko, 2000). Further, this linear relation (extrapolated) will reach $n^{\text{Ex}} = 0$ when $\bar{\rho}_{\text{ads}} = \bar{\rho}_{\text{bulk}}$.

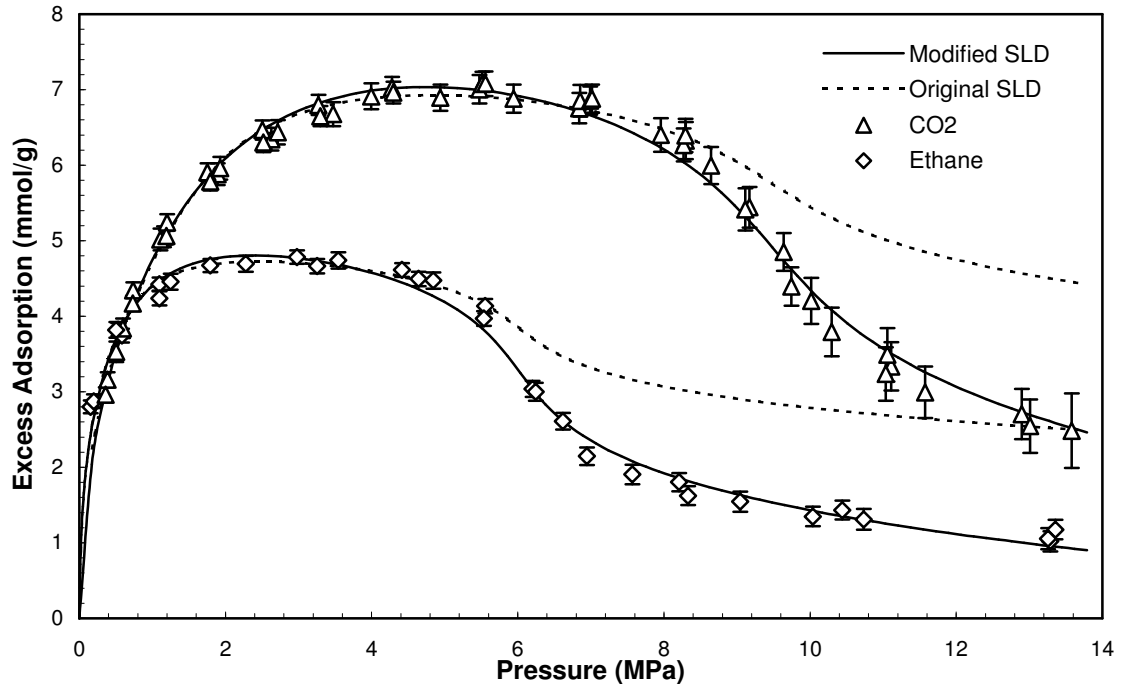


Figure 4-9. Improvement of the SLD Model Predictions by PR Covolume Modification

Based on the above reasoning, Figure 4-10 illustrates that the adsorbed-phase densities for CO₂ and ethane at zero excess adsorption are 22.6 mole/L and 14.8 mole/L, respectively (assuming a linear variation in excess adsorption with density). The SLD model yields adsorbed-phase density estimates at zero excess adsorption (obtained from data below the excess adsorption maximum) are 36.0 and 24.3 mole/L. We attribute this significant disagreement in adsorbed-phase density estimates to an inadequate accounting for repulsive interactions in the original EOS used in the SLD model.

The PR covolume, b , has a significant effect on the calculated local density of the adsorbed fluid, especially near the surface. In Equation (4-13) the logarithmic repulsive term dominates the local fluid fugacity expression, especially near the surface. To

illustrate this, when Equations (4-7), (4-12), and (4-13) are combined, the local density can be expressed as:

$$\frac{1}{\rho(z)} = b + \frac{RT}{P} \exp \left[-\frac{f_b}{P} \exp \left(\frac{-\Psi(z) - \Psi(L-z)}{kT} \right) - \lambda \right] \quad (4-17)$$

where

$$\lambda = \frac{b\rho(z)}{1 - b\rho(z)} - \frac{a_{\text{ads}}(z)\rho(z)}{RT(1 + 2\rho(z)b - b^2\rho^2(z))} - \frac{a_{\text{ads}}(z)}{2\sqrt{2}bRT} \ln \left(\frac{1 + (1 + \sqrt{2})\rho(z)b}{1 + (1 - \sqrt{2})\rho(z)b} \right)$$

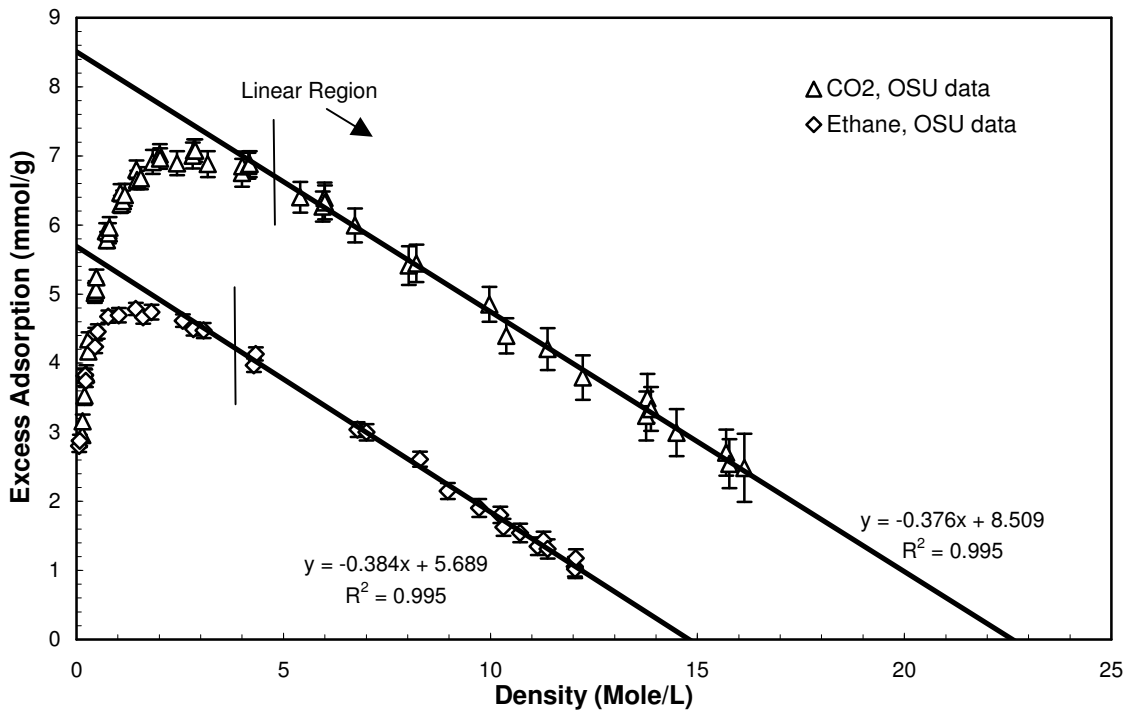


Figure 4-10. Determination of Adsorbed-Phase Density on Activated Carbon at 45°C

Near the surface, where the fluid-solid potential is large in magnitude, the exponential term containing the fluid-solid potential vanishes, and at moderate pressures the local density can be approximated by:

$$\frac{1}{\rho(z)} \approx b + \frac{RT}{P} \exp[-\lambda] \quad \text{Near the wall} \quad (4-18)$$

At higher pressures, the second term becomes small and the adsorbed density at the wall approaches the reciprocal covolume.

$$\rho(\text{wall}) \rightarrow \frac{1}{b} \quad \text{Near the wall at high pressures} \quad (4-19)$$

The covolume is the dominant factor that determines the adsorbed-density profile in the high-pressure limit. Thus, the accuracy of the repulsive expression is predominant in modeling the local density. Soule et al. (2001) used the Elliot-Suresh-Donohue equation of state to better account for the subdivision of attractive and repulsive interactions for adsorption modeling in the SLD framework. Compared to the van der Waals and PR equations of state, the ESD equation more accurately described the temperature dependence of adsorption.

Instead of incorporating a more accurate repulsive term in the PR EOS, a simple empirical modification was used to account for the repulsive interactions of the high-density adsorbed fluid. The objective was to obtain initial information regarding the impact of changes in ‘b’ on the calculated adsorption, especially for supercritical CO₂ at high pressures. Thus, the PR covolume was empirically adjusted by the parameter Λ_b :

$$b_{\text{ads}} = b \cdot (1 + \Lambda_b) \quad (4-20)$$

Equation (4-13) then becomes:

$$\ln \frac{f_{ff}(z)}{P} = \frac{b_{ads}\rho(z)}{1 - b_{ads}\rho(z)} - \frac{a_{ads}(z)\rho(z)}{RT[1 + 2b_{ads}\rho(z) - b_{ads}^2\rho(z)^2]} - \ln \left[\frac{1 - b_{ads}\rho(z)}{RT\rho(z)} \right] - \frac{a_{ads}(z)}{2\sqrt{2}b_{ads}RT} \ln \left[\frac{1 + (1 + \sqrt{2})\rho(z)b_{ads}}{1 + (1 - \sqrt{2})\rho(z)b_{ads}} \right] \quad (4-21)$$

SLD Adsorption with Peng-Robinson Covolume Modification

With the above modification, the SLD model representations for CO₂ and ethane on dry activated carbon are improved dramatically. Table 4-2 presents the regressed parameters for the modified case. For CO₂, when the covolume was increased by 52% ($\Lambda_b = 0.52$), the adsorbed-phase density at zero excess adsorption was in better agreement with our graphical estimates. Ethane had similar improvements when its covolume was increased by 56%. Figure 4-9 shows the improvement for the high-pressure adsorption for both CO₂ and ethane. Figure 4-11 demonstrates the effect of the modified covolume on the CO₂ local density profile at two pressures. Figure 4-12 normalizes the local density for CO₂ to the modified covolume b_{ads} . Even at 0.69 MPa, the wall density is roughly 96% of $1/b_{ads}$. As the pressure increases, the wall density approaches $1/b_{ads}$ as indicated by Equations (4-18) and (4-19), thus validating their use.

Table 4-2. Modified SLD Model Results on Activated Carbon at 45°C (113°F)

| | CO₂ | Ethane | Methane | Nitrogen |
|-----------------------|-----------------------|---------------|----------------|-----------------|
| A (m ² /g) | 1131 | 1126 | 774 | 643 |
| ϵ_{fs}/k (K) | 78.5 | 83.0 | 77.6 | 57.1 |
| L ₀ (nm) | 1.11 | 1.11 | 1.11 | 1.11 |
| Λ_b | 0.52 | 0.56 | 0.52 | 0.55 |
| | | | | |
| NPTS | 51 | 32 | 22 | 22 |
| % AAD | 2.5 | 4.9 | 0.6 | 0.3 |
| WRMS | 0.78 | 1.54 | 0.60 | 0.26 |
| WAAD | 0.64 | 1.19 | 0.47 | 0.24 |

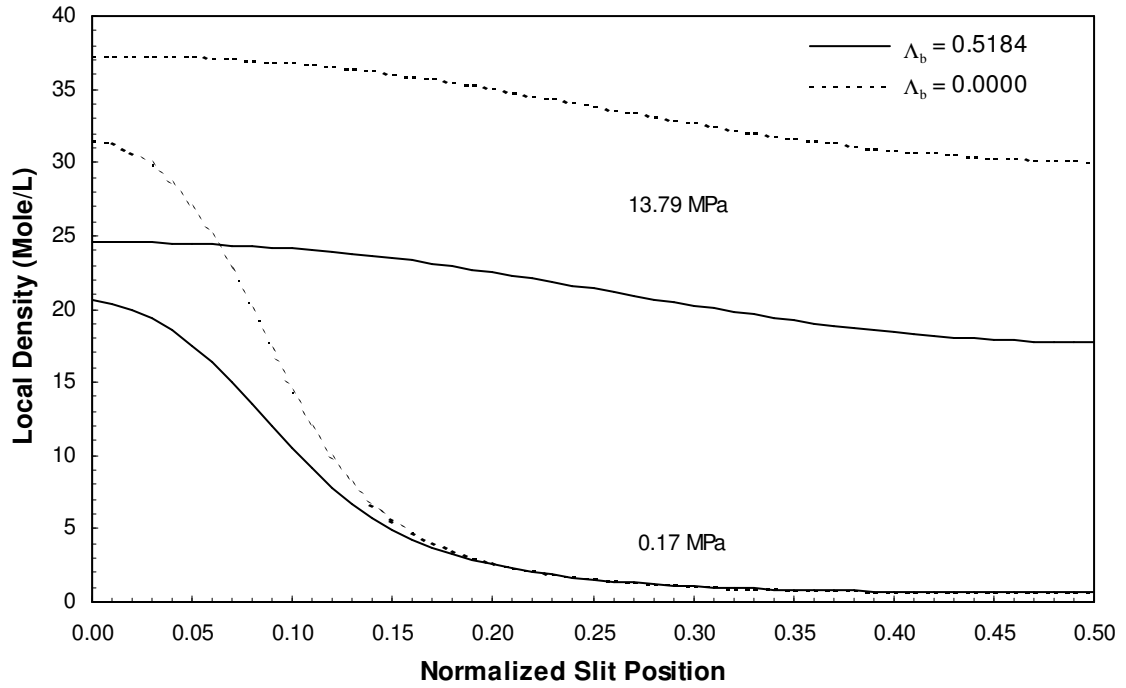


Figure 4-11. Effect of PR Covolume on Local Density: CO₂ at 45°C

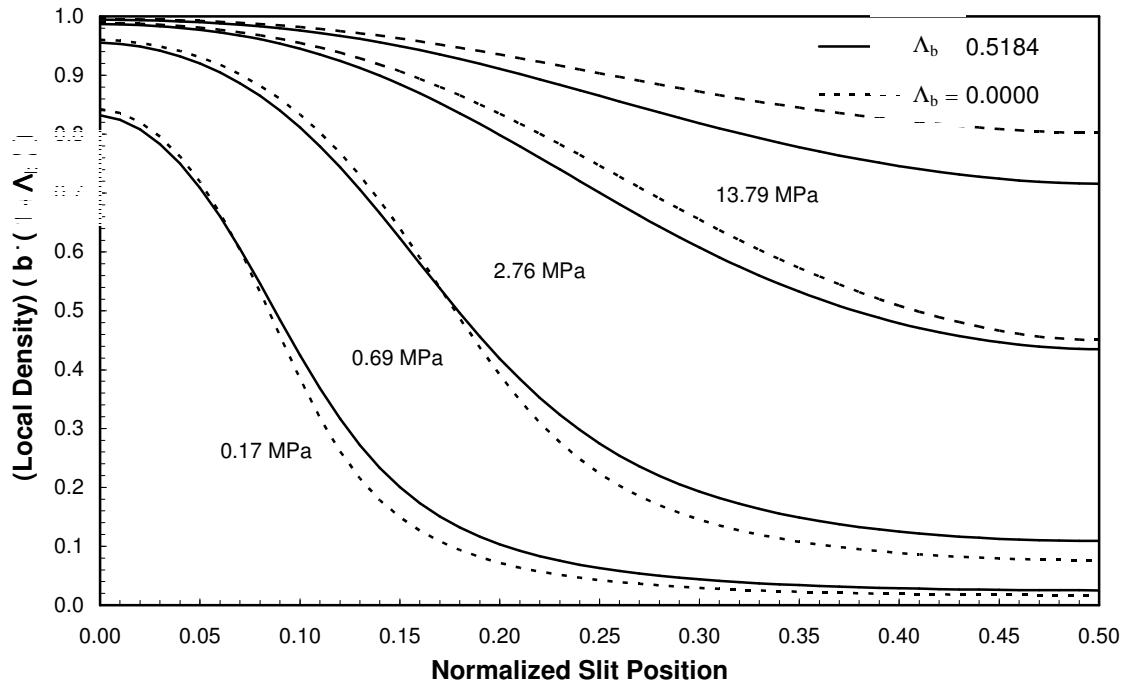


Figure 4-12. Effect of PR Covolume on Normalized Local Density: CO₂ at 45°C

Table 4-3 presents the summary results for our evaluation of gas adsorption on wet coals. In general, the modified SLD-PR model is capable of representing the adsorption data considered in this study within their experimental uncertainties. Due to the lower reproducibility of CO₂ sorption data in the high-pressure region, as shown in Figure 4-7, the covolume parameter Λ_b was set to 0.30 for modeling the wet coals rather than regressing it. Regression results show that the value of Λ_b is smaller than that observed for the dry activated carbon. A constrained value of 0.30 for Λ_b for CO₂ was used to achieve an adsorbed-phase density (at zero excess adsorption) comparable to that obtained for CO₂ adsorption on activated carbon (~1.0 g/cm³). Failing to constrain Λ_b produces model results implying that the adsorbed-phase densities are high (~1.3 - 1.8 g/cm³ for CO₂).

The wet coal isotherms differ from the dry activated carbon isotherms in at least two respects. First, the presence of water lowers the adsorptive capacity of the adsorbent and alters the shape of the isotherms. (Water was accounted for in the experimental measurements so that only physical adsorption on the coal is considered, as shown in Chapter 2). Second, the coals have significantly lower surface areas than the activated carbon, as shown in Tables 4-2 and 4-3.

Absolute Adsorption Calculations

Absolute adsorption can be calculated readily from the regressed SLD-PR parameters for a given adsorbent as follows:

$$n^{\text{Abs}} = n^{\text{Ex}} + \frac{A}{2}(L - \sigma_{\text{ff}})\rho_{\text{bulk}} \quad (4-22)$$

Table 4-3. Summary Results for the Modified SLD-PR Adsorption Model

| Model Parameters | Pure-Gas Adsorbed | | |
|-----------------------------|-------------------|----------|-----------------|
| | Methane | Nitrogen | CO ₂ |
| Wet Fruitland Coal | | | |
| A (m ² /g) | 104 | 72 | 99 |
| ϵ_{fs}/k (K) | 61 | 35 | 95 |
| L (nm) | 1.60 | 1.60 | 1.60 |
| Λ_b | 0.30 | 0.30 | 0.30 |
| NPTS | 40 | 37 | 52 |
| % AAD | 1.2 | 3.0 | 8.8 |
| WRMS | 0.36 | 0.52 | 1.28 |
| WAAD | 0.27 | 0.42 | 0.91 |
| Wet Illinois #6 Coal | | | |
| A (m ² /g) | 67 | 51 | 90 |
| ϵ_{fs}/k (K) | 49 | 24 | 70 |
| L (nm) | 1.62 | 1.62 | 1.62 |
| Λ_b | 0.30 | 0.30 | 0.30 |
| NPTS | 20 | 20 | 30 |
| % AAD | 3.0 | 3.4 | 10.9 |
| WRMS | 0.46 | 0.19 | 0.82 |
| WAAD | 0.33 | 0.17 | 0.61 |
| Wet LB Fruitland | | | |
| A (m ² /g) | 56 | 31 | 66 |
| ϵ_{fs}/k (K) | 47 | 32 | 65 |
| L (nm) | 1.12 | 1.12 | 1.12 |
| Λ_b | 0.30 | 0.30 | 0.30 |
| NPTS | 16 | 17 | 48 |
| % AAD | 4.8 | 4.7 | 6.9 |
| WRMS | 0.95 | 0.52 | 0.89 |
| WAAD | 0.83 | 0.42 | 0.68 |

In Equation (4-22), the absolute adsorption was calculated from the excess adsorption using the SLD adsorbed-phase volume, V_{ads} , and the PR bulk gas density. For

this study, the SLD adsorbed-phase volume for a slit geometry is the product of half the surface area, A , and the effective slit width, $L - \sigma_{ff}$; this is the volume where the spherical fluid molecules can reside without intersecting the hypothetical flat-plane carbon surface, i.e., the center of a fluid molecule cannot move closer than a distance of $\sigma_{ff}/2$ from each wall of the slit. The resultant absolute adsorption isotherms on dry activated carbon are depicted in Figure 4-13; and similar isotherms for the wet coals are shown in Figures 4-14 through 4-16. Note that for ethane and CO_2 on activated carbon, the capacity for the absolute adsorption corresponds to the zero-density intercept of the linearly regressed line in Figure 4-10. As indicated by Figure 4-13, methane and nitrogen adsorption isotherms have not reached their maximum adsorption capacity at 14 MPa, the highest pressure of this study.

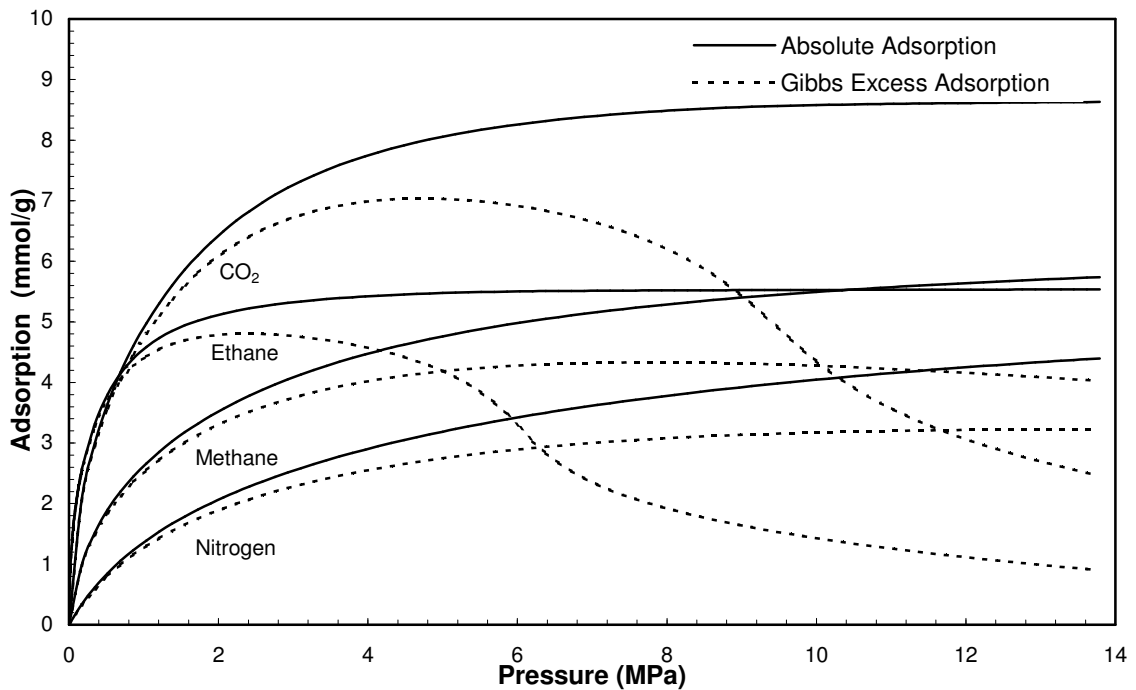


Figure 4-13. Absolute Adsorption Calculated by SLD Model for Activated Carbon at 45°C (113°F)

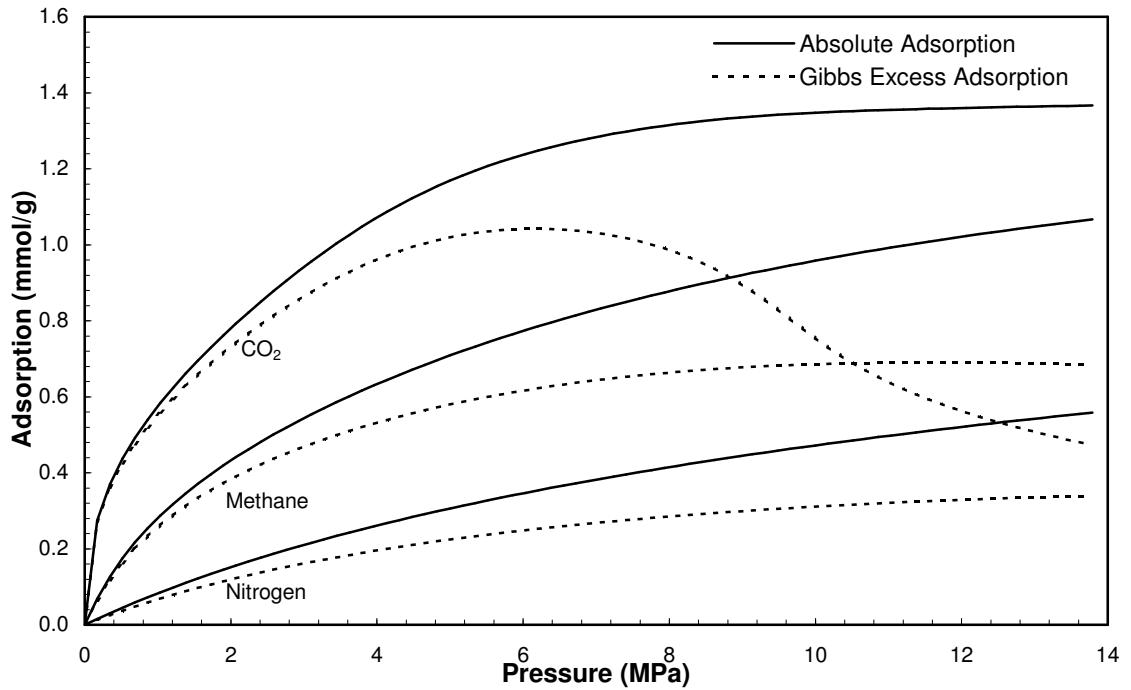


Figure 4-14. Absolute Adsorption Calculated by SLD Model for Fruitland Coal at 46.1°C (115°F)

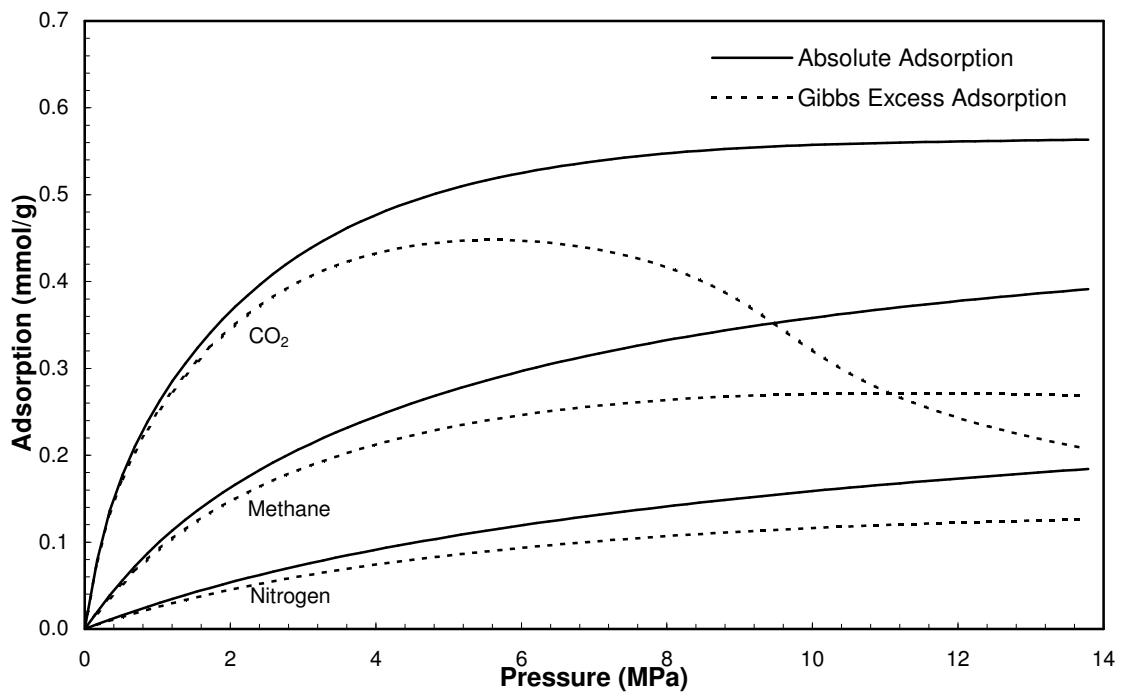


Figure 4-15. Absolute Adsorption Calculated by SLD Model for Lower Basin Fruitland at 46.1°C (115°F)

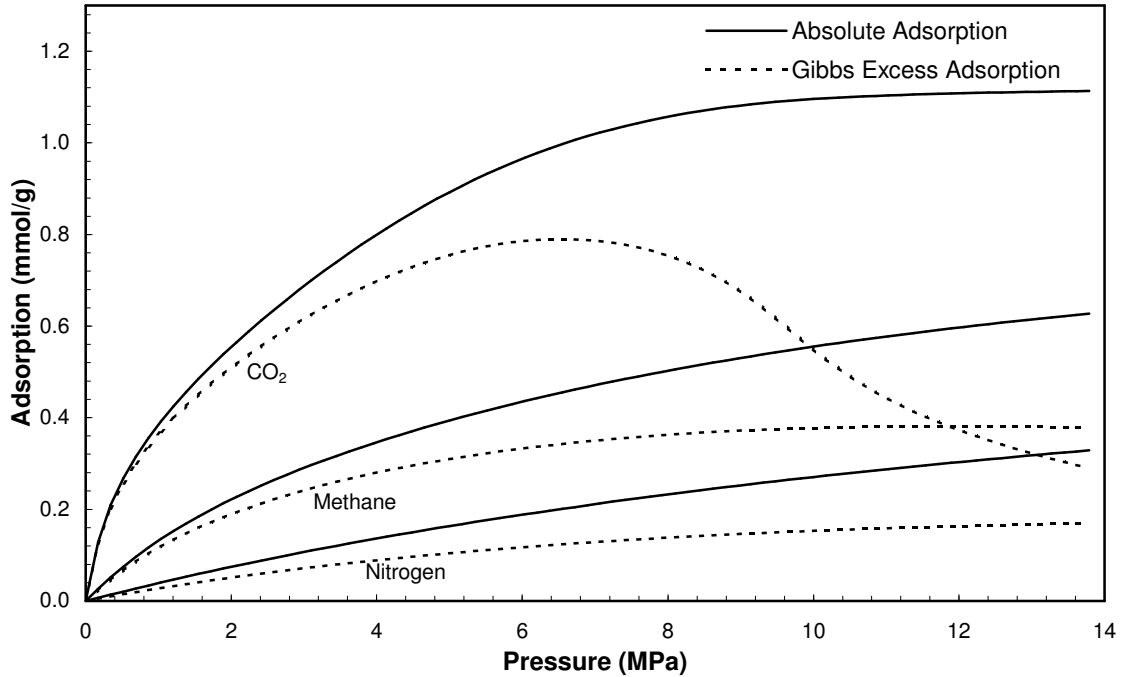


Figure 4-16. Absolute Adsorption Calculated by SLD Model for Illinois #6 Coal at 46.1°C (115°F)

Conclusions for Case Study 1

The major conclusions of Case Study 1 are as follows:

- The modified SLD-PR model is better equipped than the original model to represent adsorption isotherms encountered in CBM production and CO₂ sequestration, including those exhibiting excess adsorption maxima.
- Simple modification of the PR EOS covolume improves both the excess adsorption and the adsorbate-phase density predictions. Further study is needed to improve the description of the repulsive forces in the EOS used in SLD calculations.
- The modified SLD-PR model provides reliable representation of excess or absolute adsorption behaviors.

CASE STUDY 2: LITERATURE PURE-GAS ADSORPTION

A database was compiled for the sorption behavior on three adsorbent types: activated carbons, zeolites, and coals. Activated carbons were included because they have much larger adsorption loadings than do coals, and because of this, experimental results for activated carbons are generally more certain and more reproducible. Also, other independent laboratories may reproduce sorption results on commercial activated carbons, whereas coal samples presumably of the same type may have physical variations that confound inter-laboratory comparisons.

Zeolites can serve as a comparative basis between organic and non-organic based adsorbents. Models that refer quantitatively to gas-solid interactions may have typical values for carbon-based adsorbents such as coals and activated carbons and other values for zeolites, which normally do not contain much carbon. Such a comparative basis can help establish whether regressed model parameters make physical sense.

For all three adsorbent types, the database was generally limited to coalbed gases. An emphasis was placed on experimental data focused on high-pressure adsorption, particularly at supercritical temperatures.

A database of adsorption on activated carbons and zeolites consists of 42 systems. In addition, a database of 17 systems has been compiled for adsorption on coals, bringing the total database to 59 systems. Each "system" consists of at least one gas isotherm on a specific adsorbent. Table 4-4 lists information for each of the 59 systems including the adsorbent type, the adsorbate, the temperature and pressure ranges, and the original reference. The overall distribution of pressures for the activated carbon/zeolite database is depicted in Figure 4-17.

Table 4-4. Data Used for Pure-Gas Adsorption Model Evaluations

| System No. | Adsorbent | Adsorbent Surf. area (m ² /g) | Adsorbate | Temp. Range (K) | Pressure Range (MPa) | Reference |
|------------|--|--|-------------------------------|-----------------|---------------------------|---------------------------|
| 1 | AC, Columbia Grade L | 1152 | N ₂ | 311 - 422 | 0.028 – 1.50 | Ray and Box, 1950 |
| 2 | AC, Columbia Grade L | 1152 | CH ₄ | 311 - 422 | 0.026 – 1.48 | Ray and Box, 1950 |
| 3 | AC, Columbia Grade L | 1152 | C ₂ H ₆ | 311 - 478 | 0.007 – 1.49 | Ray and Box, 1950 |
| 4 | Carbon Black | 123 | CH ₄ | 311 - 394 | 0.05 – 65.6 | Stacy et al., 1968 |
| 5 | Charcoal | 1157 | CH ₄ | 283 - 323 | 0.5 – 13.8 | Payne et al., 1968 |
| 6 | Charcoal | 1157 | C ₃ H ₈ | 293 - 333 | 8x10 ⁻⁴ – 1.35 | Payne et al., 1968 |
| 7 | AC, BPL | 988 | CH ₄ | 213 - 301 | 0.012 – 3.83 | Reich et al., 1980 |
| 8 | AC, BPL | 988 | C ₂ H ₆ | 213 - 301 | 7x10 ⁻⁴ – 1.71 | Reich et al., 1980 |
| 9 | AC, BPL | 988 | C ₂ H ₄ | 213 - 301 | 7x10 ⁻⁴ – 1.70 | Reich et al., 1980 |
| 10 | AC, BPL | 988 | CO ₂ | 213 - 301 | 0.003 – 3.84 | Reich et al., 1980 |
| 11 | AC, PCB-Calgon Corp. | 1150-1250 | CH ₄ | 296 - 480 | 0.27 – 6.69 | Ritter and Yang, 1987 |
| 12 | AC, PCB-Calgon Corp. | 1150-1250 | CO ₂ | 296 - 480 | 0.11 – 3.67 | Ritter and Yang, 1987 |
| 13 | AC F30/470, Chemviron Carbon | 993.5 | CO ₂ | 278 - 328 | 0.05 – 3.35 | Berlier et al., 1997 |
| 14 | AC Norit R1 Extra | 1450 | N ₂ | 298 | 0.03 – 5.98 | Dreisbach et al., 1999 |
| 15 | AC Norit R1 Extra | 1450 | CH ₄ | 298 | 0.01 – 5.75 | Dreisbach et al., 1999 |
| 16 | AC Norit R1 Extra | 1450 | CO ₂ | 298 | 0.008 – 6.0 | Dreisbach et al., 1999 |
| 17 | AC from Coconut shell with KOH activation | 3106 (CO ₂ ads.) | CH ₄ | 233 - 333 | 0.09 – 9.40 | Zhou et al., 2000 |
| 18 | AC -Calgon F-400 | 850 | CO ₂ | 303 to 318 | 0.02 – 20.2 | Humayun and Tomasko, 2000 |
| 19 | AC-Norit RB1 | 1100 | CH ₄ | 294 - 351 | 0.05 – 0.8 | Vaart et al., 2000 |
| 20 | AC-Norit RB1 | 1100 | CO ₂ | 294 - 348 | 0.05 – 0.8 | Vaart et al., 2000 |
| 21 | AC from Coconut shell with KOH activation | 3106 (CO ₂ ads.) | N ₂ | 178 - 298 | 0.44 – 9.19 | Zhou et al., 2001 |

Table 4-4. Data Used for Pure-Gas Adsorption Model Evaluation (Continued)

| System No. | Adsorbent | Adsorbent Surf. Area (m²/g) | Adsorbate | Temp. Range (K) | Pressure Range (MPa) | Reference |
|-------------------|-------------------------------------|---|-------------------------------|------------------------|-----------------------------|-----------------------------|
| 22 | AC F30/470, Chemviron Carbon | 993.5 | N ₂ | 303 - 383 | 0.39 – 9.5 | Frère et al., 2002 |
| 23 | AC F30/470, Chemviron Carbon | 993.5 | CH ₄ | 303 - 383 | 0.44 – 8.98 | Frère et al., 2002 |
| 24 | AC F30/470, Chemviron Carbon | 993.5 | C ₃ H ₈ | 303 - 383 | 0.05 – 2.20 | Frère et al., 2002 |
| 25 | AC Norit R1 | 1262 | N ₂ | 298 | 0.03 – 14.56 | Beutekamp and Harting, 2002 |
| 26 | AC Norit R1 | 1262 | CO ₂ | 298 | 0.03 – 6.04 | Beutekamp and Harting, 2002 |
| 27 | AC –Calgon F-400 | 850 | N ₂ | 298 | 0.67 – 12.9 | OSU |
| 28 | AC –Calgon F-400 | 850 | CH ₄ | 298 | 0.67 – 12.9 | OSU |
| 29 | AC –Calgon F-400 | 850 | CO ₂ | 298 | 0.67 – 12.9 | OSU |
| 30 | AC –Calgon F-400 | 850 | C ₂ H ₆ | 298 | 0.67 – 12.9 | OSU |
| 31 | Zeolite, Linde 13 X | 525 | N ₂ | 298 - 348 | 0.35 – 8.23 | Wakasugi et al., 1981 |
| 32 | Zeolite, Linde 5A | ~400 | N ₂ | 298 - 348 | 0.60 – 17.61 | Wakasugi et al., 1981 |
| 33 | Zeolite, Linde 5A | ~400 | CH ₄ | 298 - 348 | 0.36 – 9.18 | Wakasugi et al., 1981 |
| 34 | Zeolite, Linde 5A | ~400 | CO ₂ | 298 - 348 | 0.03 – 11.22 | Wakasugi et al., 1981 |
| 35 | Zeolite, Linde 5A | ~400 | C ₂ H ₆ | 298 - 348 | 0.07 – 5.07 | Wakasugi et al., 1981 |
| 36 | H-Modernite, Norton Co: Type Z-900H | ~300 | CO ₂ | 283 - 333 | 3x10 ⁻⁴ – 0.29 | Talu and Zweibel, 1986 |
| 37 | H-Modernite, Norton Co: Type Z-900H | ~300 | C ₃ H ₈ | 283 - 324 | 2x10 ⁻⁵ – 0.21 | Talu and Zweibel, 1986 |
| 38 | Zeolite G5 | 430 | CH ₄ | 283 - 303 | 0.13 – 1.15 | Berlier et al., 1995 |
| 39 | Zeolite G5 | 430 | C ₂ H ₆ | 283 - 303 | 0.056 – 1.10 | Berlier et al., 1995 |
| 40 | Zeolite G5 | 430 | C ₂ H ₄ | 283 - 303 | 0.056 – 1.10 | Berlier et al., 1995 |

Table 4-4. Data Used for Pure-Gas Adsorption Model Evaluation (Continued)

| System No. | Adsorbent | Adsorbent Surf. Area (m²/g) | Adsorbate | Temp. (K) | Pressure Range (MPa) | Reference |
|-------------------|-------------------------|---|-------------------------------|------------------|-----------------------------|-----------------------------|
| 41 | Zeolite13 X | 383 | CH ₄ | 298 | 0.15 – 15.02 | Beutekamp and Harting, 2002 |
| 42 | Zeolite13 X | 383 | C ₂ H ₆ | 298 | 0.14 – 3.95 | Beutekamp and Harting, 2002 |
| 43 | Wet Fruitland Coal #2 | -- | N ₂ | 319.3 | 0.7 – 12.4 | OSU |
| 44 | Wet Fruitland Coal #2 | -- | CH ₄ | 319.3 | 0.7 – 12.4 | OSU |
| 45 | Wet Fruitland Coal #2 | -- | CO ₂ | 319.3 | 0.7 – 12.4 | OSU |
| 46 | Wet Illinois #6 Coal | -- | N ₂ | 319.3 | 0.7 – 12.4 | OSU |
| 47 | Wet Illinois #6 Coal | -- | CH ₄ | 319.3 | 0.7 – 12.4 | OSU |
| 48 | Wet Illinois #6 Coal | -- | CO ₂ | 319.3 | 0.7 – 12.5 | OSU |
| 49 | Wet Tiffany Coal | -- | N ₂ | 327.5 | 0.7 – 13.8 | OSU |
| 50 | Wet Tiffany Coal | -- | CH ₄ | 327.5 | 0.4 – 13.6 | OSU |
| 51 | Wet Tiffany Coal | -- | CO ₂ | 327.5 | 0.5 – 13.6 | OSU |
| 52 | Wet LB Fruitland Coal | -- | N ₂ | 319.3 | 1.5 – 12.4 | OSU |
| 53 | Wet LB Fruitland Coal | -- | CH ₄ | 319.3 | 1.4 – 12.5 | OSU |
| 54 | Wet LB Fruitland Coal | -- | CO ₂ | 319.3 | 0.7 – 12.4 | OSU |
| 55 | Dry Illinois #6 Coal | -- | CO ₂ | 328 | 0.7 – 13.8 | OSU |
| 56 | Dry Beulah Zap Coal | -- | CO ₂ | 328 | 0.6 – 13.8 | OSU |
| 57 | Dry Wyodak Coal | -- | CO ₂ | 328 | 0.7 – 13.8 | OSU |
| 58 | Dry Upper Freeport Coal | -- | CO ₂ | 328 | 0.7 – 13.8 | OSU |
| 59 | Dry Pocahontas Coal | -- | CO ₂ | 328 | 1.1 – 13.8 | OSU |

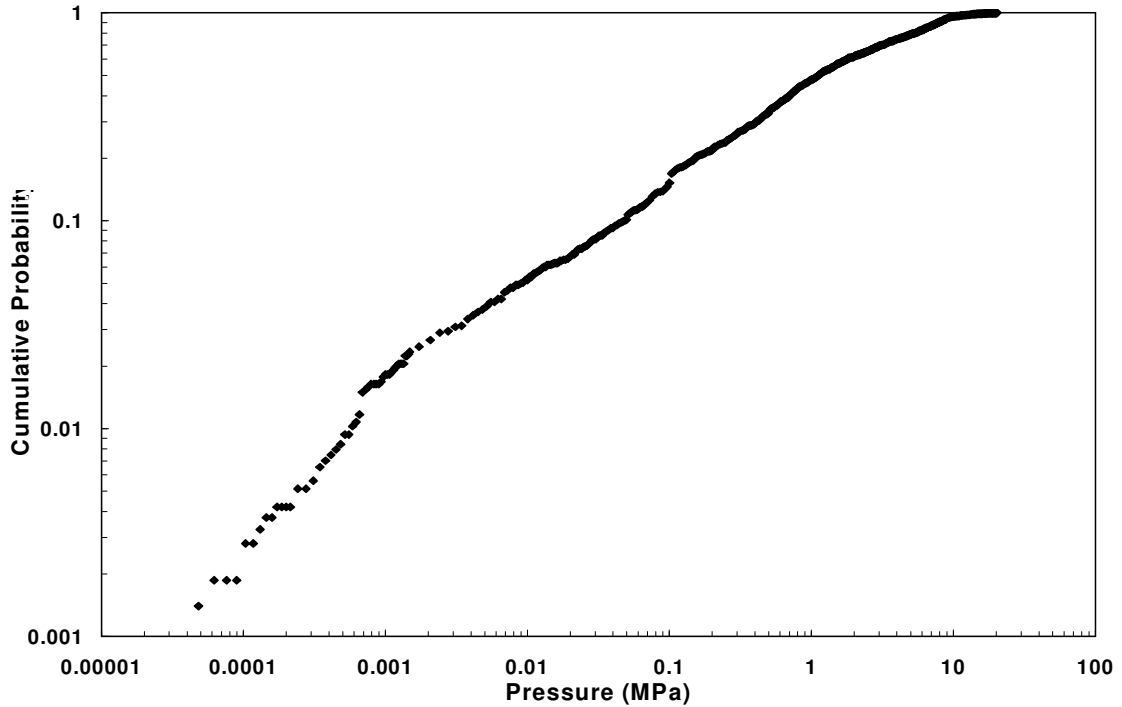


Figure 4-17. Cumulative Distribution Function of Pressure for Pure-Gas Adsorption on Activated Carbons and Zeolites (2140 Data Points)

A system may be analyzed separately or several systems may be analyzed together in an adsorbent group. Analyzing system groups helps establish whether a model can simultaneously correlate adsorption data of different gas species on the same adsorbent. For each system or adsorbent group, the weighted absolute average deviation (WAAD) was used as an objective function to regress the SLD model parameters. The set of parameters that minimizes the WAAD is assumed to be the best that characterizes each system or system group:

$$WAAD = \frac{1}{NPTS} \sum_{i=1}^{NPTS} abs \left(\frac{n_{calc} - n_{exp}}{\sigma_{exp}} \right) \quad (4-23)$$

To establish the point estimates for the weights, we consider two cases. If the sorption data are from the OSU research group, then point estimates of the expected

experimental error have been established, and the weights are set to these point estimates. Otherwise, the weights are set proportionally to each experimental point. Thus, for this scenario, the objective function will become proportional to the sum of the absolute percent deviations. In some cases, some experimental data points may compromise the goodness of the overall fit; the weight for such data points (outliers) will be changed to accommodate this situation (by setting the reciprocal weight to zero). A full discussion of all such cases is given in the results section.

For Case Study 1, the lower limit of integration (the left side of slit) was set at $\sigma_{ff}/2$ and the upper limit of integration to be $L-\sigma_{ff}/2$, the slit width adjusted by half of the fluid diameter σ_{ff} . For Case Study 2, the lower limit of integration is set to $3/8\sigma_{ff}$ to include the density profile close to the surface wall; for distances less than $1/8 \sigma_{ff}$ away from a surface wall, the local density is zero. The lower limit of integration was changed to investigate its effects on the overall fit and parameterization of the model. At limits lower than $3/8\sigma_{ff}$, the numerical routines used to solve the equilibrium equations sometimes fail; thus, limits lower than $3/8\sigma_{ff}$ were not investigated in depth. As mentioned previously, the surface area was constrained to be the same for each gas on the same adsorbent.

Data Reduction

For all systems, the following SLD parameters were regressed: the surface area A , the effective slit length L , the reduced fluid-solid interaction energy parameter ϵ_{fs}/k_B , and the covolume modification term, Λ_b , as given by $b_{ads} = b \cdot (1 + \Lambda_b)$. In addition, a parameter 'k' was included to account for the temperature dependence on the fluid-solid

interaction parameter ε_{fs}/k_B , where k_B is the Boltzmann constant. The temperature dependence of Lennard-Jones 12-6 fluid-interaction parameters has been found by comparison to other theories (Nasehzadeh et al., 2002). A temperature-dependent ε_{fs} was found effective in providing better correlations for adsorption isotherms over a wide range of temperature. The linear temperature dependence used for ε_{fs} is given below:

$$\varepsilon_{fs} = (\varepsilon_{fs})_0 + kT \quad (4-24)$$

Only those systems or adsorbent groups that contain more than one isotherm had the regressed 'k' parameter.

Table 4-5 presents regression results for the activated carbon/zeolites systems and the coal systems for each system or system group. The following information is given: the adsorbent name, adsorbates, the number of points (NPTS) for each adsorbate, the temperatures of all the isotherms for each adsorbate, the regressed SLD parameters, and percent average absolute deviation (%AAD), and the root mean square error (RMSE). In Table 4-5 for the coals, the weighted absolute average deviation (WAAD) is also given; here, the weights are the expected experimental uncertainties. The %AAD is defined by Equation (4-16) and the RMSE is defined as:

$$\text{RMSE} = \sqrt{\frac{1}{\text{NPTS}} \sum_i^{\text{NPTS}} (n_i^{\text{exp}} - n_i^{\text{model}})^2} \quad (4-25)$$

Table 4-5. Results of SLD-PR Model for Pure-Gas Adsorption on Activated Carbons, Zeolites, and Coals

| System No(s). | Adsorbent | Adsorbate | NPTS | T (K) | Parameters | | | | | %AAD | RMSE (mmol/g) |
|---------------|----------------------|--|------|--|--------------------------|--------|--|------------------------------|----------------------|------|---------------|
| | | | | | Area (m ² /g) | L (nm) | (ϵ_{fs}) ₀ /k _B (K) | Λ_b | k/k _B (K) | | |
| 1-3 | AC, Columbia Grade L | N ₂ CH ₄ C ₂ H ₆ | 139 | 310.9 338.7 366.5 394.3 422.0 449.8 477.6 | 1002 | 1.26 | 85.0 107.2 130.9 | 1.67 1.02 0.62 | -0.115 | 4.9 | 0.160 |
| 5-6 | Charcoal | CH ₄ C ₃ H ₈ | 107 | 283.2 293.2 303.2 313.2 323.2 293.2 303.2 313.2 323.2 333.2 | 997.8 | 1.17 | 97.6 118.6 | 0.38 0.02 | -0.105 | 4.6 | 0.230 |
| 7-10 | AC, BPL | CH ₄ C ₂ H ₆ C ₂ H ₄ CO ₂ | 212 | 212.7 260.2 301.4 | 1332.4 | 1.07 | 110.4 132.4 133.6 120.5 | 1.16 0.73 0.78 0.68 | -0.196 | 5.4 | 0.325 |

Table 4-5. Results of SLD-PR Model for Pure-Gas Adsorption on Activated Carbons, Zeolites, and Coals (Continued)

| System No(s). | Adsorbent | Adsorbate | NPTS | T (K) | Parameters | | | | | %AAD | RMSE (mmol/g) |
|---------------|-----------------------|-----------------|------|-------|--------------------------|--------|--|-------------|----------------------|------|---------------|
| | | | | | Area (m ² /g) | L (nm) | (ϵ_{fs}) ₀ /k _B (K) | Λ_b | k/k _B (K) | | |
| 11-12 | AC, PCB-Calgon Carbon | CH ₄ | 34 | 296 | 1079.2 | 1.22 | 104.4 | 0.81 | -0.127 | 5.2 | 0.240 |
| | | CO ₂ | | 480 | | | 115.5 | 0.49 | | | |
| 14-16 | AC, Norit R1 Extra | N ₂ | 34 | 298 | 1062.9 | 1.37 | 47.8 | 0.14 | -- | 4.7 | 0.246 |
| | | CH ₄ | | | | | 70.6 | 0.64 | | | |
| | | CO ₂ | | | | | 77.8 | 0.37 | | | |
| 17, 21 | AC, Coconut Shell | CH ₄ | 193 | 233 | 1831.9 | 1.50 | 96.9 | 0.32 | -0.140 | 2.5 | 0.302 |
| | | | | 253 | | | | | | | |
| | | | | 273 | | | | | | | |
| | | | | 293 | | | | | | | |
| | | | | 313 | | | | | | | |
| | | 333 | | 75.4 | | | 0.46 | | | | |
| | | 178 | | | | | | | | | |
| | | 198 | | | | | | | | | |
| | | 218 | | | | | | | | | |
| | | 233 | | | | | | | | | |
| 258 | | | | | | | | | | | |
| 278 | | | | | | | | | | | |
| 298 | | | | | | | | | | | |

Table 4-5. Results of SLD-PR Model for Pure-Gas Adsorption on Activated Carbons, Zeolites, and Coals (Continued)

| System No(s). | Adsorbent | Adsorbate | NPTS | T (K) | Parameters | | | | | %AAD | RMSE (mmol/g) | | | |
|---------------|-------------------------------|-------------------------------|------|---|--------------------------|--------|--|-------------|----------------------|------|---------------|-------|------|--------|
| | | | | | Area (m ² /g) | L (nm) | (ϵ_{fs}) ₀ /k _B (K) | Λ_b | k/k _B (K) | | | | | |
| 18 | AC, Calgon F-400 | CO ₂ | 116 | 303.6 305.2 309.2 313.2 318.2 | 590.9 | 1.36 | 203.3 | 0.17 | -0.359 | 7.8 | 0.40 | | | |
| 19-20 | AC, Norit RB1 | CH ₄ | 128 | 304.9 311.4 331.3 350.5 | 1228.7 | 1.23 | 122.9 | 0.60 | -0.176 | 3.4 | 0.140 | | | |
| | | CO ₂ | | 305.2 311.2 329.5 348.3 | | | | | | | | | | 181.8 |
| 13, 22-24 | AC, F30/470 Chemiviron Carbon | CO ₂ | 504 | 278 288 298 303 308 318 328 | 1147.0 | 1.42 | 189.5 | 0.74 | -0.356 | 2.6 | 0.147 | | | |
| | | CH ₄ | | 303 323 | | | | | | | | 122.8 | 1.05 | -0.187 |
| | | C ₃ H ₈ | | 343 363 | | | | | | | | 283.8 | 0.74 | -0.515 |
| | | N ₂ | | 383 | | | | | | | | 75.0 | 1.30 | -0.117 |

Table 4-5. Results of SLD-PR Model for Pure-Gas Adsorption on Activated Carbons, Zeolites, and Coals (Continued)

| System No(s). | Adsorbent | Adsorbate | NPTS | T (K) | Parameters | | | | | %AAD | RMSE (mmol/g) |
|---------------|--------------------|-------------------------------|------|-------------------|--------------------------|--------|---|-------------|----------------------|------|---------------|
| | | | | | Area (m ² /g) | L (nm) | (ϵ_{fs}) ₀ / k _B (K) | Λ_b | k/k _B (K) | | |
| 25-26 | AC, Norit R1 | N ₂ | 60 | 298 | 650.0 | 1.11 | 55.7 | 0.26 | -- | 3.2 | 0.164 |
| | | CO ₂ | | | | | 74.3 | -0.22 | | | |
| 27-30 | AC Calgon F-400 | N ₂ | 127 | 318.2 | 620.9 | 1.20 | 48.7 | 0.51 | -- | 3.3 | 0.167 |
| | | CH ₄ | | | | | 71.9 | 0.33 | | | |
| | | CO ₂ | | | | | 86.7 | 0.11 | | | |
| | | C ₂ H ₆ | | | | | 92.7 | 0.14 | | | |
| 31 | Zeolite, Linde 13X | N ₂ | 24 | 298 323 348 | 494.7 | 1.29 | 111.1 | 1.04 | -0.191 | 1.6 | 0.026 |
| 32-35 | Zeolite, Linde 5A | N ₂ | 123 | 298 323 348 | 271.4 | 0.987 | 141.2 | 0.11 | -0.230 | 3.1 | 0.112 |
| | | CH ₄ | | | | | 153.9 | 0.22 | | | |
| | | CO ₂ | | | | | 246.5 | -0.10 | | | |
| | | C ₂ H ₆ | | | | | 174.0 | 0.00 | | | |

Table 4-5. Results of SLD-PR Model for Pure-Gas Adsorption on Activated Carbons, Zeolites, and Coals (Continued)

| System No(s). | Adsorbent | Adsorbate | NPTS | T (K) | Parameters | | | | | %AAD | RMSE (mmol/g) |
|--|-------------------------------------|-------------------------------|------|-------|--------------------------|--------|---|-------------|----------------------|-------|---------------|
| | | | | | Area (m ² /g) | L (nm) | (ϵ_{fs}) ₀ / k _B (K) | Λ_b | k/k _B (K) | | |
| 36- 37 | H-Modernite, Norton Co: Type Z-900H | CO ₂ | 185 | 283.0 | 300.0 | 1.02 | 180.7 | -0.24 | -0.268 | 8.8 | 0.065 |
| | | C ₃ H ₈ | | 303.2 | | | 177.1 | 0.42 | | | |
| | | | | 324.3 | | | | | | | |
| 38-40 | Zeolite G5 | CH ₄ | 125 | 283 | 623.1 | 1.13 | 96.9 | 0.28 | -0.140 | 2.4 | 0.091 |
| | | C ₂ H ₄ | | 303 | | | 132.7 | 0.14 | | | |
| | | C ₂ H ₆ | | | | | 114.6 | 0.13 | | | |
| 41-42 | Zeolite 13X | CH ₄ | 29 | 298.2 | 408.5 | 0.60 | 52.3 | -0.10 | -- | 1.2 | 0.046 |
| | | C ₂ H ₆ | | | | | | 55.7 | | | |
| Overall Statistics for Activated Carbons and Zeolites | | | 2140 | | | | | | 4.1 | 0.133 | |

Table 4-5. Results of SLD-PR Model for Pure-Gas Adsorption on Activated Carbons, Zeolites, and Coals (Continued)

| System No(s). | Adsorbent | Adsorbate | NPTS | T (K) | Parameters | | | | WAAD | %AAD | RMSE (mmol/g) |
|---------------|--------------------------------|-----------------|------|-------|--------------------------|--------|--|-------------|------|------|---------------|
| | | | | | Area (m ² /g) | L (nm) | (ϵ_{fs}) ₀ /k _B (K) | Λ_b | | | |
| 43-45 | Wet Fruitland Coal #2 | N ₂ | 134 | 319.3 | 63.7 | 1.02 | 31.7 | 0.00 | 0.53 | 4.5 | 0.058 |
| | | CH ₄ | | | | | 56.1 | -0.23 | | | |
| | | CO ₂ | | | | | 58.4 | -0.32 | | | |
| 46-48 | Wet Illinois#6 Coal | N ₂ | 70 | 319.3 | 47.1 | 1.46 | 22.0 | 0.14 | 0.34 | 4.8 | 0.040 |
| | | CH ₄ | | | | | 48.5 | 0.00 | | | |
| | | CO ₂ | | | | | 77.1 | -0.10 | | | |
| 49-51 | Wet Tiffany Coal | N ₂ | 63 | 327.5 | 36.1 | 1.07 | 29.3 | 0.12 | 0.77 | 3.6 | 0.011 |
| | | CH ₄ | | | | | 52.0 | -0.17 | | | |
| | | CO ₂ | | | | | 66.6 | -0.26 | | | |
| 52-54 | Wet Lower Basin Fruitland Coal | N ₂ | 81 | 319.3 | 23.0 | 1.03 | 32.4 | -0.01 | 0.55 | 5.6 | 0.026 |
| | | CH ₄ | | | | | 54.3 | -0.31 | | | |
| | | CO ₂ | | | | | 64.1 | -0.38 | | | |
| 55 | Dry Illinois #6 Coal | CO ₂ | 11 | 328 | 136.0 | 1.70 | 65.2 | 0.14 | 0.29 | 1.8 | 0.025 |
| 56 | Dry Beulah Zap Coal | CO ₂ | 11 | 328 | 135.1 | 1.13 | 65.2 | -0.14 | 0.96 | 4.0 | 0.059 |

Table 4-5. Results of SLD-PR Model for Pure-Gas Adsorption on Activated Carbons, Zeolites, and Coals (Continued)

| System No(s). | Adsorbent | Adsorbate | NPTS | T (K) | <i>Parameters</i> | | | | WAAD | %AAD | RMSE (mmol/g) |
|-------------------------------------|-------------------------|-----------------|------|-------|--------------------------|--------|---|-------------|------|------|---------------|
| | | | | | Area (m ² /g) | L (nm) | (ϵ_{fs}) ₀ / k _B (K) | Λ_b | | | |
| 57 | Dry Wyodak Coal | CO ₂ | 11 | 328 | 140.0 | 1.27 | 65.2 | -0.08 | 0.95 | 4.2 | 0.062 |
| 58 | Dry Upper Freeport Coal | CO ₂ | 11 | 328 | 74.6 | 1.02 | 65.2 | -0.17 | 0.61 | 2.7 | 0.023 |
| 59 | Dry Pocahontas Coal | CO ₂ | 11 | 328 | 99.9 | 1.02 | 65.2 | -0.11 | 0.51 | 2.3 | 0.023 |
| Overall Statistics for Coals | | | 403 | | | | | | 0.56 | 4.4 | 0.023 |

Results and Discussion

Overall, the %AAD of adsorption of the activated carbons and zeolites was 4.1% and that of the coals was 4.4%. Figure 4-18 depicts the statistical distribution of percentage errors in adsorption encountered for the activated carbons and zeolites, and Figure 4-19 depicts the statistical distribution of weighted errors in adsorption (weighted to the experimental uncertainty) for the coals. Figure 4-18 presents two distribution sets: the percentage error distribution for the entire activated carbon/zeolites database and the distribution for those experimental data having pressures greater than 0.17 MPa (25 psia). As observed for Figures 4-18 and 4-19, the errors appear to be normally distributed. In Figure 18, about 75% of all the measurements lie within 5% of the SLD model calculation; for pressures greater than 0.17 MPa, about 80 % of those measurements lie within 5% of the SLD model calculation. Thus, exclusion of the data at lower pressures tends to have a small, but noticeably beneficial impact on the overall quality of fit. In Figure 19, about 80% of all measurements (on the coals) are within one expected deviation of the SLD model prediction.

Figure 4-20 depicts a scatter plot of the percentage errors of adsorption as a function of pressure; the percentage errors for the lowest pressures are higher than those at moderate pressures (around 5 MPa) due to the lower experimental adsorption values.

Although estimates of the experimental uncertainty are not available for the activated carbons and zeolites, estimates were available for all the coal systems. For the coal systems, the overall WAAD is 0.56, based on experimental uncertainties as weights. This means that the SLD-PR can correlate the coal system isotherms to 0.56 times the experimental uncertainty, on average. While this is excellent correlative ability, one must keep in mind that several empirical modifications were used to achieve this level of fit.

Also, the excellent correlative ability may also be attributed to conservative estimates (larger than the true value) of the expected experimental uncertainties.

Several regressions were performed on systems that contained more than one isotherm. For such cases, when the SLD model includes the parameter 'k' that modifies the temperature dependence of ϵ_{fs} , the statistical fit is much better. Moreover, without inclusion of the parameter 'k', the SLD model estimates a surface area that is uncharacteristically low. For example, Table 4-6 compares the regression results of adsorbent group 1-3 with and without the parameter 'k' included. With 'k', the regressed surface area is 1002 m²/g compared to the 275 m²/g without 'k'. Also, the PR covolume modification terms, Λ_i , become larger. This, and the fact that the other parameters differ greatly for the two cases, suggests that the regressed values for the SLD model are sensitive to the temperature dependence of ϵ_{fs} .

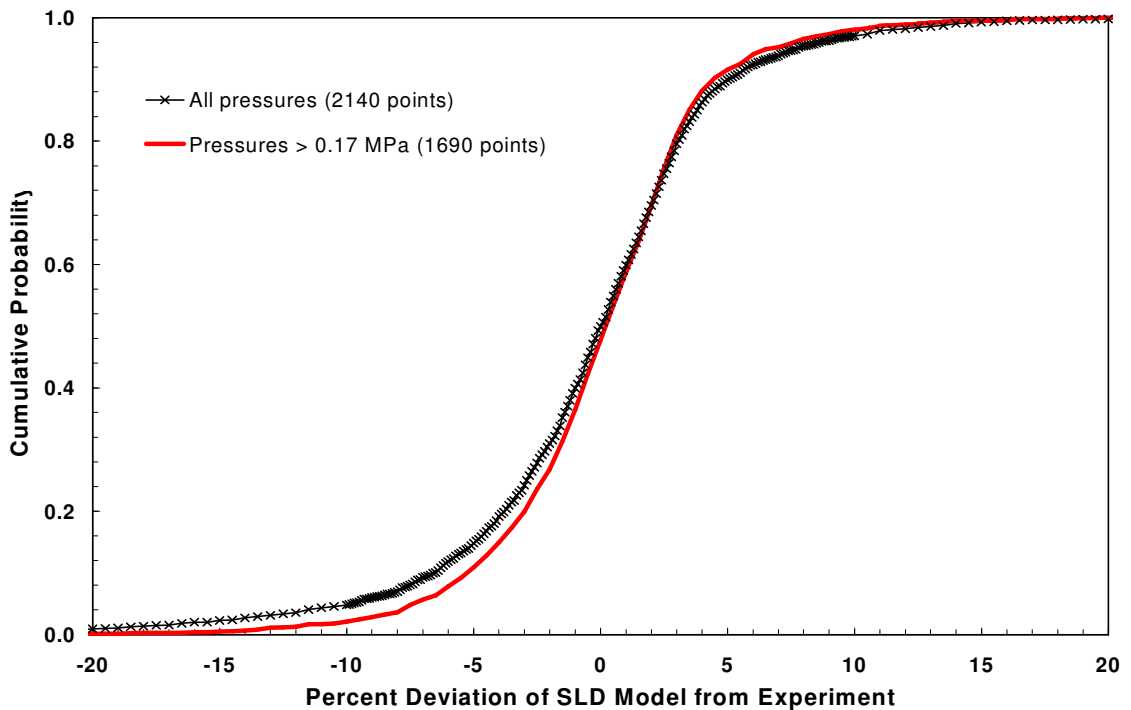


Figure 4-18. Cumulative Distribution Function of Percentage Errors of Adsorption for Activated Carbons and Zeolites

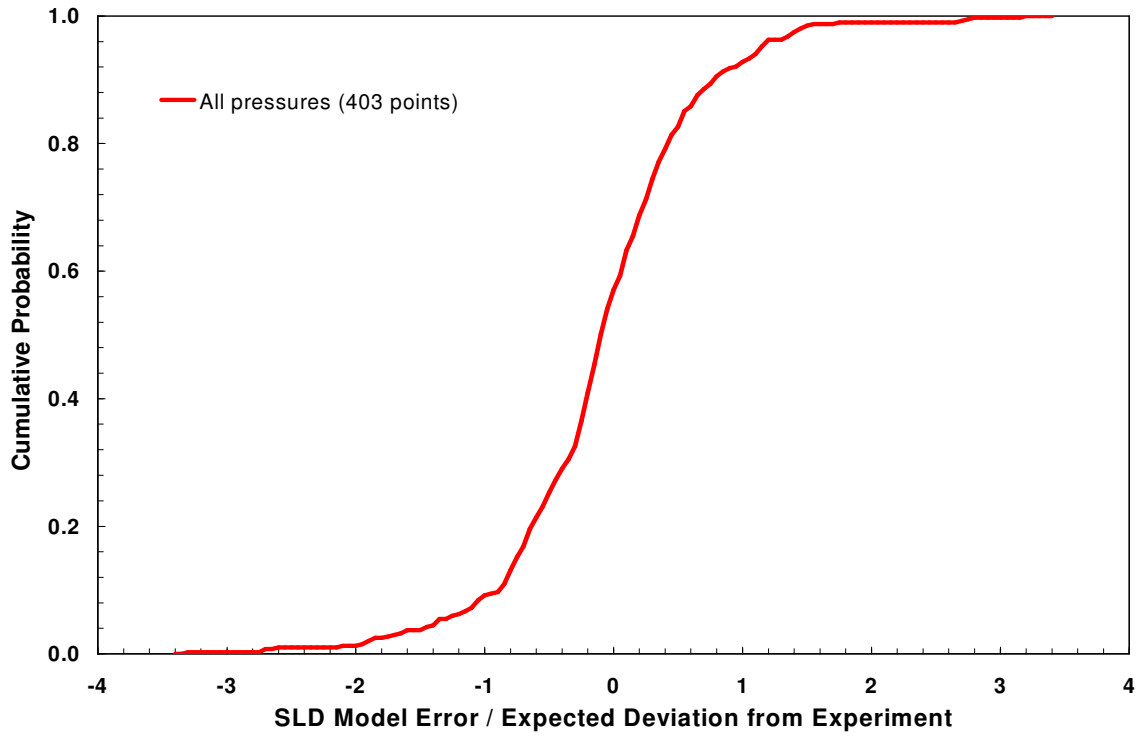


Figure 4-19. Cumulative Distribution Function of Weighted Percentage Errors of Adsorption for Coals

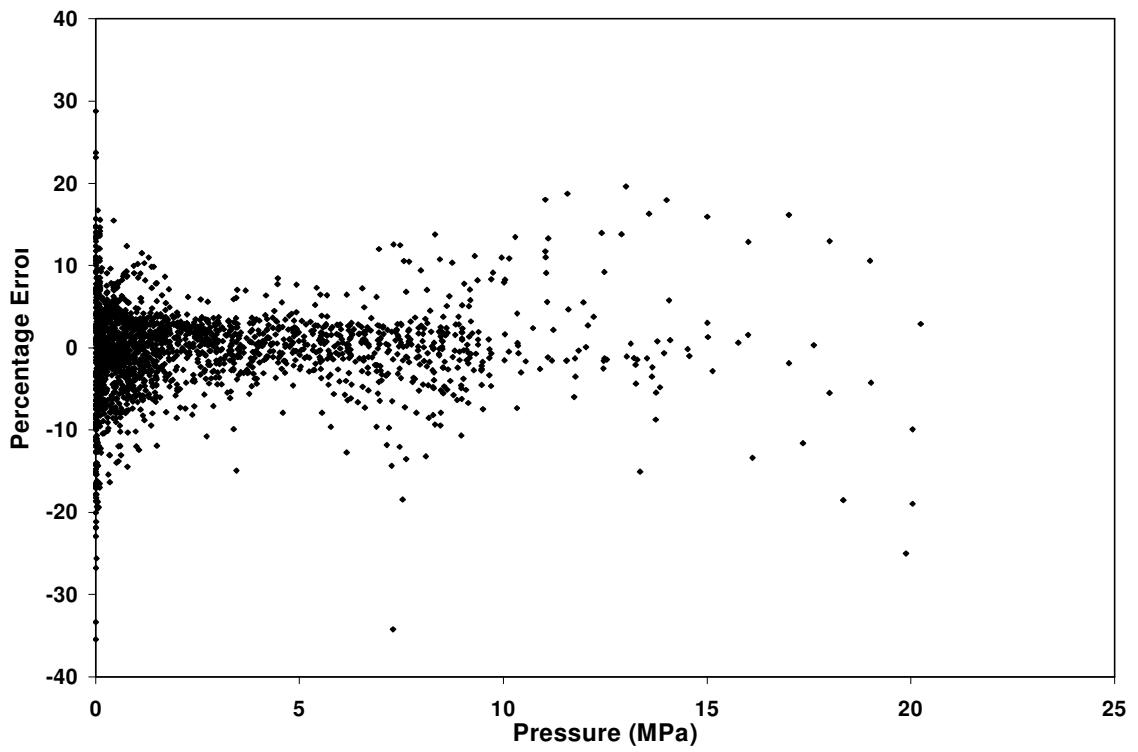


Figure 4-20. Scatter Plot of Percentage Errors of Adsorption for Activated Carbons and Zeolites

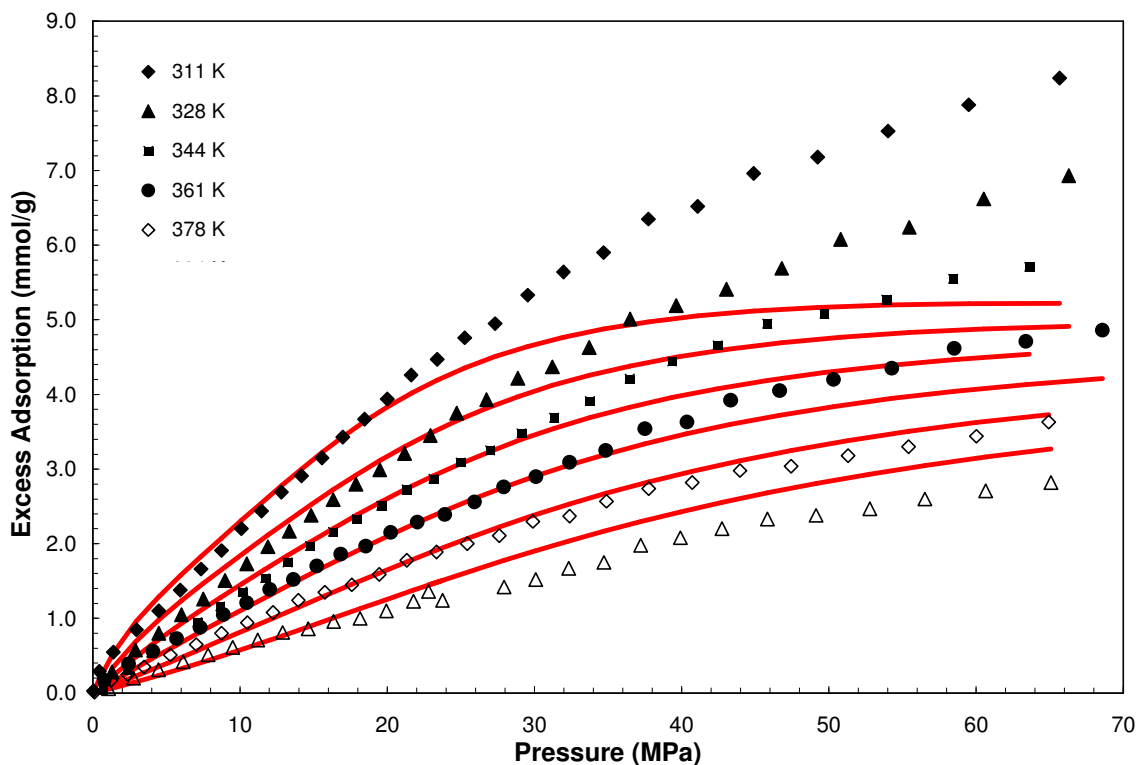


Figure 4-21. Methane Adsorption on Carbon Black at Various Temperatures with SLD Model Prediction (System 4)

Estimating the parameter ‘k’ is relatively straightforward. As shown in Table 4-6, the regressed values for the parameter ‘k’ for all system groups are negative and range from $-0.105 > k > -0.359$. Also, for all system groups except for system group 13, 22 - 24, the parameter ‘k’ could be regressed as independent of the gas adsorbed. The zeolites tend to have larger magnitude values of ‘k’ compared to activated carbons. To improve our predictions for the temperature dependence of adsorption, the SLD framework should incorporate a better equation of state and should use temperature-dependent Lennard-Jones parameters available from theory (Reid et al., 1987).

Figures 4-22 and 4-23 depict, respectively, the adsorption of methane and propane on charcoal at various temperatures. For both gas species, the SLD-PR model has some difficulty correlating the temperature dependence of the excess adsorption, especially at

higher pressures. In comparison, the SLD-PR was capable of correlating the adsorption temperature dependence for methane on activated carbon (from KOH activated coconut shell), as shown in Figure 4-24.

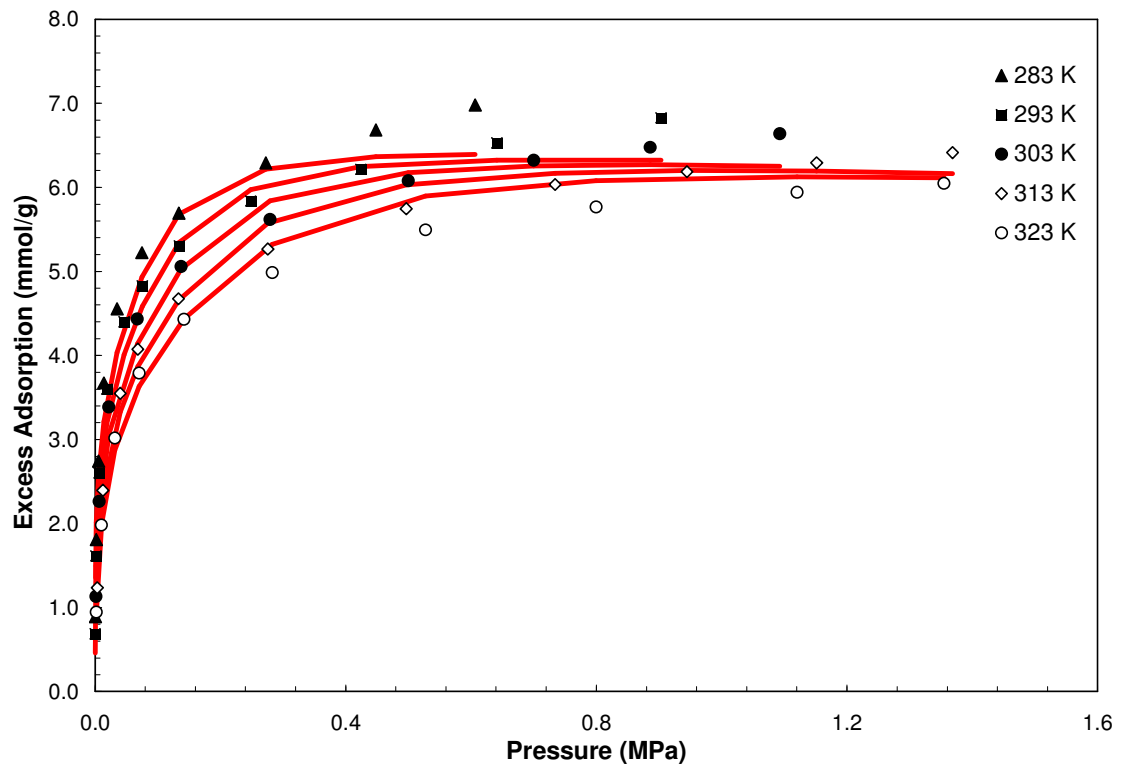


Figure 4-22. Methane Adsorption on Charcoal at Various Temperatures with SLD Model Prediction (System 5)

Table 4-6. The Effect of Parameter ‘k’ on the SLD-PR Model Representations

| System No(s). | Adsorbent | Adsorbate | NPTS | T (K) | Parameters | | | | | %AAD | RMSE (mmol/g) |
|------------------------------|----------------------------|--|------|---|--------------------------|--------|---------------------------|----------------------------|----------------------|------|---------------|
| | | | | | Area (m ² /g) | L (nm) | - ϵ_{fs}/k_B (K) | Λ_b | k/k _B (K) | | |
| 1-3 No ‘k’ | AC, Columbia Grade L | N ₂ CH ₄ C ₂ H ₆ | 139 | 310.9 338.7 366.5 394.3 422.0 449.8 477.6 | 275.3 | 1.18 | 88.3 70.3 98.2 | -0.394 -0.301 -0.474 | -- | 7.2 | 0.197 |
| 1-3 ‘k’ include- ed | AC, Columbia Grade L | N ₂ CH ₄ C ₂ H ₆ | 139 | 310.9 338.7 366.5 394.3 422.0 449.8 477.6 | 1002 | 1.26 | 85.0 107.2 130.9 | 1.67 1.02 0.62 | -0.115 | 4.9 | 0.160 |

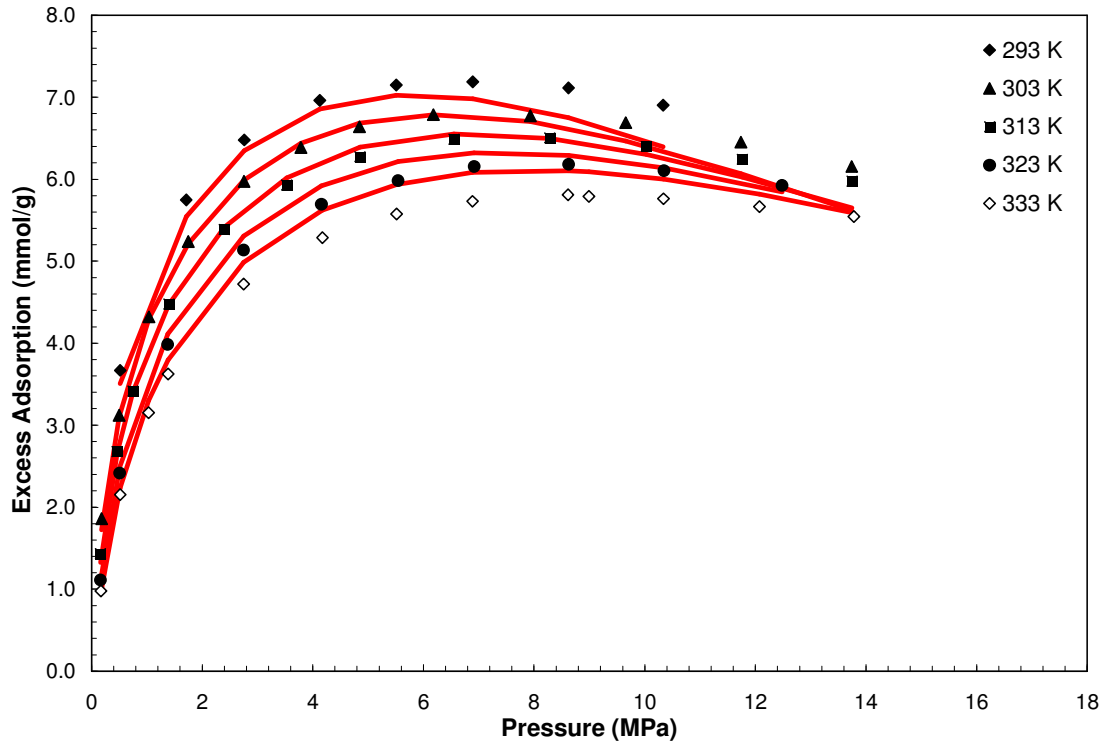


Figure 4-23. Propane Adsorption on Charcoal at Various Temperatures with SLD Model Prediction (System 6)

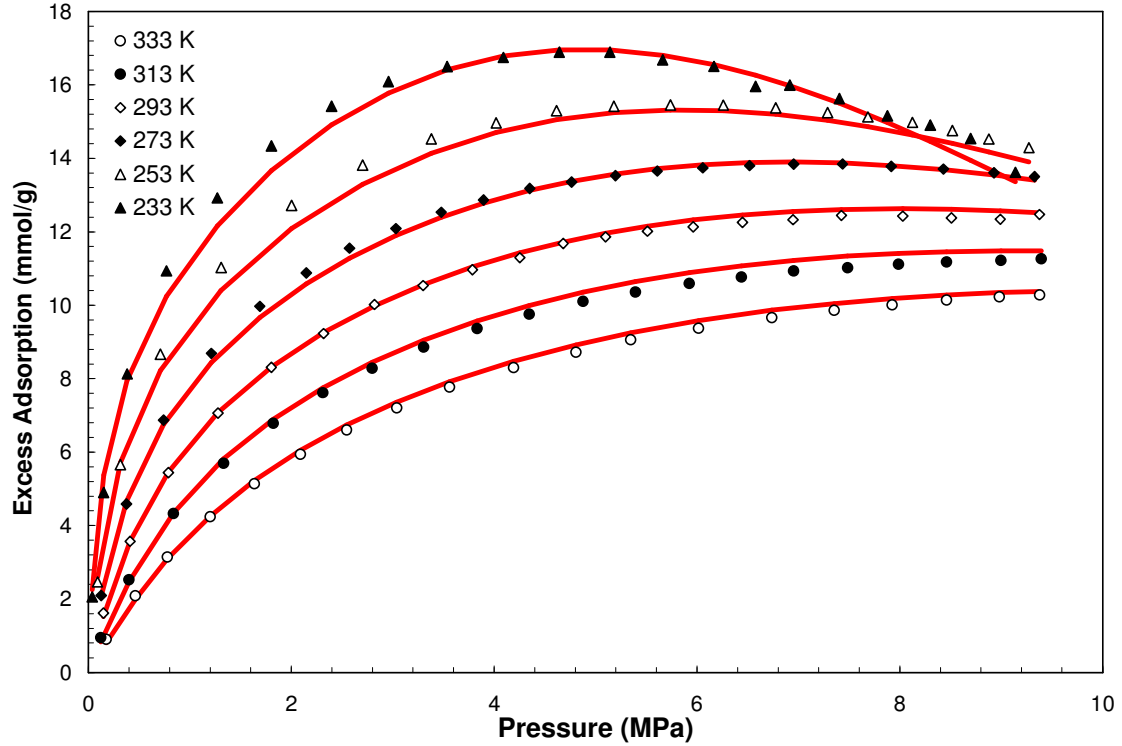


Figure 4-24. Methane Adsorption on Activated Carbon from Coconut Shell with KOH Activation at Various Temperatures with SLD Model Prediction (System 17)

Two possible explanations may be offered for why the SLD-PR model fit is better for the activated carbon (in Figure 4-24) than the charcoal (in Figures 4-22 and 4-23). First, the charcoal may swell, which can change the accessible adsorbed-phase volume for methane and propane. This possible swelling of the charcoal may be induced either by adsorption or by exposure to different temperatures. Second, the empirical constant 'k' that determines the temperature dependence of the fluid-solid interaction energy parameter, ϵ_{fs}/k , may be adsorbate dependent, or the linear temperature dependence of ϵ_{fs}/k , as given by Equation (4-24), is not suitable. Evidence that the parameter 'k' is adsorbate dependent is shown in Systems 13, 22-24 for the F30/470 Chemviron activated carbon. For this adsorbent, a regressed parameter 'k' is necessary for each gas species, and the magnitude of 'k' increases nearly linearly with the critical temperature of the gas. Thus, the SLD-PR would have more difficulty correlating gas species of widely differing critical temperatures.

The ability of the SLD-PR to correlate isotherms from low pressures to moderately high pressures is shown in Figures 4-25 and 4-26, for a zeolite and an activated carbon, respectively. For adsorption of CO₂ on H-Modernite (Figure 4-25), the SLD-PR model fits are poor at higher pressures; the model curve begins to flatten, which is indicative of a nearby maximum in the excess adsorption. The experimental data, however, clearly shows a linear pressure dependence on a log scale for the excess adsorption, even at the higher pressures. The inability of the SLD-PR to correlate precisely (without the flattening at high pressures) the entire isotherm in Figure 4-25 may be due to the ratio of the highest to lowest pressure included in the isotherm, where the

ratio at 283 K is roughly 5000. The modification of the PR co-volume 'b' cannot compensate for such ranges in pressure.

For the adsorption of methane, nitrogen, and CO₂ on activated carbon that is depicted in Figure 4-26, the SLD-PR model captures the correct behavior of the adsorption isotherm at high pressures for all three gases; albeit, for CO₂, the fit is not excellent. The adsorption of CO₂ on various dry coals is depicted in Figure 4-27. The SLD-PR model can correlate these isotherms, on average, to within the expected experimental uncertainty of the measurements. However, for correlating each isotherm, the four regressed parameters (area, slit length, ϵ_{fs}/k_B , and Λ_i) were found to have a high degree of parameter correlation; thus, the regressed parameter values were sometimes physically unrealistic. To minimize the effects of this problem, the fluid-solid interaction energy parameter was set to 65.2 K for all the dry coals (the value that was regressed for the dry Illinois #6 coal).

Because the modified SLD-PR has four or five regressed parameters, over-fitting the experimental data is a concern. Parameter insensitivity produces uncertain parameter values for pure components and thus hampers prediction of multi-component adsorption data. For each of the dry coal Systems 55-59, four parameters regressed per isotherm is clearly an over-fit.

As mentioned previously, the characterization of the coals by adsorption is more practicable with the minimum number of necessary model parameters. The problem of over-fitting can be rectified by asserting that the coal matrix has certain characteristics that are invariant to the gas being adsorbed. A common surface area and slit length are such characteristics, but for Systems 55-59, only one gas isotherm is available. To

prevent the problem of over-fitting, the SLD model should be applied to systems containing more than one gas isotherm per adsorbent.

For the wet coal Systems 43-54 as shown in Figures 4-28 through 4-30, each wet coal has isotherms for three gases: methane, nitrogen, and CO₂. For each wet coal, values for the surface area and the slit length are common to the three gases. Thus, wet coal systems have eight overall parameters that need to be regressed for the three gases, whereas the dry coal systems need four parameters for each gas. For an adsorbent in which all the experimental data is isothermal and there are isotherms available from N different gas species, the SLD-PR model requires $(2N+2)$ parameters to be regressed.

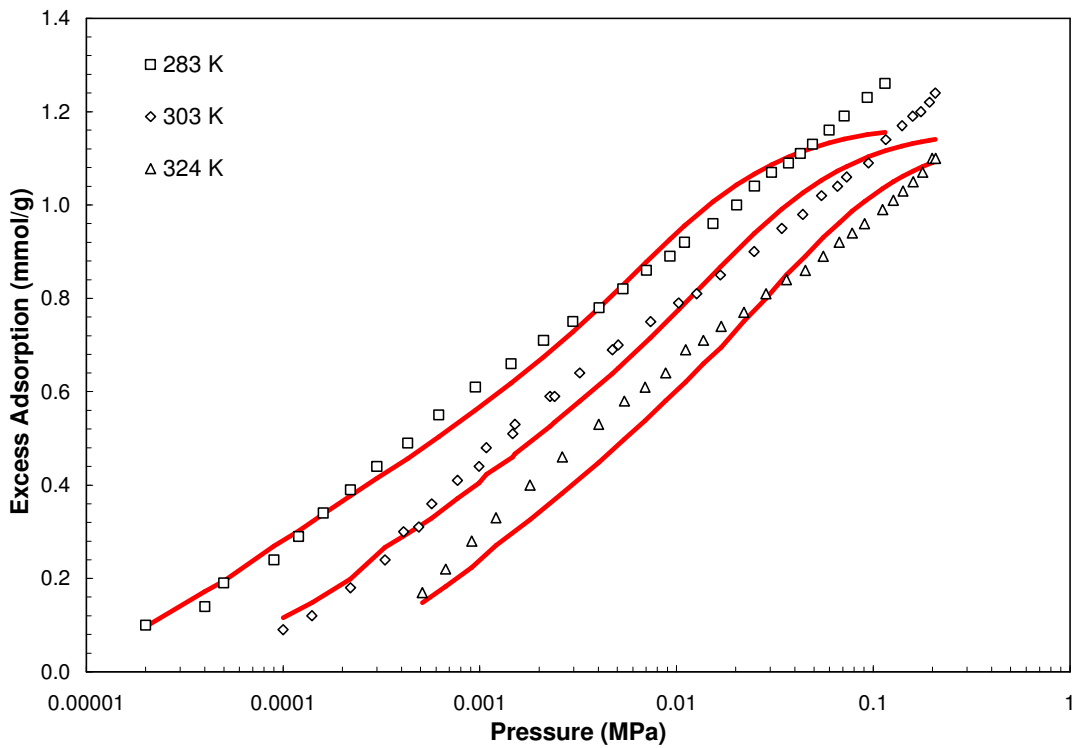


Figure 4-25. CO₂ Adsorption on H-Modernite at Various Temperatures with SLD Model Prediction (System 37)

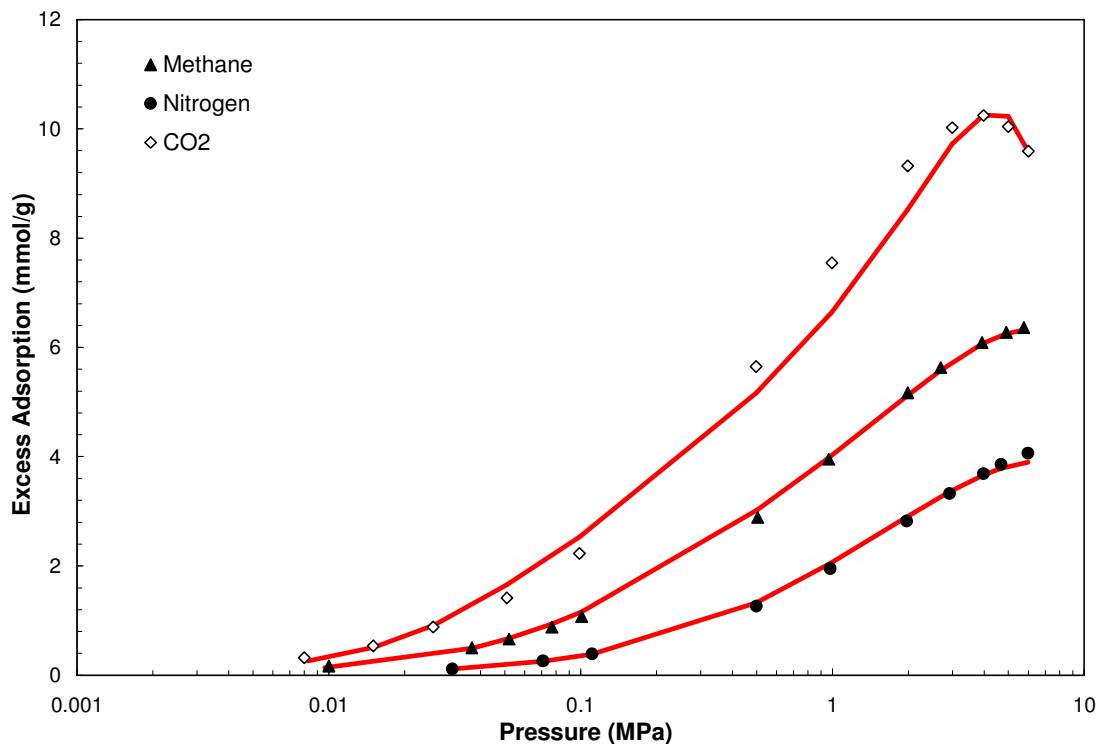


Figure 4-26. Adsorption on Norit R1 Extra Activated Carbon at 298 K with SLD Model Prediction (Systems 15-17)

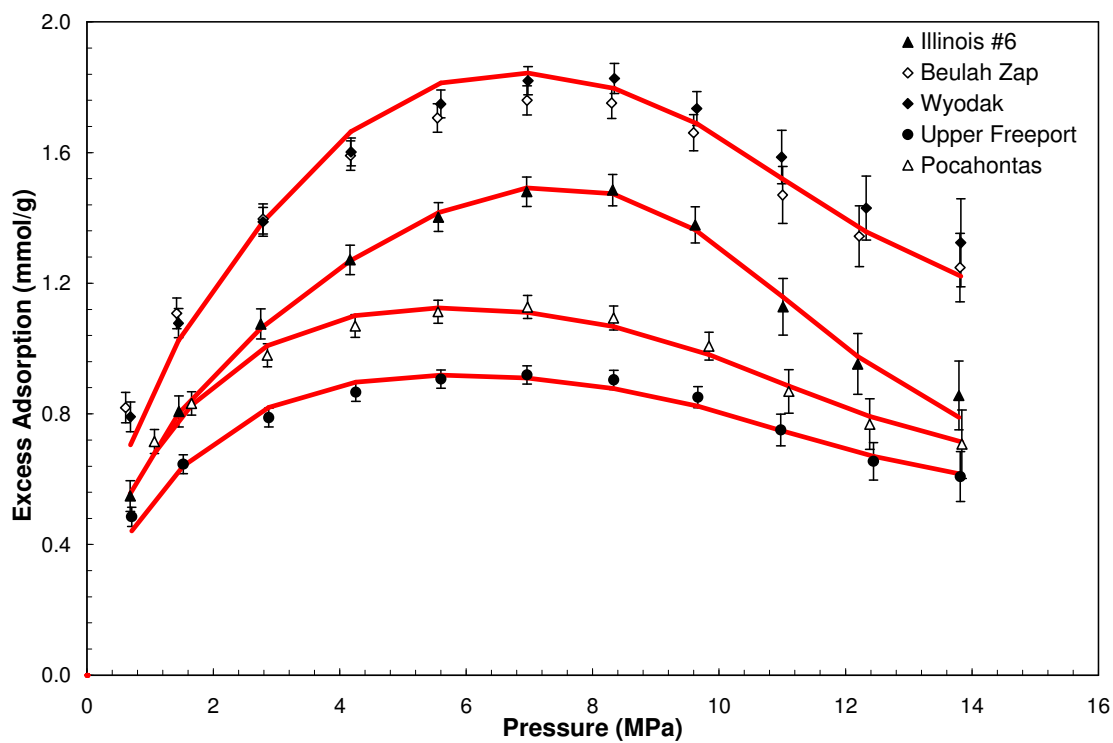


Figure 4-27. Adsorption of CO₂ on Various Dry Coals at 328 K with SLD Model Prediction (Systems 55-59)

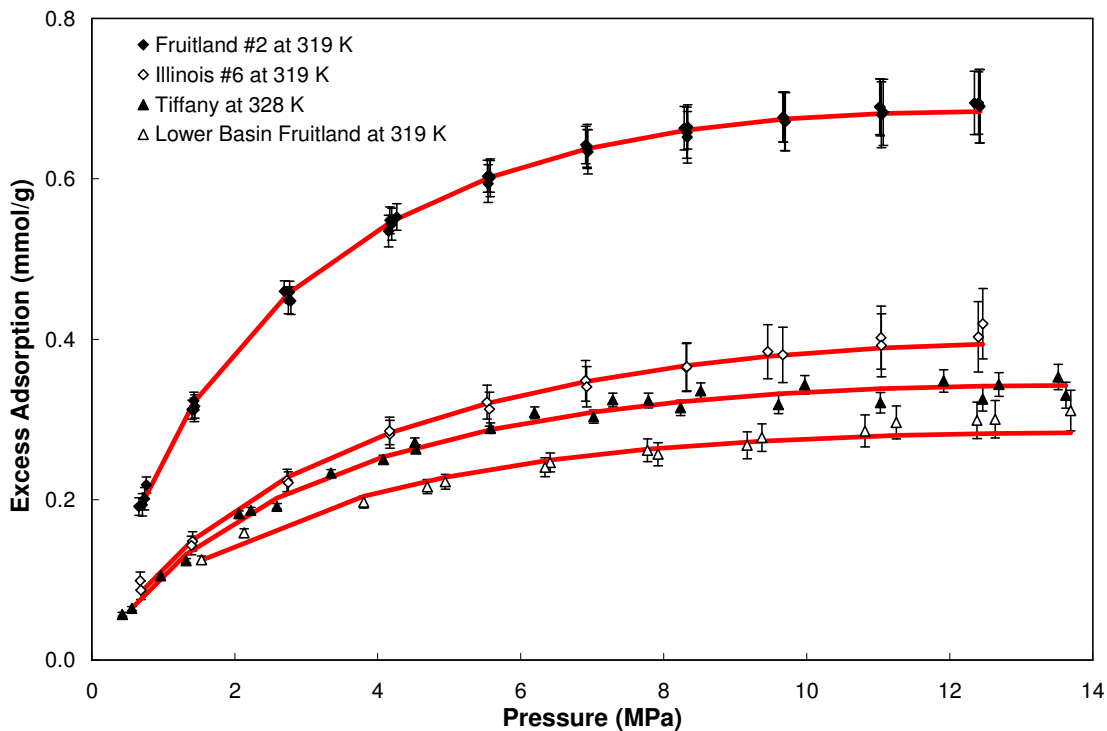


Figure 4-28. Adsorption of Methane on Various Wet Coals with SLD Model Prediction (Systems 44, 47, 50, 53)

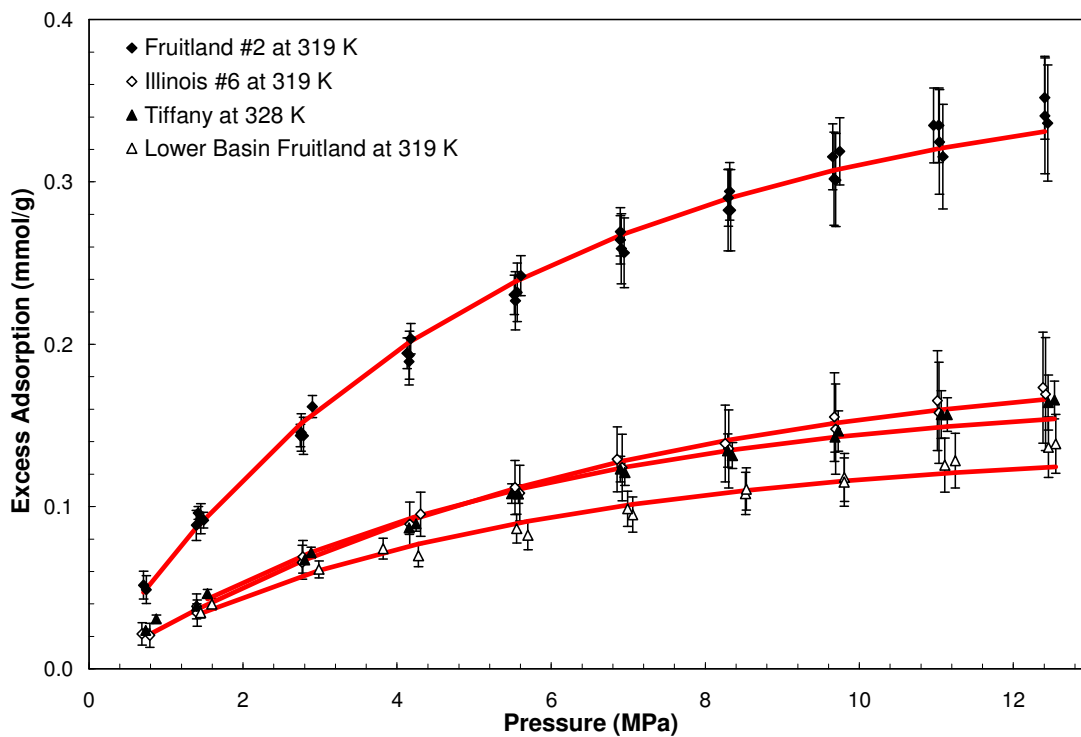


Figure 4-29. Adsorption of Nitrogen on Various Wet Coals with SLD Model Prediction (Systems 43, 46, 49, 52)

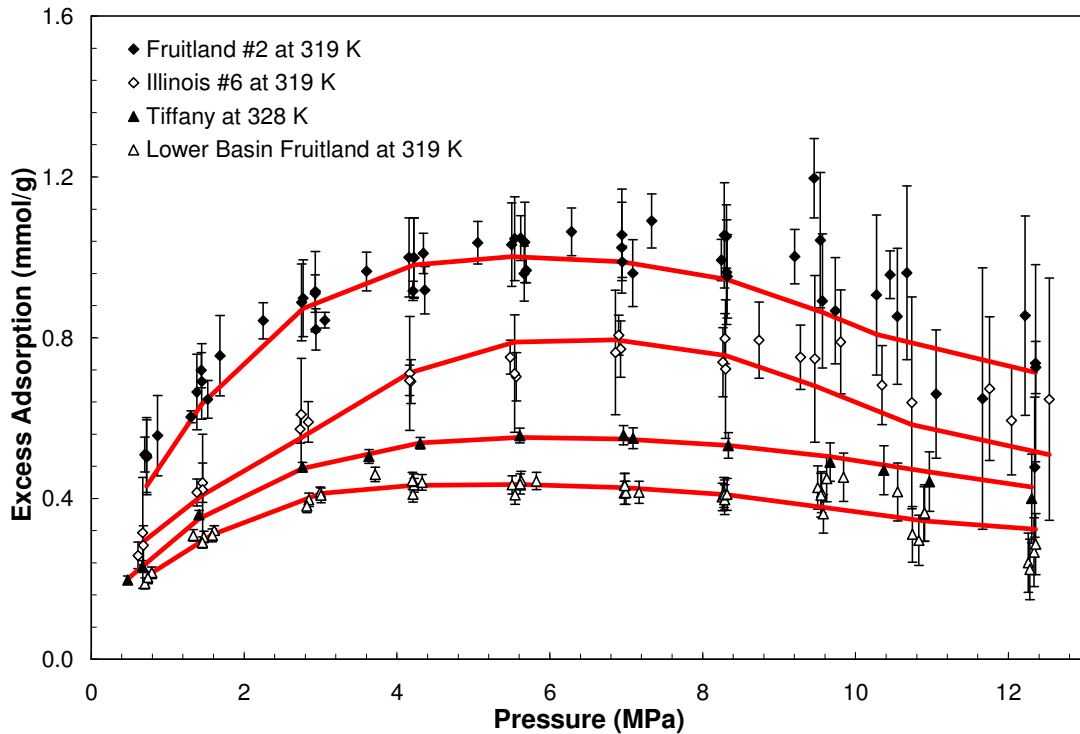


Figure 4-30. Adsorption of CO₂ on Various Wet Coals with SLD Model Prediction (Systems 45, 48, 51, 54)

Conclusions for Case Study 2

The major conclusions of this case are:

- The modified SLD-PR model can correlate pure-gas adsorption isotherms of many systems involving wet and dry coals, activated carbons, and zeolites over broad pressure and temperature ranges.
- For each adsorbent, common surface area and effective slit width values may be used for all gas species over all temperature and pressure ranges.
- To correlate accurately over broad pressure ranges, the SLD-PR covolume must be empirically modified; this effectively changes the adsorbed-phase density.

- The SLD-PR model must be empirically modified to accurately represent isotherms over wide temperature ranges. The empirical modification of the fluid-solid interaction potential parameter ϵ_{fs}/k_B has linear temperature dependence, which is adequate for most systems considered in this study.

CHAPTER 5
SIMPLIFIED LOCAL DENSITY MODEL FOR
MIXED-GAS ADSORPTION

The Simplified Local Density (SLD) model predicts adsorption by incorporating a local density profile near the adsorbent wall surface. It uses readily available fluid property information from well-known equations of state such as the Peng-Robinson, and accounts for fluid-solid interactions by familiar potential functions. The SLD model is a “simplification” of local density theory because it utilizes a mean field chemical potential approximation; i.e., no local fluctuations.

Soule (1998) used the SLD framework in conjunction with the ESD (Elliot-Suresh-Donohue) equation of state (Elliot et al., 1990) to model binary adsorption. This modeling study is different than Soule’s study in three ways:

1. The component adsorbed fraction is allowed to vary in the adsorbed phase as a function of position.
2. One-fluid solution thermodynamics is used to describe the fugacity of a component in the adsorbed and bulk phases.
3. Our model evaluations are conducted using higher-pressure data (1800 psia to his 300 psia) for many mixture combinations.

Soule (1998) did not attempt to optimize model parameters using mixture data, but rather he predicted mixture adsorption from pure-component data. We have performed model

predictions based on the pure-component parameters and on optimized model parameters from mixture adsorption data.

For mixture adsorption, the amount of each component adsorbed depends on the component mole fractions in the bulk and adsorbed phase. That is:

$$n_i^{\text{Ex}} = A/2 \int_{\sigma_{\text{ff}}/2}^{L-\sigma_{\text{ff}}/2} (\rho_{\text{ads}}(z)x_i(z) - \rho_{\text{bulk}}y_i) dz \quad (5-1)$$

In this study, the PR-EOS is employed to calculate the bulk density and local density. For the Soave-type modifier for the EOS attraction law constant, $\alpha(T)$, in the PR EOS, the Mathias-Copeman expression was used with parameters regressed by Hernández-Garduza (2002), as shown in Table 4-1. The local density and the mole fractions of the components at each position 'z' can be calculated by a local equilibrium relationship:

$$\ln\left(\frac{\hat{f}_i^{\text{ads}}(\bar{x}(z), \rho_{\text{ads}}(z))}{\hat{f}_i^{\text{bulk}}}\right) + \frac{\Psi_i^{\text{fs}}(z) + \Psi_i^{\text{fs}}(L-z)}{kT} = 0 \quad (5-2)$$

In the adsorbed phase, the fugacity of component 'i' in a mixture is a function of the local composition, local density, pressure, and temperature. In the bulk phase, the fugacity of component 'i' in a mixture is solved at the bulk density, pressure, and temperature. The fluid-solid potential is a function of slit geometry and position. Following Chen et al. (1997), Lee's partially integrated 10-4 Lennard-Jones potential is used to describe the fluid-solid interactions for each component, which is a truncated version of Steele's 10-4-3 potential function.

$$\Psi_i^{fs}(z) = 4\pi\rho_{\text{atoms}}(\epsilon_{fs})_i(\sigma_{fs})_i^2 \left(\frac{(\sigma_{fs})_i^{10}}{5(z')^{10}} - \frac{1}{2} \sum_{i=1}^4 \frac{(\sigma_{fs})_i^4}{(z' + (i-1)\sigma_{ss})^4} \right) \quad (5-3)$$

Here, ϵ_{fs} is the fluid-solid interaction energy parameter and $\rho_{\text{atoms}} = 0.382$ atoms/Å². The molecular diameter of the adsorbate and the carbon interplanar distances are σ_{ff} and σ_{ss} , respectively. The carbon interplanar distance was adopted to be 0.335 nm (Subramanian et al., 1995), and fluid diameters are 0.3758 nm, 0.3798 nm and 0.3941 nm for methane, nitrogen, and CO₂, respectively (Reid et al., 1987). For convenience, the fluid-solid diameter σ_{fs} and the dummy coordinate z' are defined as $\sigma_{fs} = (\sigma_{ff} + \sigma_{ss})/2$ and $z' = z + \sigma_{ss}/2$.

In the bulk phase, we use a linear mixing rule and a quadratic mixing rule for 'b' and 'a', respectively. The fugacity for the bulk phase using the PR-EOS is:

$$\ln \left(\frac{\hat{f}_i^{\text{bulk}}}{y_i P} \right) = \frac{b_i}{b} (Z-1) - \ln \left(Z - \frac{pb_i}{RT} \right) + \frac{b_i RT}{2\sqrt{2}a_i} \left(\frac{b_i}{b} - \frac{2\sum_j y_j a_{ij}}{a} \right) \ln \left(\frac{(1 + \rho b(1 + \sqrt{2}))}{(1 + \rho b(1 - \sqrt{2}))} \right) \quad (5-4)$$

In the adsorbed phase, we use quadratic mixing rules for both the covolume 'b' and the attraction constant 'a'. Using these rules, the fugacity in the adsorbed phase is:

$$\begin{aligned}
\ln\left(\frac{\hat{f}_i^{\text{ads}}(z)}{x_i(z)P}\right) &= \frac{2\sum_j x_j(z)b_{ij} - b}{b} \left(\frac{P}{\rho_{\text{ads}}(z)RT} - 1 \right) \\
&\quad - \ln\left(\frac{P}{\rho_{\text{ads}}(z)RT} - \frac{Pb}{RT} \right) \\
+ \frac{a(z)}{2\sqrt{2}RTb} &\left(\frac{2\sum_j x_j(z)b_{ij} - b}{b} - \frac{2\sum_j x_j(z)a_{ij}(z)}{a(z)} \right) \ln\left(\frac{(1 + \rho_{\text{ads}}(z)b(1 + \sqrt{2}))}{(1 + \rho_{\text{ads}}(z)b(1 - \sqrt{2}))} \right)
\end{aligned} \tag{5-5}$$

The formulas for $a_i(z)$ depend on the ratio of the slit width, L , to the molecular diameter, $(\sigma_{\text{ff}})_i$. Rangarajan et al. (1995) obtained these formulas by integrating the sum of all two-body interactions between an arbitrarily selected central molecule and all the other molecules around it. The results of Chen et al. (1997) were used for the equations describing ‘ a ’ as a function of position within a slit, as provided in Appendix A. Combining rules for a_{ij} follow the geometric mean. In this paper, C_{ij} is equal to zero for all component interactions in the bulk phase for simplicity, but C_{ij} is regressed for the adsorbed phase:

$$(a_{\text{ads}})_{ij} = \sqrt{(a_{\text{ads}})_i (a_{\text{ads}})_j} (1 - C_{ij}) \tag{5-6}$$

In this work, we have adjusted the covolume, ‘ b_i ’, by an empirical parameter λ_i . At high adsorptive loadings, the local fluid density at the wall decreases with increasing values of the parameter λ_i , which is nominally zero. We use a linear combining rule for the covolume interaction in the adsorbed phase:

$$(b_{\text{ads}})_{ij} = \left(\frac{b_i(1 + \lambda_i) + b_j(1 + \lambda_j)}{2} \right) \tag{5-7}$$

TESTING THE SLD ADSORPTION MODEL FOR MIXTURES

In comparison to other models, the relative ability of the SLD-PR model for mixed-gas adsorption to make certain types of predictions or to correlate precisely experimental data can be ascertained by determining the model parameters needed for those predictions or correlations. Information regarding the pure-component adsorption isotherms is necessary for prediction of mixture adsorption. As discussed in Chapter 4 for pure-gas adsorption, the SLD-PR model can correlate the isotherms of many systems involving wet and dry coals, activated carbons, and zeolites over broad pressure and temperature ranges. To correlate precisely pure-gas adsorption over broad pressure ranges, however, the SLD-PR covolume must be empirically modified for each adsorbate. Furthermore, the fluid-solid potential for each adsorbate must be regressed to correlate pure-gas isotherms since predicted values from theory do not work for the SLD-PR model. For each adsorbent, common surface area and effective slit width values may be used for all gas species over all temperature and pressure ranges. Thus, the SLD-PR model requires $(2N + 2)$ model parameters to describe pure-gas adsorption on each adsorbent, where N is the number of gas species. The primary focus of this chapter is to determine what additional information, if any, is necessary to predict or correlate mixture adsorption.

In testing the SLD-PR model efficacy for mixtures, we consider several case studies. Each case study applies the SLD-PR model to a mixture adsorption data set. These data sets consists of measurements done at Oklahoma State University, which include mixture adsorption on wet Fruitland coal, dry Calgon F-400 activated carbon, wet Tiffany coal, and wet Illinois #6 coal. Of particular interest is the adsorption data set for

dry Calgon F-400, which consists of the most extensive and reliable (as ascertained by expected experimental uncertainties) measurements for high-pressure binary mixture gas adsorption.

CASE STUDY 3: MIXTURE ADSORPTION ON CALGON F-400 ACTIVATED CARBON

Gas adsorption measurements have been conducted at Oklahoma State University (OSU) on activated carbon. Adsorption isotherms for pure methane, nitrogen, CO₂ and their binary mixtures were measured on dry activated carbon at 318.2 K (113 °F) and pressures to 12.4 MPa (1800 psia) (Sudibandriyo et al., 2003).

The pure gases used in this work were obtained from commercial vendors and have purities of 99.99% or better. Activated carbon (Filtrisorb 400, 12x40 mesh, Calgon Carbon) was used as an adsorbent and its compositional analysis is presented in Table 3-4. The activated carbon was washed in demineralized water and then dried under vacuum at 230 °F for two days before it was used for adsorption measurements. The nitrogen BET surface area at 77 K has been reported to be 850 m²/g (Humayun and Tomasko, 2000).

An error analysis indicates that the experimental uncertainties for the adsorption measurements considered here range from 2 to 6% for the pure gases. Uncertainties for all the binary gas *total* adsorption measurements are within 4% (Sudibandriyo et al., 2003). Uncertainties for individual components in the binary mixtures vary with composition.

The objective function WAAD (weighted average absolute deviation) was used to correlate data with the SLD-PR model. The function represents the average of the weighted deviations in predicted excess adsorption:

$$WAAD = \frac{1}{NPTS} \sum_{i=1}^{NPTS} \text{abs} \left(\frac{n_{\text{calc}} - n_{\text{exp}}}{\sigma_{\text{exp}}} \right) \quad (5-8)$$

Here, NPTS is the number of data points, n_{calc} and n_{exp} are the calculated and the experimental excess adsorption, and σ_{exp} is the expected experimental uncertainty for datum 'i'.

Calculation Details

The temperature, pressure, feed mole fractions, and void volume (per gram adsorbent) are needed as information to perform an adsorption flash calculation. Once performed, the flash calculation provides the component excess adsorption and the equilibrium mole fraction in the bulk gas phase for each component.

In this work, half of the adjusted slit width, $L - (\sigma_{\text{ff}})_i$, was subdivided into 50 intervals. At each interval, the local density and the adsorbed mole fractions were calculated by simultaneously solving Equation (5-2) for all components and using the mole fraction summation requirement, $\sum_i x_i = 1$. The adsorbed mole fractions were initialized to the feed mole fractions, i.e., $x_i = z_i$ for all components 'i'. The solution, however, is contingent on *equilibrium* (not feed) mole fractions, y_i , as they are needed to solve for the bulk-phase fugacity in Equation (5-4). The bulk mole fractions were initialized with the available experimental values to speed the calculation (although any reasonable initial values could be used). Once the local density and the adsorbed mole

fractions are calculated for each interval, a trial adsorbed amount was calculated by numerical integration using Simpson's rule in accordance with Equation (5-1).

The next step is to evaluate Equation (5-9), which is a system of component mole balances, as discussed in Chapter 2.

$$z_i = \frac{n_i^{\text{Ex}} + \rho_{\text{gas}} V_{\text{void}} Y_i}{n^{\text{Ex}} + \rho_{\text{gas}} V_{\text{void}}} \quad (5-9)$$

If Equation (5-9) is not satisfied for each component, then a new set of equilibrium mole fractions is used to calculate the next trial adsorbed amount. The procedure is repeated until Equation (5-9) and the adsorbed mole fraction summation are satisfied. Newton's method with numerical derivatives is used to solve Equation (5-2) and Equation (5-9). For the systems considered, convergence is always reliable for Equation (5-9) and, if suitable values of ϵ_{fs} , L are chosen, it is reliable for Equation (5-2):

Three independent scenarios (within the case study of the activated carbon) were explored. For the first two scenarios, we correlate all 335 independent adsorption data using 11 regressed parameters. (Three gas components requires $(2 \times 3) + 2 = 8$ pure gas parameters, and one binary interaction parameter per gas pair brings the total to 11). For the third scenario, the mixture adsorption is predicted based solely on pure-component regressions; here, the parameters for all available *pure* components were regressed simultaneously.

The manner in which the pore volume is calculated is important; the pore volume can exclude or include pore volume elements where the adsorbed-fluid density is assumed negligible compared to the fluid density elsewhere. The cut-off distance next to

the wall is defined as the position where the adsorbed fluid is assumed to have negligible density compared to the density elsewhere in the slit. The three scenarios are:

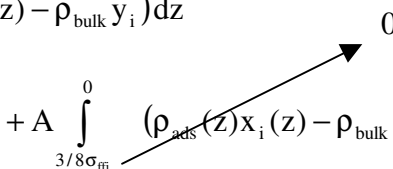
Scenario 1: The adsorbed material may reside in the slit from $\sigma_{ff}/2$ to $L-\sigma_{ff}/2$. No adsorbed material is allowed within $\sigma_{ff}/2$ adjacent to the wall. The pore volume is taken as $A(L-\sigma_{ff})/2$.

Scenario 2: Next, consider the adsorbed material to reside in the slit from $3/8\sigma_{ff}$ to $L-3/8\sigma_{ff}$. This accounts for almost all of the adsorbed material not included in the first case, as discussed in Chapter 4. The pore volume thus is presumed to be $A(L)/2$.

Scenario 3: This case is identical to the second, except that the mixtures are predicted from the pure components, rather than regressed simultaneously.

Scenario 1 assumes that the fluid molecule may not penetrate the wall at all and the local density from the wall to $\sigma_{ff}/2$ is zero. Since the fluid molecule cannot reside in the distance from the wall to $\sigma_{ff}/2$ (or from $L-\sigma_{ff}/2$), the volume contained there is excluded from the pore volume. Hence, the pore volume is taken as $A/2(L-\sigma_{ff})$.

Scenario 2 assumes that the fluid molecule may reside anywhere in the slit. The pore volume is taken to include the entire volume covered by the slit, $A/2(L)$. Though the fluid may reside anywhere, the density is negligibly small in the distance from the wall to about $3/8\sigma_{ff}$. Thus, the second integral in Equation (5-10) was accordingly assumed to be zero, as shown below:

$$n_i^{\text{Ex}} = A/2 \int_{3/8\sigma_{\text{ff}}}^{L-3/8\sigma_{\text{ff}}} (\rho_{\text{ads}}(z)x_i(z) - \rho_{\text{bulk}}y_i) dz + A \int_{3/8\sigma_{\text{ff}}}^0 (\rho_{\text{ads}}(z)x_i(z) - \rho_{\text{bulk}}y_i) dz \quad (5-10)$$


In Scenario 2, part of the spherical volume of the adsorbed molecule has crossed the imaginary solid-fluid boundary line of our model. Adsorption is defined as the adsorbate component accumulation on or outside this adsorbent *surface*, and absorption is defined as molecular accumulation or material transfer of the adsorbate within that surface, that is, within the solid phase. Based solely on these definitions, a conclusion may be drawn that Scenario 2 includes both adsorption and absorption effects and that Scenario 1 includes only adsorption effects. However, the solid adsorbent in both cases is modeled as being rigid; and physically, the adsorbent does not change its configuration (on the scale of the micropore volume) due to fluid-solid interactions. The conclusion here is that configuration changes of the adsorbent are necessary (albeit not sufficient) for absorption and that Scenario 1 and 2 both represent only adsorption phenomena.

Results and Discussion

Table 5-1 presents a summary of the results of the model evaluation for Scenarios 1 and 2 (Scenario 3 will be discussed later). In general, the SLD-PR model is capable of representing the adsorption data considered in this study within their experimental uncertainties (represented by error bars in all figures in this Chapter). On average, Scenario 2 correlates all the data slightly better than Scenario 1. On average, the SLD-PR model fits all the adsorption data (all 335 points) within one experimental standard deviation.

The error distribution of the model error for Scenario 2 is shown in Figure 5-1. The actual error distribution is very close to the expected error distribution, which suggests that the SLD-PR model has not been over-fitted when attempting to correlate the data set.

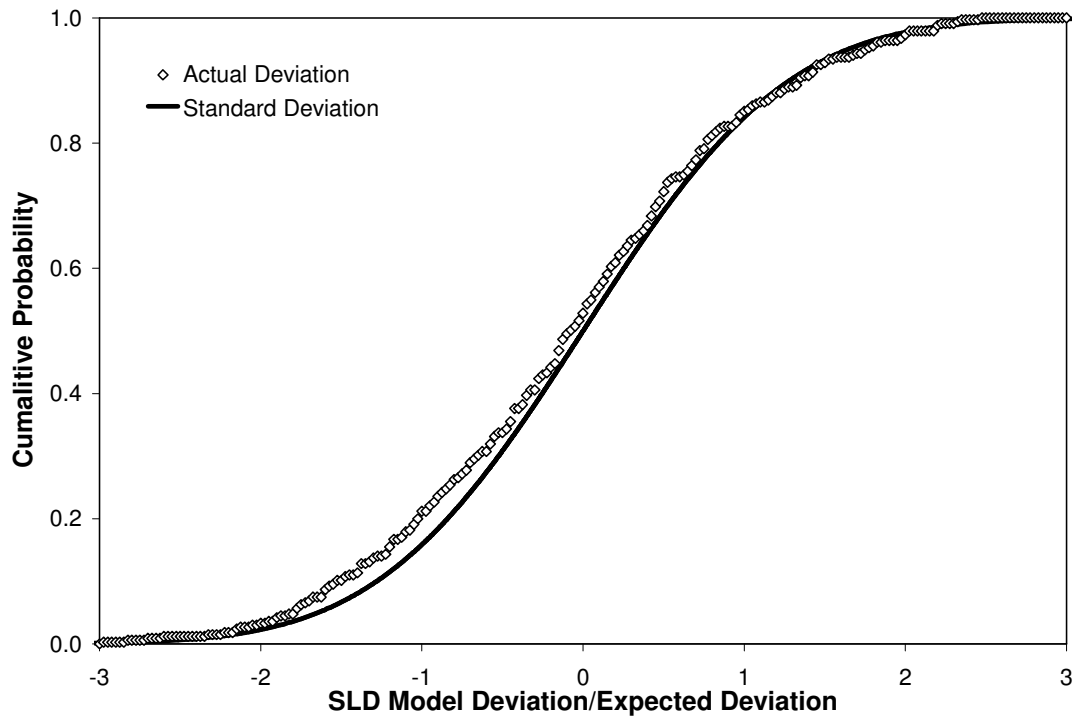


Figure 5-1. SLD-PR Model Error Distribution of Binary and Pure-Gas Adsorption on Calgon F-400 Activated Carbon

As shown in Table 5-2, the regressed parameters for Scenario 1 and Scenario 2 have a few similarities, but other parameters differ significantly from one another. The surface area for Scenario 1 is higher than Scenario 2 because the molecular diameter of the pore volume was excluded for Scenario 1. While the surface area differs between the two cases, the pore volumes for the two cases are quantitatively similar.

For all gases, the parameter Λ_b is higher for Scenario 2 than Scenario 1. Higher values of Λ_b mean lower values of the local density near the wall. Scenario 2 has lower values of Λ_b because, for this sub-case, the pore volume close to the wall is included.

This added volume decreases the average local density across the pore volume and offsets the need for a correction from Λ_b . The ratio of $(1+\Lambda_b)$ for each case and for each component is very similar, suggesting that a decrease in defined pore volume can be offset by a roughly proportional increase in $(1+\Lambda_b)$. Thus, definition of the pore volume is important for consistency in modeling efforts, as different pore volume definitions lead to different regressed parameters such as the surface area. The attractive interactions for methane-CO₂ and nitrogen-CO₂ have small corrections (C_{ij}) in Scenario 1, and methane-nitrogen and methane-CO₂ have small corrections in Scenario 2. This suggests that predictions of nitrogen/CO₂ mixture adsorption from pure-component isotherms would be better predicted if Scenario 1 were used. In contrast, methane/nitrogen mixture adsorption would be better predicted if Scenario 2 were used. The size of the correction for methane-nitrogen in Scenario 1 and nitrogen-CO₂ in Scenario 2 is rather large. This suggests that one-fluid mixing rules may not be sufficient to predict binary adsorption because the predicted binary adsorption is insensitive to deviations from one-fluid mixing rules. Other possible causes of the large correction factors include an inadequate SLD-PR theory describing fluid interactions, such as the inaccuracy of the PR-EOS repulsive pressure, $RT/(v-b)$.

To test the *predictive* capability of the SLD-PR model, the pure-component isotherms are regressed as described in Scenario 3. Using only these parameters, which are shown in Table 5-2, the mixture adsorption was predicted (setting all binary interaction parameters, C_{ij} , to zero). Figures 5-2 through 5-7 show the isotherms predicted in this manner (no BIPs) as well as isotherms predicted in Scenario 2 (correlative model). These model predictions, based solely on pure-substance adsorption

data, are within *twice* the experimental uncertainties for the methane/nitrogen mixture isotherms, and they are within *five* times the experimental uncertainties for methane/CO₂ and nitrogen/CO₂ mixture isotherms; however, for the gas component adsorbed in its more rich mixtures, the error is generally less. The SLD-PR predicts the component mixture adsorption at 2.2 times the experimental uncertainty on average for all mixture isotherms. As shown in the Figures 5-2 through 5-7, the experimental uncertainties are small for many isotherms. Predictive errors of two or three times the uncertainty translates to relatively small absolute deviations from the experimental isotherm.

Table 5-1. Comparison of SLD-PR Model Regression Results for Three Scenarios for the Pure and Binary Mixture Adsorption on Calgon F-400 Activated Carbon

| | Weighted Average Absolute Deviation, WAAD | | | | | |
|--------------------------------|--|-----------------------|-------------------|-----------------------|-------------------|-----------------------|
| Pure Gases | <i>Scenario 1</i> | | <i>Scenario 2</i> | | <i>Scenario 3</i> | |
| Methane | 1.4 | | 1.2 | | 0.64 | |
| Nitrogen | 1.0 | | 1.0 | | 0.97 | |
| CO ₂ | 1.2 | | 1.2 | | 0.87 | |
| Feed Mixture | | | | | | |
| | <i>Scenario 1</i> | | <i>Scenario 2</i> | | <i>Scenario 3</i> | |
| Methane/Nitrogen | <i>methane</i> | <i>nitrogen</i> | <i>methane</i> | <i>nitrogen</i> | <i>methane</i> | <i>nitrogen</i> |
| 20/80 | 0.24 | 0.97 | 0.33 | 0.97 | 0.26 | 1.3 |
| 40/60 | 1.5 | 0.88 | 1.4 | 0.86 | 1.7 | 1.0 |
| 60/40 | 1.4 | 0.37 | 1.3 | 0.21 | 1.8 | 0.4 |
| 80/20 | 1.4 | 0.89 | 1.4 | 0.75 | 2.0 | 1.4 |
| All Feeds | 1.1 | 0.78 | 1.1 | 0.70 | 1.4 | 1.0 |
| Methane/CO₂ | | | | | | |
| | <i>methane</i> | <i>CO₂</i> | <i>methane</i> | <i>CO₂</i> | <i>methane</i> | <i>CO₂</i> |
| 20/80 | 0.79 | 0.81 | 0.66 | 0.93 | 3.9 | 0.90 |
| 40/60 | 0.51 | 0.66 | 0.50 | 0.54 | 4.8 | 2.0 |
| 60/40 | 0.66 | 0.57 | 0.57 | 0.40 | 3.6 | 2.7 |
| 80/20 | 0.21 | 0.75 | 0.21 | 0.63 | 2.0 | 4.0 |
| All Feeds | 0.54 | 0.70 | 0.49 | 0.62 | 3.6 | 2.4 |
| Nitrogen/CO₂ | | | | | | |
| | <i>nitrogen</i> | <i>CO₂</i> | <i>nitrogen</i> | <i>CO₂</i> | <i>nitrogen</i> | <i>CO₂</i> |
| 20/80 | 0.73 | 0.76 | 0.73 | 0.78 | 4.4 | 2.2 |
| 40/60 | 0.63 | 0.54 | 0.53 | 0.67 | 3.4 | 1.5 |
| 60/40 | 0.66 | 1.1 | 0.78 | 1.2 | 2.2 | 2.0 |
| 80/20 | 0.21 | 1.1 | 0.42 | 0.79 | 1.2 | 2.0 |
| All Feeds | 0.54 | 0.86 | 0.60 | 0.84 | 2.3 | 1.9 |

Table 5-2. Regressed Parameters for SLD-PR Model on Calgon F-400 Activated Carbon

| | Scenario 1 | | | Scenario 2 | | | Scenario 3 | | |
|--|----------------|-----------------|-----------------------|----------------|-----------------|-----------------------|----------------|-----------------|-----------------------|
| Surface Area (m ² /g) | 844 | | | 604 | | | 621 | | |
| Slit Length (nm) | 1.13 | | | 1.09 | | | 1.20 | | |
| | <i>methane</i> | <i>nitrogen</i> | <i>CO₂</i> | <i>methane</i> | <i>nitrogen</i> | <i>CO₂</i> | <i>methane</i> | <i>nitrogen</i> | <i>CO₂</i> |
| ϵ_{fs}/k (K) | 76.1 | 50.0 | 88.3 | 70.5 | 49.7 | 76.9 | 71.9 | 48.7 | 86.7 |
| Λ_b | 0.62 | 0.85 | 0.29 | 0.23 | 0.43 | 0.00 | 0.33 | 0.51 | 0.12 |
| <i>Binary Interaction, C_{ij}</i> | | | | | | | | | |
| Methane-Nitrogen | 0.229 | | | 0.078 | | | None | | |
| Methane-CO ₂ | 0.066 | | | -0.0013 | | | None | | |
| Nitrogen-CO ₂ | -0.021 | | | -0.247 | | | None | | |

The SLD-PR model can correlate adsorption isotherms that exhibit a maximum. Of particular interest is the nitrogen adsorption in the 40%/60% and 20%/80% nitrogen/CO₂ mixtures (Figure 5-6). These two isotherms each exhibit a maximum, inflect and become concave up with pressure, and finally crossover and become negative. To date, no other published experimental data exhibit these features for a binary system.

The *correlative* model is least accurate for the methane adsorption at high methane concentrations of methane/nitrogen mixtures. Also, for pure CO₂ at high pressures, the model is noticeably higher than the data. These errors could be in part due to systematic experimental error (for methane adsorption), and in part due to inadequate fluid property accuracy (for CO₂ near the critical point).

The models predict quantitatively the gas phase composition as a function of pressure, as shown for methane/nitrogen mixtures in Figure 5-8. Other mixtures have similar quantitative agreement. As discussed in Chapter 2, this pressure dependence is a function of how much adsorbent is in the total system volume under analysis – the specific helium void volume. As shown in Figure 5-8, the gas phase composition approaches the feed gas composition at higher pressures, because the gas adsorbed at higher pressures is less significant relative to that in the gas phase. For systems that have less adsorbent per total system volume, i.e., higher specific void volumes, the gas phase composition is closer to the feed composition. Any model that can predict the component excess adsorption can also use the gas phase composition and specific void volume to predict the feed gas composition.

The local density and the local composition of the adsorbed phase in a slit at three different pressures are shown in Figure 5-9. The profiles are plotted against a normalized

slit position ($L = 1.09$ nm) such that the center position of the slit is 0.5 and the wall surface is 0.0. The local density at each pressure is highest at half the molecular hard-sphere diameter σ_{ff} . The local adsorbed mole fraction exhibits peaks in the same position. For Scenario 1, the local density and composition are calculated only to the right of local density peaks. Scenario 2 is shown in Figure 5-9, which includes positions in the slit $3/8 \sigma_{ff}$ from the wall surface.

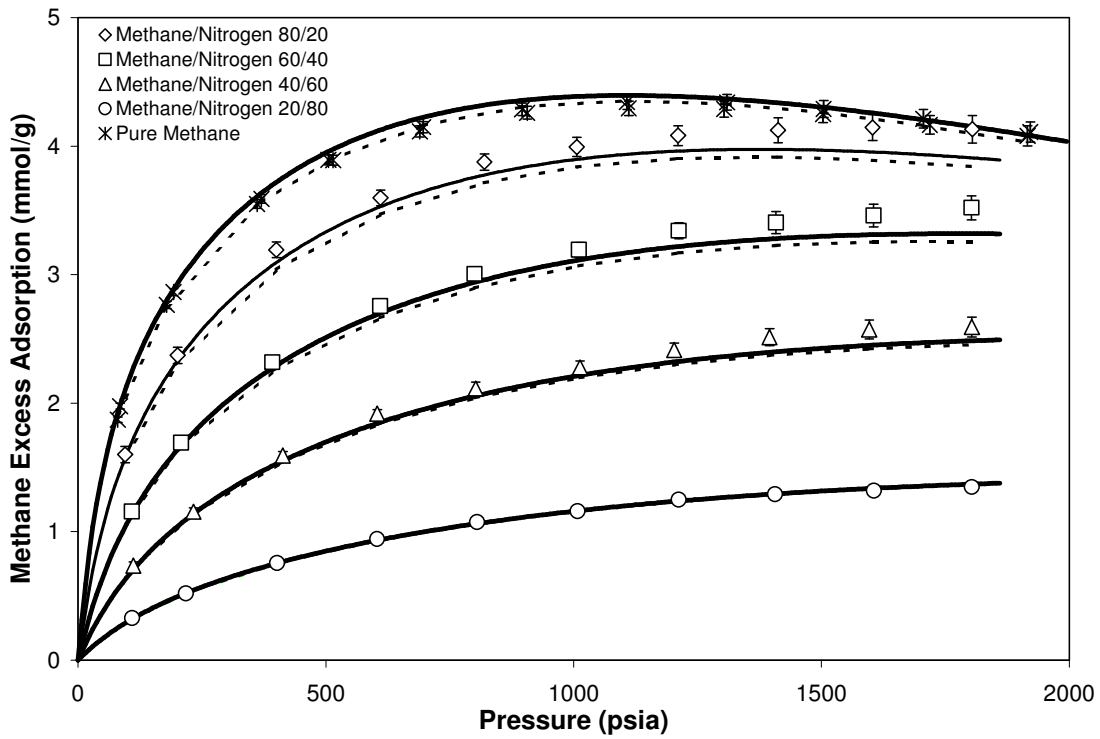


Figure 5-2. SLD Model of Methane Adsorption in Methane/Nitrogen Mixtures on Calgon F-400 Activated Carbon (Solid Line – Regressed C_{ij} , Dashed Line – $C_{ij}=0.0$)

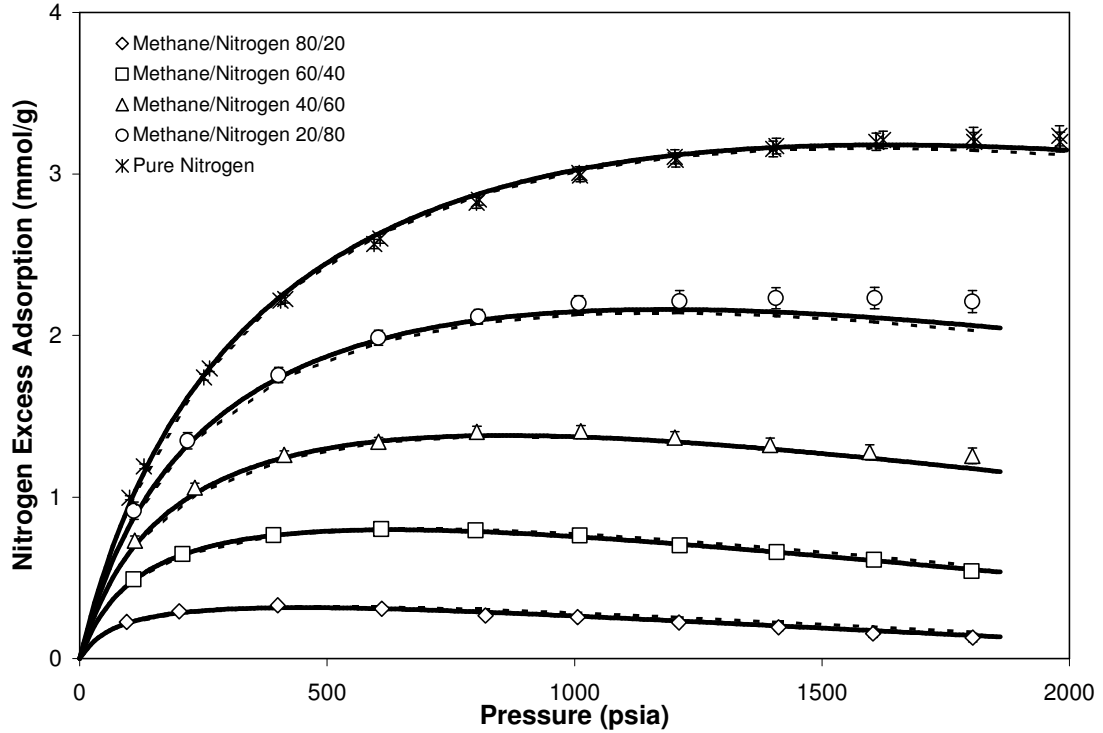


Figure 5-3. SLD Model of Nitrogen Adsorption in Methane/Nitrogen Mixtures on Calgon F-400 Activated Carbon

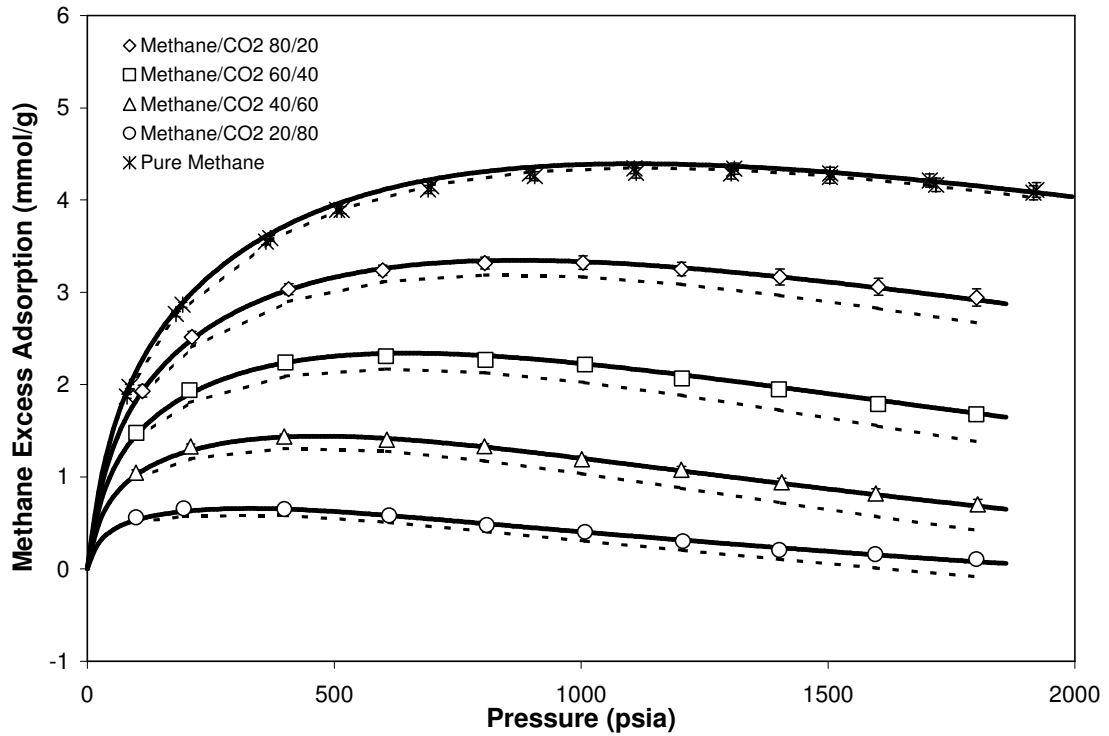


Figure 5-4. SLD Model of Methane Adsorption in Methane/CO₂ Mixtures on Calgon F-400 Activated Carbon

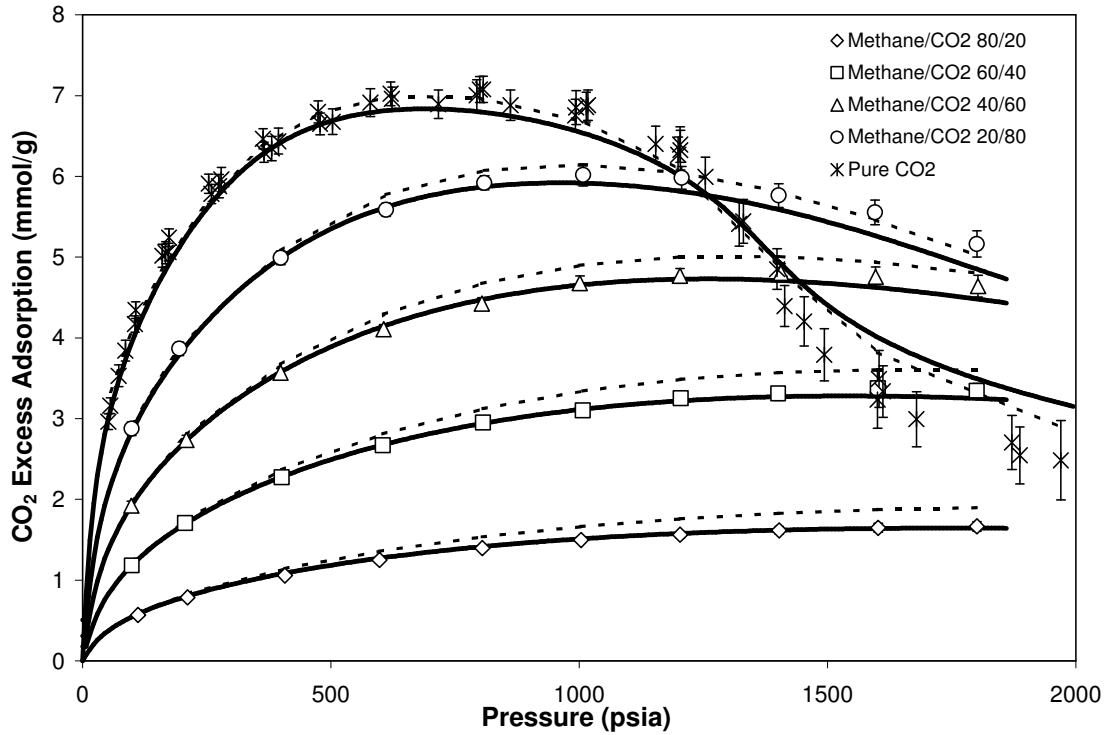


Figure 5-5. SLD Model of CO₂ Adsorption in Methane/CO₂ Mixtures on Calgon F-400 Activated Carbon

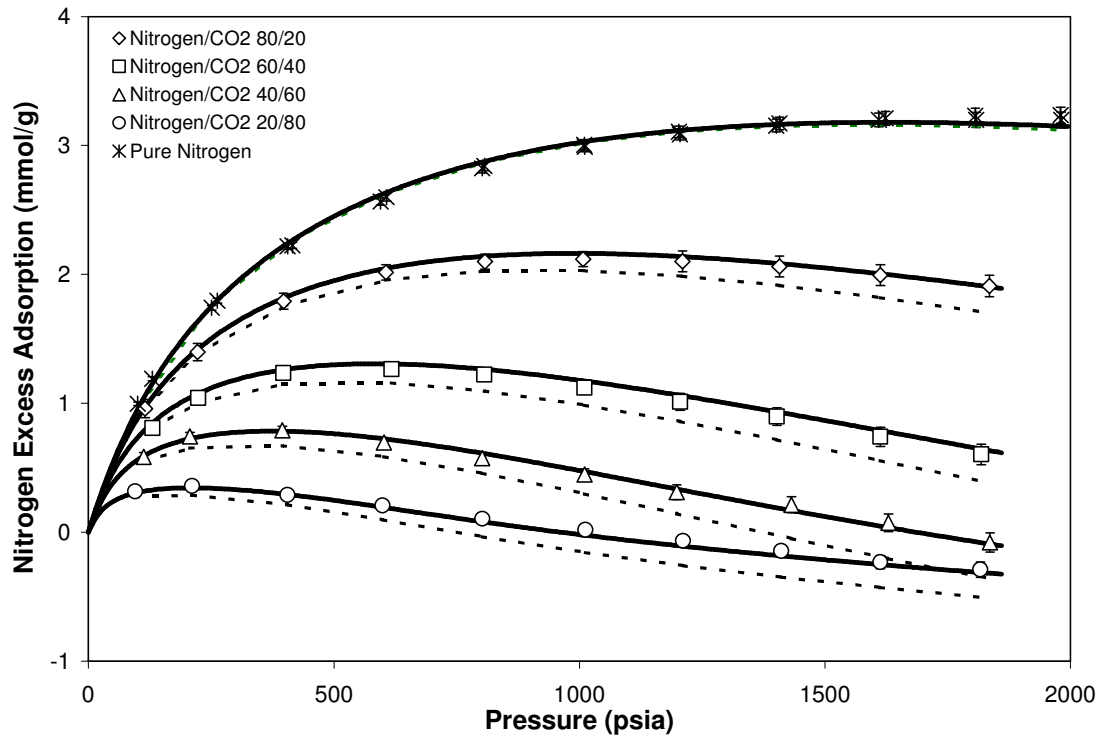


Figure 5-6. SLD Model of Nitrogen Adsorption in Nitrogen/CO₂ Mixtures on Calgon F-400 Activated Carbon

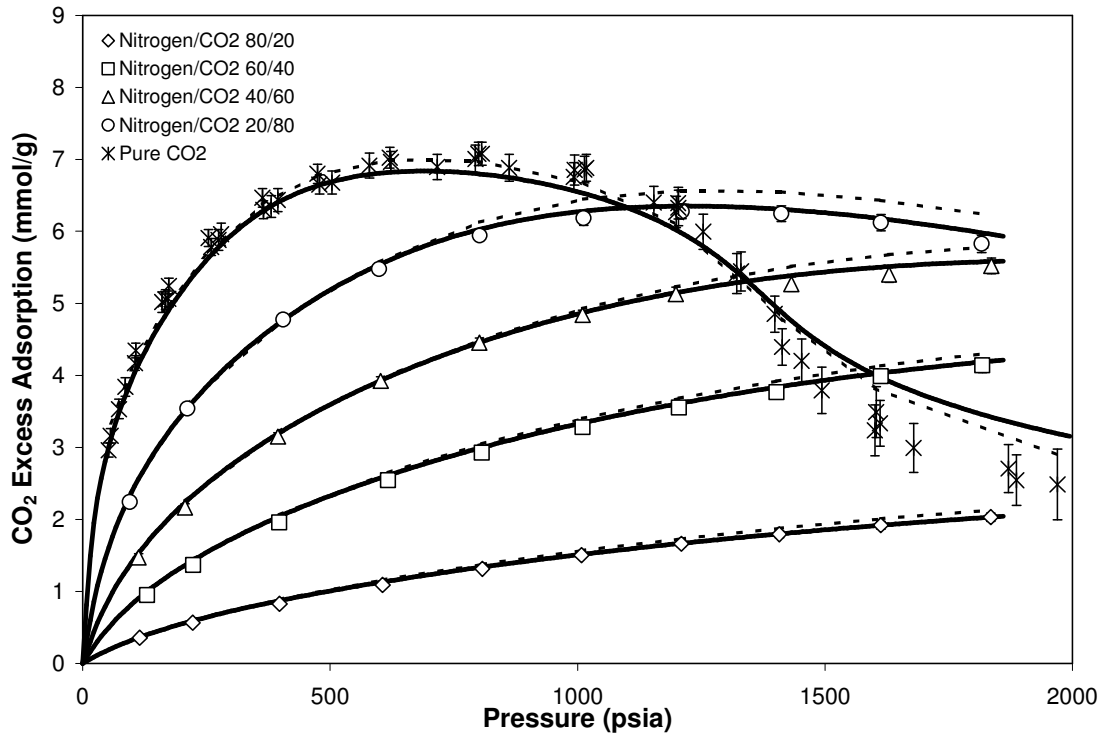


Figure 5-7. SLD Model of CO₂ Adsorption in Nitrogen/CO₂ Mixtures on Calgon F-400 Activated Carbon

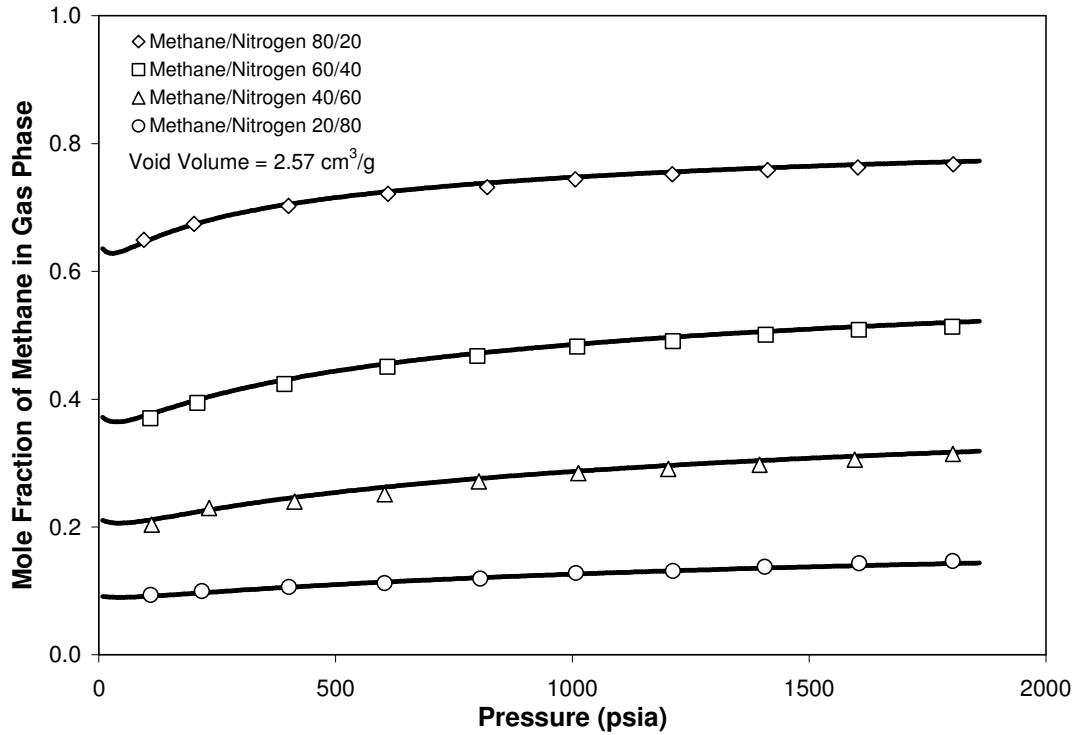


Figure 5-8. SLD Model Prediction of Gas-Phase Compositions for Methane/Nitrogen Feed Mixtures on Calgon F-400 Activated Carbon

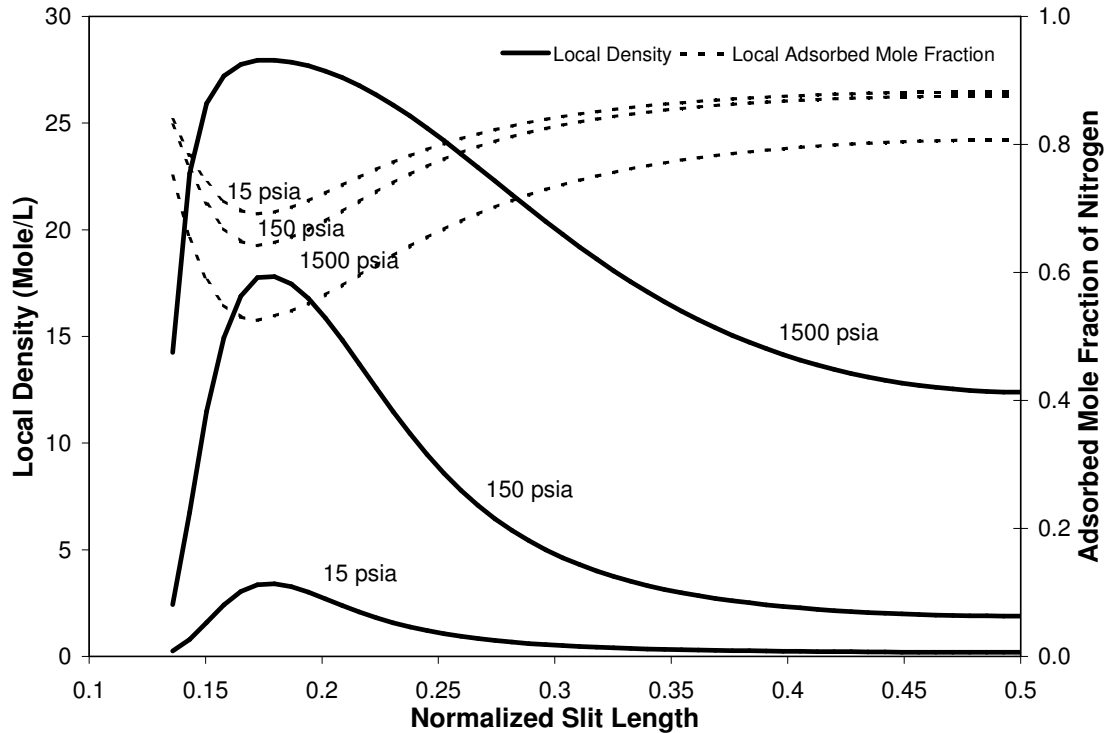


Figure 5-9. SLD Model Prediction of Local Densities and Adsorbed Phase Compositions for a 20/80 Methane/Nitrogen Gas Mixture on Calgon F-400 Activated Carbon

Adsorption measurements also were conducted for a 10/40/50 methane/nitrogen/ CO_2 feed mixture. These measurements facilitate model testing of ternary mixture adsorption solely from pure-component measurements or from correlated binary isotherms. For those cases, Figure 5-10 depicts the SLD model predictions for the component excess isotherms of methane, nitrogen, and CO_2 . The model predictions of gas adsorption for CO_2 and methane are within, on average, the experimental uncertainty for each isotherm, and for nitrogen, the predictions are within, on average, three experimental uncertainties.

The modeled adsorption isotherms have satisfactory predictions of binary and ternary gas adsorption without BIPs. Large BIPs are required sometimes for representation of these isotherms within their experimental uncertainty, as depicted in

Table 5-2 in Scenario 1 for methane/nitrogen mixtures and in Scenario 2 for nitrogen/CO₂ mixtures. The question arises on how these BIPs influence the isotherm behavior. To investigate this effect, the excess volume of the adsorbed phase as a percentage of the specific adsorbed-phase volume is plotted against molar composition for BIP values of -0.5, 0.0, and 0.5 and at pressures of 25 and 2000 psia (using SLD-PR model parameters from Case 3). Figures 5-11 through 5-13 depict these percentages of the excess volumes for methane-nitrogen, methane-CO₂, and nitrogen/CO₂ mixtures. The greater the percentage excess volume becomes in magnitude, the greater the change of the excess isotherm is from an isotherm calculated from ideal mixing conditions.

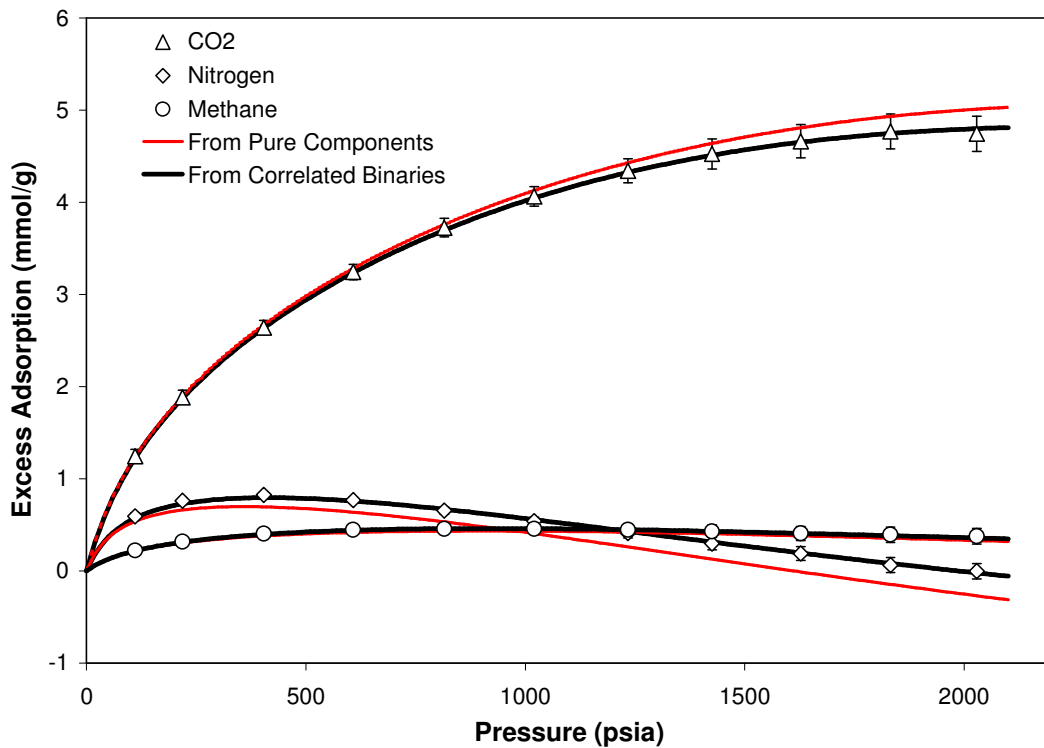


Figure 5-10. SLD Model of Ternary Adsorption of 10/40/50 Methane/Nitrogen/CO₂ Mixture on Calgon F-400 Activated Carbon

The default case of zero-valued BIPs show that the percentage excess volume is not zero for any of the mixtures. At 25 psia, however, the excess volume for methane-nitrogen mixtures is less than 0.25% in magnitude, and at 2000 psia, it is less than 1.5%.

Changes in the BIPs for methane/nitrogen mixtures from -0.5 to 0.5 will have effects on the percentage excess volume of less than 4.5% in magnitude. Thus, large changes in the BIP values (large in comparison to the BIP values used for VLE calculations) are necessary to effect a small change in the excess volume of the adsorbed phase, and consequently, a small change in the excess adsorption. For methane/ CO_2 and nitrogen/ CO_2 mixtures, BIPs values of -0.5 or 0.5 can change the percentage excess volume at a maximum of about 10% from the percentage excess volume of the zero-valued BIPs.

The insensitivity of the BIPs to changes in the excess volume (i.e., dC_{ij} / dv^E is relatively small), and consequently, to changes in the excess adsorption suggests that large BIPs are necessary for correlation of some binary adsorption systems. The magnitude of the BIPs, however, can be greatly diminished by correlating pure and binary adsorption simultaneously. Binary gas adsorption is better correlated by altering slightly the pure-gas isotherms because such changes have comparable impacts in the predicted binary adsorption as do large changes in BIP values.

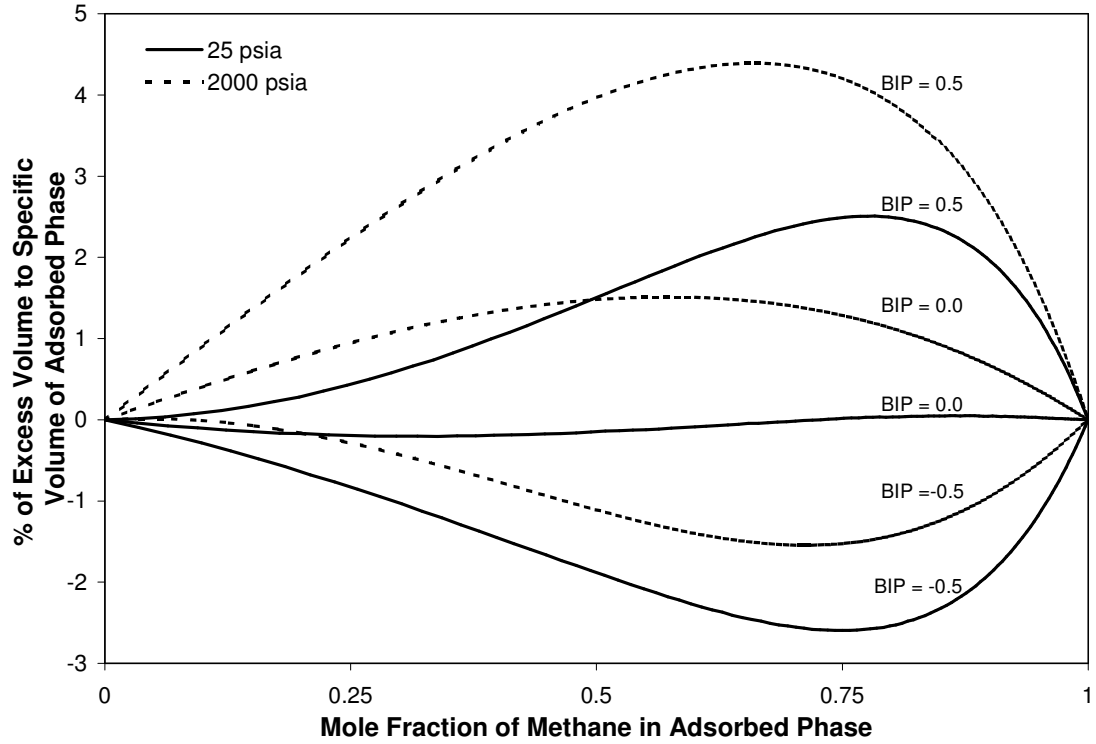


Figure 5-11. SLD Model of Methane/Nitrogen Excess Volumes at 25 psia and 2000 psia at C_{ij} Values of 0.0, -0.5 and 0.5

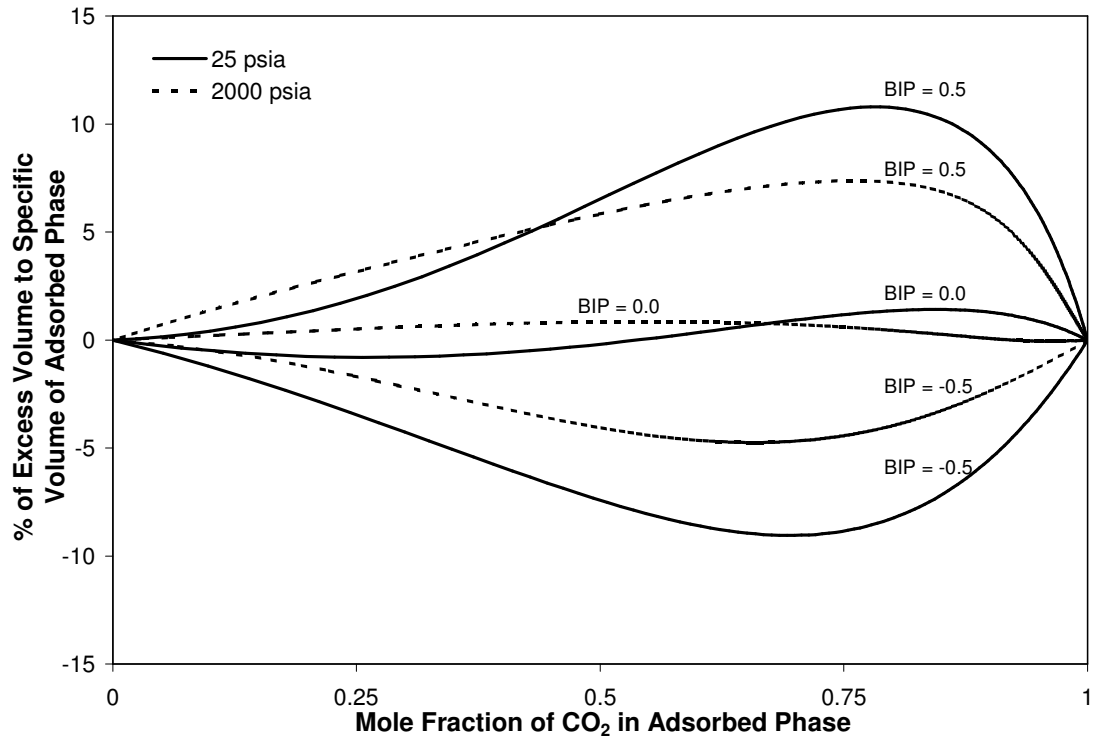


Figure 5-12. SLD Model of Methane/CO₂ Excess Volumes at 25 psia and 2000 psia at C_{ij} Values of 0.0, -0.5 and 0.5

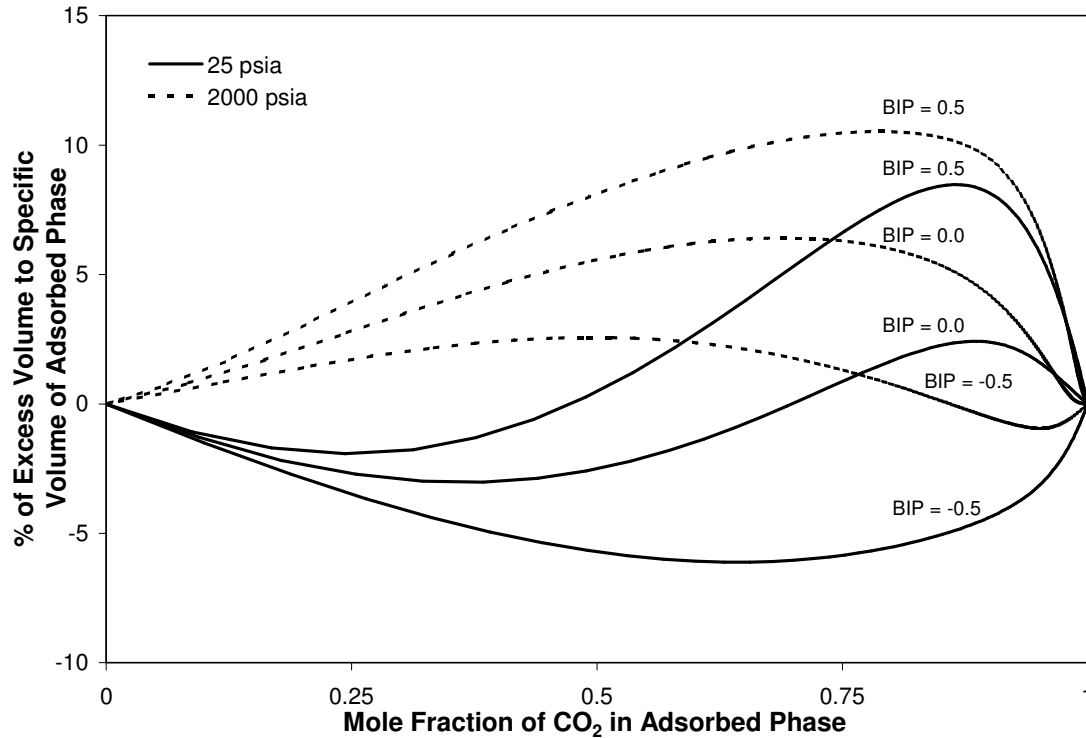


Figure 5-13. SLD Model of Nitrogen/CO₂ Excess Volumes at 25 psia and 2000 psia at C_{ij} Values of 0.0, -0.5 and 0.5

Conclusions for Case Study 3

Major conclusions of this study are:

- For adsorption on activated carbon, the SLD-PR *predicts* the component mixture adsorption at 2.2 times the experimental uncertainty on average, based solely on pure-component adsorption isotherms. This includes component-adsorption isotherms exhibiting excess adsorption maxima and negative excess adsorption.
- The SLD-PR model *correlates* the binary mixture adsorption behavior of the systems considered within one standard deviation of experimental error.
- The one-fluid mixing rules are suitable for the task of correlation; however, they require large corrections for some binary interactions.

- Case studies show that the SLD pore volume definition has a significant effect on the values of regressed parameters, such as surface area.

CASE STUDY 4: MIXTURE ADSORPTION ON WET TIFFANY COAL

British Petroleum (BP) Amoco provided OSU representative coal samples from Tiffany Injection Wells #1 and #10, which are located in the San Juan Basin in Colorado, near the New Mexico-Colorado border. OSU determined the equilibrium moisture content and particle size distribution of each coal sample. Compositional coal analyses for both samples were performed by Huffman Laboratories, Inc.

Coal characterization measurements are presented in Tables 5-3 and Figure 5-14 (See Chapter 3 for details on coal characterization of Tiffany coal). Table 5-3 presents the compositional analyses for coal samples from Wells #1 and #10 on a wet and dry basis. Figure 5-14 presents the coal particle size distribution for the two samples. The analyses indicate that the two coal samples are similar in composition and particle size distribution.

Table 5-3. Compositional Analyses of Tiffany Coal Samples

| Analysis | Well #1 | Well #10 | Well #1 Dried Basis | Well #10 Dried Basis |
|-------------------|----------------|-----------------|--------------------------------|---------------------------------|
| Dry Loss % | 6.85 | 18.33 | | |
| Carbon % | 44.51 | 46.35 | 47.78 | 56.75 |
| Hydrogen % | 3.20 | 4.30 | 2.62 | 2.77 |
| Oxygen % | 11.85 | 20.51 | 6.19 | 5.16 |
| Nitrogen % | 0.86 | 0.83 | 0.92 | 1.02 |
| Sulfur % | 0.53 | 0.42 | 0.57 | 0.52 |
| Ash % | 46.30 | 38.99 | 49.71 | 47.74 |
| Proximate | | | | |
| Volatile Matter % | 14.41 | 12.54 | 15.48 | 15.35 |
| Fixed Carbon % | 32.43 | 30.14 | 34.82 | 36.91 |

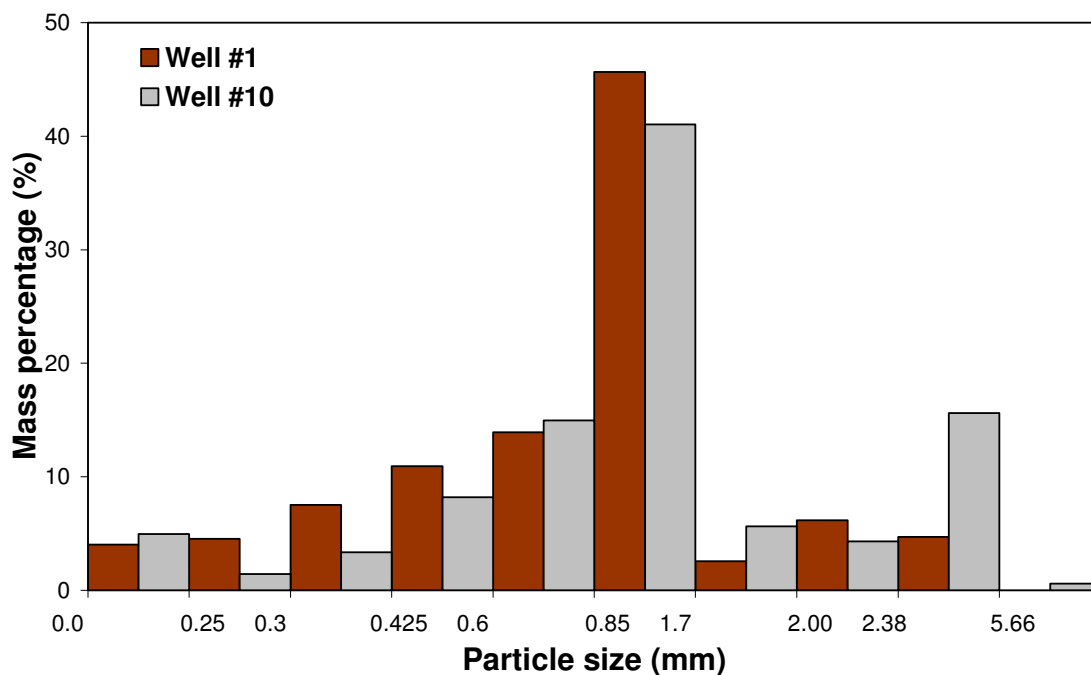


Figure 5-14. Tiffany Well #1 Coal Particle Size Distribution

The density of the compact solid coal is called the coal helium density (see Chapter 2 for details), in reference to the helium displacement measurements used to determine the adsorbent density. The coal helium densities were measured for Well #1, Well #10, and an equal-weighted mixed sample. They are 1.73, 1.57, and 1.67 ± 0.07 g/cc, respectively. The equilibrium moisture content of Well #1 coal sample is $3.8 \pm 0.2\%$ and the equilibrium moisture content of Well #10 coal sample is $3.7 \pm 0.2\%$.

Vitrinite reflectance analyses conducted by National Petrographic Services indicate that the present Tiffany coal samples are medium volatility bituminous coal. As summarized in Table 5-4, Wells #1 and 10 have average oil-based vitrinite reflectance values of 1.31 and 1.35, respectively.

Table 5-4. Vitrinite Reflectance Analysis

| | Well #1 | Well #10 |
|--------------------|--------------------------------------|--------------------------------------|
| Average VRO | 1.31 | 1.35 |
| Range | 1.19-1.43 | 1.21-1.50 |
| Grain Count | 50 | 50 |
| Rank | Medium Volatility Bituminous Coal | Medium Volatility Bituminous Coal |

Measurements

Pure-gas adsorption measurements for methane on wet Tiffany coal samples from Injection Wells #1 and #10 were done separately at 130°F (327.6 K) and pressures to 2000 psia (13.7 MPa). The average expected uncertainty in these data is about 3%. For the samples from the two wells, a maximum variation of about 5% in the amount adsorbed is observed at 2000 psia.

Because of the similarity in the methane adsorption behavior for Tiffany Well #1 and Well #10 coal samples, and upon agreement with BP Amoco personnel, coal samples from the two wells were mixed on an equal-mass basis. Large chunks of coal (dime-size) were broken up and the coal mixture was gently shaken to ensure a final homogenous mixture. The coal samples were placed into a tightly-capped jar. Helium was injected into the jar to prevent oxidation of the coal.

Gas adsorption isotherms were measured for pure methane, nitrogen and CO₂ on the wet, mixed Tiffany coal sample. As mentioned previously, the coal sample was an equal-mass mixture of coals from Well #1 and Well #10. The adsorption measurements were conducted at 130°F at pressures to 2000 psia.

Adsorption isotherms were measured for methane/nitrogen, methane/CO₂ and nitrogen/CO₂ binary mixtures on wet, mixed Tiffany coal at 130°F and pressures to 2000

psia. These measurements were conducted for a single molar feed composition for each mixture. An adsorption isotherm also was measured for a single methane/nitrogen/CO₂ ternary mixture on wet, mixed Tiffany coal at 130°F and pressures to 2000 psia. The nominal molar feed composition was 10/40/50, from a specific request from reservoir modelers at Advanced Resources Inc. For all binary and ternary measurements on wet Tiffany coal, the void volume was measured to be at 0.885 cm³/(gram wet coal).

Calculation Details

The adsorbed material is considered to reside in the slit from $3/8\sigma_{ff}$ to $L-3/8\sigma_{ff}$. The pore volume thus is presumed to be $A(L)/2$. Within these constraints, two independent scenarios (within the case study of Tiffany coal) were explored:

Scenario 1: For the first case, the pure-component isotherms of methane, nitrogen, and carbon dioxide are regressed. From the pure-component regressions, the binary and ternary mixture component adsorption was predicted.

Scenario 2: The pure-component isotherms of methane, nitrogen, and carbon dioxide and their binary mixtures simultaneously are regressed using three binary interaction parameters.

Results and Discussion

Figures 5-15 through 5-19 depict the model results for both Scenarios 1 and 2 for all the experimental data. Table 5-5 shows the model parameters regressed for Scenarios 1 and 2. The regression results in Table 5-6 indicate that the component methane adsorbed in a methane/CO₂ mixture is the worst predicted (under Scenario 1).

Experimental data for this isotherm show increasing excess adsorption (Figure 5-17), whereas the model predicts an adsorption maximum at 500 psia. Moderately successful predictions are made for methane/nitrogen and nitrogen/CO₂ mixtures. Ternary predictions are only qualitatively successful.

The correlative results overall are much better than the predictive results of Scenario 1. Upon comparison of the two scenarios, pure-component regressions are worse in Scenario 2 because they are part of the overall regression. From the correlative pure and binary regressions, the ternary mixture component adsorption was predicted. Results shown in Table 5-6 indicate that the component adsorption for all three components can be represented within three experimental uncertainties on average. Note, however, the large values of the BIPs for methane/CO₂ and nitrogen/CO₂ mixtures in Table 5-5.

Table 5-5. Regressed Parameters for SLD-PR Model on Tiffany Coal at 130°F

| | Scenario 1 | | | Scenario 2 | | |
|--|----------------|-----------------|-----------------------|----------------|-----------------|-----------------------|
| Surface Area (m ² /g) | 36.0 | | | 49.4 | | |
| Slit Length (nm) | 1.06 | | | 1.02 | | |
| | <i>methane</i> | <i>nitrogen</i> | <i>CO₂</i> | <i>methane</i> | <i>nitrogen</i> | <i>CO₂</i> |
| ϵ_{fs}/k (K) | 51.7 | 30.3 | 64.0 | 47.4 | 23.8 | 60.9 |
| Λ_b | -0.19 | 0.09 | -0.30 | 0.02 | 0.08 | -0.11 |
| Binary Interaction, C_{ij} | | | | | | |
| Methane-Nitrogen | None | | | -0.08 | | |
| Methane-CO ₂ | None | | | -0.42 | | |
| Nitrogen-CO ₂ | None | | | -0.82 | | |

Table 5-6. Summary Results for the SLD-PR Model of Gas-Mixture Adsorption on Wet Tiffany Coal at 130°F

| <i>Pure Gases</i> | Weighted Average Absolute Deviation, WAAD | | | | | |
|----------------------------------|--|-----------------------|-----------------------|-----------------------|-----------------|-----------------------|
| | Scenario 1 | | Scenario 2 | | | |
| Methane | 1.0 | | 1.23 | | | |
| Nitrogen | 0.82 | | 1.1 | | | |
| CO ₂ | 0.32 | | 0.50 | | | |
| <i>Feed Mixtures</i> | | | | | | |
| Methane/Nitrogen | <i>methane</i> | <i>nitrogen</i> | <i>methane</i> | <i>nitrogen</i> | | |
| 0/50 | 2.4 | 0.83 | 1.5 | 0.31 | | |
| Methane/CO ₂ | <i>methane</i> | <i>CO₂</i> | <i>methane</i> | <i>CO₂</i> | | |
| 41/59 | 7.3 | 2.9 | 1.0 | 0.63 | | |
| Nitrogen/CO ₂ | <i>nitrogen</i> | <i>CO₂</i> | <i>nitrogen</i> | <i>CO₂</i> | | |
| 20/80 | 2.6 | 1.2 | 0.6 | 1.1 | | |
| Methane/Nitrogen/CO ₂ | <i>methane</i> | <i>nitrogen</i> | <i>CO₂</i> | <i>methane</i> | <i>nitrogen</i> | <i>CO₂</i> |
| 10/40/50 | 1.7 | 5.0 | 3.3 | 0.51 | 2.9 | 2.0 |

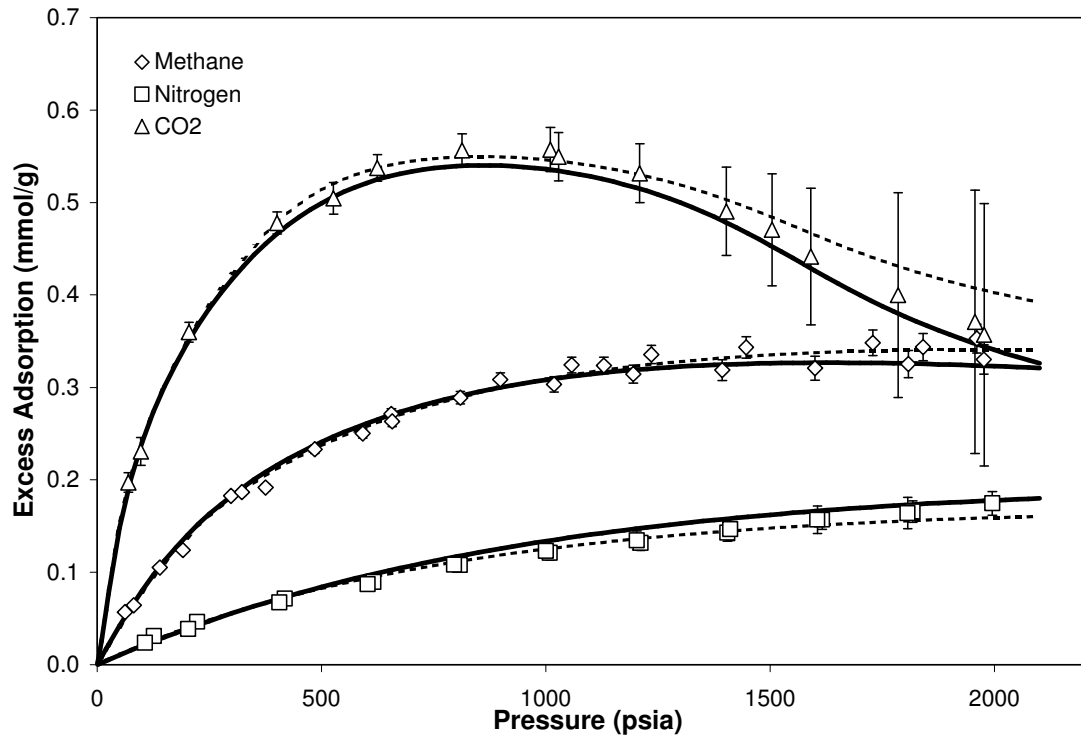


Figure 5-15. SLD Model of Pure-Gas Adsorption on Wet Tiffany Coal at 130°F (Solid Line - Correlated with Binaries, Dashed Line -No BIPs)

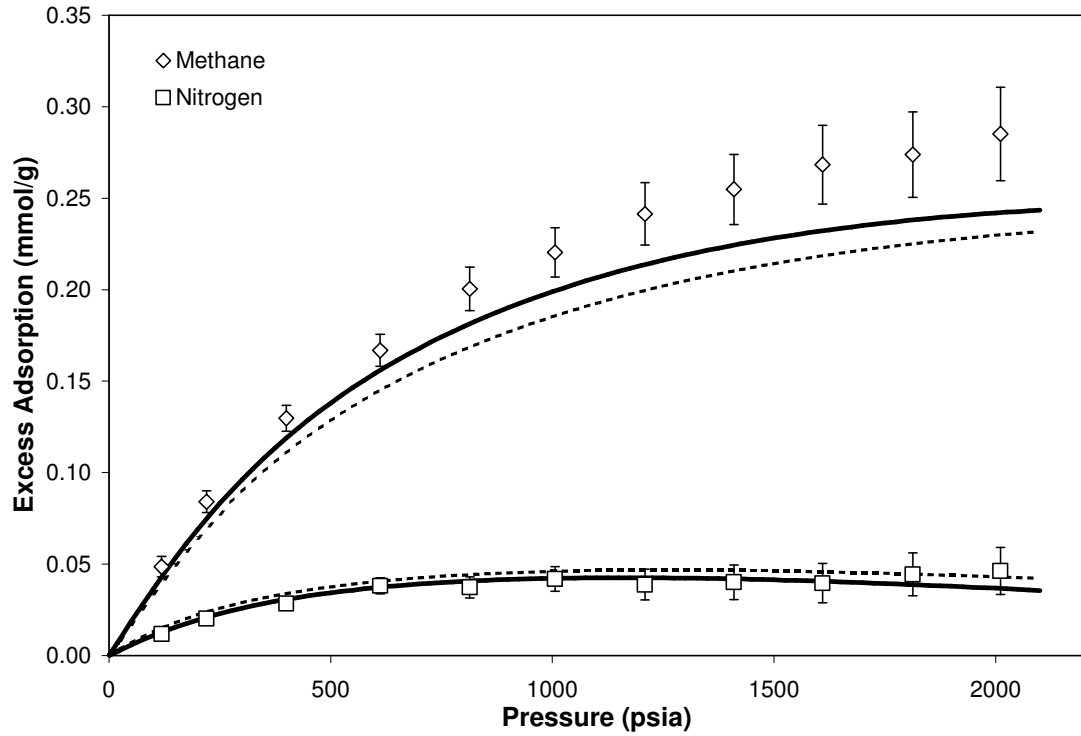


Figure 5-16. SLD Model of Methane/Nitrogen 50/50 Feed Gas Adsorption on Wet Tiffany Coal at 130°F (Solid Line - Correlated with Binaries, Dashed Line -No BIPs)

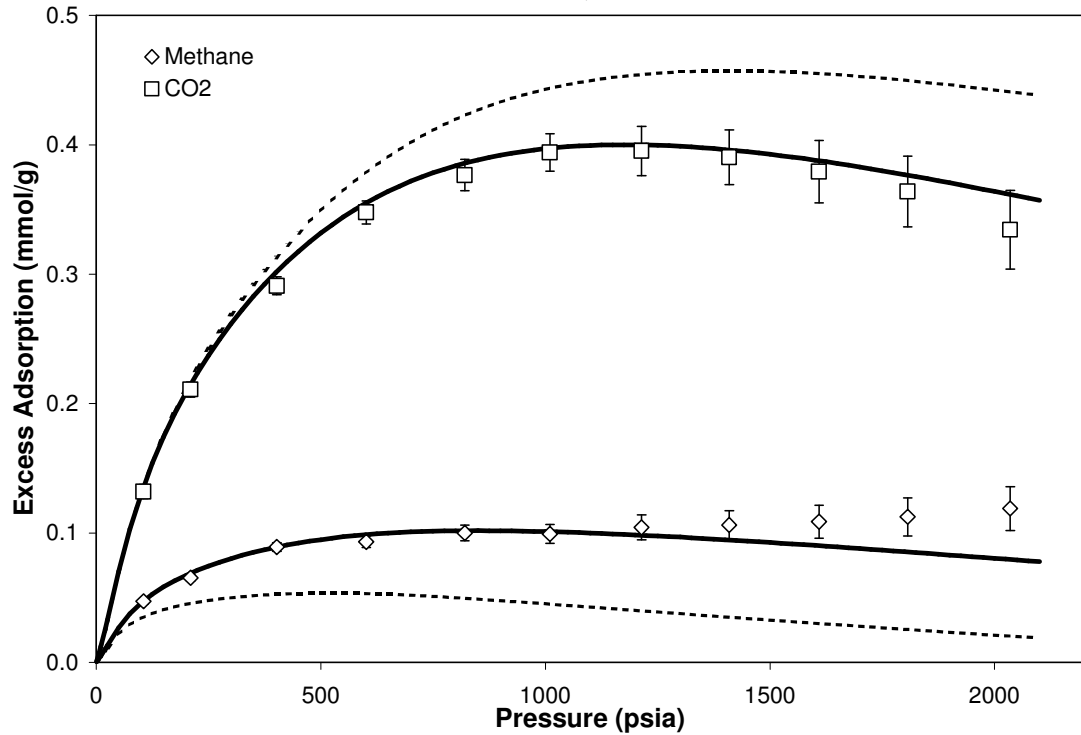


Figure 5-17. SLD Model of Methane/CO₂ 41/59 Feed Gas Adsorption on Wet Tiffany Coal at 130°F

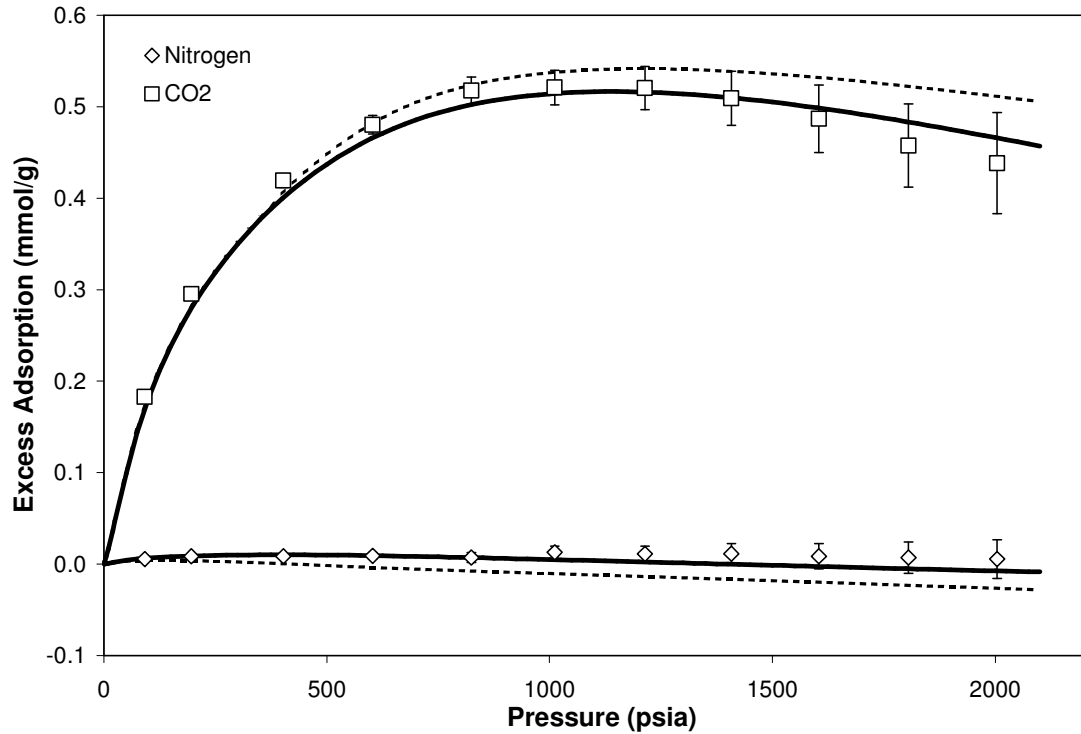


Figure 5-18. SLD Model of Nitrogen/CO₂ 20/80 Feed Gas Adsorption on Wet Tiffany Coal at 130°F

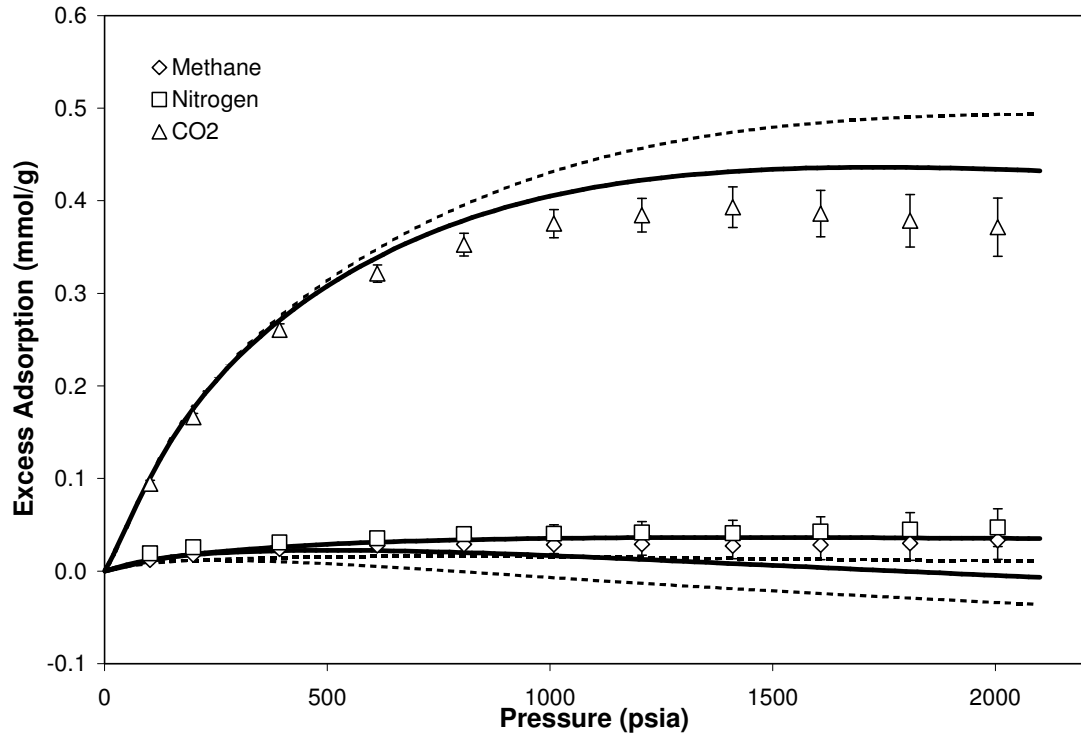


Figure 5-19. SLD Model of Methane/Nitrogen/CO₂ 10/40/50 Feed Gas Adsorption on Wet Tiffany Coal at 130°F

Conclusions for Case Study 4

Major conclusions of this case study are:

- For adsorption on wet Tiffany coal, the SLD-PR *predicts* qualitatively the binary mixture adsorption from pure-gas component regressions of methane, nitrogen, and CO₂. Prediction results of the weighted average absolute deviation vary from 7.9 for methane in a methane/CO₂ mixture to 0.83 for nitrogen in a methane/nitrogen mixture.
- Model representation of individual binary and ternary isotherms with one BIP per gas pair is within 2.0 experimental uncertainties except for nitrogen in the ternary gas mixture.
- Large BIP values are required for optimized representations of all isotherms.

CASE STUDY 5: MIXTURE ADSORPTION ON WET FRUITLAND COAL

Hall published in his thesis (1993) and elsewhere (Hall and Zhou, 1994) the pure and binary measurements of methane, nitrogen, and CO₂ on Fruitland coal at 115°F. At that time, many of the published adsorption measurements containing CO₂ were calculated incorrectly. Specifically, an inadequate equation of state was used to calculate the gas compressibility factors employed to infer the adsorption from the primary measurements of pressure, temperature, and volume. The Peng-Robinson equation of state was inadvertently used instead of the more precise equation of state obtained from BP Amoco.

Hall's raw data were used to recalculate the adsorption on Fruitland coal and estimate the uncertainty for each datum.

Calculation Details

The adsorbed material is considered to reside in the slit from $3/8\sigma_{ff}$ to $L-3/8\sigma_{ff}$. The pore volume thus is presumed to be $A(L)/2$. Within these constraints, two independent scenarios (within the case study of Fruitland coal) were explored.

Scenario 1: For the first case, the pure-component isotherms of methane, nitrogen, and carbon dioxide are regressed. From the pure-component regressions, the binary mixture component adsorption was predicted.

Scenario 2: The pure-component isotherms of methane, nitrogen, and carbon dioxide and their binary mixtures simultaneously are regressed using three binary interaction parameters.

Results and Discussion

Figures 5-20 through 5-25 depict the model results for both Scenario 1 and 2 for all the experimental data. Table 5-7 presents the regression results and Table 5-8 lists the model parameters. As shown in Table 5-8, the SLD can predict the component adsorption within the experimental uncertainties on average for the three binary gas mixtures, although some specific isotherms are outside their experimental uncertainties. For example, the amount of nitrogen adsorbed in a methane/nitrogen mixture (Figure 5-21), or the nitrogen adsorbed in a nitrogen/CO₂ mixture (Figure 5-24) is under-predicted, especially for mixtures that are more dilute in nitrogen, where the predictions are generally outside the experimental uncertainties.

As shown in Table 5-7, the WAAD for each component in the three binary mixtures shown are much better than the WAAD of the predictive model. Comparing the regression of binary gas mixtures with BIPs to the predictions based solely on pure-gas isotherms, the percentage improvement of the WAAD for the lesser-adsorbed component is better than the WAAD for the more-adsorbed component.

On the basis that the WAAD is less than unity for the predicted adsorption of each component in a binary mixture (Table 5-7), the use of BIPs to regress binary mixture adsorption is not readily justified – to do so would be an over-fit (unless the experimental uncertainties are smaller than the used values). Nevertheless, the use of BIPs allows for correlation of the lesser-adsorbed component in dilute mixtures within the experimental uncertainties, and, in this context, the BIPs are justified.

As shown in Table 5-8, both the surface area, A , and the pore volume, $A(L)/2$, are higher for Scenario 2 than for Scenario 1; that each scenario calculates near-identical isotherms with different surfaces areas or pore volumes is possible because for each gas, the parameter Λ_b is higher for Scenario 2 than for Scenario 1. Higher values of Λ_b correspond to lower values of the adsorbed-phase density, which is offset by the higher pore volume for Scenario 2. That Scenario 2 has a better statistical fit of the experimental data can be construed as supporting evidence that values for the pore volume and the adsorbed-phase densities are closer to physical reality than for Scenario 1.

After analyzing the same Fruitland coal experimental data, Hall (1993) recommended that, in order to reduce overall experimental uncertainty, that one should “obtain better estimates of the adsorbed-phase volume”. By “adsorbed-phase volume”, Hall’s terminology meant the *specific volume of the adsorbed phase*, or, as addressed in

this work, the *adsorbed-phase density*. The adsorbed-phase density was used to calculate the absolute adsorption from the excess adsorption for both pure gases and binary mixtures. Various adsorption models (such as the extended Langmuir) were fitted to the calculated absolute adsorption. The calculated absolute adsorption was sensitive, especially at higher pressures, to the values used for the adsorbed-phase density. (Small changes in the value of the adsorbed-phase density can translate to large changes in the calculated absolute adsorption). For this work, the problem is circumvented with the SLD model by simply calculating the excess adsorption rather than the absolute adsorption. Thus, better estimates of the adsorbed-phase density are only needed for predicting or correlating the experimental *excess* adsorption within the context of a model, or for better understanding of the adsorption phenomena.

For binary mixtures, Hall (1993) and others (Sudibandriyo et al., 2003) used the following formula to calculate the adsorbed-phase density by setting the excess volume term to zero:

$$\frac{1}{\bar{\rho}_{\text{ads}}} = \frac{X_1^{\text{Abs}}}{\bar{\rho}_{\text{ads},1}} + \frac{X_2^{\text{Abs}}}{\bar{\rho}_{\text{ads},2}} + v^{\text{Ex}} \quad (5-11)$$

This is the same formula presented in Chapter 2 as Equation (2-26). The accuracy of the mixture adsorbed-phase density is predicated on estimates for the two pure components densities, and whether the excess volume term is actually zero. In this work, we do not use Equation (5-11) for data reduction because the SLD model calculates the excess adsorption rather than the absolute adsorption. However, Equation (5-11) can be used to evaluate the absolute mole fractions and the excess volume, as done previously in Figures 5-11 through 5-13 for activated carbon.

Table 5-7. Comparison of Regression Results for Two Scenarios for the Pure and Binary Mixture Adsorption on Fruitland Coal at 115°F

| | Weighted Average Absolute Deviation, WAAD | | | |
|--------------------------------|--|-----------------------|-------------------|-----------------------|
| Pure Gases | <i>Scenario 1</i> | | <i>Scenario 2</i> | |
| Methane | 0.25 | | 0.28 | |
| Nitrogen | 0.37 | | 0.30 | |
| CO ₂ | 0.80 | | 0.78 | |
| <hr/> | | | | |
| Feed Mixture | <i>Scenario 1</i> | | <i>Scenario 2</i> | |
| Methane/Nitrogen | <i>methane</i> | <i>nitrogen</i> | <i>methane</i> | <i>nitrogen</i> |
| 20/80 | 0.54 | 0.16 | 0.18 | 0.18 |
| 40/60 | 0.12 | 0.35 | 0.10 | 0.62 |
| 60/40 | 0.28 | 1.8 | 0.21 | 0.36 |
| 80/20 | 0.41 | 1.6 | 0.21 | 0.30 |
| All Feeds | 0.33 | 0.97 | 0.17 | 0.37 |
| <hr/> | | | | |
| Methane/CO₂ | <i>methane</i> | <i>CO₂</i> | <i>methane</i> | <i>CO₂</i> |
| 20/80 | 0.86 | 0.87 | 0.20 | 0.80 |
| 40/60 | 0.93 | 0.53 | 0.27 | 0.45 |
| 60/40 | 0.27 | 0.54 | 0.25 | 0.34 |
| 80/20 | 0.31 | 0.75 | 0.56 | 0.33 |
| All Feeds | 0.59 | 0.67 | 0.32 | 0.48 |
| <hr/> | | | | |
| Nitrogen/CO₂ | <i>nitrogen</i> | <i>CO₂</i> | <i>nitrogen</i> | <i>CO₂</i> |
| 20/80 | 0.58 | 0.51 | 0.38 | 0.54 |
| 40/60 | 0.81 | 0.73 | 0.21 | 0.50 |
| 60/40 | 0.87 | 0.72 | 0.43 | 0.40 |
| 70/30 | 1.2 | 0.58 | 0.30 | 0.31 |
| 80/20 | 0.92 | 0.58 | 0.37 | 0.24 |
| All Feeds | 0.87 | 0.62 | 0.34 | 0.40 |

Table 5-8. Regressed Parameters for SLD-PR Model on Fruitland Coal at 115°F

| | Scenario 1 | | | Scenario 2 | | |
|--|----------------|-----------------|-----------------------|----------------|-----------------|-----------------------|
| Surface Area (m ² /g) | 63.4 | | | 73.3 | | |
| Slit Length (nm) | 1.02 | | | 1.16 | | |
| | <i>methane</i> | <i>nitrogen</i> | <i>CO₂</i> | <i>methane</i> | <i>nitrogen</i> | <i>CO₂</i> |
| ϵ_{is}/k (K) | 56.1 | 31.7 | 58.4 | 56.7 | 29.3 | 64.5 |
| Λ_b | -0.23 | 0.00 | -0.32 | -0.07 | 0.18 | -0.16 |
| Binary Interaction, C_{ij} | | | | | | |
| Methane-Nitrogen | None | | | -0.54 | | |
| Methane-CO ₂ | None | | | -0.07 | | |
| Nitrogen-CO ₂ | None | | | -0.50 | | |

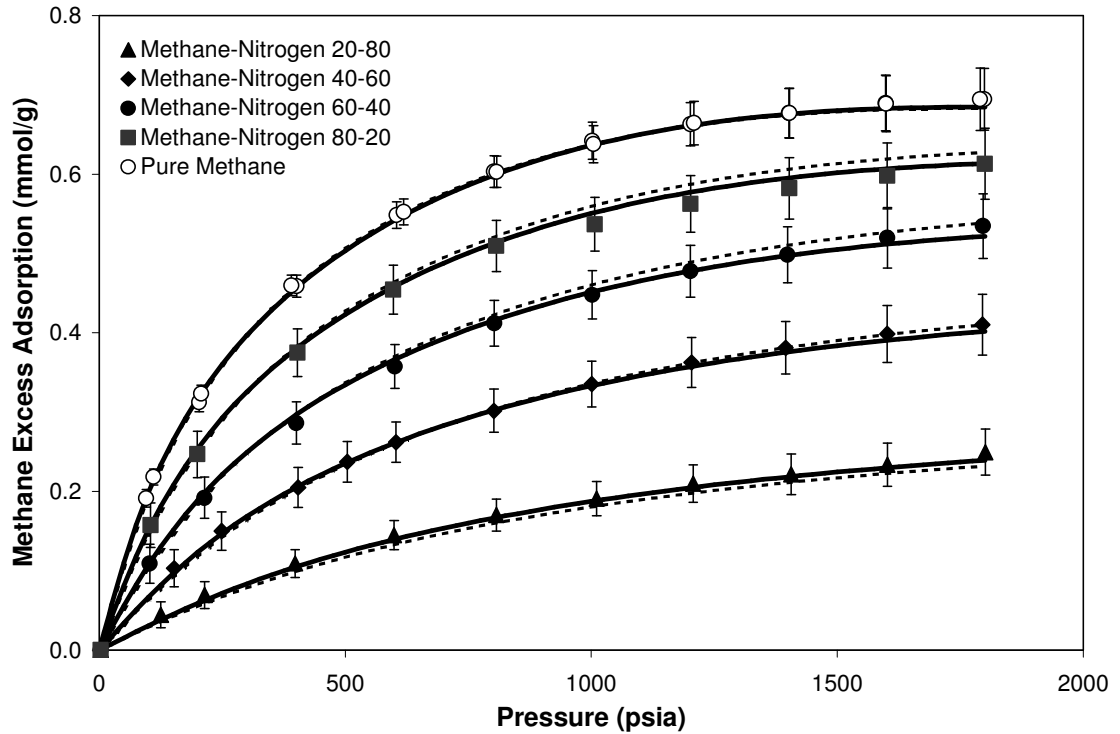


Figure 5-20. SLD Model of Methane Adsorption in Methane/Nitrogen Mixtures on Wet Fruitland Coal at 115°F (Solid Line – Regressed C_{ij} , Dashed Line – $C_{ij}=0.0$)

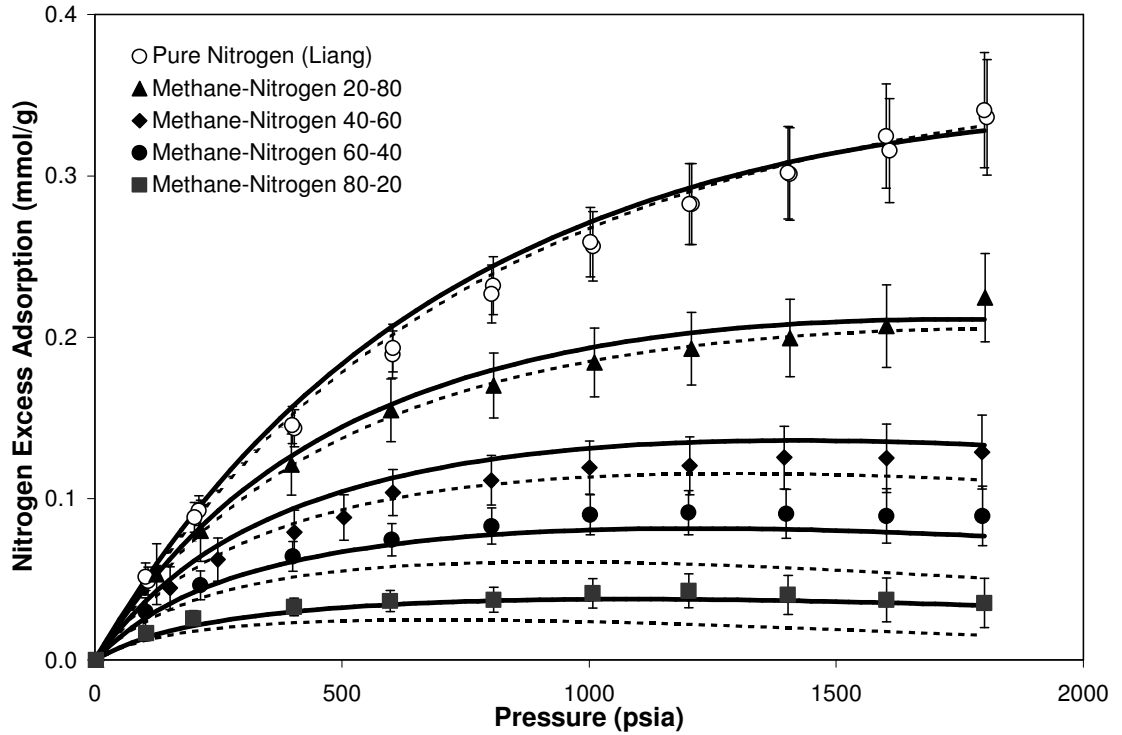


Figure 5-21. SLD Model of Nitrogen Adsorption in Methane/Nitrogen Mixtures on Wet Fruitland Coal at 115°F – (Hall Data Unless Noted)

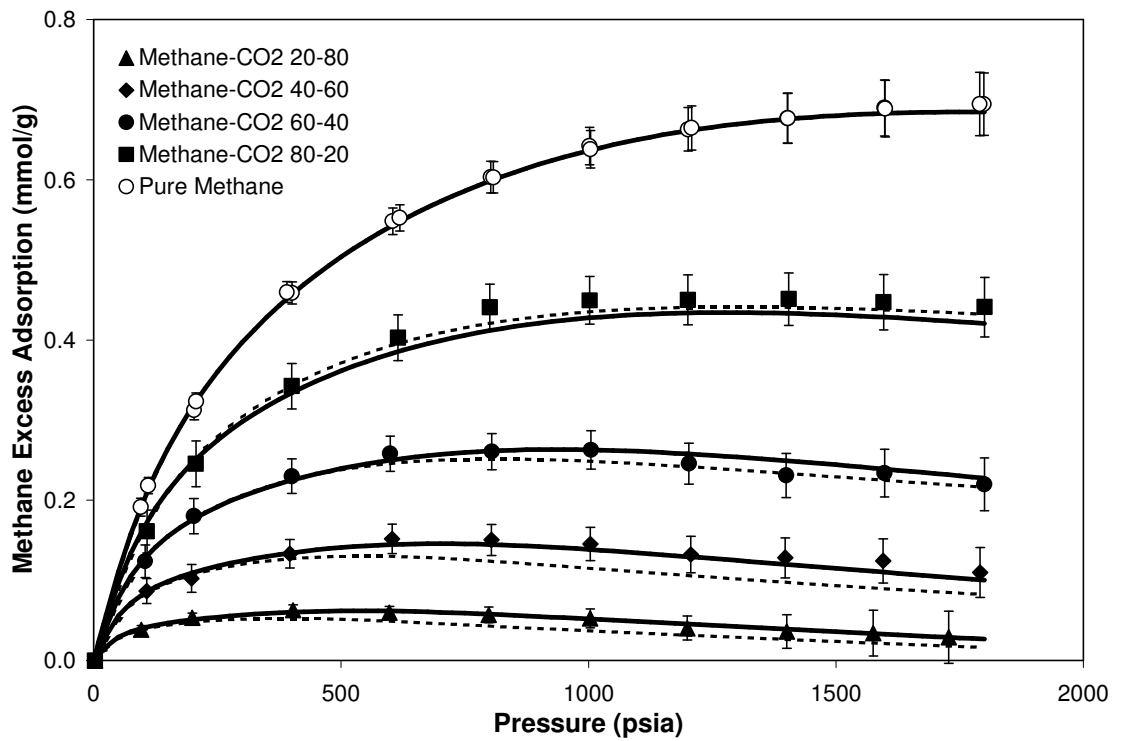


Figure 5-22. SLD Model of Methane Adsorption in Methane/CO₂ Mixtures on Wet Fruitland Coal at 115°F

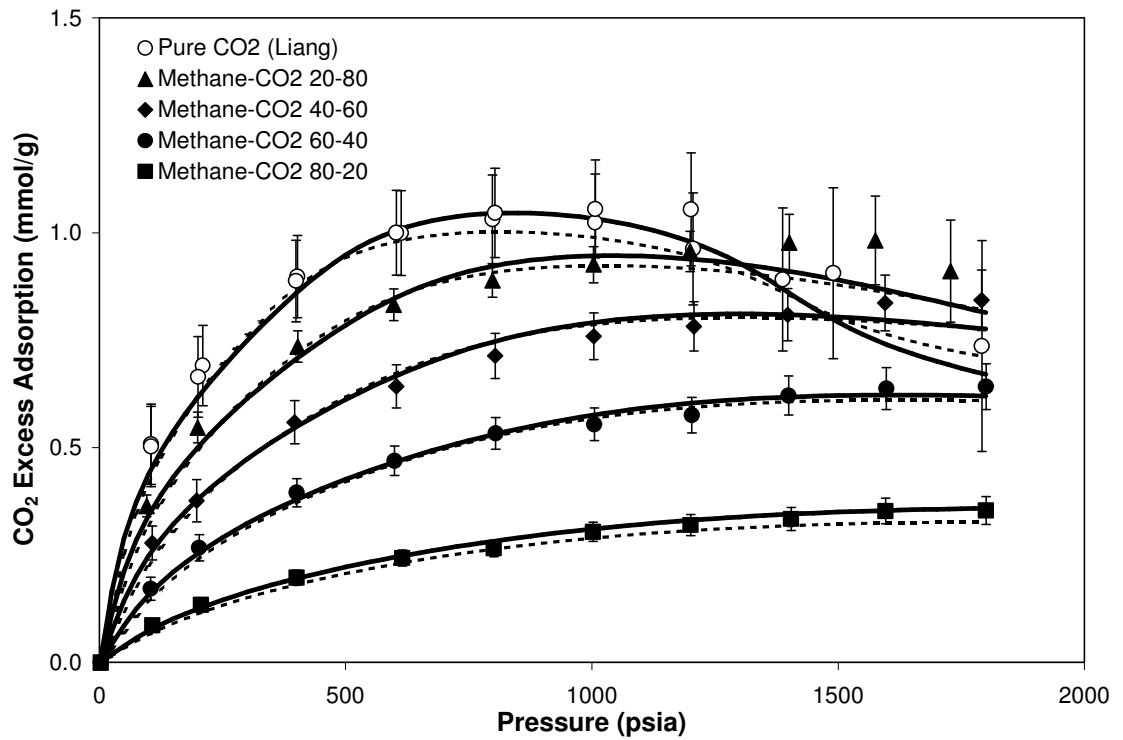


Figure 5-23. SLD Model of CO₂ Adsorption in Methane/CO₂ Mixtures on Wet Fruitland Coal at 115°F

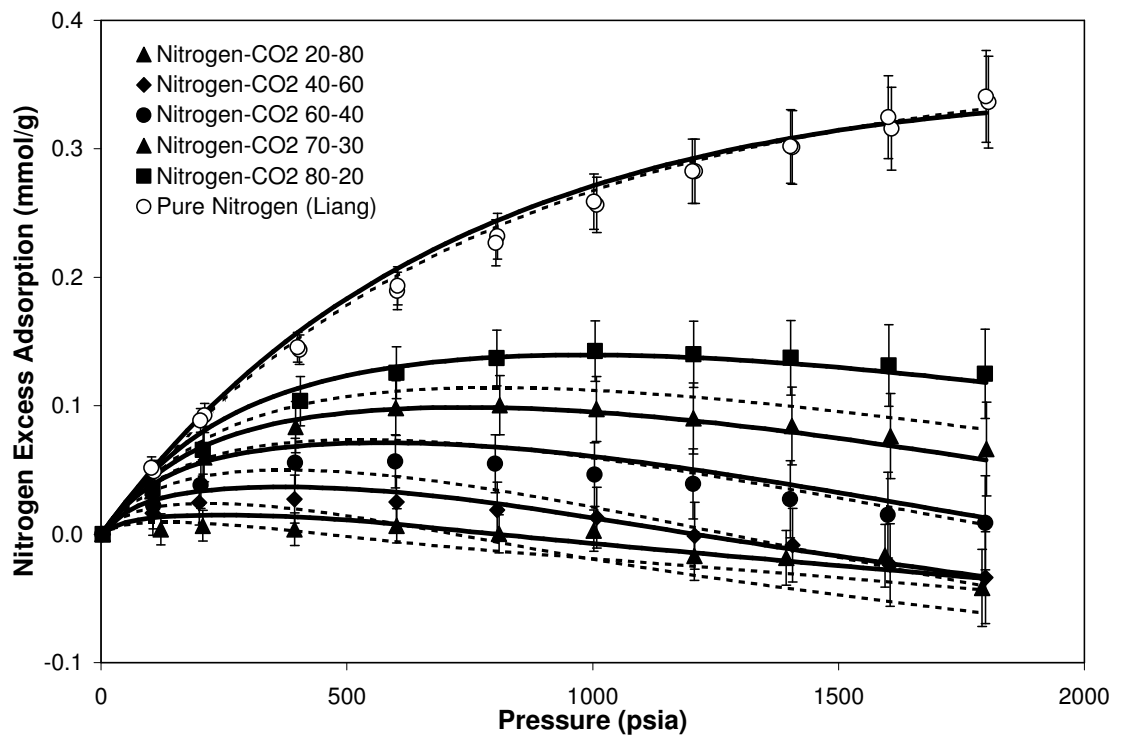


Figure 5-24. SLD Model of Nitrogen Adsorption in Nitrogen/CO₂ Mixtures on Wet Fruitland Coal at 115°F

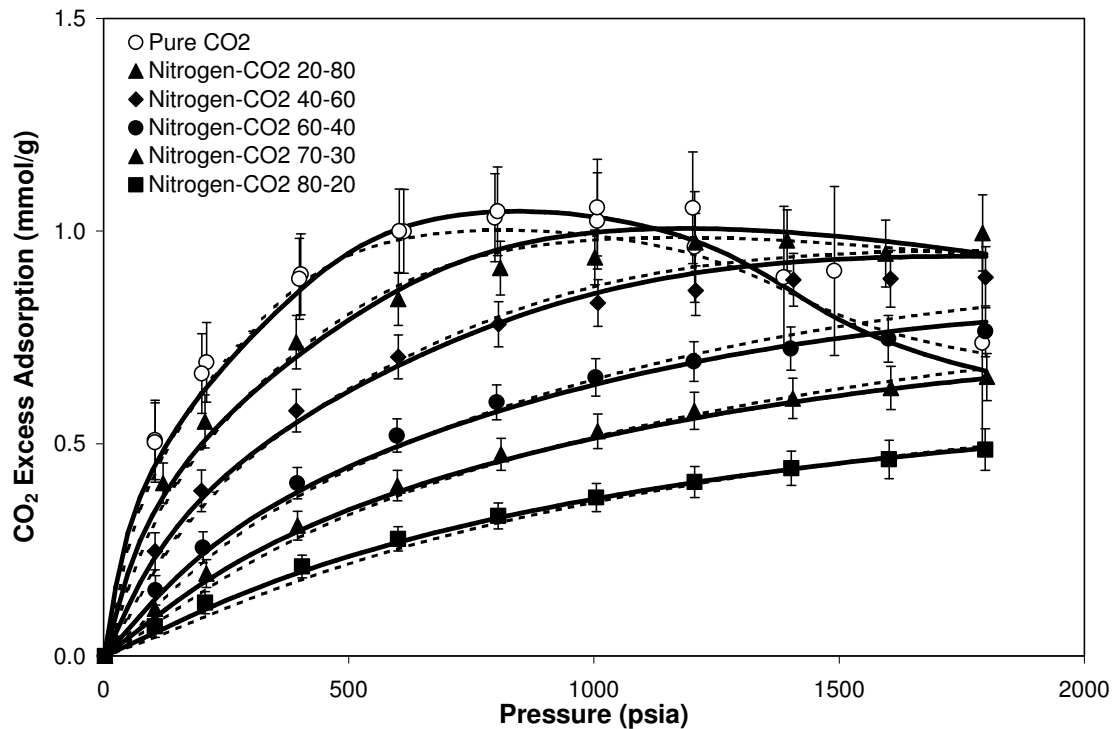


Figure 5-25. SLD Model of CO₂ Adsorption in Nitrogen/CO₂ Mixtures on Wet Fruitland Coal at 115°F

Conclusions for Case Study 5

Major conclusions of this study are:

- For adsorption on wet Fruitland coal, the SLD can predict the component adsorption within the experimental uncertainties on average for the three binary gas mixtures, although some specific isotherms are outside their experimental uncertainties.
- The SLD-PR model *correlates* the binary mixture adsorption behavior of the systems considered well within one standard deviation of experimental error. The one-fluid mixing rules are suitable for the task of correlation; however, they require large corrections for some binary interactions.

- The use of BIPs allows for correlation of the lesser-adsorbed component in dilute mixtures within the experimental uncertainties.
- For the two modeling scenarios conducted, the regressed parameters - such as the surface area, pore volume, and Λ_b - were significantly different even though both modeling scenarios represented the experimental data within the experimental uncertainties, on average.
- Predicting the excess adsorption directly from models is preferred over the standard method of using a model to predict the calculated absolute adsorption, which is obtained from a data reduction procedure.

CASE STUDY 6: MIXTURE ADSORPTION ON WET ILLINOIS #6 COAL

The adsorption measurements on wet Illinois #6 were performed by Liang (1999). These measurements indicate that both methane and nitrogen adsorption on wet Illinois #6 are about half that adsorbed on wet Fruitland coal at the same conditions. Although the adsorption measurements for Tiffany are performed at a slightly higher temperature (131°F) than Illinois #6 (115°F), both methane and nitrogen adsorption amounts are comparable for the two coals (within 15%).

Replicate runs were conducted for each gas to confirm the precision of the measurements and to investigate the effect of variations in moisture content and coal sample preparation on the adsorption behavior. The Illinois #6 data were acquired using two coal samples of different moisture content. Both measurement sets indicate that water content values above the equilibrium water content do not significantly affect the adsorption behavior.

Details on intra-laboratory reproducibility for wet Illinois #6 coal can be found elsewhere (Fitzgerald et al., 2003); for dry Illinois #6 coal, inter-laboratory reproducibility has also been investigated (Goodman et al., 2004).

Calculation Details

The adsorbed material is considered to reside in the slit from $3/8\sigma_{ff}$ to $L-3/8\sigma_{ff}$. The pore volume thus is presumed to be $A(L)/2$. Within these constraints, two independent scenarios (within the case study of Illinois #6 coal) were explored.

Scenario 1: For the first case, the pure-component isotherms of methane, nitrogen, and carbon dioxide are regressed. From the pure-component regressions, the binary mixture component adsorption was predicted.

Scenario 2: The pure-component isotherms of methane, nitrogen, and carbon dioxide and their binary mixtures simultaneously are regressed using three binary interaction parameters, one for each gas pair.

Results and Discussion

Figures 5-26 through 5-31 depict the model results for both Scenario 1 and 2 for all the experimental data. Table 5-9 shows the regression results and Table 5-10 shows the model parameters. As shown in Table 5-9, the SLD can predict the component adsorption well within the experimental uncertainties on average for the three binary gas mixtures. Such predictions suggest that the expected experimental uncertainties may be smaller than those used. With use of BIPs, the SLD model improved the overall WAAD mainly through improvements for adsorption in methane/nitrogen mixtures, although

such improvements are probably unwarranted upon consideration that the predictions were already well within experimental uncertainties.

In Figure 5-31, the nitrogen adsorption in the nitrogen/CO₂ mixture isotherms shows behavior that is aberrant to the adsorption behavior typified by Calgon F-400 activated carbon and Fruitland coal in Figures 5-6 and 5-24, respectively. Specifically, the nitrogen adsorption for all feed mixtures rises with pressure at high pressures after having reached a maximum with pressure at a lower pressure. The SLD model does not predict such behavior but, because of the large experimental uncertainties for these isotherms, the SLD model will predict within the uncertainties on average for each isotherm. This and the discontinuous nature of some of these isotherms suggest that the observed aberrant behavior of the nitrogen adsorption in nitrogen/CO₂ mixtures may be an experimental artifact.

As shown in Table 5-9, both the surface area, A , and the pore volume, $A(L)/2$, are about the same for Scenario 2 and Scenario 1. The parameters ϵ_{fs} and Λ_b are slightly different for each scenario. The BIPs regressed for Illinois #6 are large compared to the respective VLE BIPs, although they are comparable in magnitude to the BIPs regressed for Fruitland coal, as shown in Table 5-8.

Table 5-9. Comparison of Regression Results for Two Scenarios for the Pure and Binary Mixture Adsorption on Illinois #6 at 115°F

| | Weighted Average Absolute Deviation, WAAD | | | |
|--------------------------------|--|-----------------------|-------------------|-----------------------|
| Pure Gases | <i>Scenario 1</i> | | <i>Scenario 2</i> | |
| Methane | 0.38 | | 0.45 | |
| Nitrogen | 0.17 | | 0.27 | |
| CO ₂ | 0.63 | | 0.76 | |
| <hr/> | | | | |
| Feed Mixture | <i>Scenario 1</i> | | <i>Scenario 2</i> | |
| Methane/Nitrogen | <i>methane</i> | <i>nitrogen</i> | <i>methane</i> | <i>nitrogen</i> |
| 20/80 | 0.48 | 0.35 | 0.12 | 0.27 |
| 40/60 | 0.64 | 0.38 | 0.22 | 0.16 |
| 60/40 | 0.48 | 0.48 | 0.22 | 0.21 |
| 80/20 | 0.39 | 0.40 | 0.25 | 0.40 |
| All Feeds | 0.50 | 0.40 | 0.20 | 0.26 |
| <hr/> | | | | |
| Methane/CO₂ | <i>methane</i> | <i>CO₂</i> | <i>methane</i> | <i>CO₂</i> |
| 23/77 | 0.42 | 0.67 | 0.31 | 0.49 |
| 40/60 | 0.66 | 0.60 | 0.54 | 0.48 |
| 60/40 | 0.88 | 0.64 | 0.77 | 0.57 |
| 77/23 | 0.63 | 0.50 | 0.43 | 0.65 |
| All Feeds | 0.65 | 0.60 | 0.51 | 0.55 |
| <hr/> | | | | |
| Nitrogen/CO₂ | <i>nitrogen</i> | <i>CO₂</i> | <i>nitrogen</i> | <i>CO₂</i> |
| 20/80 | 0.85 | 0.56 | 0.82 | 0.21 |
| 42/58 | 0.93 | 0.41 | 0.96 | 0.34 |
| 60/40 | 0.89 | 0.40 | 0.79 | 0.41 |
| 82/18 | 0.84 | 0.41 | 0.75 | 0.39 |
| All Feeds | 0.88 | 0.45 | 0.83 | 0.34 |

Table 5-10. Regressed Parameters for SLD-PR Model on Illinois #6 Coal at 115°F

| | Scenario 1 | | | Scenario 2 | | |
|--|----------------|-----------------|-----------------------|----------------|-----------------|-----------------------|
| Surface Area (m ² /g) | 56.3 | | | 54.7 | | |
| Slit Length (nm) | 1.35 | | | 1.33 | | |
| | <i>methane</i> | <i>nitrogen</i> | <i>CO₂</i> | <i>methane</i> | <i>nitrogen</i> | <i>CO₂</i> |
| ϵ_{is}/k (K) | 44.4 | 19.5 | 63.6 | 43.2 | 20.2 | 65.5 |
| Λ_b | 0.08 | 0.17 | -0.06 | 0.04 | 0.27 | -0.05 |
| Binary Interaction, C_{ij} | | | | | | |
| Methane-Nitrogen | None | | | 0.59 | | |
| Methane-CO ₂ | None | | | -0.07 | | |
| Nitrogen-CO ₂ | None | | | -0.51 | | |

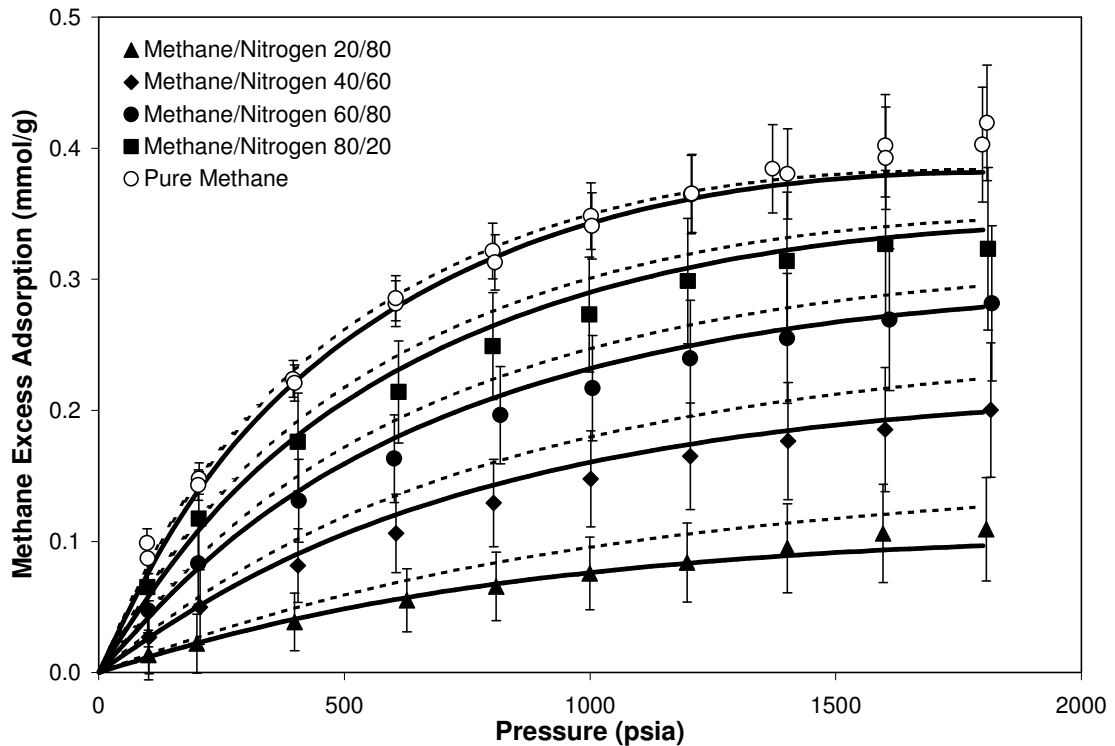


Figure 5-26. SLD Model of Methane Adsorption in Methane/Nitrogen Mixtures on Wet Illinois #6 Coal at 115°F (Solid Line – Regressed C_{ij} , Dashed Line – $C_{ij}=0.0$)

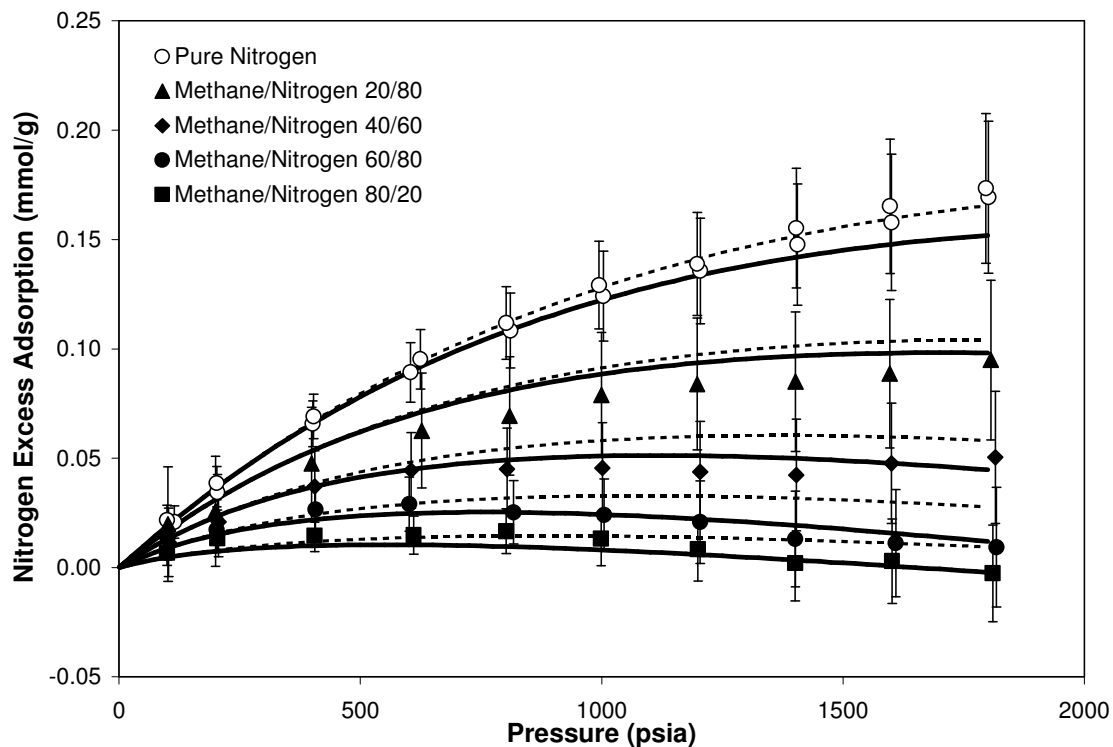


Figure 5-27. SLD Model of Nitrogen Adsorption in Methane/Nitrogen Mixtures on Wet Illinois #6 Coal at 115°F

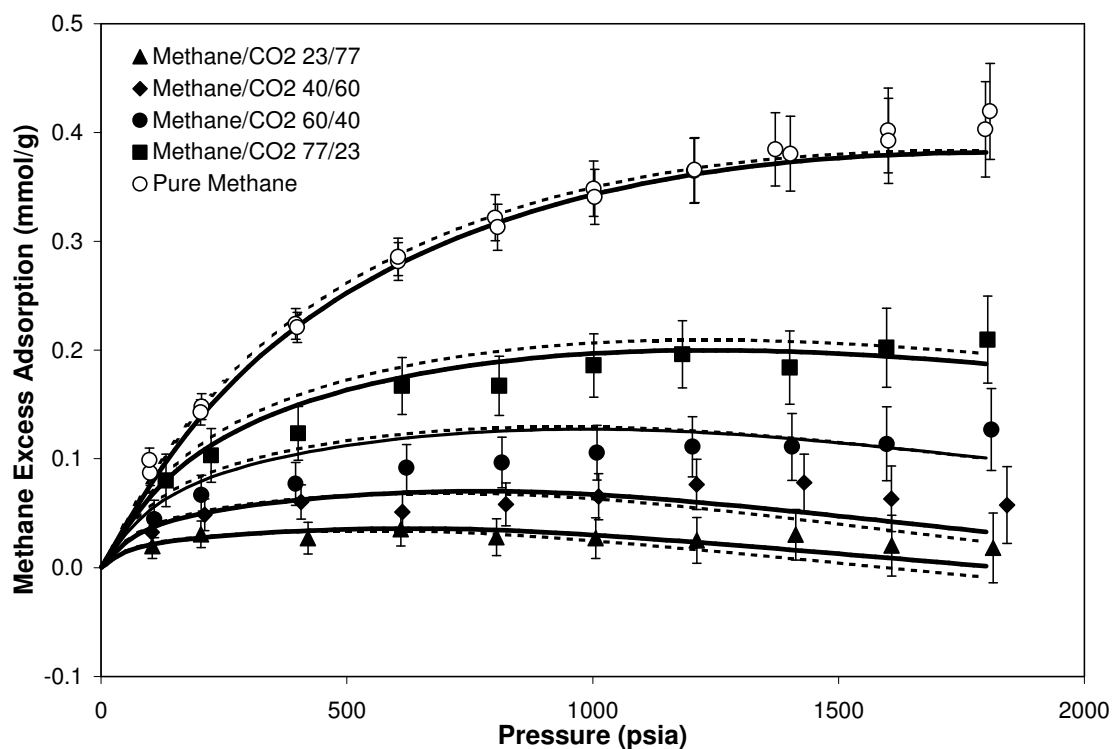


Figure 5-28. SLD Model of Methane Adsorption in Methane/CO₂ Mixtures on Wet Illinois #6 Coal at 115°F

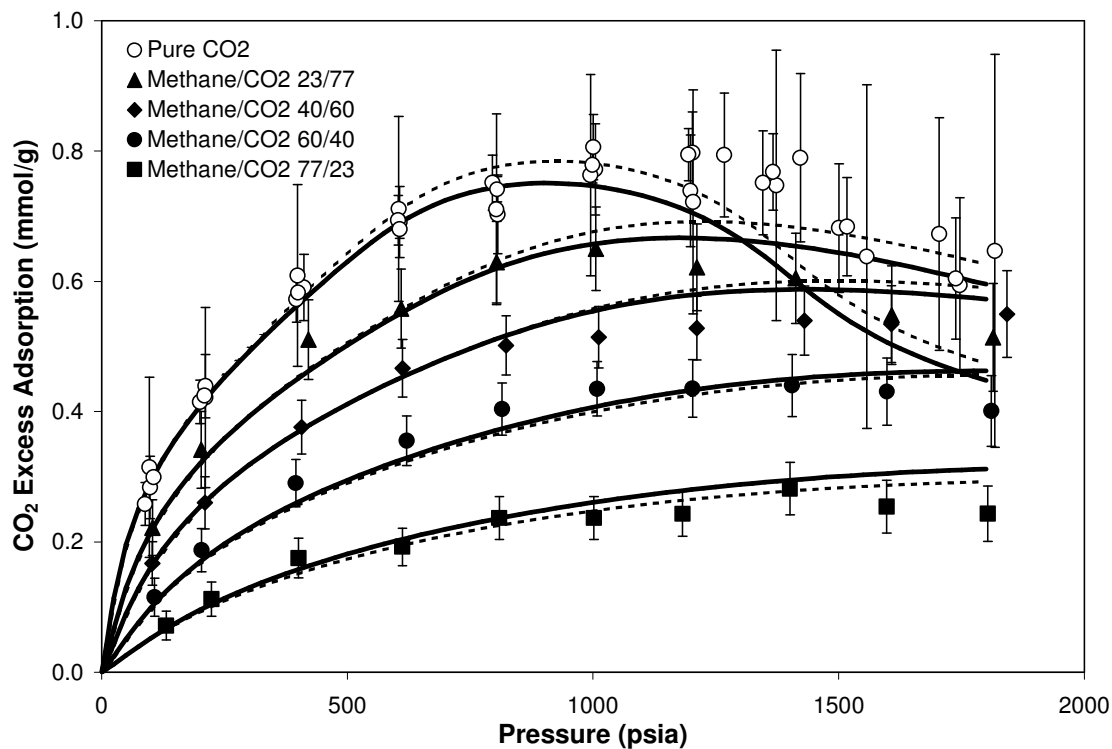


Figure 5-29. SLD Model of CO₂ Adsorption in Methane/CO₂ Mixtures on Wet Illinois #6 Coal at 115°F

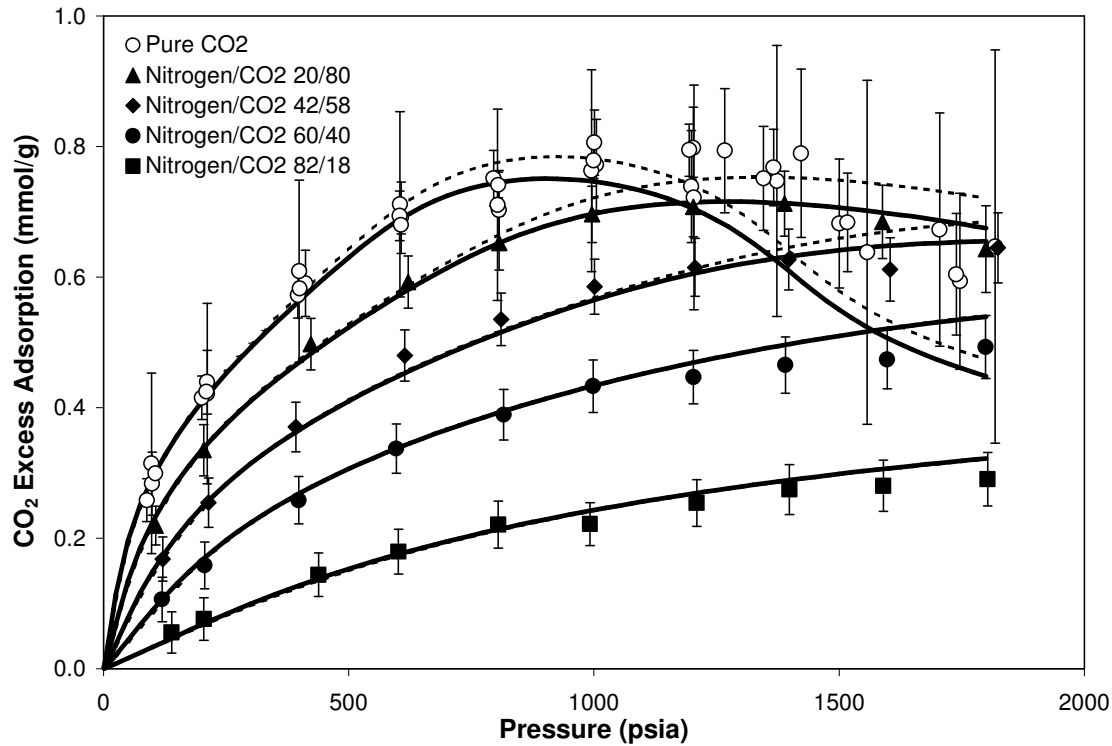


Figure 5-30. SLD Model of CO₂ Adsorption in Nitrogen/CO₂ Mixtures on Wet Illinois #6 Coal at 115°F

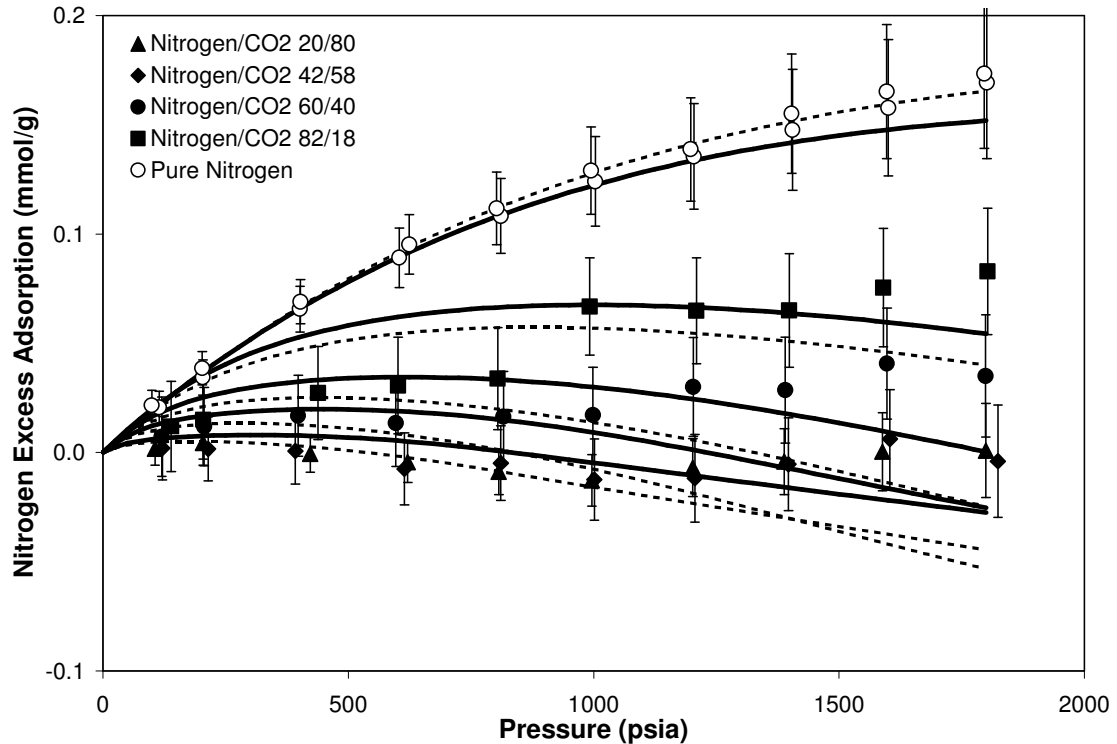


Figure 5-31. SLD Model of Nitrogen Adsorption in Nitrogen/CO₂ Mixtures on Wet Illinois #6 Coal at 115°F

Conclusions for Case Study 6

Major conclusions of this study are:

- For adsorption on wet Illinois #6, the SLD can predict the component adsorption within the experimental uncertainties on average for the three binary gas mixtures.
- Using BIPs, the SLD model improved the overall WAAD mainly through improvements for adsorption in methane/nitrogen mixtures, although such improvements are probably unwarranted since the predictions were already well within experimental uncertainties.
- The nitrogen adsorption in the nitrogen/CO₂ mixture isotherms shows behavior that is aberrant to the adsorption behavior typified by Calgon F-400

activated carbon and Fruitland coal. The SLD model does not predict such behavior but, because of the large experimental uncertainties for these isotherms, the SLD model will predict within the uncertainties on average for each isotherm.

COMPARISON OF SLD-PR MODEL TO THE ONO-KONDO MODEL

Recently, Sudibandriyo (2003) and Pan (2003), respectively, performed an extensive study on the predictive and correlative capability of the Ono-Kondo (OK) Lattice Model and the two-dimensional equation of state (2D EOS). A comparison is sought between the relative predictive abilities of these models with the SLD-PR model. The methodology employed by Pan (2003), however, precludes a fair comparison between the SLD-PR and the 2D EOS model. Pan (2003) uses a data reduction procedure that converts the experimental excess adsorption to absolute adsorption, then he models the absolute adsorption. In this study, however, the excess adsorption is modeled directly. Therefore, the SLD-PR model is compared only to the OK model, where the data reduction and modeling methodologies are comparable.

As mentioned previously, the experimental data set on dry Calgon carbon (Sudibandriyo et al., 2003) is the most extensive and reliable measurements for high-pressure mixture gas adsorption (as ascertained by expected experimental uncertainties). Therefore, comparing the predictive ability of the two models probably is accomplished best by examining the modeling results for the activated carbon system.

To perform mixture predictions, the SLD-PR model requires $(2N+2)$ regressed parameters to model a set of pure-gas isotherms, whereas the OK model requires either

(4N) parameters or (2N+2) parameters, depending on the modeling case studies as discussed by Sudibandriyo (2003). Thus, for the three gases considered in this comparison, the SLD-PR model requires 8 parameters and the OK requires 8 or 12 parameters, depending on the modeling case. The 8-parameter OK model is compared to the SLD model for the sake of parity in the number of model parameters

The model predictions of the SLD-PR model (corresponding to Scenario 3 under Case 2 in this chapter) and the Ono-Kondo model are presented in Table 5-11. For both models, the mixed-gas adsorption is predicted using parameters based solely on pure isotherm data regressions. The pure-gas adsorption results are presented only for the SLD-PR model. For each gas component listed in a binary mixture, the results presented pertain to all gas compositions. The results presented for the ternary mixture are for the 10/40/50 methane/nitrogen/CO₂ isotherm.

The 8-parameter OK model performs better than the SLD-PR model for 6 out of the 9 predictions for mixtures. The ability to predict the adsorption of methane-CO₂ mixtures is the largest discrepancy between the OK and SLD-PR models, where the OK model clearly outperforms the SLD-PR model. The 8-parameter OK has better predictive capabilities for the nitrogen adsorbed in the nitrogen-CO₂ mixtures and the nitrogen in the ternary mixture, but both the OK and SLD-PR have errors greater than twice the experimental uncertainties. Both models tend to predict worse for the lesser-adsorbed component adsorption in binary mixtures.

Table 5-11. Comparison of the SLD-PR and Ono-Kondo Model Predictions of Mixed-Gas Adsorption on Activated Carbon

| | Ono-Kondo WAAD | SLD-PR WAAD |
|--|---------------------------|------------------------|
| Pure Gases | | |
| Methane | Not Given | 0.6 |
| Nitrogen | Not Given | 1.0 |
| CO ₂ | Not Given | 0.9 |
| Mixtures | | |
| Methane-Nitrogen | | |
| Methane | 1.2 | 1.4 |
| Nitrogen | 1.5 | 1.0 |
| Methane-CO₂ | | |
| Methane | 1.9 | 3.6 |
| CO ₂ | 0.8 | 2.4 |
| Nitrogen-CO₂ | | |
| Nitrogen | 2.6 | 2.3 |
| CO ₂ | 1.0 | 1.9 |
| Methane-Nitrogen-CO₂ | | |
| Methane | 0.9 | 0.6 |
| Nitrogen | 2.3 | 2.9 |
| CO ₂ | 0.5 | 0.6 |

Sudibandriyo (2003) also explored for the ability of the OK model to represent the adsorption data on activated carbon with an extra interaction parameter per binary gas system. (This is similar to Scenario 2 under Case 2 in this Chapter.) Results show that the representative ability is virtually the same between the OK and SLD-PR model. The WAAD is within 0.1 for each gas in every gas mixture except for nitrogen in the nitrogen-CO₂ mixtures, where the OK and SLD-PR have respective WAADs of 1.4 and 0.8.

The ability of the OK model to predict the ternary gas adsorption (using one interaction parameter per gas mixture) from the correlated binaries is worse than the SLD-PR model, although both models have excellent predictive capability that is, on average for all three gases, far better than the expected experimental uncertainties. For

methane, nitrogen, and CO₂, the WAAD is, respectively, 0.2, 0.4, and 1.2 for the OK model and 0.1, 0.4 and 0.2 for the SLD-PR model.

In summary, both models have similar quantitative results for the predictive and correlative behavior of mixed-gas adsorption on activated carbon. One model may outperform another for a specific isotherm, but overall, neither model clearly has a consistent predictive or correlative advantage over the other. Similar comparative analyses of the mixed-gas predictions on Fruitland, Tiffany, and Illinois #6 reach the same conclusion.

CHAPTER 6
FLUID HARD-SPHERE EQUATION OF STATE
INTRODUCTION

The original scope of this dissertation was expanded to set the stage for improved predictions of SLD adsorption modeling using a more accurate EOS. This chapter concerns the development of such an EOS for pure fluids to facilitate the accurate representation of pressure-volume-temperature (PVT) behavior for a wide range of fluid densities.

The impetus for creating this new EOS is to develop further the prediction of gas adsorption at high pressures through the SLD theory, which requires a fluid EOS. EOSs from the National Institute of Standards and Technology NIST (Linstrom and Mallard, 2003) have the most accurate predictive capability for pure-fluid density behavior; however, these equations are not partitioned into attractive and repulsive parts. Accurate representation of high-density behavior and the accurate partitioning of the EOS into “repulsive” and “attractive” molecular contributions are hypothesized to allow for the predictive capability of high-pressure adsorption.

The desired predictive abilities for adsorption include the estimation of high-pressure adsorption from low-pressure data, and the prediction of adsorption of a particular gas solely from adsorption data on another gas. Such abilities are hypothesized

to be necessary prerequisites based on the physical-chemical characterization of coal (for prediction of gas adsorption data).

The purpose is to develop an EOS that yields better representation of PVT behavior than any generalized cubic EOS, such as the Peng-Robinson (PR) or Redlich-Kwong (RK) (3-5% AAD for optimized pure-fluid saturation properties and 3-10% AAD for single-phase density predictions). However, it will not have the complete descriptive accuracy (AAD less than 0.2% for pure-fluid saturation properties) of a highly-parameterized EOS, such as a 33-parameter modified Benedict-Webb-Rubin (mBWR) EOS. Highly-parameterized models generally do not include a reference fluid (such as a hard-sphere fluid) for property predictions that can be utilized in the SLD theory for adsorption predictions. Although such a reference fluid can be added to a highly-parameterized EOS, the parameters needed for the reference fluid are not known.

EQUATIONS OF STATE AND SLD THEORY FOR ADSORPTION

The van der Waals (vdW) (Rangarajan et al., 1995), Peng-Robinson (PR) (Chen et al., 1997; Fitzgerald et al., 2003), Elliot-Suresh-Donohue ESD (Soule et al., 2001; Soule, 1998), and Bender EOS (Ustinov et al., 2002) have been used previously within the SLD theoretical framework for gas adsorption representation and prediction. Of these EOSs, only the Bender EOS has the capability for accurate representation of the PVT relationships near density values expected in high-pressure adsorption (density values near the reciprocal of the PR-covolume b).

In the approach of Ustinov et al. (2002), which made use of the Bender EOS, the adsorbent characterization from gas adsorption requires a distribution function that

describes how the local free energy, $\Delta\mu$, changes with differential elements of the pore volume, $dV_{\text{pore}}/d\Delta\mu$. The local free energy includes information about the fluid-solid potential and the free energy change of the adsorbed fluid relative to the gas phase, due to the effect of pore confinement. In this methodology, the attractive properties and gas-solid interactions of the adsorbed fluid, which vary locally within a pore, are not predicted theoretically from such functions as developed by Rangarajan et al. (1995) (as shown in Appendix A); rather, these properties are regressed by minimizing a distribution function of $dV_{\text{pore}}/d\Delta\mu$, which is not of known shape and is not linked directly to pore geometry. In summary, the use of the Bender EOS in the SLD by Ustinov (2002) precludes the use of theoretical functions describing fluid-fluid interactions within specified pore geometries because it does not partition itself accurately into repulsive and attractive contributions. (It is possible, however, to use Ustinov's method with the Bender EOS and specify a repulsive contribution to the EOS *ad hoc*, thereby allowing use of theoretical predictions for the pore-confined fluid-fluid interactions. This has not been attempted to date).

A partitioned EOS used in the SLD theory is hypothesized to allow for adsorbent characterization for well-structured and rigid adsorbents such as activated carbons, and to eliminate the need for some empirical adjustments, as used with the modified SLD-PR formulation in Chapters 4 and 5.

When written explicitly in pressure, vdW-type EOSs like the PR are separable into two parts commonly referred to as the “repulsive” and “attractive” pressure. The repulsive pressure of the PR-EOS has been shown to fail even for moderate densities when evaluated against molecular simulation studies. Figure 6-1 compares five repulsive

EOSs and selected simulation data (Barker and Henderson, 1971; Alder and Wainright, 1960); the van der Waals repulsive compressibility (which the PR-EOS utilizes) demonstrably fails at relatively low reduced densities. The moderate success of the PR-EOS in predicting PVT behavior lies in the fact that errors in the repulsive pressure are offset by errors in the attractive pressure. Nevertheless, density predictions for high-density fluids (reduced densities of 2+) using the PR-EOS are inadequate owing to poor representation in repulsive pressure. Accurate density prediction is needed at these high pressures in the study of adsorption.

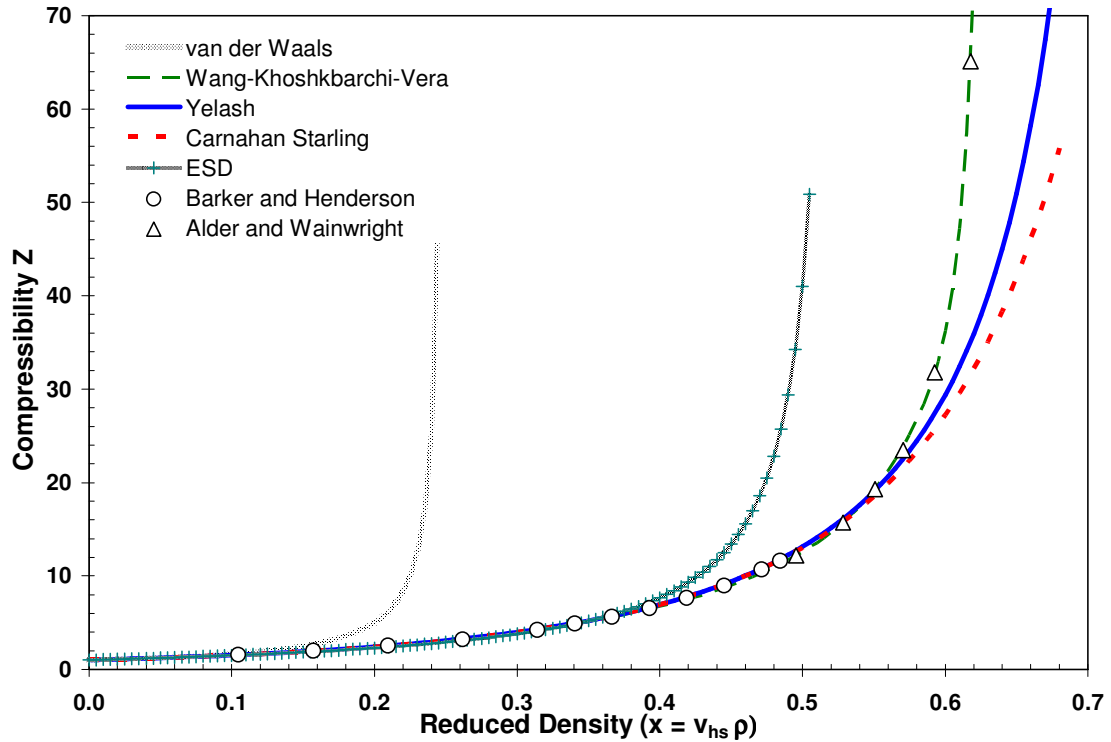


Figure 6-1. Comparison of Various Hard-Sphere Equations of State

DEVELOPMENT OF EQUATION OF STATE FOR FLUIDS

In addition to the EOS attributes that are needed to predict adsorption with SLD theory, a fluid EOS should satisfy some general considerations that are expected for

theoretical and practical reasons. For the practical ease of calculating saturated fluid properties (and for adsorption calculations), the EOS should have an explicit formula for the fugacity. As stated by Deiters and De Reuck (1999), other practical considerations include the relationship of critical properties (T_c , P_c , ρ_c) to EOS parameters through application of critical point constraint equations, the prediction of PVT behavior at single-phase and saturation conditions (some EOSs are incapable of predicting saturation properties, such as the truncated virial EOS), and the prediction of caloric data, such as specific heat capacities. Although caloric properties will not be addressed at this time, the qualitative behavior of the second virial coefficient, which must be accurate for prediction of caloric properties, is discussed in detail. Other considerations include the following limiting trends of an EOS (Gasem, 2001):

1. Ideal gas limit at low pressures; i.e., $P v = RT$ as $P \rightarrow 0$
2. Ideal gas limit at high temperatures; i.e., as $1/T \rightarrow 0$, $v/T = R / P$ along an isobar.

These ideal gas limits are satisfied by a majority of the fluid EOSs.

An important step for the development of the fluid EOS is determining the proper functional dependence of pressure on density. As stated previously, the EOS must be able to describe accurately the near-critical PVT behavior; this becomes more feasible as the polynomial order of the EOS is increased, or if exponential terms in density are included. For ease of analysis and to avoid convergence problems, the EOS was chosen to be algebraic: i.e., the pressure can be written as the quotient of two rational polynomials in density (whose coefficients have arbitrary temperature functional dependence). For representation of the critical isotherm, Peters (1991) has concluded that

EOSs that have an odd polynomial order are superior to those of even polynomial order. For example, the representation of the critical isotherm for a 6th-order EOS is only marginally better than that of a 5th-order EOS; however, the 5th-order EOS is vastly superior to the 4th-order EOS. There are diminishing returns of representation for EOSs past the 7th-order, and convergence problems arise for 9th-order EOSs (Peters, 1991). Also, a 7th-order EOS is most prudent for three-phase calculations (Sofyan, 2001). For these reasons, a 7th-order EOS will be used.

To parameterize the EOS, the critical-point constraints typically used are [see, e.g. Peters (1991)]:

$$P_c = \rho_c RT_c Z_c \quad (6-1)$$

$$\left(\frac{\partial P}{\partial \rho} \right)_{\substack{T=T_c \\ \rho=\rho_c}} = 0 \quad (6-2)$$

$$\left(\frac{\partial^2 P}{\partial \rho^2} \right)_{\substack{T=T_c \\ \rho=\rho_c}} = 0 \quad (6-3)$$

These three constraints will be applied to the overall EOS, and by doing so, three of the seven polynomial EOS constants used to describe the critical isotherm can be predicted based on experimental values of P_c , T_c and ρ_c .

These classical constraints, however, are only approximations to real fluid behavior. The critical point of a real fluid is non-analytical; that is, at the critical point, the equation is not completely differentiable (intensive properties with respect to extensive properties). For example, to represent the correct scaling law behavior of a fluid close to the critical point (and $T = T_c$), the EOS must be of the following form:

$$\frac{P}{P_c} - 1 = k \left(\frac{\rho}{\rho_c} - 1 \right)^{4.8} \quad \text{for } \rho \geq \rho_c \quad (6-4)$$

$$\frac{P}{P_c} - 1 = -k \left(1 - \frac{\rho}{\rho_c} \right)^{4.8} \quad \text{for } \rho < \rho_c \quad (6-5)$$

All analytical EOSs, such as the one in this study, have integer exponents such as 3 or 5 instead of the 4.8 as shown in Equation (6-5). Solutions for fixing an analytical EOS so that it has the proper non-analytical behavior have been devised (Span and Wagner, 1996; Fox, 1983; Chao and Prausnitz, 1989) but are not included here.

In consideration of the conclusions by Peters (1991) and in comparison with the Span and Wagner EOS for CO₂ (1996), a seventh-order polynomial EOS is required for representation of near-critical isotherms of CO₂ when applying a polynomial regression to the classical constraints at the critical point. Data from NIST reference EOSs (Setzmann and Wagner, 1991; Span et al., 2000; Span and Wagner, 1996) reveal that the critical isotherms of methane, nitrogen and CO₂, if compared in reduced pressure-density coordinates, are virtually indistinguishable for reduced pressures up to 50, or correspondingly, to reduced densities of 2.9. The quadruple moment of CO₂ has little effect on the critical isotherm pressure-density behavior. Figure 6-2 depicts how the pressure of polar fluids along the critical isotherm at a given density is generally lower than the pressures for methane, nitrogen, and CO₂ (only methane is represented for all three gases); some refrigerants, however, deviate from this behavior for some undetermined reason. All these isotherms will be represented by a 7th-order HS EOS. Bearing that constraint in mind, the next step is to choose the functional dependency of the repulsive and attractive terms.

HARD-SPHERE COMPRESSIBILITY

The hard-sphere compressibility is used as the reference fluid for the new EOS. It is based on the hard-sphere potential, $u_{hs}(r)$, which assumes that inside a sphere of diameter σ_{ff} , the potential is infinity and elsewhere it is zero:

$$\begin{aligned} u_{HS}(r) &= +\infty && \text{for } r \leq \sigma_{ff} \\ u_{HS}(r) &= 0 && \text{for } r > \sigma_{ff} \end{aligned} \quad (6-6)$$

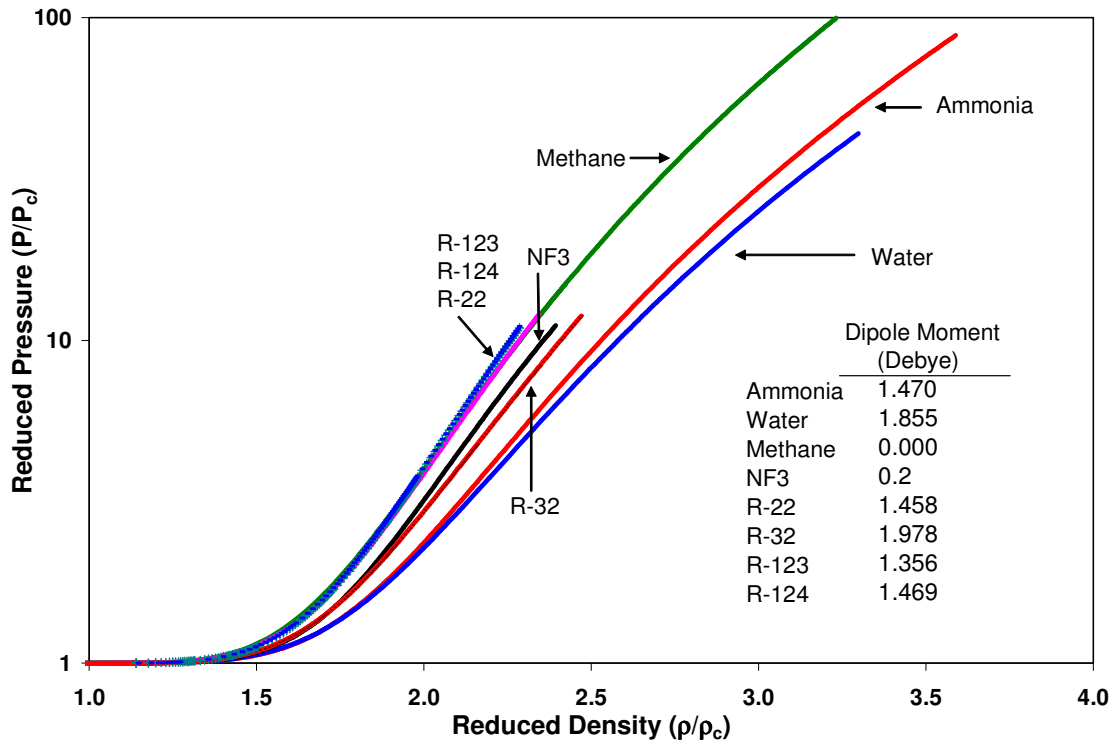


Figure 6-2. Comparison of Critical Isotherms in Reduced Coordinates

Using this potential, Monte Carlo and molecular dynamics simulations can determine the compressibility of hard spheres at various pressures. These results have been tabulated by several researchers (Barker and Henderson, 1971; Alder and Wainright, 1960; Woodcock, 1976, Wu and Sadus, 2004) and fitted to algebraic functions that best represent the simulation results. In a review of these functional forms, Mulero

and coworkers (Mulero et al., 2001) provide average absolute percent deviations (%AAD) of the hard-sphere compressibility in several density regimes against the Monte Carlo simulations. Based on its accuracy (compared to the results of Mulero), its simple form, and its polynomial order, the Yelash HS EOS will be used (Yelash and Kraska, 2001) as given here:

$$Z^{\text{rep}} = 1 + B_2 x + B_3 x^2 + B_4 x^3 + \frac{C(x/\xi)^4}{1 - x/\xi} \quad (6-7)$$

where $C = 9$ and $\xi = 0.75$. The hard sphere constants B_2 , B_3 , and B_4 are 4, 10, and 18.36, respectively. For this study, the reduced density (packing fraction) is defined as $x = v_{\text{hs}}/v$, where v_{hs} is the hard-sphere volume of the fluid.

To test the relative accuracy of the Yelash HS EOS, it was compared to other HS-EOSs. According to Mulero, three HS EOSs most accurately represent the compressibility depending on the density regimes as shown in Table 6-1. Their accuracy is characterized by the average absolute percent deviation in compressibility (%AAD_Z) from simulation data. At reduced densities of $x < 0.5$, the Yelash HS EOS has a maximum deviation of 1.0%; at higher densities, the Yelash HS EOS is less accurate compared to the Wang-Khoshkbarchi-Vera (WKV) EOS. The WKV EOS is not used in this present study despite its accuracy, because of its functional complexity.

In Figure 6-3, the Yelash HS EOS is compared with recently published values (Wu and Sadus, 2004) of the hard-sphere compressibility that include a solid-liquid phase transition. (These data, which include compressibility factors for $x > 0.62$, were published after the EOS had been developed). Also marked is the approximate location where $v_{\text{hs}}\rho_c$, $3v_{\text{hs}}\rho_c$, and $v_{\text{hs}}/b_{\text{PR}}$ lie on the reduced density curve. The Yelash EOS has the

ability to represent the hard-sphere compressibility of the fluid phase up to v_{hs}/b_{PR} . After that, it diverges at the packing fraction of 0.75 for solids (more precisely $\pi\sqrt{2}/6$), rather than at the random packing fraction of the fluid, which is approximately 0.64.

Table 6-1. Most Accurate HS EOS for Different Density Regimes and Comparison to the Yelash EOS

| Reduced Density Regime | Most Accurate EOS | %AAD _Z of EOS | %AAD _Z from Yelash EOS |
|------------------------|--------------------|--------------------------|-----------------------------------|
| $0.03 < x < 0.43$ | Kolafa | 0.01 | 0.06 |
| $0.30 < x < 0.49$ | Malihevsky-Veverka | 0.05 | 0.16 |
| $0.49 < x < 0.57$ | Malihevsky-Veverka | 0.56 | 1.8 |
| $0.46 < x < 0.62$ | WKV | 0.94 | 10.5 |

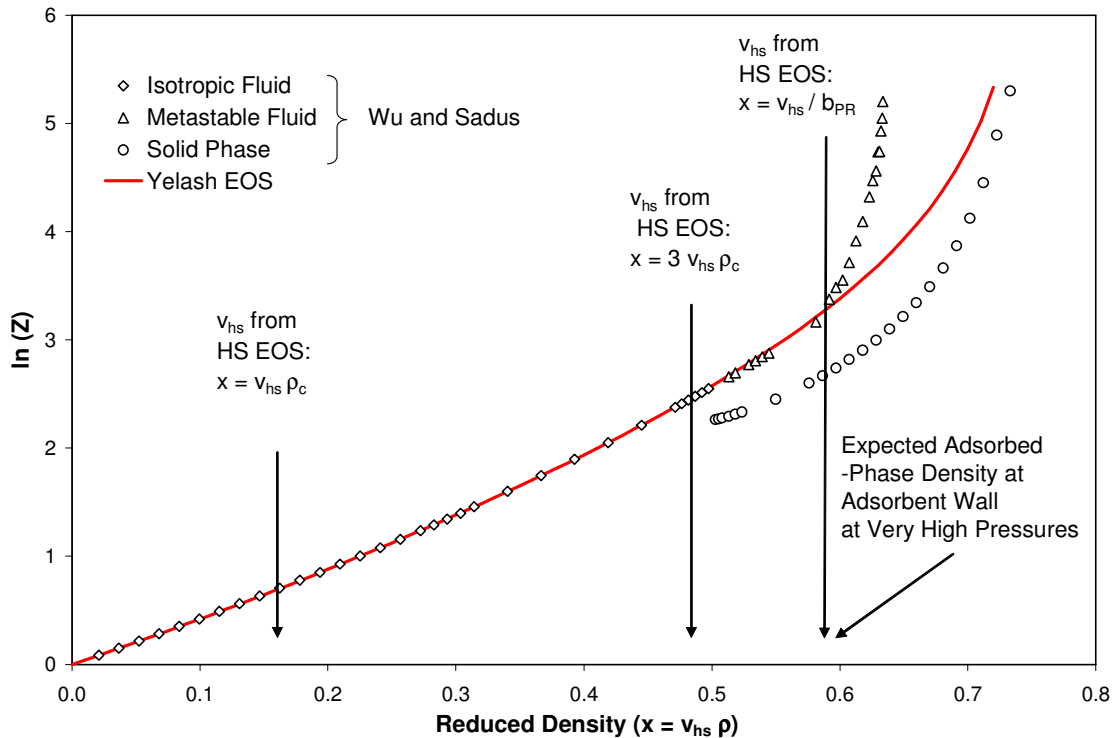


Figure 6-3. Hard-Sphere Compressibility Data at Very High Compressibilities and Comparison with the Yelash EOS

ATTRACTIVE TERMS

Attractive perturbation terms have been studied in reference to a hard-sphere EOS, most notably for the Carnahan-Starling hard-sphere EOS, Z^{CS} . In particular, the ability to represent accurately critical isotherms has been studied using several functional attractive forms in conjunction with Z^{CS} and the van der Waals compressibility (Dohrn and Prausnitz, 1990). In their study, an EOS was fitted to the critical isotherm that applied the constraints of Equation (6-2) and (6-3) (the critical density was not constrained). For representation of the critical isotherm with the Z^{CS} , results indicated that adding a generalized polynomial attractive term (Z^{att} was cubic in density) was far superior to adding attractive terms from well-known EOSs, such as the Peng-Robinson or Redlich-Kwong. However, the normal PR-EOS (without the Z^{CS}) was the second best in representative ability of the critical isotherm among the eight EOSs evaluated.

In this work, an empirical attractive compressibility was used that has a similar functional form in density to those in most cubic EOSs. Extra terms then were added by trial and error until a suitable overall form was found. To keep the overall EOS at a 7th-order polynomial, the attractive term must include a rational polynomial that is quadratic in density for its denominator; furthermore, a polynomial with a root of $x = \xi$ does not count toward being quadratic because this is the packing fraction of the repulsive compressibility (where a root of $x = \xi$ already exists).

The complete HS EOS can be written explicitly in compressibility, Z , in terms of reduced density x and reduced temperature $T_r = T / T_c$; the HS EOS is separated by its repulsive and attractive parts, as shown below:

$$Z = \{Z^{\text{rep}}\} + \{Z^{\text{att}}\} = \left\{ 1 + B_2 x + B_3 x^2 + B_4 x^3 + \frac{C(x/\xi)^4}{1 - x/\xi} \right\} + \left\{ -\frac{aT_r^{-C_1} e^{(1/T_r-1)}}{(v_{\text{hs}})RT} \left(\frac{D_6 T_r^{C_4} x^4 - x}{1 + D_1 x + D_2 x^2} + D_3 T_r^{1-C_2} x + D_4 (1 + C_3 \ln(T_r)) x^2 \right) \right\} \quad (6-8)$$

The attractive compressibility Z^{att} has several constants, which are optimized using VLE and PVT data. Constants denoted by “C” and that have a subscript are used in temperature-dependent functions. Some of the constants were universal for all fluids: $D_1 = 5$, $D_2 = 12.5$ and $D_6 = 100$. The constants a , D_3 , and D_4 are specified by the critical point constraint equations and for all fluids. The hard-sphere volume v_{hs} and the constants C_1 , C_2 , C_3 , and C_4 were regressed. Details are in Appendix B.

Additional terms were added for use with polar fluids, which are defined as having a permanent dipole moment.

$$Z = 1 + B_2 x + B_3 x^2 + B_4 x^3 + \frac{C(x/\xi)^4}{1 - x/\xi} - \frac{aT_r^{-C_1} e^{(1/T_r-1)}}{(v_{\text{hs}})RT} \left(\frac{D_6 T_r^{C_4} x^4 - x}{1 + D_1 x + D_2 x^2} + D_3 T_r^{1-C_2} x + D_4 (1 + C_3 \ln(T_r)) x^2 \right) - \frac{yT_r^{-C_1} e^{(1/T_r-1)}}{(v_{\text{hs}})RT} \left(-\frac{x}{1 + D_1 x + D_2 x^2} + D_7 T_r^{1-C_2} x + (1 + C_5 \ln(T_r))(D_8 x^2 + D_9 x^3) + D_{10} x^4 + \frac{D_{11} (1 + C_6 \ln(T_r) + C_7 (T_r - 1))(x/\xi)^4}{1 - x/\xi} \right) \quad (6-9)$$

A term in x^3 was omitted because it had little or no influence in representation of PVT or saturated property behavior.

For polar fluids, six more constants, in addition to the ones used for non-polar fluids were regressed: y , D_9 , D_{11} , C_5 , C_6 , C_7 . For complete details, see Appendix B.

For pure components, the fugacity is needed to evaluate saturated properties. This expression is derived and presented in analytical form in Appendix C.

METHODS

Pure-fluid equations used by the National Institute of Standards and Technology (Linstrom and Mallard, 2003) are highly accurate in predictions of PVT behavior, but they do not partition between repulsive and attractive parts; i.e., a hard-sphere compressibility and a dispersion (attractive) term. However, the NIST EOS property predictions are sufficiently accurate to serve as “smoothed data” - in lieu of actual measurements - to serve the purpose in creating a generalized EOS for all these fluids. These NIST EOS fluid EOSs are

“part of overall quality assurance programs, to verify the accuracy of specific measurements and to support the development of new measurement methods. Industry, academia, and government use NIST SRMs [Standard Reference Material] to facilitate commerce and trade and to advance research and development” (Linstrom and Mallard, 2003).

For each NIST EOS fluid, relevant experimental measurements were used to develop the multi-parameter EOS. A list of these fluids, the date each NIST fluid was published, and the authors are listed in Table 6-2. Also listed for each NIST fluid is the temperature range where saturated property data are used to help construct the new HS EOS, and the corresponding lowest saturated pressure used. In general, the saturated properties for all these fluids are within 0.1-0.2% on average, except near the critical point.

Table 6-2. NIST Fluids Used in the HS EOS

| Fluid | Year Published | Authors | T/Tc Range for Saturated Properties | P_{sat} at T_{low} NIST / EOS (psia) |
|-----------------|-----------------------|--|--|---|
| CO ₂ | 1996 | Span and Wagner | 0.714-0.999 | 76.60 74.72 |
| Methane | 1991 | Setzmann and Wagner | 0.477-0.996 | 1.748 1.692 |
| Nitrogen | 2000 | Span, Lemmon, Jacobsen, Wagner, and Yokozeki | 0.500-0.998 | 1.816 1.784 |
| Ethane | 1991 | Friend, Ingham, and Ely | 0.471-0.995 | 0.7965 0.7873 |
| Propane | 2000 | Miyamoto and Watanabe | 0.485-0.999 | 0.6911 0.6838 |
| n-Butane | 1987 | Younglove and Ely | 0.496-0.993 | 0.6310 0.6289 |
| Iso-Butane | 1987 | Younglove and Ely | 0.490-0.997 | 0.5378 0.5338 |
| Pentane | 2000 | Span | 0.455-0.993 | 0.09497 0.09400 |
| Ethylene | 2000 | Smukala, Span, and Wagner | 0.501-0.999 | 1.9626 1.9415 |
| Argon | 1982 | Tegeler, Span, and Wagner | 0.559-0.994 | 10.527 10.408 |
| Fluorine | 1990 | de Reuck | 0.453-0.976 | 0.7223 0.7136 |
| Oxygen | 1985 | Schmidt and Wagner | 0.502-0.998 | 3.118 3.075 |
| NF ₃ | 1982 | Younglove | 0.379-0.999 | 0.009487 0.008891 |
| R-32 | 1997 | Tillner-Roth and Yokozeki | 0.458-0.999 | 0.1668 0.1672 |
| Ammonia | 1993 | Tillner-Roth, Harms-Watzenberg and Baehr | 0.486-0.993 | 0.9984 0.9998 |
| R-123 | 1994 | Younglove and McLinden | 0.456-0.999 | 0.07651 0.07640 |
| R-124 | 1995 | de Vries, Tillner-Roth, and Baehr | 0.477-0.999 | 0.1651 0.1648 |
| R-22 | 1995 | Kamei, Beyerlein, and Jacobsen | 0.421-0.992 | 0.04438 0.04330 |
| Water | 2002 | Wagner and Pruss. | 0.423-0.997 | 0.09230 0.09160 |

Densities for PVT behavior are generally less than 0.1% except for some gases at very high pressures or temperatures where the errors can be 0.5-1.0%.

Optimization Procedure

In optimizing the EOS, five adjustable parameters were used for the non-polar fluids, and 11 adjustable parameters were used (at most) for polar fluids. The parameters for the polar fluids include those for the non-polar fluids plus six more additional parameters. The hard-sphere volume, v_{hs} , is the most sensitive parameter to the calculations of single-phase and saturated densities; small changes on the order of 0.001 cm^3/mol can change the saturated vapor pressure at temperatures near $T_r = 0.45$ by more than 5%.

For optimization, the hard-sphere volume was initially chosen to be the critical volume divided by 6.100. As shown in Figure 6-4, the hard-sphere volume is very close to this value. For comparison, the ratio of the critical volume to the Peng-Robinson covolume b (which is equal to four v_{hs}) is also depicted.

The hard-sphere volume was held constant while the other parameters were optimized using the Levenberg-Marquardt method. After the first optimization was completed, the hard-sphere volume parameter was changed slightly and the other parameters were re-optimized. This procedure continued until the objective function was minimized.

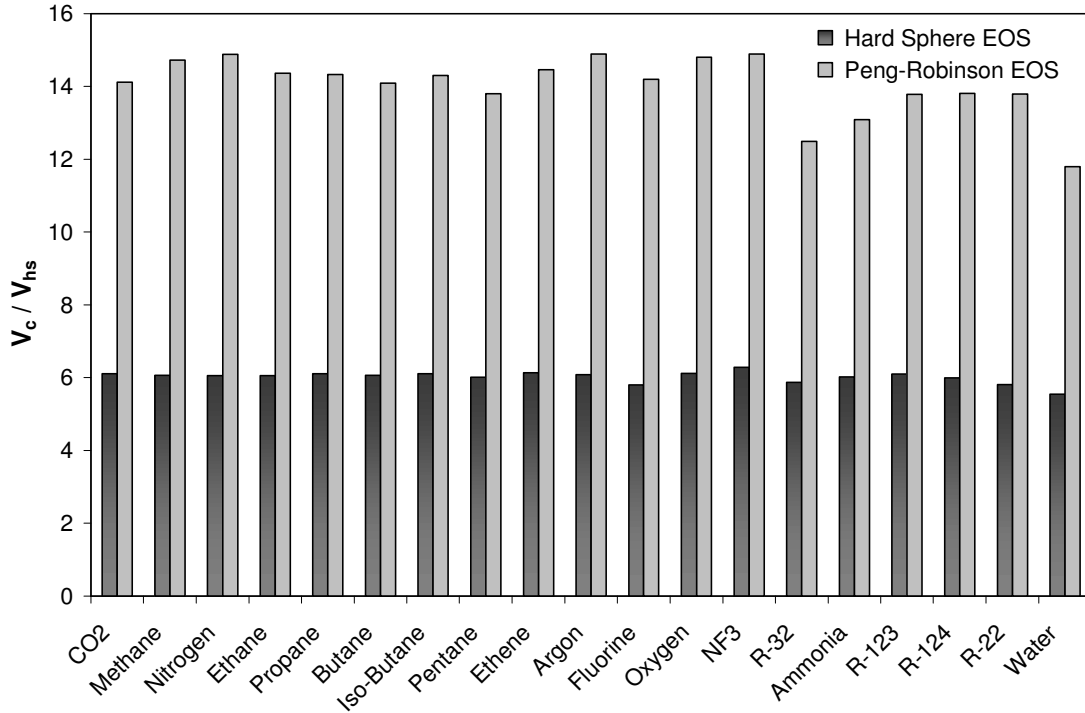


Figure 6-4. Ratios of the Critical Volume to the Hard-Sphere Volume for the Hard-Sphere EOS and the Peng-Robinson EOS for Several Fluids

Once the global minimum is found, all parameters were re-optimized by slightly changing the initial values of the parameters to assure that the minimum was truly global.

The following objective function was used:

$$\begin{aligned}
 \text{OF} = & \frac{1}{w_{\text{Sat.Liq}}} \sum_i^{\text{Sat.Liq}} \text{abs} \left(\frac{\rho_i^{\text{Exp}} - \rho_i^{\text{Calc}}}{w_i \rho_i^{\text{Exp}}} \right) + \frac{1}{w_{\text{Sat.Vap}}} \sum_i^{\text{Sat.Vap}} \text{abs} \left(\frac{\rho_i^{\text{Exp}} - \rho_i^{\text{Calc}}}{w_i \rho_i^{\text{Exp}}} \right) \\
 & + \frac{1}{w_{\text{Sat.Press.}}} \sum_i^{\text{Sat.Press.}} \text{abs} \left(\frac{P_i^{\text{Exp}} - P_i^{\text{Calc}}}{w_i P_i^{\text{Exp}}} \right) + \frac{1}{w_{1-\phi}} \sum_i^{1-\phi} \text{abs} \left(\frac{\rho_i^{\text{Exp}} - \rho_i^{\text{Calc}}}{w_i \rho_i^{\text{Exp}}} \right)
 \end{aligned} \quad (6-10)$$

The objective function adds up the weighted absolute average percent deviations for all the properties of interest. It consists of weighted data from four possible types: saturated liquid densities, saturated vapor densities, saturated vapor pressures, and single-phase (1- ϕ) densities. Weights for each group were assigned arbitrary values based on

the relative number of data from each group. In addition to group weights, individual data were re-weighted after initial optimizations so that subsequent optimizations would increase the accuracy in certain PVT areas considered more crucial. For example, the single-phase density data near 2.5-3.0 in reduced density were weighted more heavily. Near-critical densities were weighted relatively less, based on the observation that further improvement in this region significantly compromised the fit in other areas. Saturated vapor densities were weighted less than saturated pressures and saturated liquid densities. In short, the weights were set subjectively to reflect the purpose of the EOS: to calculate accurately the properties of dense fluids, which in turn should help to better predict the high-pressure adsorption through the SLD framework.

QUALITY OF GENERALIZED PREDICTIONS

Figures 6-5 and 6-7 present typical EOS results in reduced pressure-density coordinates for CO₂ and methane. Figure 6-6 presents the deviation plot in liquid and supercritical densities relative to the Span and Wagner EOS for CO₂. Figure 6-8 presents the saturated and compressed liquid behavior of water. Points represent the “input data” calculated from the NIST EOS, and smoothed lines represent the HS-EOS fit at various isotherms.

Tables 6-3 through 6-5 summarize some of the deviation statistics in density for CO₂, methane, and nitrogen from the NIST EOS. Typically, each category except the critical isotherm has an average absolute error of 1.2% or less. Other gases have similar results, as shown in Table 6-6.

For fluids such as methane or nitrogen that have relatively low critical temperatures, the EOS represents the PVT behavior less accurately at reduced temperatures of about 1.5 or higher and reduced densities of about 1.5 and higher; densities in this regime are under-predicted at given pressure. At most, the density is under-predicted for methane by 4.6% at $T_r = 1.8$ (157.8°F). This can be observed in Figure 6-7. This inaccuracy is due, in part, because the third virial coefficient of the EOS is deficient at these temperatures, and the second virial coefficient is close to zero.

Methane and nitrogen, which are not close to the critical regime for coalbed reservoir conditions, have respectively a 0.9% and 0.6% AAD for densities ranging from 85°F and 166°F and pressures to 2000 psia. CO₂ has respectively 2.2%, 0.9%, 0.8%, and 0.6% for densities at 88°F, 115°F, 143°F and 170°F and pressures to 2000 psia.

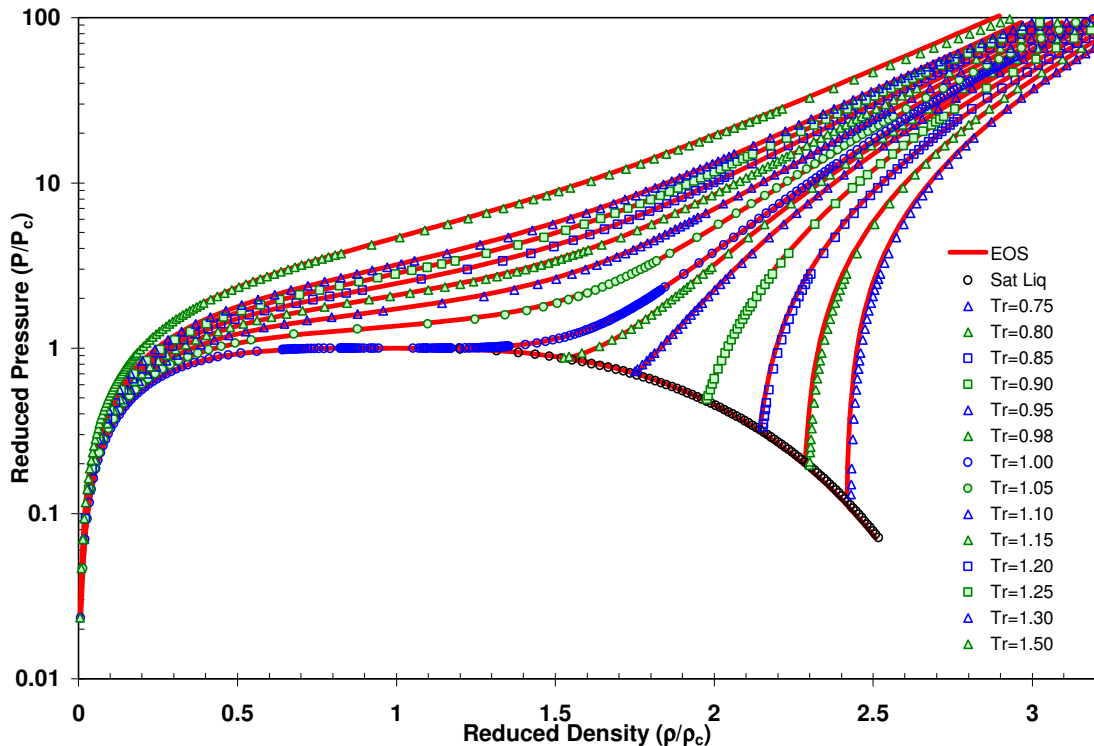


Figure 6-5. Overall PVT Representation for CO₂ Using NIST EOS as Reference

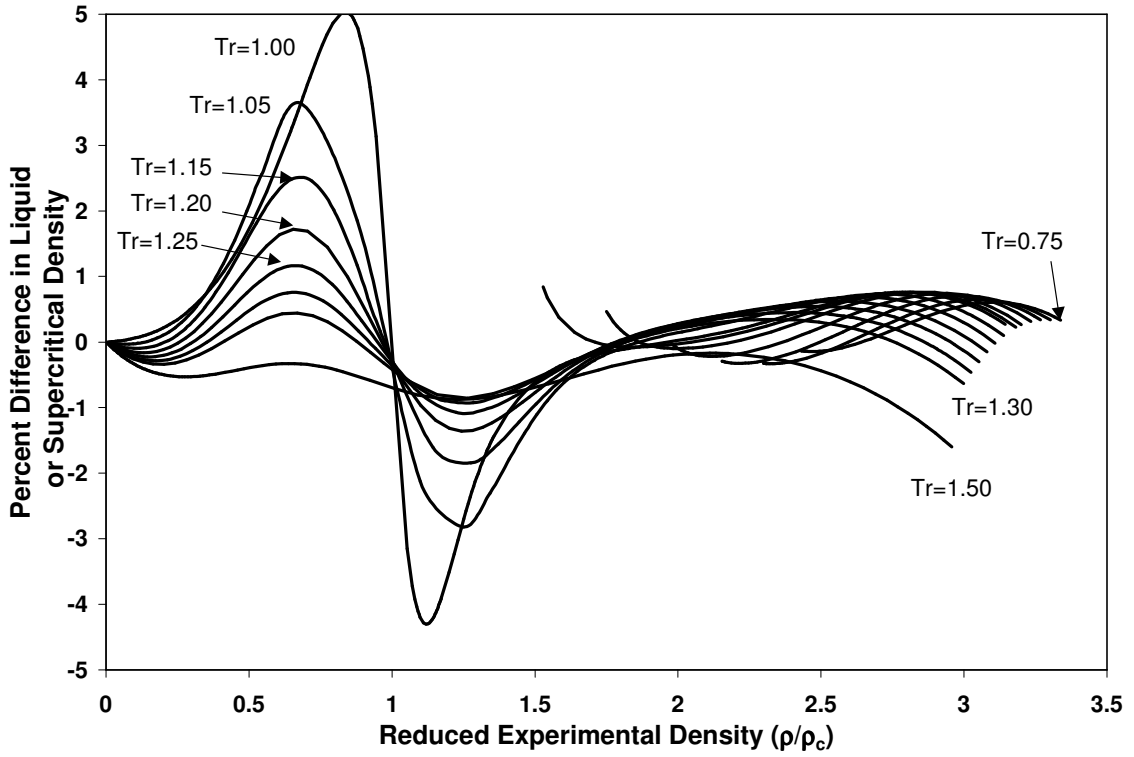


Figure 6-6. Deviation Plot for CO₂ Density Using NIST EOS as Reference

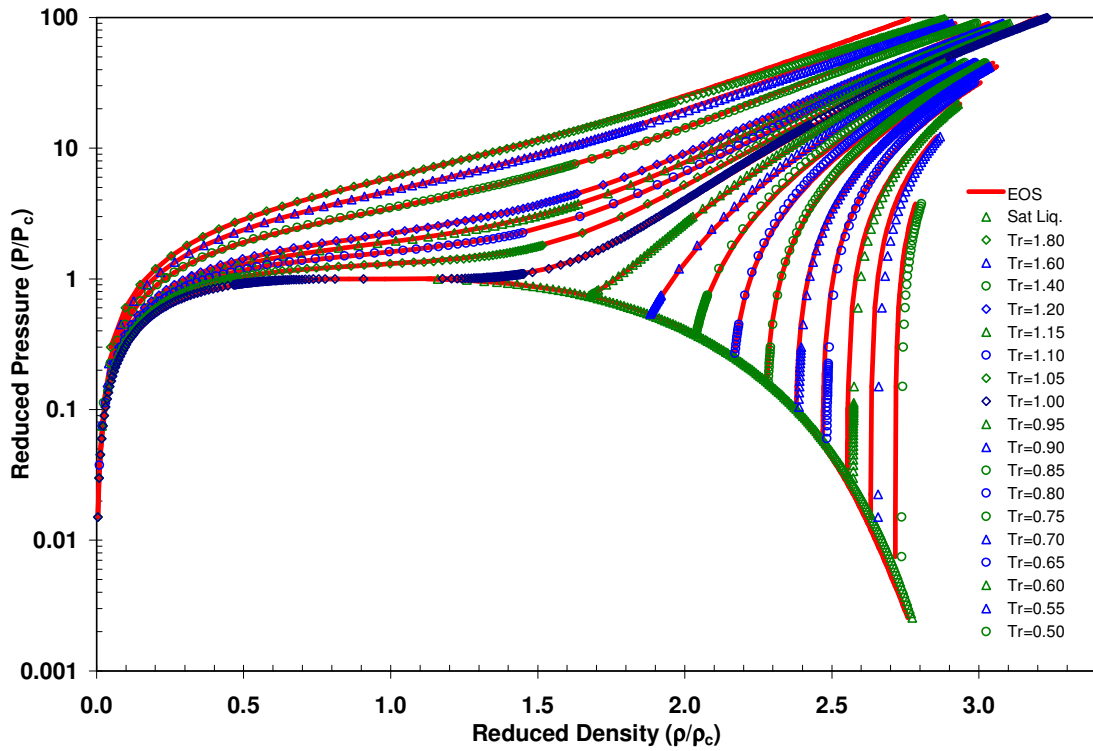


Figure 6-7. Overall PVT Representation for Methane Using NIST EOS as Reference

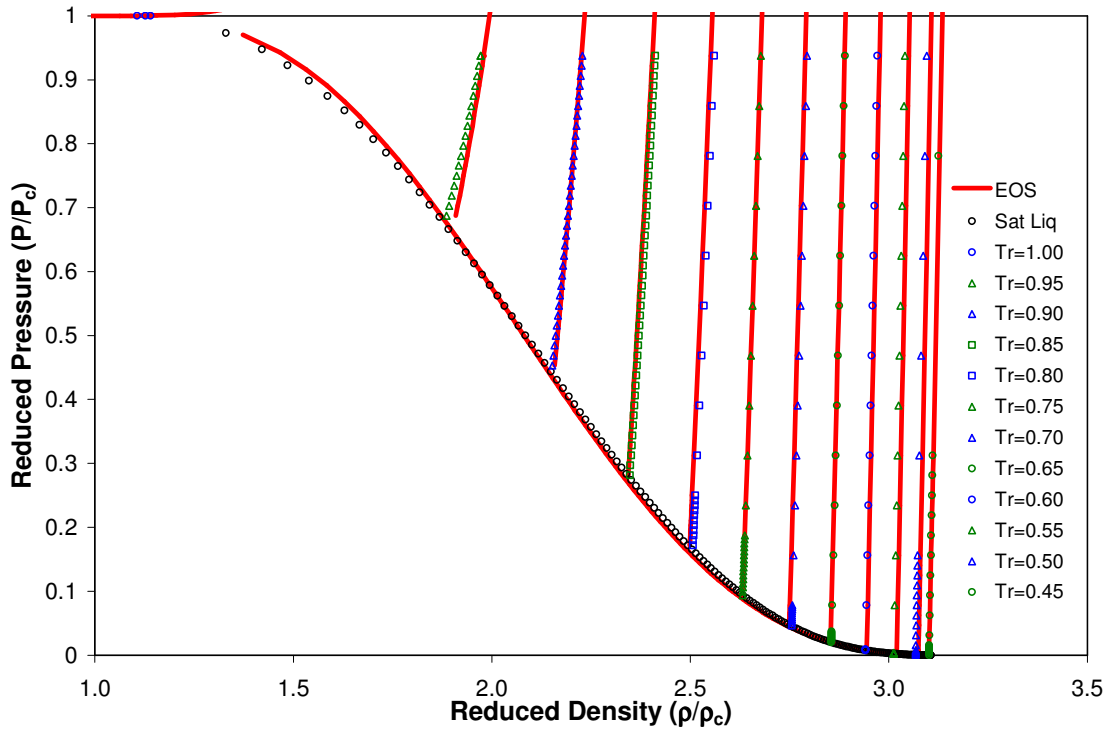


Figure 6-8. Representation of Saturated and Compressed Liquid Densities for Water Using NIST EOS as Reference

Table 6-3. Absolute Percent Differences in Density and Saturated Pressure between the HS EOS and the NIST EOS for CO₂

| | Average | Median | Standard Deviation | Maximum | # Points |
|----------------------------|---------|--------|--------------------|---------|----------|
| Critical Isotherm | 1.4 | 0.6 | 1.7 | 5.0 | 269 |
| Saturated Pressure | 0.4 | 0.2 | 0.4 | 2.2 | 79 |
| Saturated Liquid | 0.3 | 0.2 | 0.4 | 1.2 | 79 |
| Saturated Vapor | 0.7 | 0.7 | 0.4 | 2.3 | 79 |
| Compressed Liq. Density | 0.2 | 0.2 | 0.2 | 1.2 | 287 |
| Subcritical Vap. Density | 0.2 | 0.2 | 0.1 | 0.5 | 74 |
| Supercritical Vap. Density | 0.4 | 0.3 | 0.4 | 3.7 | 623 |

Table 6-4. Absolute Percent Differences in Density and Saturated Pressure between the HS EOS and the NIST EOS for Methane

| | Average | Median | Standard Deviation | Maximum | # Points |
|----------------------------|---------|--------|--------------------|---------|----------|
| Critical Isotherm | 1.2 | 0.7 | 1.3 | 7.9 | 489 |
| Saturated Pressure | 1.0 | 0.9 | 0.9 | 7.0 | 180 |
| Saturated Liquid | 0.7 | 0.7 | 0.3 | 3.2 | 180 |
| Saturated Vapor | 0.7 | 0.4 | 1.0 | 6.8 | 180 |
| Compressed Liq. Density | 0.9 | 1.0 | 0.2 | 1.4 | 981 |
| Subcritical Vap. Density | 0.8 | 0.7 | 0.5 | 2.0 | 162 |
| Supercritical Vap. Density | 1.2 | 0.9 | 1.1 | 4.6 | 1247 |

Table 6-5. Absolute Percent Differences in Density and Saturated Pressure between the HS EOS and the NIST EOS for Nitrogen

| | Average | Median | Standard Deviation | Maximum | # Points |
|----------------------------|---------|--------|--------------------|---------|----------|
| Critical Isotherm | 1.2 | 0.7 | 1.3 | 6.1 | 232 |
| Saturated Pressure | 0.8 | 0.7 | 0.4 | 1.8 | 114 |
| Saturated Liquid | 0.7 | 0.5 | 0.5 | 3.4 | 114 |
| Saturated Vapor | 0.8 | 0.5 | 0.8 | 5.0 | 114 |
| Compressed Liq. Density | 0.7 | 0.8 | 0.4 | 1.3 | 942 |
| Subcritical Vap. Density | 0.6 | 0.5 | 0.4 | 1.8 | 574 |
| Supercritical Vap. Density | 1.0 | 0.6 | 1.2 | 6.2 | 1258 |

Table 6-6. Absolute Percent Differences in Density and Saturated Pressure between the HS EOS and the NIST EOS for Various Fluids

| | Average | Median | Standard Deviation | Maximum | # Points |
|--------------------|---------|--------|--------------------|---------|----------|
| Ethane | | | | | |
| Critical Isotherm | 1.3 | 0.6 | 1.6 | 5.4 | 153 |
| Saturated Pressure | 0.2 | 0.1 | 0.2 | 1.2 | 97 |
| Saturated Liquid | 0.4 | 0.4 | 0.2 | 1.2 | 97 |
| Saturated Vapor | 0.3 | 0.2 | 0.3 | 2.7 | 97 |
| Propane | | | | | |
| Critical Isotherm | 0.8 | 0.6 | 0.6 | 4.4 | 419 |
| Saturated Pressure | 0.2 | 0.2 | 0.2 | 1.1 | 114 |
| Saturated Liquid | 0.3 | 0.2 | 0.3 | 1.9 | 114 |
| Saturated Vapor | 0.3 | 0.2 | 0.4 | 3.1 | 114 |
| Butane | | | | | |
| Critical Isotherm | 0.7 | 0.5 | 0.6 | 4.8 | 155 |
| Saturated Pressure | 0.3 | 0.3 | 0.2 | 0.7 | 77 |
| Saturated Liquid | 0.3 | 0.2 | 0.2 | 0.9 | 77 |
| Saturated Vapor | 0.3 | 0.2 | 0.3 | 1.3 | 77 |
| Iso-Butane | | | | | |
| Critical Isotherm | 0.8 | 0.7 | 0.7 | 3.8 | 221 |
| Saturated Pressure | 0.3 | 0.2 | 0.2 | 0.7 | 94 |
| Saturated Liquid | 0.3 | 0.3 | 0.2 | 0.9 | 94 |
| Saturated Vapor | 0.4 | 0.2 | 0.5 | 1.8 | 94 |

Table 6-6. Absolute Percent Differences in Density and Saturated Pressure between the HS EOS and the NIST EOS for Various Fluids (Continued)

| | Average | Median | Standard Deviation | Maximum | # Points |
|--------------------|---------|--------|--------------------|---------|----------|
| Pentane | | | | | |
| Critical Isotherm | 1.0 | 0.7 | 0.9 | 4.6 | 198 |
| Saturated Pressure | 0.6 | 0.4 | 0.4 | 1.2 | 92 |
| Saturated Liquid | 0.2 | 0.2 | 0.2 | 0.7 | 92 |
| Saturated Vapor | 0.8 | 0.4 | 1.0 | 3.7 | 92 |
| Ethene | | | | | |
| Critical Isotherm | 1.0 | 0.6 | 1.2 | 5.8 | 277 |
| Saturated Pressure | 1.3 | 1.4 | 0.6 | 2.1 | 60 |
| Saturated Liquid | 0.2 | 0.1 | 0.3 | 2.1 | 60 |
| Saturated Vapor | 0.5 | 0.3 | 0.7 | 4.0 | 60 |
| Argon | | | | | |
| Critical Isotherm | 1.0 | 0.6 | 1.2 | 5.8 | 277 |
| Saturated Pressure | 1.3 | 1.4 | 0.6 | 2.1 | 60 |
| Saturated Liquid | 0.2 | 0.1 | 0.3 | 2.1 | 60 |
| Saturated Vapor | 0.5 | 0.3 | 0.7 | 4.0 | 60 |
| Fluorine | | | | | |
| Critical Isotherm | 4.0 | 0.5 | 7.0 | 32.5 | 132 |
| Saturated Pressure | 0.8 | 0.8 | 0.3 | 1.4 | 30 |
| Saturated Liquid | 0.4 | 0.3 | 0.3 | 1.4 | 30 |
| Saturated Vapor | 0.4 | 0.4 | 0.3 | 1.2 | 30 |

Table 6-6. Absolute Percent Differences in Density and Saturated Pressure between the HS EOS and the NIST EOS for Various Fluids (Continued)

| | Average | Median | Standard Deviation | Maximum | # Points |
|--------------------|---------|--------|--------------------|---------|----------|
| Oxygen | | | | | |
| Critical Isotherm | 1.2 | 1.1 | 1.0 | 5.4 | 133 |
| Saturated Pressure | 0.9 | 0.7 | 0.7 | 2.0 | 45 |
| Saturated Liquid | 0.7 | 0.6 | 0.6 | 2.4 | 45 |
| Saturated Vapor | 1.3 | 0.5 | 1.4 | 4.5 | 45 |
| NF3 | | | | | |
| Critical Isotherm | 1.4 | 1.2 | 0.9 | 3.4 | 319 |
| Saturated Pressure | 0.8 | 0.8 | 0.9 | 6.8 | 59 |
| Saturated Liquid | 0.6 | 0.4 | 0.8 | 3.1 | 59 |
| Saturated Vapor | 1.0 | 0.8 | 1.0 | 6.9 | 59 |
| R-32 | | | | | |
| Critical Isotherm | 0.5 | 0.3 | 0.5 | 3.7 | 215 |
| Saturated Pressure | 0.8 | 0.7 | 0.6 | 1.7 | 78 |
| Saturated Liquid | 0.8 | 0.8 | 0.4 | 1.7 | 78 |
| Saturated Vapor | 1.1 | 0.3 | 1.4 | 4.6 | 78 |
| Ammonia | | | | | |
| Critical Isotherm | 0.8 | 0.7 | 0.6 | 2.3 | 233 |
| Saturated Pressure | 0.2 | 0.2 | 0.2 | 0.5 | 99 |
| Saturated Liquid | 0.2 | 0.1 | 0.2 | 0.8 | 99 |
| Saturated Vapor | 0.4 | 0.2 | 0.4 | 1.6 | 99 |

Table 6-6. Absolute Percent Differences in Density and Saturated Pressure between the HS EOS and the NIST EOS for Various Fluids (Continued)

| | Average | Median | Standard Deviation | Maximum | # Points |
|--------------------------|---------|--------|--------------------|---------|----------|
| R-123 | | | | | |
| Critical Isotherm | 0.8 | 0.7 | 0.6 | 2.3 | 233 |
| Saturated Pressure | 0.2 | 0.2 | 0.2 | 0.5 | 99 |
| Saturated Liquid | 0.2 | 0.1 | 0.2 | 0.8 | 99 |
| Saturated Vapor | 0.4 | 0.2 | 0.4 | 1.6 | 99 |
| R-124 | | | | | |
| Critical Isotherm | 1.1 | 0.7 | 1.0 | 4.0 | 251 |
| Saturated Pressure | 0.2 | 0.2 | 0.2 | 0.5 | 81 |
| Saturated Liquid | 0.4 | 0.4 | 0.3 | 1.3 | 81 |
| Saturated Vapor | 0.5 | 0.2 | 0.7 | 2.4 | 81 |
| R-22 | | | | | |
| Critical Isotherm | 1.6 | 1.3 | 1.4 | 6.7 | 196 |
| Saturated Pressure | 0.5 | 0.3 | 0.4 | 2.5 | 77 |
| Saturated Liquid | 0.6 | 0.2 | 0.7 | 2.2 | 77 |
| Saturated Vapor | 0.6 | 0.4 | 0.5 | 3.1 | 77 |
| Water | | | | | |
| Critical Isotherm | 1.3 | 1.0 | 0.7 | 4.2 | 217 |
| Saturated Pressure | 0.5 | 0.5 | 0.3 | 1.1 | 168 |
| Saturated Liquid | 0.5 | 0.4 | 0.4 | 2.6 | 168 |
| Saturated Vapor | 1.8 | 0.7 | 2.1 | 7.0 | 168 |
| Compressed Liq. Density | 0.4 | 0.4 | 0.3 | 1.6 | 1393 |
| Subcritical Vap. Density | 0.5 | 0.4 | 0.5 | 3.2 | 1436 |

Polar fluids tend to have about the same representation of the saturation properties as the non-polar fluids; some of the polar fluids, however, need 6 additional parameters for this representation. The extra terms added to the EOS for the polar fluids were necessary for accurate representation of water. Without them, the phase diagram of water can not be accurately represented. Some of these extra terms were not needed for other polar substances. For the refrigerants and nitrogen trifluoride, this is partly an artifact that the critical isotherm was fitted up to only 11 reduced pressures (the NIST EOS was not valid for higher pressures).

CRITICAL BEHAVIOR

Accurate description of the near-critical behavior of fluids is important because CO₂ and ethane have critical temperatures that are near those of operating coalbed methane wells. In Figure 6-9, the critical isotherm of CO₂ close to the critical point is shown for the HS EOS and the Span and Wagner EOS (1996), which has corrections for near-critical behavior and therefore can obey Equations (6-4) and (6-5). The HS EOS does not have these corrections (although it is possible to add these). Nevertheless, the maximum deviation for the critical isotherm for CO₂ is 5% as shown in Figure 6-6.

SECOND VIRIAL COEFFICIENT

The second virial coefficient, B(T) is the second term in the virial equation of state, most often written as a series in density.

$$Z = 1 + B(T)\rho + C(T)\rho^2 + D(T)\rho^3 \dots \quad (6-11)$$

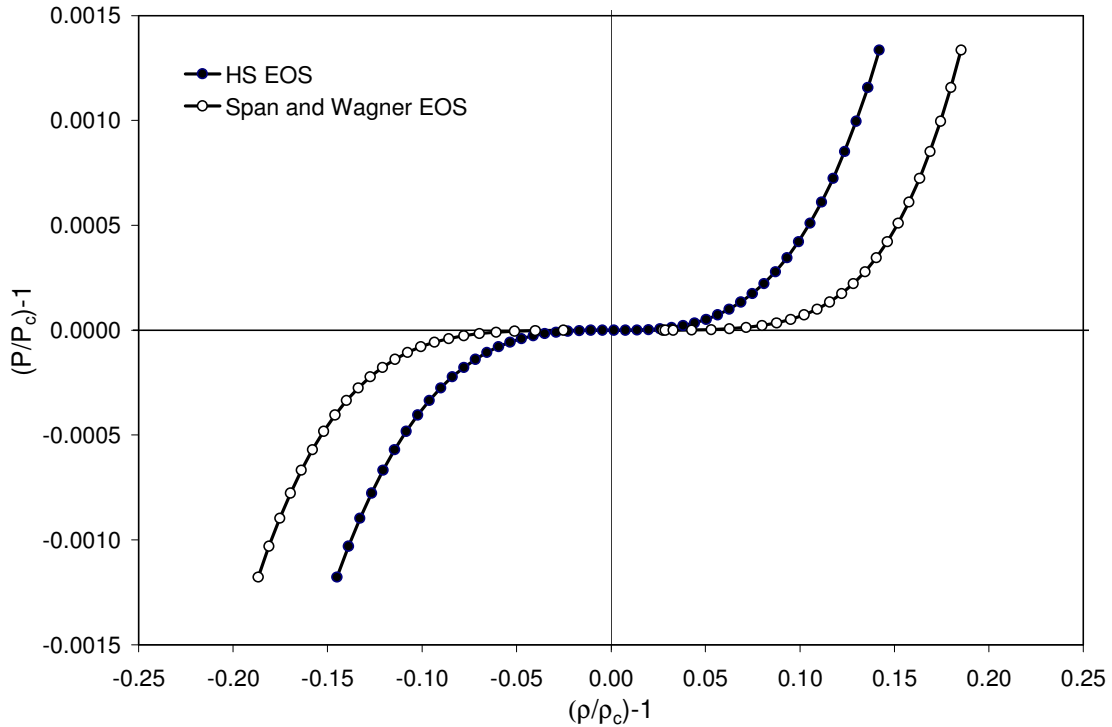


Figure 6-9. CO₂ Critical Isotherm Close to the Critical Point

The first term (unity) represents ideal gas law behavior (where $Z = 1$). The second virial coefficient (SVC) is the first-order correction from the ideal gas compressibility in terms of density or pressure – respectively (the Leiden and Berlin forms of the virial equations). The Leiden form has been shown to be conclusively better than the Berlin form in the accuracy and sensitivity of various physical properties (Eubank et al., 2003). Any fluid EOS generally will have poor property predictions for the gas phase unless the SVC is described accurately. For the non-polar HS EOS, the SVC is derived as:

$$B(T) = B_2 v_{hs} - \frac{a T_r^{-C_1} e^{(1/T_r-1)}}{RT} (D_3 T_r^{1-C_2} - 1) \quad (6-12)$$

For the polar HS EOS, the SVC is:

$$B(T) = B_2 v_{hs} - \frac{T_r^{-c_1} e^{(1/T_r-1)}}{RT} (T_r^{1-c_2} (aD_3 + yD_7) - a - y) \quad (6-13)$$

The SVC for the HS EOS is comprised of two terms: a constant temperature-independent term and an attractive term that approaches zero asymptotically for higher temperatures. As the SVC approaches $B_2 v_{hs}$, the temperature approaches infinity, which is four times the hard sphere volume ($B_2 = 4$).

Other semi-empirical correlations for the SVC have similar behavior; e.g., Equation (6-12) has been found to be similar in functional form to a generalized SVC derived from the square-well (SW) potential (McFall et al., 2002). The SW potential $u_{sw}(r)$ has three parameters: the hard-sphere diameter of the fluid σ_{ff} , the well depth ε_{ff} , and an attractive range multiplier λ :

$$\begin{aligned} u_{sw}(r) &= +\infty & \text{for } r < \sigma_{ff} \\ u_{sw}(r) &= -\varepsilon_{ff} & \text{for } \sigma_{ff} < r < \lambda \sigma_{ff} \\ u_{sw}(r) &= 0 & \text{for } r > \lambda \sigma_{ff} \end{aligned} \quad (6-14)$$

The SVC can be derived from any spherically symmetric potential $u(r)$ using the following formula:

$$B(T) = -2\pi \int_0^{\infty} (e^{-u(r)/kT} - 1) r^2 dr \quad (6-15)$$

Using this formula, the SVC for the SW potential is:

$$B_{sw}(T) = \frac{2\pi\sigma_{ff}^3}{3} - \frac{2\pi\sigma_{ff}^3}{3} (\lambda^3 - 1) (e^{\varepsilon_{ff}/kT} - 1) \quad (6-16)$$

Like the SVC for the HS EOS, the SW SVC approaches a specific volume at infinite temperature, namely $2\pi\sigma_{ff}^3/3$, which is 4 times the hard-sphere volume $\pi\sigma_{ff}^3/6$. For the attractive term, both utilize an exponential functionality of the reciprocal temperature.

For most gases, the hard-sphere volume, $\pi\sigma_{ff}^3/6$, predicted using tabulated Lennard-Jones σ_{ff} parameters (Reid et al. 1987) is roughly twice that predicted from the HS EOS hard-sphere volume, v_{hs} . This illustrates that values of v_{hs} used for the HS EOS may differ significantly from values calculated for other purposes, such as estimating gas viscosity data from the LJ potential.

As shown in Figure 6-10, the linear correlation has a R^2 value of 0.88, which suggests that HS EOS v_{hs} cannot be predicted with sufficient accuracy using tabulated σ_{ff} parameters. However, if the parameters from Equation (6-16) are regressed from experimental SVC data (McFall et al., 2002), then the hard sphere volumes correlate much better with $R^2 = 0.998$, as shown in Figure 6-11. The HS EOS v_{hs} is 1.4 times the v_{hs} values regressed by McFall et al.

The SVC derived from the SW potential and from the HS EOS share the trait that at infinite temperature, they approach four times their respective hard sphere volume. This contrasts with theoretical predictions when the SVC is derived from a potential function $u(r)$ such as the LJ potential:

$$u(r) = 4\epsilon_{ff} \left\{ \left(\frac{\sigma_{ff}}{r} \right)^{12} - \left(\frac{\sigma_{ff}}{r} \right)^6 \right\} \quad (6-17)$$

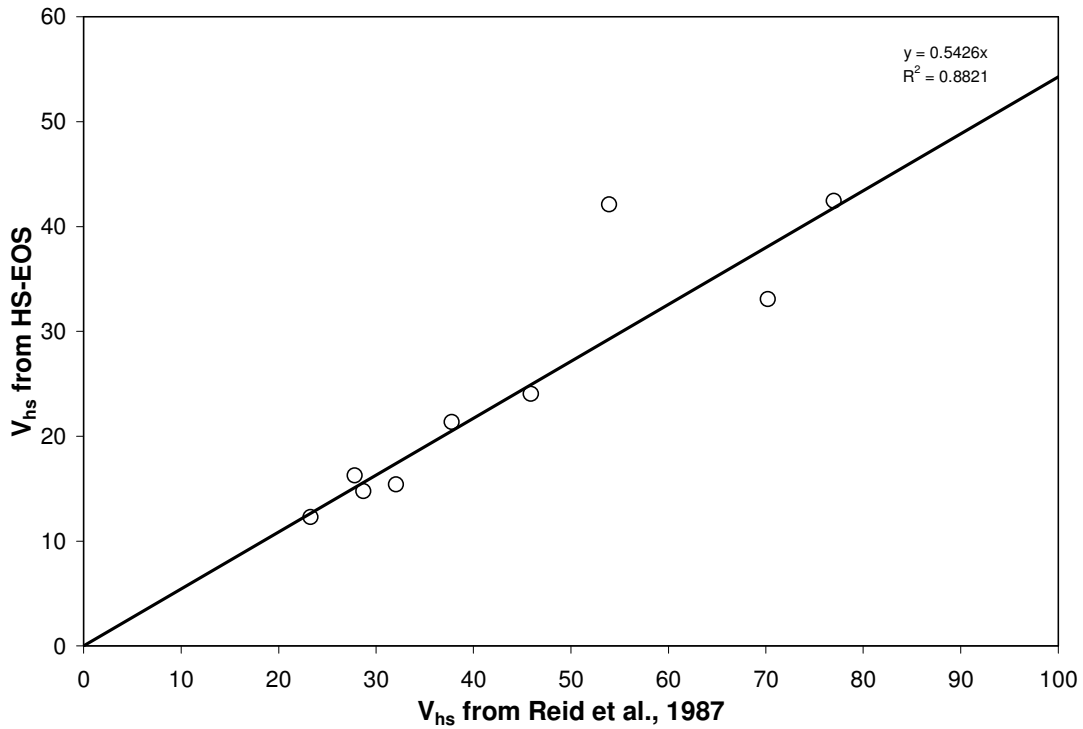


Figure 6-10. Correlation of Hard Sphere Volumes Regressed from the HS EOS and versus Tabulated Values from Reid et al., 1987

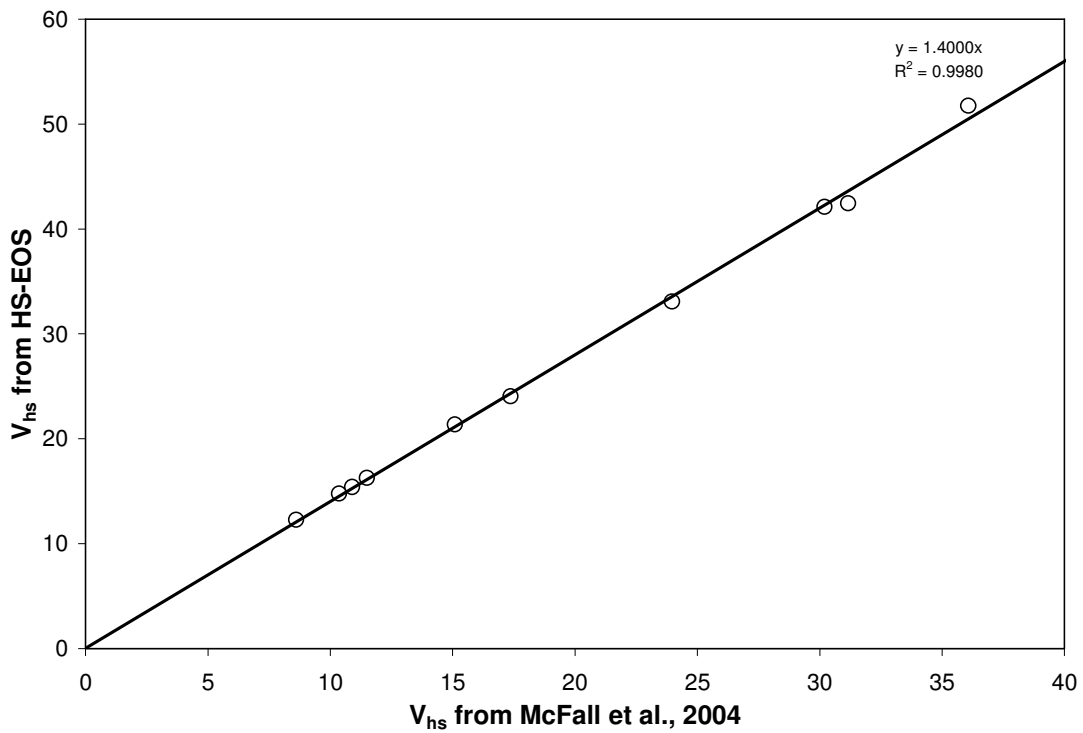


Figure 6-11. Correlation of Hard Sphere Volumes Regressed from the HS EOS versus Tabulated Values from McFall et al., 2004

From Figure 6-12, the LJ SVC approaches zero in the high-temperature limit. Thus, the HS EOS will not obey the correct high temperature limit. However, these high temperatures where the SVC reaches its maximum have not been measured experimentally except for helium (Rigby et al., 1986).

As shown in Figures 6-12 and 6-13 the Boyle temperature (the temperature where $B(T) = 0$) from the LJ and the HS-EOS SVC are nearly the same. The Boyle temperatures for CO_2 from the LJ and HS-EOS SVC are respectively $T_r = 2.217$ and $T_r = 2.221$. For methane, the Boyle temperatures are respectively $T_r = 2.694$ and $T_r = 2.699$. For each gas, the Boyle temperature from the LJ potential is dependent solely on the fluid interaction parameter ϵ_{ff}/k_b (Vargas et al., 2001), which are tabulated elsewhere for many gases (Reid et al., 1987). The Boyle temperature predicted from the LJ potential in Equation (6-18) uses a theoretically correct value of 3.4179 (Vargas et al., 2001), which closely matches a previously reported value of 3.415 that was calculated against empirical data and semi-empirical equations (Masalov, 1968).

$$T_r^{\text{Boyle,LJ}} = \frac{3.4179}{T_c} \frac{\epsilon_{ff}}{k} \quad (6-18)$$

The Boyle temperature predicted from the HS EOS for a non-polar fluid is dependent on v_{hs} , C_1 , and C_2 , and the critical fluid parameters, as found by setting Equation (6-12) to zero. In theory, a HS-EOS parameter such as C_2 could be predicted if v_{hs} , C_1 , the critical fluid parameters, and ϵ_{ff} are known. However, the Boyle temperature predicted from the LJ potential, as predicted from Equation (6-18), does not always correlate well with the Boyle temperature predicted from setting Equation (6-12) to zero. Comparisons of the predicted Boyle temperatures from the LJ potential and the HS EOS

(reduced by the critical temperature) are presented in Figure 6-14; the Boyle temperature predicted from a popular SVC correlation (Tsonopoulos, 1974) is also shown.

In Figure 6-15, Equation (6-12) is compared to a popular correlation from the literature (Tsonopoulos, 1974) for most non-polar gases. As shown, the SVC for most gases is qualitatively similar to the 1974 Tsonopoulos correlation. However, the HS-EOS SVC for methane is noticeably lower than the Tsonopoulos correlation for temperatures less than 180 K, which is near its critical temperature. Argon and nitrogen have similar anomalies. At temperatures where dB/dT becomes large, the predictability of the SVC using Equation (6-12) from optimized PVT and VLE data is only qualitatively similar to the Tsonopoulos correlation.

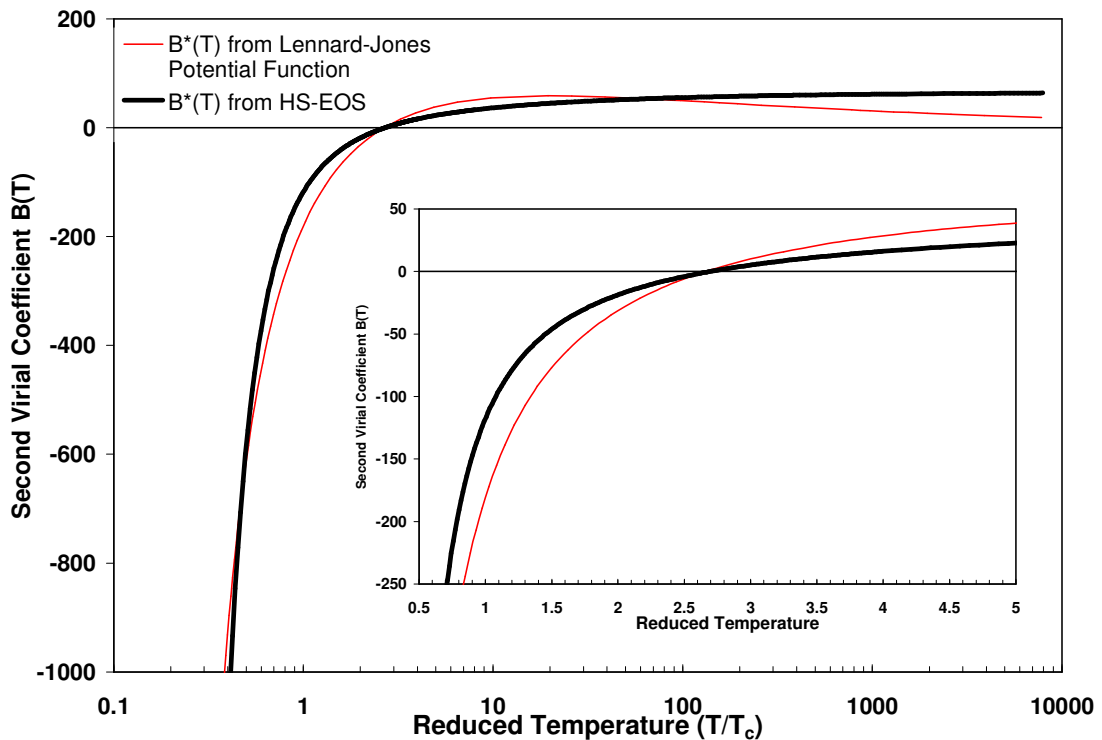


Figure 6-12. Comparison of the Second Virial Coefficient from the HS EOS and the Lennard-Jones Potential for Methane

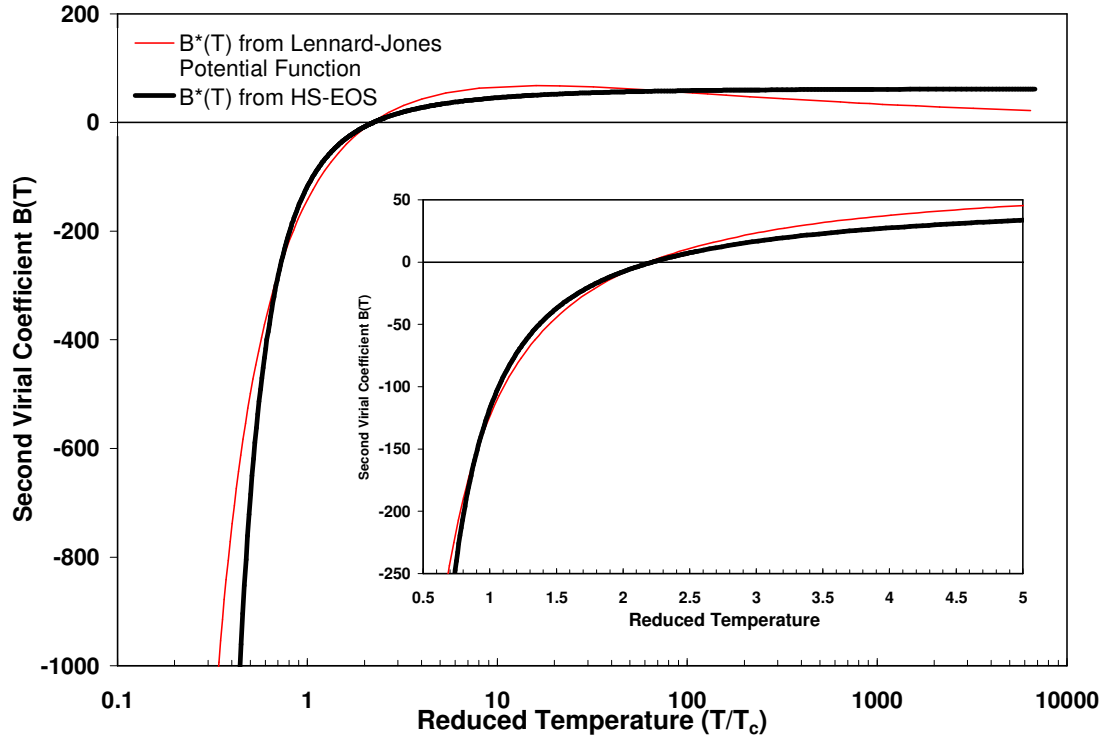


Figure 6-13. Comparison of the Second Virial Coefficient from the HS EOS and the Lennard-Jones Potential for CO₂

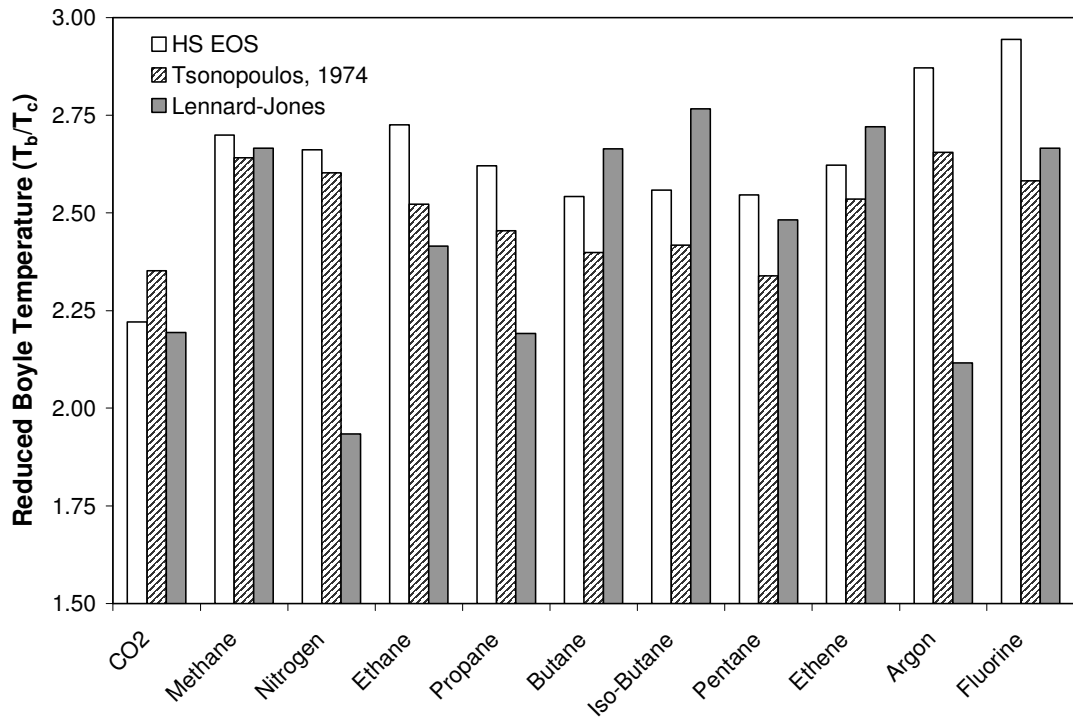


Figure 6-14. Comparison of the Predicted Boyle Temperatures from Several Gases

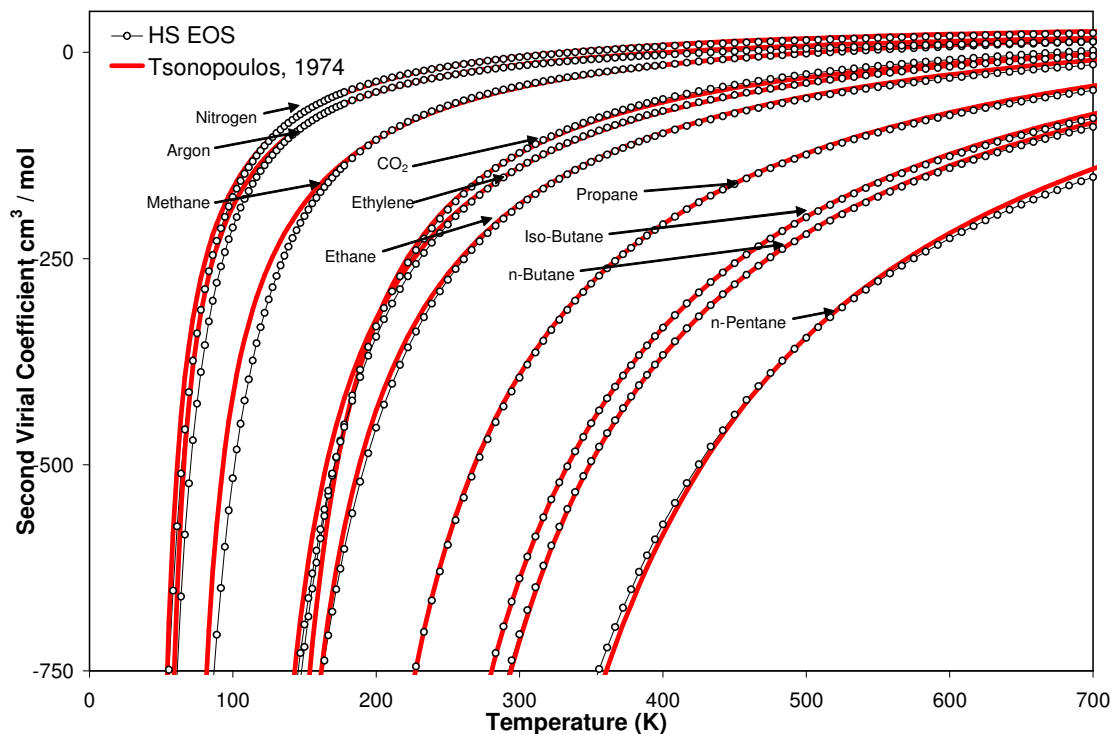


Figure 6-15. Comparison of the Second Virial Coefficient from the HS EOS and from the 1974 Tsonopoulos Correlation for non-Polar Gases

CONCLUSIONS

A new pure-fluid EOS capable of accurately representing high-density behavior was developed. This new EOS utilizes an accurate hard-sphere repulsive term, reproduces the second virial coefficient accurately, and covers a wide range of phase conditions. The EOS is algebraic, 7th-order in density, and uses three constraint formulas at the critical point. A total of five and 11 regressed parameters were used to optimize the EOS for non-polar and polar fluids, respectively.

Our results for coalbed gases (CO₂, methane, and nitrogen) and other fluids, including water, indicate that the new EOS can precisely represent PVT behavior of these pure fluids up to reduced pressures of 100, and can represent saturated vapor-liquid equilibrium (VLE) properties to within 1% in general. The ability to represent critical

isotherm density has a maximum deviation of 5-8% and median deviation of 0.5-1.0%, (with the exception of fluorine). This new HS EOS is expected to set the stage for improved predictions of SLD adsorption modeling.

CHAPTER 7

CONCLUSIONS AND RECOMMENDATIONS

The main objectives of this work were (1) to obtain pure-component, binary, and ternary adsorption measurements for light hydrocarbon gases, nitrogen, and CO₂ for pressures up to 2000 psia and temperatures near 115 °F on various coals and activated carbons; (2) within the SLD framework, to modify the Peng-Robinson equation of state so that it (a) correlates the experimental adsorption data to within one standard deviation for pure components, binary mixtures and ternary mixtures, and (b) predicts accurately binary adsorption from pure component information to within two standard deviations; and (3) to develop a new pure-fluid EOS capable of describing accurately volumetric fluid behavior at high densities.

CONCLUSIONS

Based on this study, the following conclusions are drawn:

1. Valuable experimental adsorption measurements were completed using a constant-pressure, volumetric technique at temperatures between 318 and 328 K (113-131°F) and pressures to 13.8 MPa (2000 psia). These measurements include pure-gas (methane, nitrogen, ethane, and CO₂) measurements on nine solid matrices: wet Fruitland coal (OSU#1 and OSU#2), wet Lower Basin Fruitland coal (OSU#3), wet /

- dry Illinois #6 coal, wet Tiffany coal, dry Beulah Zap coal, dry Wyodak coal, dry Upper Freeport coal, dry Pocahontas coal, and dry activated carbon. Mixed-gas measurements for methane, nitrogen and CO₂ were conducted on two matrices: activated carbon and wet Tiffany coal. These newly-acquired experimental data have been indispensable in the development of pure and mixed-gas adsorption models.
2. Modification of the PR-EOS co-volume improves both the excess adsorption and allows for adsorbate-phase density predictions consistent with experimental data. The modified SLD-PR model is better equipped than the original model to represent adsorption isotherms encountered in CBM production and CO₂ sequestration, including those exhibiting excess adsorption maxima. It can correlate pure-gas adsorption isotherms of many systems involving wet and dry coals, activated carbons, and zeolites over broad pressure and temperature ranges.
 3. For each adsorbent, the SLD-PR model can be applied using a common value for the surface area and an effective slit width for all gas species over all temperature and pressure ranges.
 4. For the adsorption of methane, nitrogen, and CO₂ on dry activated carbon, the SLD-PR can *predict* the component mixture adsorption at 2.2 times the experimental uncertainty on average, based solely on pure-component adsorption isotherms.
 5. For the adsorption of methane, nitrogen, and CO₂ on wet coals (excluding Tiffany coal), the SLD-PR model can *predict* the component adsorption within the experimental uncertainties on average for all feed fractions (nominally 20/80, 40/60, 60/40 and 80/20) of the three binary gas mixture combinations, although some

- specific isotherms (for a specific feed fraction) are predicted outside their experimental uncertainties.
6. The SLD-PR model can *correlate* the binary mixture component adsorption of methane, nitrogen and CO₂ on coals and activated carbon within one standard deviation of the experimental error. The one-fluid mixing rules are suitable for the task of correlation; however, the large corrections for some binary interactions raise questions regarding the physical reality of the rules.
 7. Both the Ono-Kondo (Sudibandriyo, 2003) and SLD-PR models have similar quantitative results for the predictive and correlative behavior of mixed-gas adsorption on activated carbon and the coals. One model may outperform another for a specific isotherm, but overall, neither model clearly has a consistent predictive or correlative advantage over the other.
 8. A new pure-fluid EOS capable of accurate representation of high-density behavior was developed. This EOS utilizes an accurate hard-sphere repulsive term, reproduces the second virial coefficient accurately, and covers a wide range of phase conditions. Results for coalbed gases (CO₂, methane, and nitrogen) and other fluids, including water, indicate that the new EOS can represent precisely PVT behavior of these pure fluids up to reduced pressures (P/P_c) of 100, and can represent saturated vapor-liquid equilibrium properties to within 1% in general.

RECOMMENDATIONS

Based on knowledge gained in this work, the following recommendations for future studies are made:

1. Develop mixing rules for the hard-sphere terms of the EOS using theoretical and computer simulation data. Also develop generalized mixing rules for parameters in the attractive terms by comparing predicted model results with the experimental data of mixtures including, in particular, the second and third virial coefficient data and phase equilibria data for mixtures of CO₂, methane, nitrogen, ethane, and water.
2. Utilize the new HS-EOS to replace the PR-EOS in the SLD modeling of high-pressure isotherms. After fitting the adsorption model to experimental data, correlate the model parameters to the characteristics of the coal and investigate the predictive capability of pure-gas isotherms from the isotherm of another gas.
3. Investigate whether an excess volume model (within the context of the excess-adsorption concept) can be used for the data reduction and/or modeling high-pressure gas adsorption on coals of varying moisture content.
4. Use a density-measuring apparatus to determine the gas-phase density in the adsorption experiments of wet and dry adsorbents. This would allow more precise data reduction by circumventing the use of an EOS to infer density from pressure, temperature, and gas composition measurements. Such density measurements will be especially beneficial for gas-mixture measurements and for wet systems, where no established EOS exists for calculating the densities of such systems.

REFERENCES

1. Alder B.J., Wainwright T.E. *Studies in Molecular Dynamics. II Behavior of a Small Number of Elastic Spheres*, J. Chem. Phys., 33 (5) 1439-1451 (1960).
2. Angus S., Armstrong B., de Reuck K.M. *International Thermodynamic Tables of the Fluid State-5: Methane*, IUPAC Chemical Data Series No.16, Pergamon Press, New York, (1978).
3. Angus S., de Reuck K.M., Armstrong B. *International Thermodynamic Tables of the Fluid State-6: Nitrogen*, IUPAC Chemical Data Series No.20, Pergamon Press, New York, (1979).
4. Arri L.E., Yee D. *Modeling Coalbed Methane Production with Binary Gas Sorption*, SPE Paper 24363, presented at the SPE Rocky Mountain Regional Meeting, Casper, Wyoming, May 18-21, (1992).
5. Barker J.A., Henderson D. *Monte Carlo Values for the Radial Distribution Function of a System of Fluid Hard Spheres*, Mol. Phys. 21 (1) 187-191 (1971).
6. Berlier K., Olivier M-G., Jadot R. *Adsorption of Methane, Ethane, and Ethylene on Zeolite*, J. Chem. Eng. Data, 40 1206-1208 (1995).
7. Berlier K., Frère M. *Adsorption of CO₂ on Microporous Materials. 1. On Activated Carbon and Silica Gel*, J. Chem. Eng. Data, 42 533-537 (1997).
8. Beutekamp S., Harting P. *Experimental Determination and Analysis of High Pressure Adsorption Data of Pure Gases and Gas Mixture*, Adsorption, 8 255-269 (2002).
9. Brunauer S., Emmett P.H., Teller E.J. *Adsorption of Gases in Multimolecular Layers*, Am.Chem.Soc., 60 309-319 (1938).
10. Chang R.F., Morrison G., Levelt Sengers J.M.H. *The critical dilemma of dilute mixtures*, J. Phys. Chem., 88 (16) 3389-3391 (1984).
11. Chao G.F., Prausnitz J.M. *A Phenomenological Correction to an Equation of State for the Critical Region*, 35 (9) 1487-1496 (1989).

12. Chen J.H., Wong D.S.H., Tan C.S., Subramanian R., Lira C.T., Orth M. *Adsorption and Desorption of Carbon Dioxide onto and from Activated Carbon at High Pressures.*, Ind. Eng. Chem. Res., 36 (7) 2808-2815 (1997).
13. Clayton J.L. *Geochemistry of Coalbed Gas – A Review.* Inter. J. of Coal Geology, 35 159-173 (1998).
14. Crosdale P.J., Beamish B.B., Valix M. *Coalbed Methane Sorption Related to Coal Composition*, Inter. J. of Coal Geology, 35 147-158 (1998).
15. DeGance A.E. *Multicomponent High-Pressure Adsorption Equilibria on Carbon Substrates: Theory and Data*, Fluid Phase Equilib., 78 99-137 (1992).
16. Deiters U.K., de Reuck K.M. *Guidelines for Publication of Equations of State – I. Pure Fluids*, Chem. Eng. J., 69 69-81 (1998).
17. de Reuck K.M. *International Thermodynamic Tables of the Fluid State-11 Fluorine.* International Union of Pure and Applied Chemistry, Pergamon Press, Oxford, (1990).
18. de Vries B., Tillner-Roth R., Baehr H.D. *Thermodynamic Properties of HCFC 124.* 19th International Congress of Refrigeration, The Hague, The Netherlands, International Institute of Refrigeration, Paris, 582-589 (1995).
19. Dhima A., de Hemptinne J., Jose J. *Solubility of Hydrocarbons and CO₂ Mixtures in Water under High Pressure*, Ind. & Eng. Chem. Res., 38 (8) 3144-3161 (1999).
20. Dohrn R., Prausnitz J.M. *A Simple Perturbation Term for the Carnahan-Starling Equation of State*, Fluid Phase Equilib., 61 53-59 (1990).
21. Dreisbach F., Staudt R., Keller J.U. *High Pressure Adsorption Data of Methane, Nitrogen, Carbon Dioxide and Their Binary and Ternary Mixtures on Activated Carbon*, Adsorption, 5 215-227 (1999).
22. Dubinin M.M. “Chemistry and Physics of Carbon Vol. 2”, Walker P.L., Eds., Jr. Edward Arnold Ltd., New York, (1966).
23. Do D.D. “Adsorption Analysis: Equilibria and Kinetics”, Imperial College Press, (1998).
24. Do D.D., Do H.D. *Adsorption of Supercritical Fluids in Non-porous and Porous Carbons: Analysis of Adsorbed Phase Volume and Density*, Carbon, 41 1777-1791 (2003).

25. Elliott J.R., Suresh S.J., Donohue M.D., *A Simple Equation of State for Nonspherical and Associating Molecules*, Ind. Eng. Chem. Res., 29 (7) 1476-1485 (1990).
26. Energy Information Administration. *Advance Summary: U.S. Crude Oil, Natural Gas, and Natural Gas Liquids Reserves 2003 Annual Report*, http://www.eia.doe.gov/oil_gas/fwd/adsum2003.html (2005).
27. Eubank P.T., Kruggel-Emden H., Santana-Rodriquez S., Wang X. *Determination of the Accuracy of Truncated Leiden and Berlin Virial Expansions for Pure Gases*, Fluid Phase Equilib., 207 35-52 (2003).
28. Fitzgerald, J.E., Sudibandriyo, M., Pan, Z., Robinson R.L. Jr., Gasem, K.A.M. *Modeling the Adsorption of Pure Gases on Coals with The SLD Model*, Carbon 41 2203-2216 (2003).
29. Fitzgerald J.E., Pan Z., Sudibandriyo M., Robinson R.L. Jr., Gasem K.A.M. *Adsorption of Methane, Nitrogen, Carbon Dioxide and Their Mixtures on Wet Tiffany Coal*, Fuel, in press (2005).
30. Fox J.R. *Method for Construction of Non-Classical Equations of State*. Fluid Phase Equilib., 14 45-53 (1983).
31. Frère M.G., De Weireld G.F. *High-Pressure and High-Temperature Excess Adsorption Isotherms of N₂, CH₄, and C₃H₈ on Activated Carbon*, J. Chem. Eng. Data, 47 823-829 (2002).
32. Friend D.G., Ingham H., Ely J.F. *Thermophysical Properties of Ethane*, J. Phys. Chem. Ref. Data, 20 (2) 275-347 (1991).
33. Gasem K.A.M., Ross C.H., Robinson R.L. Jr. *Prediction of Ethane and Carbon Dioxide Solubilities in Heavy Normal Paraffins Using Generalized-parameter Soave and Peng-Robinson Equations of State*. Can. J. Chem. Eng. 71 (5) 805-816 (1993).
34. Gasem K.A.M., Robinson R.L. Jr., Fitzgerald J.E., Pan Z., Sudibandriyo M. ., *Sequestering Carbon Dioxide in Coalbeds*, Final Technical Report, 1998-2003, prepared for the U.S. Department of Energy, (2003).
35. Gasem K.A.M. *Class Notes: Process Thermodynamics*, (2001) Unpublished.
36. Goodman A.L., Busch A., Duffy G.J., Fitzgerald J.E., Gasem K.A.M., Gensterblum Y., Krooss B.M., Levy J., Ozdemir E., Pan Z., Robinson R.L. Jr., Schroeder K., Sudibandriyo M., White C.M. *An Inter-laboratory Comparison of CO₂ Isotherms Measured on Argonne Premium Coal Samples*, Energy & Fuels 18 1175-1182 (2004).

37. Gumma S., Talu O. *Gibbs Dividing Surface and Helium Adsorption*, *Adsorption*, 9 (1) 17-28 (2003).
38. Gunter W.D., Gentzis T., Rottenfusser B.A., Richardson R.J.H. *Deep Coalbed Methane in Alberta, Canada: A Fuel Resource with the Potential of Zero Greenhouse Gas Emissions*, *Energy Conversion Management*, 38 suppl. pp. S217 to S222 (1997).
39. Hall F.E. Jr. "Adsorption of Pure and Multicomponent Gases on Wet Fruitland Coal", M.S. Thesis, Oklahoma State University, Stillwater, Oklahoma (1993).
40. Hall F., Zhou C., Gasem K.A.M., Robinson, R.L. Jr. *Adsorption of Pure Methane, Nitrogen, and Carbon Dioxide and Their Binary Mixtures on Wet Fruitland Coal*, presented at the Eastern Regional Conference & Exhibition, Charleston, November 8-10, (1994).
41. Hall F., Zhou C., Gasem K.A.M., Robinson, R.L. Jr. *Adsorption of Pure Methane, Nitrogen, and Carbon Dioxide and Their Binary Mixtures on Wet Fruitland Coal*, SPE Paper 29194 (1994).
42. Henderson D. "Fundamentals of Inhomogeneous Fluids". Chapter 1, Marcel Dekker, Inc. (1992).
43. Hernández-Garduza O., Garcia-Sanchez F., Apam-Martinez D., Vazquez-Roman R. *Vapor Pressures of Pure Compounds Using the Peng-Robinson Equation of State with Three Different Attractive Terms*, *Fluid Phase Equil.*, 198 (2) 195-228 (2002).
44. Holloway S. *Underground Sequestration of Carbon Dioxide – A Viable Greenhouse Mitigation Option*, *Energy*, 30 2318-2333 (2005).
45. Humayun R., Tomasko D.L. *High-Resolution Adsorption Isotherms of Supercritical Carbon Dioxide on Activated Carbon*, *AIChE J.*, 46 2065-2075 (2000).
46. Joubert J.I., Grein C.T., Bienstock D. *Sorption of Methane in Moist Coal*, *Fuel*, 52 181-185 (1973).
47. Kamei A., Beyerlein S.W., Jacobsen R.T. *Application of Nonlinear Regression in the Development of a Wide Range Formulation for HCFC-22*, *Int. J. Thermophys.*, 16 1155-1164 (1995).
48. Keller J.U., Dreisbach F., Rave H., Staudt R., Tomalla M. *Measurement of Gas Mixture Adsorption Equilibria of Natural Gas Compounds on Microporous Sorbents*, *Adsorption* 5, 199-213 (1998).

49. Killingley J.K., Levy J., Day S. *Methane Adsorption on Coals of the Bowen Basin, Queensland, Australia*. Intergas '95. University of Alabama at Tuscaloosa, Alabama. (1995).
50. King A.D. Jr., Coan C.R. *Solubility of Water in Compressed Carbon Dioxide, Nitrous Oxide and Ethane. Evidence for Hydration of Carbon Dioxide and Nitrous Oxide in the Gas Phase*, J. Am. Chem. Soc., 93 (8) 1857-1862 (1971).
51. Langmuir, I. *The Adsorption of Gases on Plane Surfaces of Glass, Mica, and Platinum*, J. Am. Chem. Soc. 40 1361 (1918).
52. Lee L.L. "Molecular Thermodynamics of Non-Ideal Fluids"; Butterworths: Stoneham, Ma, (1998).
53. Liang X. "Adsorption of Pure and Multi-Component Gas on Wet Coal", Stillwater, M.S. Thesis, Oklahoma State University, Stillwater, Oklahoma (1999).
54. Linstrom P.J., Mallard, W.G. Eds. NIST Chemistry WebBook, NIST Standard Reference Database Number 69, March 2003, National Institute of Standards and Technology, Gaithersburg MD, 20899 (<http://webbook.nist.gov>).
55. Magee J.W., Howley J.A., Ely J.F. *A Predictive Model for the Thermophysical Properties of Carbon Dioxide Rich Mixtures*. Gas Processors Association RR-136 March (1994).
56. Manik J. "Compositional Modeling of Enhanced Coalbed Methane Recovery". Ph.D. Thesis, Pennsylvania State University, Dept. of Energy and Geo-Environmental Engineering (1999).
57. Masalov Ya. F. *Calculation of Boyle's Temperature for Gases*, Teploenergetika, 15 (6) 88-90 (1968).
58. Mavor M., Pratt T., DeBruyn R. *Study Quantifies Powder River Coal Seam Properties*, Oil and Gas Journal, 35-50, April 26 (1999).
59. McCarty R.D. *Thermophysical Properties of Helium-4 from 2 to 1500 K with Pressures to 1000 Atmospheres*. NBS Technical Note 631, U.S. Dept of Commerce (1972).
60. McFall J.H., Wilson D.H., Lee L.L. *Accurate Correlation of the Second Virial Coefficients of Some 40 Chemicals Based on Anisotropic Square-Well Potential*, Ind. Eng. Chem. Res., 41 (5) 1107-1112 (2002).
61. Miyamoto, H. and Watanabe, K. *A Thermodynamic Property Model for Fluid-Phase Propane*, Int. J. Thermophys. 21, 5, 1045-1072 (2000)

62. Mulero A., Galan C., Cuadros F. *Equations of State for Hard Spheres. A Review of Accuracy and Applications*, Phys. Chem. Chem. Phys., 3 (22) 4991-4999 (2001).
63. Myers A.L., Prausnitz J.M. *Thermodynamica of Mixed-Gas Adsorption*, AIChE J., 11 121 (1965).
64. Myers, A.L. *Thermodynamics of Adsorption in Porous Materials*, AIChE J., 48 145-160 (2002).
65. Michelsen J.K., Khavari-Khorasani G. *Coal Bed Gas Content and Gas Undersaturation*, in "Coalbed Methane: Scientific, Environmental and Economic Evaluation", Mastalerz M., Kluwer Academic Publishers (1999).
66. Nasehzadeh A., Mohseni M., Azizi K. *The Effect of Temperature on the Lennard-Jones (6-12) pair potential*, J. Molecular Structure, 589-590 329-335. (2002).
67. Ono S., Kondo S. *Molecular Theory of Surface Tension in Liquids*, in "Encyclopedia of Physics (S. Flugge, Ed.), Vol. X.", Springer-Verlag, Gottingen, (1960).
68. Ozdemir E., Morsi B.I., Schroeder K. *Importance of Volume Effects to Adsorption Isotherms of Carbon Dioxide on Coals*, Langmuir, 19 9764-9773 (2003).
69. Pan Z. "Modeling of Gas Adsorption Using Two-Dimensional Equations of State", Ph.D. Dissertation, Oklahoma State University, Stillwater, Oklahoma (2003).
70. Payne H.K., Sturdevant G.A., Leland T.W. *Improved Two-Dimensional Equation of State to Predict Adsorption of Pure and Mixed Hydrocarbons*, I&EC Fundamentals, 7 363-374 (1968).
71. Peters V. *The Approximation of the Critical Isotherm with Broken Rational Function*, Fluid Phase Equil., 69 1-14 (1991).
72. Pitzer K.S., Curl R.F. Jr. *Volumetric and Thermodynamic Properties of Fluids. III. Empirical Equation for the Second Virial Coefficient*, J. Amer. Chem. Soc., 79 2369-70 (1957).
73. Pray H.A., Schweickert C.E., Minnich B.H., *Solubility of Hydrogen, Oxygen, Nitrogen, and Helium in Water at Elevated Temperatures*, Ind. Eng. Chem. Res., 44 1146-1151 (1952).
74. Puri R., Yee D. *Enhanced Coalbed Methane Recovery*, SPE Paper 20732 (1990).
75. Rangarajan B., Lira C.T., Subramanian R. *Simplified local density model for adsorption over large pressure ranges*, AIChE J., 41 (4) 838-845 (1995).

76. Ray G.C., Box E.O. *Adsorption of Gases on Activated Carbon*, Ind. Eng. Chem. Res., 42 1315-1318 (1950).
77. Reich R., Ziegler W.T., Rogers K.A. *Adsorption of Methane, Ethane, and Ethylene Gases and Their Binary and Ternary Mixtures and Carbon Dioxide on Activated Carbon at 212-301 K and Pressures to 35 Atmospheres*, Ind. Eng. Chem. Process Des. Dev., 19 336 (1980).
78. Reid R.C., Prausnitz J.M., Poling B.E. "The Properties of Gases and Liquids", McGraw Hill, Inc. (1987).
79. Rigby M., Smith E.B., Wakeham W.A., Maitland G.C. "The Forces between Molecules", Oxford University Press. (1986).
80. Ritter J.A., Yang R.T. *Equilibrium Adsorption of Multicomponent Gas Mixtures at Elevated Pressures*, Ind. Eng. Chem. Res., 26 1679-1686 (1987).
81. Schmidt R., Wagner W. *A New Form of the Equation of State for Pure Substances and its Application to Oxygen*, Fluid Phase Equil., 19 175-200 (1985).
82. Setzmann U., Wagner W. *A New Equation of State and Tables of Thermodynamic Properties for Methane Covering the Range from the Melting Line to 625 K at Pressures up to 1000 MPa*, J. Phys. Chem. Ref. Data., 20 (6) 1061-1151 (1991).
83. Smukala J., Span R., Wagner W. *A New Equation of State for Ethylene Covering the Fluid Region for Temperatures from the Melting Line to 450 K at Pressures up to 300 MPa*, J. Phys. Chem. Ref. Data, 29 5 1053-1122 (2000).
84. Soule A.D., Smith C.A., Yang X., Lira C.T. *Adsorption Modeling with the ESD equation of state*, Langmuir, 17 (10) 2950-2957 (2001).
85. Soule A.D. "Studies of Gas Adsorption on Activated Carbon and Cherry Flavor Recovery from Cherry Pits", M.S. Thesis, Michigan State University, East Lansing, Michigan (1998).
86. Sofyan Y. "Development of Multiphase Equilibrium Algorithms: Cloud Point Temperature and Solid Precipitation Predictions", Ph.D. Thesis, Oklahoma State University, Stillwater, Oklahoma (2001).
87. Span R., Wagner W. *A New Equation of State for Carbon Dioxide Covering the Fluid Region from the Triple Point Temperature to 1100 K at Pressures up to 800 MPa*, J. Phys. Chem. Ref. Data, 25 1509-1590 (1996).
88. Span R. "Multiparameter Equations of State - An Accurate Source of Thermodynamic Property Data", Springer, Berlin, 367, (2000).

89. Span R., Lemmon E., Jacobsen R.T., Wagner W., Yokozeki A. *A Reference Equation of State for the Thermodynamic Properties of Nitrogen for Temperatures from 63.151 to 1000 K and Pressures to 2200 MPa*, J. Phys. Chem. Ref. Data, 29 (6) 1361-1433 (2000).
90. Stacy T.D., Hough E.W., Mc.Cain W.D. Jr. *Adsorption of Methane on Carbon at Temperature to 121 °C and Pressures to 650 Atm.*, J. Chem. Eng. Data, 13 74-77 (1968).
91. Stevens S., Spector D., Reimer P. SPE 48881. *Enhanced Coalbed Methane Recovery Using CO₂ Injection: Worldwide Resource and CO₂ sequestration Potential*, Proceedings, Sixth International Oil and Gas Conference and Exhibition in China, Vol. 1 (1998).
92. Stevenson M.D., Pinczewski W.K. *Economic Evaluation of Nitrogen Injection of Coalseam Gas Recovery*, SPE Paper 26199, (1993).
93. Sudibandriyo M., "Generalized Ono-Kondo Lattice Model for High-pressure Adsorption on Carbon Adsorbents", Ph.D. Dissertation, Oklahoma State University, Stillwater, Oklahoma (2003).
94. Sudibandriyo M., Pan Z., Fitzgerald J.E., Robinson R.L. Jr., Gasem K.A.M. *Adsorption of Methane, Nitrogen, Carbon Dioxide and their Binary Mixtures on Dry Activated Carbon at 318.2 K and Pressures to 13.6 MPa*, Langmuir, 19 (13) 5323-5331 (2003).
95. Subramanian R., Pyada H., Lira C.T. *An Engineering Model for Adsorption of Gases onto Flat Surfaces and Clustering in Supercritical Fluids*, Ind. Eng. Chem. Res., 34 (11) 3830-37 (1995).
96. Talu O., Zwiebel I. *Multicomponent Adsorption Equilibria of Nonideal Mixtures*, AIChE J., 32 1263-1276 (1986).
97. Tegeler Ch., Span R., Wagner W. *A New Equation of State for Argon Covering the Fluid Region for Temperatures from the Melting Line to 700 K at Pressures up to 1000 MPa*, J. Phys. Chem. Ref. Data, 28 (3) 779-850 (1999).
98. Tillner-Roth R., Harms-Watzenberg F., Baehr H.D., *Eine neue Fundamentalgleichung für Ammoniak*. DKV-Tagungsbericht. 20 167-181 (1993).
99. Tillner-Roth R. Yokozeki A. *An International Standard Equation of State for Difluoromethane (R-32) for Temperatures from the Triple Point at 136.34 K to 435 K and Pressures up to 70 Mpa*, J. Phys. Chem. Ref. Data, 26 (6) 1273-1328 (1997).
100. Tsonopoulos, C. *Empirical Correlation of Second Virial Coefficients*, AIChE J., 20 263-272 (1974).

101. U. S. Department of Energy. *The Capture, Utilization and Disposal of Carbon Dioxide from Fossil Fuel-fired Power Plants*. DE94-002377 (1993).
102. Ustinov E.A., Do D.D., Herbst A., Staudt R., Harting, P. *Modeling of Gas Adsorption Equilibrium Over a Wide Range of Pressure: A Thermodynamic Approach Based on Equation of State*, J. Colloid Interface Sci., 250 (1) 49-62 (2002).
103. van der Vaart R., Huiskes C., Bosch H., Reith T. *Single and Mixed Gas Adsorption Equilibria of Carbon Dioxide/Methane on Activated Carbon*, Adsorption, 6 311-323 (2000).
104. Vargas P., Munoz E., Rodriguez L. *Second Virial Coefficient for the Lennard-Jones Potential*, Physica A, 290 92-100 (2001).
105. Wagner W., Pruss A. *The IAPWS formulation 1995 for the Thermodynamic Properties of Ordinary Water Substance for General and Scientific Use*, J. Phys. Chem. Ref. Data, 31 (2) 387-535 (2002).
106. Wakasugi Y., Ozawa S., Ogino Y. *Physical Adsorption of Gases at High Pressure, V. An Extension of a Generalized Adsorption Equation to System with Polar Adsorbents*, J. Col. and Inter. Sci., 79 399-409 (1981).
107. Weibe R., Gaddy V. *The Solubility of Carbon Dioxide in Water at Various Temperatures from 12° to 40° and at Pressures to 500 Atmospheres, Critical Phenomena*, J. Amer. Chem. Soc., 62 815-817 (1940).
108. White C.M., Smith D.H., Jones K.L, Goodman A.L., Jikich S.A., LaCount R.B., DuBose S.B., Ozdemir E., Morsi B.I., Schroeder K.T. *Sequestration of Carbon Dioxide in Coal with Enhanced Coalbed Methane Recovery – A Review*, Energy & Fuels, 19 (3) 659-724 (2005).
109. Winter E.M., Bergman P.D. *Availability of Depleted Oil and Gas Reservoirs for Disposal of Carbon Dioxide in the United States*, Energy Convers. Manag., 34 (9-11) 1177-87 (1993).
110. Woodcock L.V. *Hard-Sphere Fluid Equation of State*, J. Chem. Soc. Faraday Trans. 2, 72 (3) 731-735 (1976).
111. Wu G., Sadus R.J. *Hard Sphere Compressibility Factors for Equation of State Development*, AIChE J., 51 (1) 309-313 (2004).
112. Yaginuma R., Sato Y., Kodama D., Tanaka H., Kato M. *Saturated Densities of Carbon Dioxide + Water Mixture at 304.1 K and Pressures to 10 MPa*, J. Japanese Institute of Energy, 79 (2) 144-146 (2000).

113. Yamasaki A. *An Overview of CO₂ Mitigation Options for Global Warming – Emphasizing CO₂ Sequestration Options*, J. Chem. Eng. of Japan, 36 (4) 361-375 (2003).
114. Yelash L.V., Kraska T. *A Generic Equation of State for the Hard-Sphere Fluid Incorporating the High-Density Limit*, Phys. Chem. Chem. Phys., 3 (15) 3114-3118 (2001).
115. Younglove B.A. *Thermophysical Properties of Fluids. I. Argon, Ethylene, Parahydrogen, Nitrogen, Nitrogen Trifluoride, and Oxygen*, J. Phys. Chem. Ref. Data, 11 1-11 (1982).
116. Younglove B.A., Ely J.F. *Thermophysical Properties of Fluids. II. Methane, Ethane, Propane, Isobutane and Normal Butane*, J. Phys. Chem. Ref. Data, 16 577-798 (1987).
117. Younglove B.A., McLinden M.O. *An International Standard Equation-of-state Formulation of the Thermodynamic Properties of Refrigerant 123 (2,2-dichloro-1,1,1-trifluoroethane)*, J. Phys. Chem. Ref. Data, 23 731-779 (1994).
118. Zhang J., Zhang X., Han B., He J., Liu Z., Yang G. *Study on the Intermolecular Interactions in Supercritical Fluids by Partial Molar Volume and Isothermal Compressibility*, J. Supercritical Fluids, 22 15-19 (2002).
119. Zhou C., Hall F., Gasem K.A.M., Robinson R.L. Jr. *Predicting Gas Adsorption Using Two-Dimensional Equations of State*, I&EC Research, 33 1280-1289 (1994).
120. Zhou L., Zhou Y., Li M., Chen P., Wang Y. *Experimental and Modeling Study of the Adsorption of Supercritical Methane on a High Surface Activated Carbon*, Langmuir, 16 5955-5959 (2000).
121. Zhou L., Zhou Y., Bai S., Lu C., Yang B. *Determination of the Adsorbed Phase Volume and Its Application in Isotherm Modeling for the Adsorption of Supercritical Nitrogen on Activated Carbon*, J. Colloid Interface Sci., 239 33-38 (2001).
122. Zuber M. *The Use of Monte Carlo Analysis to Evaluate Prospective Coalbed Methane Properties*, in “Coalbed Methane: Scientific, Environmental and Economic Evaluation”, Mastalerz M., Kluwer Academic Publishers (1999).

APPENDIX A: LOCAL $a(z)$ FOR FLUID IN A SLIT

Table A-1. Equations for the Local Attractive Parameter $a(z)$

| Region | Case 1: $\frac{L}{\sigma_{ff}} \geq 3$ |
|---|---|
| $0.5 \leq \frac{z}{\sigma_{ff}} \leq 1.5$ | $\frac{a(z)}{a_b} = \frac{3}{8} \left(\frac{z}{\sigma_{ff}} + \frac{5}{6} - \frac{1}{3 \left(\frac{L-z}{\sigma_{ff}} - 0.5 \right)^3} \right)$ |
| $1.5 \leq \frac{z}{\sigma_{ff}} \leq \frac{L}{\sigma_{ff}} - 1.5$ | $\frac{a(z)}{a_b} = \frac{3}{8} \left(\frac{8}{3} - \frac{1}{3 \left(\frac{z}{\sigma_{ff}} - 0.5 \right)^3} - \frac{1}{3 \left(\frac{L-z}{\sigma_{ff}} - 0.5 \right)^3} \right)$ |
| $\frac{L}{\sigma_{ff}} - 1.5 \leq \frac{z}{\sigma_{ff}} \leq \frac{L}{\sigma_{ff}} - 0.5$ | $\frac{a(z)}{a_b} = \frac{3}{8} \left(\frac{L-z}{\sigma_{ff}} + \frac{5}{6} - \frac{1}{3 \left(\frac{z}{\sigma_{ff}} - 0.5 \right)^3} \right)$ |
| Case 2: $2 \leq \frac{L}{\sigma_{ff}} \leq 3$ | |
| $0.5 \leq \frac{z}{\sigma_{ff}} \leq \frac{L}{\sigma_{ff}} - 1.5$ | $\frac{a(z)}{a_b} = \frac{3}{8} \left(\frac{z}{\sigma_{ff}} + \frac{5}{6} - \frac{1}{3 \left(\frac{L-z}{\sigma_{ff}} - 0.5 \right)^3} \right)$ |
| $\frac{L}{\sigma_{ff}} - 1.5 \leq \frac{z}{\sigma_{ff}} \leq 1.5$ | $\frac{a(z)}{a_b} = \frac{3}{8} \left(\frac{L}{\sigma_{ff}} - 1 \right)$ |
| $1.5 \leq \frac{z}{\sigma_{ff}} \leq \frac{L}{\sigma_{ff}} - 0.5$ | $\frac{a(z)}{a_b} = \frac{3}{8} \left(\frac{L-z}{\sigma_{ff}} + \frac{5}{6} - \frac{1}{3 \left(\frac{z}{\sigma_{ff}} - 0.5 \right)^3} \right)$ |
| Case 3: $1.5 \leq \frac{L}{\sigma_{ff}} \leq 2$ | |
| Anywhere within slit | $\frac{a(z)}{a_b} = \frac{3}{8} \left(\frac{L}{\sigma_{ff}} - 1 \right)$ |

APPENDIX B: DERIVATIONS AND SUPPLEMENTARY INFORMATION FOR THE HARD-SPHERE EOS

Application of the constraint equations at the critical point allows for calculation of three additional constants. For polar fluids, three additional empirical constraint equations are added to minimize the number of regressed parameters. The derivation and procedure to solve all these constraint equations simultaneously without numerical solution is presented in this appendix. Following the solution of these constraint equations, the derivation of the fugacity is presented.

For convenience, the constraint equations at the critical point are broken up between the hard-sphere, attractive, and polar terms. Henceforth all derivative values and critical properties are understood to be applied at the critical point, unless otherwise stated.

$$\frac{\partial P_{\text{att}}}{\partial v} = \alpha \quad \frac{\partial P_{\text{hs}}}{\partial v} = \beta \quad \frac{\partial P_{\text{polar}}}{\partial v} = \delta \quad (\text{B-1,2,3})$$

$$\frac{\partial^2 P_{\text{att}}}{\partial v^2} = \gamma \quad \frac{\partial^2 P_{\text{hs}}}{\partial v^2} = \lambda \quad \frac{\partial^2 P_{\text{polar}}}{\partial v^2} = \Phi \quad (\text{B-4,5,6})$$

In terms of these symbols, the three classical constraint equations at the critical point are:

$$\alpha + \beta + \delta = 0, \quad \gamma + \lambda + \Phi = 0 \quad P_c = (P_{\text{polar}})_{\text{cp}} + (P_{\text{att}})_{\text{cp}} + (P_{\text{hs}})_{\text{cp}} \quad (\text{B-7,8,9})$$

The procedure is to find expressions for the first and second derivatives as shown in Equations (1-6) and then apply them in Equations (7-9). To begin, the hard-sphere EOS obtained from Yelash and Kraska (2001) is restated here for completeness:

$$Z_{\text{HS}} = 1 + B_2x + B_3x^2 + B_4x^3 + \frac{C(x/\xi)^4}{1 - x/\xi} \quad \text{where } x = \frac{v_{\text{hs}}}{v} \quad (\text{B-10})$$

The hard-sphere term is written explicitly in terms of pressure to facilitate conveniently the application of its derivative with respect to specific volume.

$$P_{\text{HS}} = \frac{RT}{v_{\text{hs}}} \left[x + B_2x^2 + B_3x^3 + B_4x^4 + \frac{C\xi(x/\xi)^5}{1 - x/\xi} \right] \quad (\text{B-11})$$

Constants for B are regressed from hard-sphere simulation data. The hard sphere constants B_2 , B_3 , and B_4 are 4, 10, and 18.36, respectively; $C = 9$ and $\xi = 0.75$. The generalized attractive term, written explicitly in terms of the attractive pressure:

$$P_{\text{att}} = -\frac{a}{(v_{\text{hs}})^2} \left(\begin{array}{l} -\frac{x^2}{1 + D_1x + D_2x^2} + D_3x^2 + D_4x^3 \\ + D_5x^4 + \frac{D_6x^5}{1 + D_1x + D_2x^2} \end{array} \right) \quad (\text{B-12})$$

The temperature dependent functions are omitted here for simplicity and because at the critical point they are all equal to unity. Note that Equation (12) contains the constant D_5 , which is zero for all fluids. Nevertheless, it is carried throughout this derivation as if it were non-zero in order to provide reference in future studies.

The generalized polar term is written explicitly in terms of the polar pressure:

$$P_{\text{polar}} = -\frac{y}{(v_{\text{hs}})^2} \left(\begin{array}{l} -\frac{x^2}{1 + D_1x + D_2x^2} + D_7x^2 + D_8x^3 \\ + D_9x^4 + D_{10}x^5 + \frac{D_{11}\xi(x/\xi)^5}{1 - x/\xi} \end{array} \right) \quad (\text{B-13})$$

Equations (12-14) are rewritten in terms of specific volume:

$$P_{\text{hs}} = \frac{RT}{v_{\text{hs}}} \left[\frac{v_{\text{hs}}}{v} + B_2 \left(\frac{v_{\text{hs}}}{v} \right)^2 + B_3 \left(\frac{v_{\text{hs}}}{v} \right)^3 + B_4 \left(\frac{v_{\text{hs}}}{v} \right)^4 + \frac{C\xi(v_{\text{hs}}/(v\xi))^5}{1 - (v_{\text{hs}}/(v\xi))} \right] \quad (\text{B-14})$$

$$P_{\text{att}} = -\frac{a}{v^2} \left(\begin{aligned} & -\frac{v^2}{v^2 + D_1(v_{\text{hs}})v + D_2(v_{\text{hs}})^2} + D_3 + D_4 \frac{v_{\text{hs}}}{v} \\ & + D_5 \left(\frac{v_{\text{hs}}}{v} \right)^2 + \frac{D_6 v^2 \left(\frac{v_{\text{hs}}}{v} \right)^3}{v^2 + D_1(v_{\text{hs}})v + D_2(v_{\text{hs}})^2} \end{aligned} \right) \quad (\text{B-15})$$

$$P_{\text{polar}} = -\frac{y}{v^2} \left(\begin{aligned} & -\frac{v^2}{v^2 + D_1(v_{\text{hs}})v + D_2(v_{\text{hs}})^2} + D_7 + D_8 \frac{v_{\text{hs}}}{v} \\ & + D_9 \left(\frac{v_{\text{hs}}}{v} \right)^2 + D_{10} \left(\frac{v_{\text{hs}}}{v} \right)^3 + \frac{D_{11} (v_{\text{hs}}/(v\xi))^3}{\xi (1 - v_{\text{hs}}/(v\xi))} \end{aligned} \right) \quad (\text{B-16})$$

The derivatives of these equations contain common repetitive expressions or contain expressions that are represented as new symbols for typographical convenience:

$$\theta = v^2 + D_1 v_{\text{hs}} v + D_2 (v_{\text{hs}})^2 \quad (\text{B-17})$$

$$M = D_1 v_{\text{hs}} + 2v \quad (\text{B-18})$$

$$\gamma_0 = \frac{x^3}{\theta} \quad (\text{B-19})$$

$$\gamma_1 = \frac{3x^4}{\theta v_{\text{hs}}} + \frac{Mx^3}{\theta^2} \quad (\text{B-20})$$

$$\gamma_2 = \frac{12x^5}{\theta(v_{\text{hs}})^2} + \frac{6Mx^4}{\theta^2 v_{\text{hs}}} - \frac{2x^3}{\theta^2} + \frac{2M^2 x^3}{\theta^3} \quad (\text{B-21})$$

$$\psi_0 = \frac{\xi}{(v_{\text{hs}})^2} \left(\frac{v_{\text{hs}}}{v\xi} \right)^5 \frac{1}{(1 - v_{\text{hs}}/(v\xi))} \quad (\text{B-22})$$

$$\psi_1 = \frac{\xi^2}{(v_{\text{hs}})^3} \left(\frac{v_{\text{hs}}}{v\xi} \right)^6 \frac{(5 - 4(v_{\text{hs}}/(v\xi)))}{(1 - (v_{\text{hs}}/v\xi))^2} \quad (\text{B-24})$$

$$\psi_2 = \frac{2\xi^3}{(v_{hs})^4} \left(\frac{v_{hs}}{v\xi} \right)^7 \frac{(10(v_{hs}/(v\xi))^2 - 24(v_{hs}/(v\xi)) + 15)}{(1 - (v_{hs}/v\xi))^3} \quad (\text{B-25})$$

The first-order derivatives are as follows:

$$\frac{\partial P_{hs}}{\partial v} = \beta = -\frac{RT}{(v_{hs})^2} \left[\left(\frac{v_{hs}}{v} \right)^2 + 2B_2 \left(\frac{v_{hs}}{v} \right)^3 + 3B_3 \left(\frac{v_{hs}}{v} \right)^4 + 4B_4 \left(\frac{v_{hs}}{v} \right)^5 + C(v_{hs})^3 \psi_1 \right] \quad (\text{B-26})$$

$$\begin{aligned} \frac{\partial P_{att}}{\partial v} = \alpha = & -\frac{aM}{\theta^2} + 2\frac{D_3 a}{v^3} + 3\frac{D_4 a(v_{hs})}{v^4} + 4\frac{D_5 a(v_{hs})^2}{v^5} \\ & + \left(\frac{3D_6 a}{v} \right) \gamma_0 + \frac{D_6 aM \gamma_0}{\theta} \end{aligned} \quad (\text{B-27})$$

$$\begin{aligned} \frac{\partial P_{polar}}{\partial v} = \delta = & -\frac{yM}{\theta^2} + 2\frac{D_7 y}{v^3} + 3\frac{D_8 y(v_{hs})}{v^4} + 4\frac{D_9 y(v_{hs})^2}{v^5} \\ & + 5\frac{D_{10} y(v_{hs})^3}{v^6} + D_{11} \psi_1 \end{aligned} \quad (\text{B-28})$$

The second-order derivatives are as follows:

$$\frac{\partial^2 P_{hs}}{\partial v^2} = \gamma = \frac{RT}{(v_{hs})^3} \left[2 \left(\frac{v_{hs}}{v} \right)^3 + 6B_2 \left(\frac{v_{hs}}{v} \right)^4 + 12B_3 \left(\frac{v_{hs}}{v} \right)^5 + 20B_4 \left(\frac{v_{hs}}{v} \right)^6 + C(v_{hs})^4 \psi_2 \right] \quad (\text{B-29})$$

$$\begin{aligned} \frac{\partial^2 P_{att}}{\partial v^2} = \lambda = & -\frac{2a}{\theta^2} + \frac{2aM^2}{\theta^3} - 6\frac{D_3 a}{v^4} - 12\frac{D_4 a v_{hs}}{v^5} \\ & - 20\frac{D_5 a(v_{hs})^2}{v^6} - aD_6 \gamma_2 \end{aligned} \quad (\text{B-30})$$

$$\begin{aligned} \frac{\partial^2 P_{\text{polar}}}{\partial v^2} = \Phi = & -\frac{2y}{\theta^2} + \frac{2yM^2}{\theta^3} - 6\frac{D_7 y}{v^4} - 12\frac{D_8 y v_{\text{hs}}}{v^5} \\ & - 20\frac{D_9 y (v_{\text{hs}})^2}{v^6} - 30\frac{D_{10} y (v_{\text{hs}})^3}{v^7} - yD_{11}\Psi_2 \end{aligned} \quad (\text{B-31})$$

At this point, the attractive and polar terms contain constants that are unknown. However, the hard-sphere pressure and its derivatives can be calculated readily from critical properties and the hard-sphere volume, which is a regressed parameter. With this in mind, constraint Equations (7) and (8) are written here so that only the terms in the attractive and polar pressure are expressed explicitly:

$$\begin{aligned} 2(a+y)\left(-\frac{1}{\theta^2} + \frac{M^2}{\theta^3}\right) = & -\lambda + \frac{6}{v^4}(D_3 a + D_7 y) + \frac{12v_{\text{hs}}}{v^5}(D_4 a + D_8 y) \\ & + \frac{20(v_{\text{hs}})^2}{v^6}(D_5 a + D_9 y) + \frac{30(v_{\text{hs}})^3}{v^7}(D_{10} y) \\ & + (aD_6)\gamma_2 + D_{11} y\Psi_2 \end{aligned} \quad (\text{B-32})$$

$$\begin{aligned} -(a+y)\frac{M}{\theta^2} = & -\beta - \frac{2}{v^3}(D_3 a + D_7 y) - \frac{3v_{\text{hs}}}{v^4}(D_4 a + D_8 y) \\ & - \frac{4(v_{\text{hs}})^2}{v^5}(D_5 a + D_9 y) - \frac{5(v_{\text{hs}})^3}{v^6}(D_{10} y) - (aD_6)\gamma_1 - D_{11} y\Psi_1 \end{aligned} \quad (\text{B-33})$$

The constants D_3 and D_7 are eliminated by multiplying Equation (33) by $3/v$ and adding the result to Equation (32):

$$\begin{aligned} 2(a+y)\left(-\frac{1}{\theta^2} + \frac{M^2}{\theta^3}\right) - 3(a+y)\frac{M}{\theta^2 v} = & -\lambda - \frac{3\beta}{v} + \frac{3v_{\text{hs}}}{v^5}(D_4 a + D_8 y) \\ & + \frac{8(v_{\text{hs}})^2}{v^6}(D_5 a + D_9 y) + \frac{15(v_{\text{hs}})^3}{v^7}(D_{10} y) \\ & + (aD_6)\left(\gamma_2 - 3\frac{\gamma_1}{v}\right) + D_{11} y\left(\Psi_2 - 3\frac{\Psi_1}{v}\right) \end{aligned} \quad (\text{B-34})$$

Equation (9) can be represented with the attractive and polar pressure terms expressed explicitly:

$$\begin{aligned} \frac{(a+y)}{\theta} = & P_c - (P_{hs})_{cp} + \frac{1}{v^2} (D_3 a + D_7 y) + \frac{v_{hs}}{v^3} (D_4 a + D_8 y) \\ & + \frac{(v_{hs})^2}{v^4} (D_5 a + D_9 y) + \frac{(v_{hs})^3}{v^5} (D_{10} y) + (a D_6) \gamma_0 + D_{11} y \Psi_0 \end{aligned} \quad (B-35)$$

The constants D_3 and D_7 are also eliminated by multiplying Equation (35) by $2/v$ and adding the result to Equation (33). The resulting equation, multiplied by $3/v$, is:

$$\begin{aligned} \frac{3 v_{hs}}{v^5} (D_4 a + D_8 y) = & \frac{3M}{\theta^2 v} (a+y) - 3 \frac{\beta}{v} - (a+y) \frac{6}{\theta v^2} + 6 \frac{(P_c - (P_{hs})_{cp})}{v^2} \\ & - \frac{6(v_{hs})^2}{v^6} (D_5 a + D_9 y) - \frac{9(v_{hs})^3}{v^7} (D_{10} y) \\ & + \frac{3(2\gamma_0 / v - \gamma_1)}{v} (D_6 a) + \frac{3(2\Psi_0 / v - \Psi_1)}{v} (D_{11} y) \end{aligned} \quad (B-36)$$

By adding Equation (36) to (34), the constants D_4 and D_8 are eliminated. The resulting sum has all terms that contain the constant 'a' grouped together on one side of the equation:

$$\begin{aligned} 2a \left(-\frac{1}{\theta^2} + \frac{M^2}{\theta^3} \right) - a \frac{6M}{\theta^2 v} + a \frac{6}{\theta v^2} - D_5 a \frac{2(v_{hs})^2}{v^6} \\ - D_6 a \frac{(6\gamma_0 - 6\gamma_1 v + \gamma_2 v^2)}{v^2} = -\lambda - \frac{6\beta}{v} + \frac{6(P_c - P_{hs})}{v^2} \\ - 2y \left(-\frac{1}{\theta^2} + \frac{M^2}{\theta^3} \right) + y \frac{6M}{\theta^2 v} - y \frac{6}{\theta v^2} + D_9 y \frac{2(v_{hs})^2}{v^6} \\ + D_{10} y \frac{6(v_{hs})^3}{v^7} + D_{11} y \frac{(6\Psi_0 - 6\Psi_1 v + \Psi_2 v^2)}{v^2} \end{aligned} \quad (B-37)$$

Solving for the constant 'a' gives:

$$a = \frac{\theta^3 \left(\begin{array}{c} -\lambda v^2 - 6\beta v \\ + 6(P_c - (P_{hs})_{cp}) \end{array} \right) - y \left[\begin{array}{c} -2\theta v^2 + 2M^2 v^2 - 6M\theta v \\ + 6\theta^2 - 2D_9 \theta^3 (v_{hs})^2 / v^4 \\ - 6D_{10} \theta^3 (v_{hs})^3 / v^5 \\ - D_{11} \theta^3 (6\Psi_0 - 6\Psi_1 v + \Psi_2 v^2) \end{array} \right]}{\left[\begin{array}{c} -2\theta v^2 + 2M^2 v^2 - 6M\theta v + 6\theta^2 \\ - 2D_5 \theta^3 (v_{hs})^2 / v^4 - D_6 \theta^3 (6\gamma_0 - 6\gamma_1 v + \gamma_2 v^2) \end{array} \right]} \quad (\text{B-38})$$

Through use of Equation (34), back solution gives D_4 :

$$D_4 = \left(1 + \frac{y}{a} \right) \left(-\frac{2v^5}{3\theta^2 v_{hs}} + \frac{2M^2 v^5}{3\theta^3 v_{hs}} - \frac{M v^4}{\theta^2 v_{hs}} \right) - \frac{y}{a} \left(D_8 + \frac{8D_9 v_{hs}}{3v} + \frac{5D_{10} (v_{hs})^2}{v^2} + \frac{D_{11} v^5}{3v_{hs}} \left(\Psi_2 - 3\frac{\Psi_1}{v} \right) \right) + \frac{\lambda v^5}{3v_{hs} a} + \frac{\beta v^4}{v_{hs} a} - \frac{8D_5 v_{hs}}{3v} - \frac{D_6 v^5}{3v_{hs}} \left(\gamma_2 - 3\frac{\gamma_1}{v} \right) \quad (\text{B-39})$$

Through use of Equation (35), back solution gives D_3 :

$$D_3 = \frac{y}{a} \left[\frac{v^2}{\theta} - D_7 - \frac{v_{hs}}{v} D_8 - \left(\frac{v_{hs}}{v} \right)^2 D_9 - \left(\frac{v_{hs}}{v} \right)^3 D_{10} - D_{11} \Psi_0 v^2 \right] + \frac{v^2}{\theta} - \frac{v^2}{a} [P_c - (P_{hs})_{cp}] - \frac{v_{hs}}{v} D_4 - \left(\frac{v_{hs}}{v} \right)^2 D_5 - D_6 \gamma_0 v^2 \quad (\text{B-40})$$

The values for D_3 and D_4 are constrained to remain unchanged for polar and non-polar fluids. To do this, the values of D_7 and D_8 are solved that make them unchanged.

The two constraints are:

$$(D_3)_{\text{polar}} = (D_3)_{\text{non-polar}} \quad (D_4)_{\text{polar}} = (D_4)_{\text{non-polar}} \quad (\text{B-41,42})$$

By using Equation (40), the constraint equation for D_3 can be written as:

$$\begin{aligned}
& \frac{y}{a_p} \left[\frac{v^2}{\theta} - D_7 - \frac{v_{hs}}{v} D_8 - \left(\frac{v_{hs}}{v} \right)^2 D_9 - \left(\frac{v_{hs}}{v} \right)^3 D_{10} - D_{11} \Psi_0 v^2 \right] \\
& + \frac{v^2}{\theta} - \frac{v^2}{a_p} \left[P_c - (P_{hs})_{cp} \right] - \frac{v_{hs}}{v} D_4 - \left(\frac{v_{hs}}{v} \right)^2 D_5 - D_6 \gamma_0 v^2 \\
& = \frac{v^2}{\theta} - \frac{v^2}{a_{n-p}} \left[P_c - (P_{hs})_{cp} \right] - \frac{v_{hs}}{v} D_4 - \left(\frac{v_{hs}}{v} \right)^2 D_5 - D_6 \gamma_0 v^2
\end{aligned} \tag{B-43}$$

In Equation (43), the subscript ‘P’ on the constant ‘a’ refers to the value of the constant ‘a’ solved with the polar constants in Equation (38); the subscript ‘n-P’ (non-polar) on the constant ‘a’ refers to the value of the constant ‘a’ solved with the polar constant ‘y’ set to zero. Equation (43) is simplified and solved explicitly for D_7 :

$$\begin{aligned}
D_7 = & \left[\frac{v^2}{\theta} - \frac{v_{hs}}{v} D_8 - \left(\frac{v_{hs}}{v} \right)^2 D_9 - \left(\frac{v_{hs}}{v} \right)^3 D_{10} - D_{11} \Psi_0 v^2 \right] \\
& - \frac{v^2}{y} \left(1 - \frac{a_p}{a_{n-p}} \right) \left[P_c - (P_{hs})_{cp} \right]
\end{aligned} \tag{B-44}$$

By using Equation (39), the constraint equation for D_3 can be written as:

$$\begin{aligned}
& \left(-\frac{2v^5}{3\theta^2 v_{hs}} + \frac{2M^2 v^5}{3\theta^3 v_{hs}} - \frac{M v^4}{\theta^2 v_{hs}} \right) + \frac{\lambda v^5}{3v_{hs} a_{n-p}} + \frac{\beta v^4}{v_{hs} a_{n-p}} - \frac{8D_5 v_{hs}}{3v} \\
& - \frac{D_6 v^5}{3v_{hs}} \left(\gamma_2 - 3\frac{\gamma_1}{v} \right) = \left(1 + \frac{y}{a_p} \right) \left(-\frac{2v^5}{3\theta^2 v_{hs}} + \frac{2M^2 v^5}{3\theta^3 v_{hs}} - \frac{M v^4}{\theta^2 v_{hs}} \right) \\
& - \frac{y}{a_p} \left(D_8 + \frac{8D_9 v_{hs}}{3v} + \frac{5D_{10} (v_{hs})^2}{v^2} + \frac{D_{11} v^5}{3v_{hs}} \left(\Psi_2 - 3\frac{\Psi_1}{v} \right) \right) \\
& + \frac{\lambda v^5}{3v_{hs} a_p} + \frac{\beta v^4}{v_{hs} a_p} - \frac{8D_5 v_{hs}}{3v} - \frac{D_6 v^5}{3v_{hs}} \left(\gamma_2 - 3\frac{\gamma_1}{v} \right)
\end{aligned} \tag{B-45}$$

Equation (45) is simplified and solved explicitly for D_7 :

$$\begin{aligned}
D_8 = & \left(-\frac{2v^5}{3\theta^2 v_{hs}} + \frac{2M^2 v^5}{3\theta^3 v_{hs}} - \frac{M v^4}{\theta^2 v_{hs}} \right) \\
& - \left(\frac{8D_9 v_{hs}}{3v} + \frac{5D_{10} (v_{hs})^2}{v^2} + \frac{D_{11} v^5}{3v_{hs}} \left(\psi_2 - 3\frac{\psi_1}{v} \right) \right) \\
& + \frac{1}{y} \left(\frac{\lambda v^5}{3v_{hs}} + \frac{\beta v^4}{v_{hs}} \right) \left(1 - \frac{a_p}{a_{n-p}} \right)
\end{aligned} \tag{B-46}$$

The final constraint is that

$$D_{10} = -D_9 \tag{B-47}$$

The general ordered procedure for solving the constraint equations is as follows:

1. Solve Equations (17-26, 29) using the parameters provided in Tables 1-3.
2. Set Equation (47).
3. Solve Equation (38). If the fluid is polar, solve Equation (38) with $y = 0$ to obtain a_{n-p} .
4. If the fluid is polar, solve for D_7 and D_8 using Equations (44, 46). Otherwise, they are zero.
5. Solve for D_4 and then D_3 using equations (39, 40).

Table B-1: NIST Critical Property Values for Fluids Used in the HS-EOS (Linstrom and Mallard, 2003)

| | Critical Temperature (°R) | Critical Pressure (psia) | Critical Volume (cm³/mol) |
|-----------------|----------------------------------|---------------------------------|---|
| CO ₂ | 547.43076 | 1069.987 | 94.1185 |
| Methane | 343.015 | 667.06 | 98.6291 |
| Nitrogen | 227.146 | 492.52 | 89.4142 |
| Ethane | 549.594 | 706.59 | 145.5604 |
| Propane | 665.685 | 615.988 | 201.8106 |
| Butane | 765.225 | 550.56 | 255.1020 |
| Iso-Butane | 734.071 | 527.94 | 259.0674 |
| Pentane | 845.5 | 488.78 | 310.9840 |
| Ethene | 508.23 | 731.25 | 130.9415 |
| Argon | 271.237 | 705.32 | 74.5857 |
| Fluorine | 259.945 | 750.19 | 64.0902 |
| Oxygen | 278.246 | 731.43 | 73.3676 |
| NF ₃ | 421.2 | 646.97 | 126.2626 |
| R-32 | 632.259 | 838.6 | 122.6981 |
| Ammonia | 729.72 | 1643.71 | 75.6899 |
| R-123 | 822.296 | 531.1 | 278.0544 |
| R-124 | 711.765 | 525.6596 | 243.7053 |
| R-22 | 664.731 | 723.7 | 165.0650 |
| Water | 1164.77 | 3200.11 | 55.9480 |

Table B-2: Regressed Parameter Values for Fluids Used in the HS-EOS

| | V_{hs} (cm^3/mol) | C_1 | C_2 | C_3 | C_4 |
|-----------------|--|-----------|----------|---------|---------|
| CO ₂ | 15.412 | 0.35661 | 0.31773 | -8.6595 | -1.9121 |
| Methane | 16.264 | 0.13010 | 0.29940 | -10.930 | -1.4836 |
| Nitrogen | 14.768 | 0.12355 | 0.30736 | -12.273 | -1.4574 |
| Ethane | 24.052 | 0.18990 | 0.25077 | -7.8339 | -1.3376 |
| Propane | 33.073 | 0.25254 | 0.22787 | -7.1778 | -1.3294 |
| Butane | 42.108 | 0.30152 | 0.21610 | -6.5457 | -1.3140 |
| Iso-Butane | 42.449 | 0.28353 | 0.22067 | -6.9888 | -1.3232 |
| Pentane | 51.749 | 0.37219 | 0.15553 | -5.5725 | -1.2498 |
| Ethene | 21.361 | 0.13093 | 0.34228 | -8.2610 | -1.3930 |
| Argon | 12.281 | 0.10712 | 0.27006 | -11.859 | -1.4062 |
| Fluorine | 11.045 | 0.097463 | 0.27305 | -9.1866 | -1.2982 |
| Oxygen | 11.992 | 0.15891 | 0.29284 | -10.930 | -1.5128 |
| NF ₃ | 20.100 | 0.10941 | 0.33054 | -9.0037 | -1.3110 |
| R-32 | 20.907 | -0.043303 | 0.71405 | -12.117 | -1.5253 |
| Ammonia | 12.570 | -0.15536 | 0.95500 | -19.578 | -1.5616 |
| R-123 | 45.615 | 0.18001 | 0.50153 | -6.7692 | -1.2466 |
| R-124 | 40.684 | 0.24992 | 0.40448 | -7.2119 | -1.2730 |
| R-22 | 28.404 | 0.071094 | 0.56775 | -12.188 | -1.4251 |
| Water | 10.100 | -0.23184 | -0.26835 | -25.653 | -1.6630 |

Table B-3: Additional Regressed Parameter Values for Polar Fluids Used in the HS-EOS

| | $\frac{y}{\text{(psi L}^2/\text{mol}^2)}$ | D_9 | D_{11} | C_5 | C_6 | C_7 |
|---------|---|--------|----------|----------|----------|---------|
| NF3 | 1.1597 | 0.0000 | 0.81439 | 0.10000 | -3.5000 | 0.89664 |
| R-32 | 0.87715 | 819.83 | 56.045 | -0.85962 | -0.58634 | 3.0248 |
| Ammonia | 0.51868 | 964.69 | 84.164 | -1.1999 | -0.61906 | 3.0220 |
| R-123 | 0.15125 | 248.15 | 10.000 | -15.000 | -1.0000 | 4.2000 |
| R-124 | 0.31111 | 196.99 | 0.000 | -5.6056 | 0.000 | 0.000 |
| R-22 | 0.71113 | 540.20 | 51.873 | -1.4996 | -0.37543 | 2.9164 |
| Water | 1.0144 | 760.02 | 72.959 | -0.55205 | -0.76967 | 2.6498 |

APPENDIX C: FUGACITY DERIVATIONS FOR THE HARD-SPHERE EOS

For a *pure*-component gas, the fugacity, f , is given by:

$$\ln \frac{f}{P} = -\int_{\infty}^v \left(\frac{P}{RT} - \frac{1}{v} \right) dv - \ln Z + Z - 1 \quad (\text{C-1})$$

First the fugacity expression for a non-polar gas is derived. The integrand required for the integral (absent temperature dependent functions) is:

$$\begin{aligned} \frac{P}{RT} - \frac{1}{v} = & \frac{1}{v_{\text{hs}}} \left(B_2 \left(\frac{v_{\text{hs}}}{v} \right)^2 + B_3 \left(\frac{v_{\text{hs}}}{v} \right)^3 + B_4 \left(\frac{v_{\text{hs}}}{v} \right)^4 + \frac{C\xi(v_{\text{hs}}/(v\xi))^5}{1 - (v_{\text{hs}}/(v\xi))} \right) \\ & - \frac{a}{RT} \left(-\frac{1}{v^2 + D_1(v_{\text{hs}})v + D_2(v_{\text{hs}})^2} + \frac{D_3}{v^2} + D_4 \frac{v_{\text{hs}}}{v^3} + D_5 \frac{(v_{\text{hs}})^2}{v^4} + \frac{D_6 \left(\frac{v_{\text{hs}}}{v} \right)^3}{v^2 + D_1(v_{\text{hs}})v + D_2(v_{\text{hs}})^2} \right) \end{aligned} \quad (\text{C-2})$$

Upon integration we arrive at:

$$\begin{aligned}
\int \left(\frac{P}{RT} - \frac{1}{v} \right) dv = & -B_2 \left(\frac{v_{hs}}{v} \right) - \frac{B_3}{2} \left(\frac{v_{hs}}{v} \right)^2 - \frac{B_4}{3} \left(\frac{v_{hs}}{v} \right)^3 + C \left(\frac{1}{3} \left(\frac{v_{hs}}{v\xi} \right)^3 + \frac{1}{2} \left(\frac{v_{hs}}{v\xi} \right)^2 + \left(\frac{v_{hs}}{v\xi} \right) + \ln \left(\frac{v - v_{hs}/\xi}{v} \right) \right) \\
& - \frac{a}{v_{hs}RT} \left(\begin{aligned} & - \frac{2 \tan^{-1} \left(\frac{2v + D_1 v_{hs}}{v_{hs} \sqrt{4D_2 - D_1^2}} \right)}{\sqrt{4D_2 - D_1^2}} - D_3 \frac{v_{hs}}{v} - \frac{D_4}{2} \left(\frac{v_{hs}}{v} \right)^2 - \frac{D_5}{3} \left(\frac{v_{hs}}{v} \right)^3 \\ & - \frac{D_6}{2D_2} \left(\frac{v_{hs}}{v} \right)^2 + \frac{D_6 D_1}{D_2^2} \frac{v_{hs}}{v} + \frac{D_6}{D_2^3} (3D_1 D_2 - D_1^3) \frac{\tan^{-1} \left(\frac{2v + D_1 v_{hs}}{v_{hs} \sqrt{4D_2 - D_1^2}} \right)}{\sqrt{4D_2 - D_1^2}} \\ & + \frac{D_6}{2D_2^3} (D_1^2 - D_2) \ln \left(\frac{v^2}{v^2 + D_1 v_{hs} v + D_2 v_{hs}^2} \right) \end{aligned} \right) \quad (C-3)
\end{aligned}$$

and upon simplification of Equation (C-3):

$$\begin{aligned}
\int \left(\frac{P}{RT} - \frac{1}{v} \right) dv = & -B_2 x - \frac{B_3}{2} x^2 - \frac{B_4}{3} x^3 + C \left(\frac{1}{3} (x/\xi)^3 + \frac{1}{2} (x/\xi)^2 + (x/\xi) + \ln(1 - x/\xi) \right) \\
& - \frac{a}{v_{hs}RT} \left(\begin{aligned} & \frac{2 \tan^{-1} \left(\frac{2 + D_1 x}{x \sqrt{4D_2 - D_1^2}} \right)}{\sqrt{4D_2 - D_1^2}} \left(\frac{D_6}{2D_2^3} (3D_1 D_2 - D_1^3) - 1 \right) - D_3 x - \frac{D_4}{2} x^2 \\ & - \frac{D_5}{3} x^3 - \frac{D_6}{2D_2} x^2 + \frac{D_6 D_1}{D_2^2} x - \frac{D_6}{2D_2^3} (D_1^2 - D_2) \ln(1 + D_1 x + D_2 x^2) \end{aligned} \right) \quad (C-4)
\end{aligned}$$

We take the limits of the integral and multiply by negative one:

$$\begin{aligned}
 - \int_{x=0}^x \left(\frac{P}{RT} - \frac{1}{v} \right) dv = & B_2 x + \frac{B_3}{2} x^2 + \frac{B_4}{3} x^3 - C \left(\frac{1}{3} (x/\xi)^3 + \frac{1}{2} (x/\xi)^2 + (x/\xi) + \ln(1 - x/\xi) \right) \\
 & + \frac{a}{v_{hs} RT} \left(\frac{\left(2 \tan^{-1} \left(\frac{2 + D_1 x}{x \sqrt{4D_2 - D_1^2}} \right) - \pi \right)}{\sqrt{4D_2 - D_1^2}} \left(\frac{D_6}{2D_2^3} (3D_1 D_2 - D_1^3) - 1 \right) - D_3 x - \frac{D_4}{2} x^2 - \frac{D_5}{3} x^3 \right. \\
 & \left. - \frac{D_6}{2D_2} x^2 + \frac{D_6 D_1}{D_2^2} x - \frac{D_6}{2D_2^3} (D_1^2 - D_2) \ln(1 + D_1 x + D_2 x^2) \right) \quad (C-5)
 \end{aligned}$$

Finally, we evaluate the complete fugacity expression (for non-polar fluids), inserting the temperature-dependent functions for completeness:

$$\begin{aligned}
 \ln \frac{f}{P} = & B_2 x + \frac{B_3}{2} x^2 + \frac{B_4}{3} x^3 - C \left(\frac{1}{3} (x/\xi)^3 + \frac{1}{2} (x/\xi)^2 + (x/\xi) + \ln(1 - x/\xi) \right) + Z - 1 - \ln Z \\
 & + \frac{a T_r^{-C_1} e^{(1/T_r - 1)}}{v_{hs} RT} \left(\frac{\left(2 \tan^{-1} \left(\frac{2 + D_1 x}{x \sqrt{4D_2 - D_1^2}} \right) - \pi \right)}{\sqrt{4D_2 - D_1^2}} \left(\frac{D_6 T_r^{C_4}}{2D_2^3} (3D_1 D_2 - D_1^3) - 1 \right) + x \left(\frac{D_1 D_6 T_r^{C_4}}{D_2^2} - D_3 T_r^{1-C_2} \right) \right. \\
 & \left. - x^2 \left(\frac{D_6 T_r^{C_4}}{2D_2} + \frac{D_4 (1 + C_3 \ln(T_r))}{2} \right) - \frac{D_6 T_r^{C_4}}{2D_2^3} (D_1^2 - D_2) \ln(1 + D_1 x + D_2 x^2) \right) \quad (C-6)
 \end{aligned}$$

For a polar and pure gas, the integrand required (absent temperature dependent functions) is:

$$\begin{aligned}
 \frac{P}{RT} - \frac{1}{v} = & \frac{1}{v_{hs}} \left(B_2 \left(\frac{v_{hs}}{v} \right)^2 + B_3 \left(\frac{v_{hs}}{v} \right)^3 + B_4 \left(\frac{v_{hs}}{v} \right)^4 + \frac{C\xi (v_{hs}/(v\xi))^5}{(1 - (v_{hs}/(v\xi)))} \right) \\
 & - \frac{a}{RT} \left(-\frac{1}{v^2 + D_1(v_{hs})v + D_2(v_{hs})^2} + \frac{D_3}{v^2} + D_4 \frac{v_{hs}}{v^3} + D_5 \frac{(v_{hs})^2}{v^4} + \frac{D_6 \left(\frac{v_{hs}}{v} \right)^3}{v^2 + D_1(v_{hs})v + D_2(v_{hs})^2} \right) \quad (C-7) \\
 & - \frac{y}{RT} \left(-\frac{1}{v^2 + D_1(v_{hs})v + D_2(v_{hs})^2} + \frac{D_7}{v^2} + D_8 \frac{v_{hs}}{v^3} + D_9 \frac{(v_{hs})^2}{v^4} + D_{10} \frac{(v_{hs})^3}{v^5} + \frac{D_{11}\xi}{(v_{hs})^2} \frac{(v_{hs}/(v\xi))^5}{(1 - v_{hs}/(v\xi))} \right)
 \end{aligned}$$

The only new terms in Equation (C-7) compared to Equation (C-2) are those multiplied by the constant y . The fugacity expression for the polar fluid can be calculated by steps similar to those for the non-polar fluid. The expression for the fugacity for the polar fluid is:

$$\begin{aligned}
\ln \frac{f}{P} = & B_2 x + \frac{B_3}{2} x^2 + \frac{B_4}{3} x^3 - C \left(\frac{1}{3} (x/\xi)^3 + \frac{1}{2} (x/\xi)^2 + (x/\xi) + \ln(1 - x/\xi) \right) + Z - 1 - \ln Z \\
& + \frac{a T_r^{-C_1} e^{(1/T_r - 1)}}{v_{hs} RT} \left(\frac{\left(2 \tan^{-1} \left(\frac{2 + D_1 x}{x \sqrt{4D_2 - D_1^2}} \right) - \pi \right)}{\sqrt{4D_2 - D_1^2}} \left(\frac{D_6 T_r^{C_4}}{2D_2^3} (3D_1 D_2 - D_1^3) - 1 \right) + x \left(\frac{D_1 D_6 T_r^{C_4}}{D_2^2} - D_3 T_r^{1-C_2} \right) \right. \\
& \left. - x^2 \left(\frac{D_6 T_r^{C_4}}{2D_2} + \frac{D_4 (1 + C_3 \ln(T_r))}{2} \right) - \frac{D_6 T_r^{C_4}}{2D_2^3} (D_1^2 - D_2) \ln(1 + D_1 x + D_2 x^2) \right) \\
& + \frac{y T_r^{-C_1} e^{(1/T_r - 1)}}{v_{hs} RT} \left(- \frac{2 \tan^{-1} \left(\frac{2v + D_1 x}{x \sqrt{4D_2 - D_1^2}} \right) - \pi}{\sqrt{4D_2 - D_1^2}} - D_7 T_r^{1-C_2} x - x^2 \left(\frac{D_8}{2} + \frac{D_9}{3} x \right) (1 + C_5 \ln(T_r)) - \frac{D_{10}}{4} x^4 \right. \\
& \left. + D_{11} (1 + C_6 \ln(T_r) + C_7 (T_r - 1)) \left(\frac{1}{3} (x/\xi)^3 + \frac{1}{2} (x/\xi)^2 + (x/\xi) + \ln(1 - x/\xi) \right) \right)
\end{aligned} \tag{C-8}$$

VITA

James Edward Fitzgerald

Candidate for the Degree of

Doctor of Philosophy

Thesis: ADSORPTION OF PURE AND MULTI-COMPONENT GASES OF
IMPORTANCE TO ENHANCED COALBED METHANE RECOVERY:
MEASUREMENTS AND SIMPLIFIED LOCAL DENSITY MODELING

Major Field: Chemical Engineering

Biographical:

Personal Data: Born in Tulsa, Oklahoma, on December 1, 1976, the son of
Ken Fitzgerald and Ellen Eastwood

Education: Graduated from Booker T. Washington High School, Tulsa,
OK, in May 1995; received Bachelor of Science in Chemical
Engineering from Oklahoma State University, Stillwater,
Oklahoma in May 1999.
Completed the requirements for the Doctor of Philosophy degree
with a major in Chemical Engineering at Oklahoma State University in
July 2005.

Experience: employed by Oklahoma State University, School of
Chemical Engineering, as a teaching assistant and research assistant,
2000-present.

Professional Membership: American Institute of Chemical Engineers

Name: James Fitzgerald

Date of Degree: July, 2005

Institution: Oklahoma State University

Location: Stillwater, Oklahoma

Title of Study: ADSORPTION OF PURE AND MULTI-COMPONENT GASES OF IMPORTANCE TO ENHANCED COALBED METHANE RECOVERY: MEASUREMENTS AND SIMPLIFIED LOCAL DENSITY MODELING

Pages in Study: 226

Candidate for the Degree of Doctor of Philosophy

Major Field: Chemical Engineering

Scope and Method of Study:

The Simplified Local Density (SLD) theory was investigated to facilitate precise representations and accurate predictions for high-pressure, supercritical adsorption isotherms encountered in coalbed methane (CBM) recovery and CO₂ sequestration. Specifically, the ability of the SLD model to describe pure and mixed-gas adsorption was assessed using a modified Peng-Robinson (PR) equation of state (EOS). High-pressure adsorption measurements acquired in this study and data from the literature were used in this evaluation. In addition, a new pure-fluid EOS was developed to accommodate the future needs of high-pressure adsorption modeling.

Findings and Conclusions:

Precise gas adsorption measurements were completed using a constant-pressure, volumetric technique at temperatures between 318 and 328 K (113-131°F) and pressures to 13.8 MPa (2000 psia). These measurements included the pure-gas adsorption of methane, nitrogen, ethane, and CO₂ on eight coals and one activated carbon (wet Fruitland, wet Lower Basin Fruitland coal, wet / dry Illinois #6, wet Tiffany, dry Beulah Zap, dry Wyodak, dry Upper Freeport, dry Pocahontas, and dry Calgon Filtrasorb 400). Mixed-gas measurements for methane, nitrogen and CO₂ were conducted on the activated carbon and wet Tiffany coal.

Analysis of the SLD-PR model indicated that the limiting high-pressure adsorption behavior is governed by the high-density limit of the EOS, which is determined by the EOS covolume. Consequently, modification of the EOS covolume allowed for precise representation of pure-gas high-pressure adsorption and the reliable prediction of binary and ternary gas mixture adsorption. Specifically, the model can (a) represent adsorption on activated carbon and coals within their expected experimental uncertainties, and (b) provide generalized binary and ternary predictions, within two to three times the experimental uncertainties, based on regressed parameters from pure-gas adsorption data.

A new pure-fluid EOS capable of accurate representation of high-density behavior was developed. This EOS, which covers a wide range of phase conditions, utilizes an accurate hard-sphere repulsive term. Evaluation results for 19 fluids, including coalbed gases (CO₂, methane, and nitrogen) and water, indicated that the new EOS can represent precisely the volumetric behavior and the saturated vapor-liquid equilibrium properties of these pure fluids with average errors of 1%.

ADVISOR'S APPROVAL: _____ KHALED A. M. GASEM